UNIVERSITÉ DE STRASBOURG

ÉCOLE DOCTORALE DES SCIENCES DE LA TERRE, DE L'UNIVERS ET DE L'ENVIRONNEMENT

PhD Thesis presented by

Floriane PROVOST

For obtaining the degree
Doctor of the University of Strasbourg (PhD)

Clayey landslide seismology: use of endogenous seismic catalog for understanding the deformation pattern

Discipline : Geophysics

Public defense June 20^{th}, 2018

Promotor : **Jean-Philippe MALET**
Co-promotor : **Cécile DOUBRE**

Examination committee

Prof. Emma Suriñach,	University of Barcelona (UB), Barcelona	Reviewer
Dr. Gilles, Grandjean,	BRGM, Orléans	Reviewer
Dr. Jean Schmittbuhl,	EOST/IPGS, Strasbourg	Oral Examinator
Prof. Niels Hovius,	GFZ, Helmholtz Centre, Postdam	Oral Examinator
Dr. Fabian Walter,	ETH, Zurich	Oral Examinator
Dr. Jean-Philippe Malet,	EOST/IPGS, Strasbourg	Promotor
Dr. Agnès Helmstetter,	IsTerre, Grenoble	Invited

ACKNOWLEDGEMENTS

This thesis is the result of three years (and a little more) of research at the Institut de Physique du Globe de Strasbourg (IPGS) and at Ecole et Observatoire des Sciences de la Terre (EOST). This work could not have been done without the help and support of many people.

First, I thank my PhD promotor, Dr. Jean-Philippe Malet for encouraging me to start this research project, and to let me realize it with a lot of freedom. His support and advices have been invaluable to me in carrying out the various stages of this thesis. His energy, involvement and constant availability have been a motor to give the best of myself. Second, I would like to thank Dr. Cecile Doubre for her comments and pertinent remarks that allowed me to improve my work as well as Dr. Agnès Helmstetter of Institut des Sciences de la Terre (ISTerre) for giving me access to her processing codes and for her detailed and attentive comments when reading my draft papers. The arrival of Dr. Clément Hibert at EOST in the middle of my thesis has infused a new dynamic to the evolution of my knowledge and my work that evolved to a common reflexion and a true friendship. I strongly hope that both will continue.

I want to thank Prof. Emma Sũrinach and Dr. Gilles Grandjean to have accepted to be the reviewers of my thesis as well as the other members of the jury Dr. Jean Schmittbuhl, Prof. Niels Hovius and Prof. Fabian Walter to have accepted to assess my work.

During the course of my thesis I received generous support from several programs and institutes: the French National Research Agency (ANR) through the projects HYDROSLIDE "Hydrogeophysical Monitoring of Clayey Landslides", SAMCO "Adaptation de la Société aux Risques Gravitaires en Montagne dans un Contexte de Changement Global" and TIMES "High-performance processing techniques for mapping and monitoring environmental changes from massive, heterogeneous and high frequency data times series". Support of the Open Partial Agreement Major Hazards of Council of Europe through the project "Development of cost-effective ground-based and remote monitoring systems for detecting landslide initiation" is also acknowledged. I also benefit from the continuous seismic, geodetic and hydro-meterological data at Super-Sauze landslide provided by the Observatoire Multi-disciplinaire des Instabilités de Versant (OMIV) RESIF/OMIV (2015).

This thesis work is the result of many fieldwork periods. Without the help of all the people who accompanied me in the Alps, the data presented in this manuscript could not have been collected. Thanks to Julien G., my first guide at Super-Sauze and Juliette T., Candide L., Benoit C. for their helps. A big thank you to Patrice U. for his patience and giving me a hand. As Strasbourg is not located in the Alps, I would like to thank A. Remaître for his musical play-lists packed with his interesting conversations that made several travel trips feel shorter. Thanks to Pierre B. for this unforgettable hike around the Super-Sauze landslide and E. Faustin for this memorable return from Aiguilles. Thanks to the good mood of Martine T., G. Skupinski., K. Susanto, P. Bornemann., J. Vergne, C. Bertrand, G. Ferhat and all of those I could possibly forget... I will keep very good memories of those days. Thanks to Maxime B. for his availability (even at the really last minute). I also want to

thank the Chardenal family for their welcome and their helps in the Ubaye valley and to the staff of ONF-RTM: G. Guiter and P. Diot for their logistic support, I hope I adopted and kept their good moods.

I had the chance to contribute during the first two years of my PhD to the projects of the "Jardin des Sciences" and promote Earth Sciences through the Museum of Seismology of Strasbourg University. I learned a lot from this experience and I would like to thank Christelle S. who offered me the possibility to join their team, Cécile C., Manu, Marion, Claire, Natacha, Quentin, Sylvain. It was a great pleasure to work with you.

I have been dragging myself along the University of Strasbourg for a few years now. It has allowed me to meet many persons as people arrived and left while I remained. I would like to begin by thanking the different people with whom I shared Room 304: Aline D. and her jokes on Friday 4 pm, Eric H. with whom I shared these last months his good mood was very appreciated, Hugo L. for his support and long-standing friendship, Yann Z. who occasionally contributed to the Friday 4pm jokes, JR who was never far away for coffee breaks as well as Emilie K, Tom B and Alex more recently. Lately, the "landslide team" at EOST has increased giving me the occasion to meet wonderful persons: Andre S., Odin M., David M, Clément H. with whom I shared pleasant lunch at the Chariot talking about landslides, sciences and politics. Most of you contributed to broaden my ideas both on my research project and on many other subjects.

For all my friends I would like to thank you truly for your support and all the good moments I have shared so far in your company. I will keep so many good memories of my lifetime in Strasbourg, thanks to Camille J. one of the first persons I met in Strasbourg and one of the most generous one, Arthur T. and his machiavellian support, Fabien, Guillaume, for their visits, Anne-Sophie, Andrew, Marion, Ramon (and their sunday paellas), Delphine, Sara, Saskia (for the discussions in the Spessbourg kitchen), Sylvain, Chris, Charlène, Edouard, Jackson, Rico and by extension all the person I had the occasion to share a moment with. JB, Bérengère, Claire, Camille, Patrice your friendships mean a lot for me. It has been long years now I crossed the pass of the Leroy family who brought me so much: vegetables (Damien), massages (Sidoine), enthusiasm and friendships (all of you). In particular I would like to thank Mathilde for her endless friendship and Marine L. w(h)o accepted the tough task to become my roommate during my PhD. Her technical support during these last months is invaluable, her humor, tolerance and moral support also. It was a real pleasure to spend these three years together. I don't forget Claire G., who offered me so many getaways in the Strasbourg nightlife as well as in botanic hiking trips or juggling sessions.

I must acknowledge my family to a large extent. I had the chance to grow in freedom and love among you all. Especially, to my (still) little brothers whose love, support and sometimes confrontation contributed to made me become what I am presently. I want to express my heartfelt thanks to my parents for their constant encouragement and support. They always took care of each of our personalities and guided us throughout our own paths, I'm so grateful for that.

So far I managed to find words to express my gratitude … as I miss stronger ones I will simply thank Alberto. I am glad our life paths crossed in cold Norway. I can't wait to see where the future will drive us...

ABSTRACT

This research project aims at increasing knowledge on the mechanisms controlling the deformation of clayey landslides through the combination of passive seismic and geodetic monitoring. Recent studies have demonstrated that seismic monitoring is able to give interesting information on landslide mechanics and in some case to provide precursory patterns useful for failure forecasting. The recent installation of seismometers on landslides revealed a variety of seismic signals of law magnitude (ML < 1) suspected to be generated by slope deformation (falling, toppling, sliding, flowing), weathering of the slope material or fluid circulation. This endogenous seismicity needs to be categorized. We thus proposed a standard classification of the endogenous seismic sources; the objective of this standard is to be able to compare the seismic activity of several landslides and identify the mechanisms generating these seismic signals as well as their correlation with external forcing. Several signal properties (i.e. duration, spectral content and spectrogram shape) are taken into account to describe the different class of signals and allow generic comparison. We observe that similar signals recorded at different sites present the same properties and discussed the possible seismic sources considering the type of deformation observed on the studied slopes. These signal properties are used as features to classify the endogenous sources using machine learning algorithms. Indeed, manual classification of long seismological records is time-consuming and may be highly subjective. We proposed an automatic classification method based on the computation of 71 seismic attributes and the use of a supervised classifier. No attribute was selected a priori in order to create a generic multi-class classification method applicable to many landslide contexts. The method can be applied directly on the results of a simple detector. The automatic algorithm retrieves nearly 90% of sensitivity in comparison to a manually interpreted catalogs considered as references. We then proposed a new method (APOLoc) for automatizing seismic source location. Source location is a difficult problem on landslides because of the limitations imposed either by picking errors on the seismic waves arrival and by the use of inappropriate (or too simplistic) seismic velocity models. We propose a methodology to take into account these two sources of error. The methodology is iterative and uses an accurate P-wave velocity model (constructed from refraction seismic profiles) to locate the sources. The picking of the P-wave arrivals is performed initially with a Kurtosis-based algorithm and a first estimate of the location is calculated by analyzing the amplitude of the signal; the picking and the location are then iteratively improved until the correlation of the first arrivals is maximized. Finally, advanced catalogs of seismic sources are constructed for both long-term and short-term observation periods at selected landslides. The number of events, their properties and their location are correlated to the surface deformation pattern measured by GNSS and ground-based radar data, and to environmental parameters such as rainfall, snowmelt and pore-water pressures. Seismic activity rates are analyzed, and the regime of slope deformation are discussed.

The approach and the methods are developed and tested on the seismological and geodetic datasets acquired at the Super-Sauze landslide (Southeast French Alps).

RÉSUMÉ LONG

Les instabilités gravitaires représentent chaque année un risque majeur pour les sociétés à la fois en termes de dégâts matériels et humains. Sur les vingt dernières années (1995-2014), elles ont été responsables de 2154 victimes dont 1370 morts en Europe (Haque et al., 2016). Dans le monde, elles ont causé 32 322 victimes entre 2004 et 2010 (Petley, 2012). En moyenne, elles représentent de 1 à 4 milliards d'euros de pertes économiques par an (e.g. Europe, (Haque et al., 2016), USGS). La gestion de ce risque naturel reste difficile en particulier parce que les mécanismes physiques responsables du déclenchement et de l'accélération des glissements de terrain restent encore mal compris. En effet, plusieurs facteurs extérieurs, comme les fortes pluies, les tremblements de terre ou la fonte des neiges, peuvent interagir pour contrôler leur déclenchement. Lorsqu'une instabilité gravitaire est identifiée, des interventions de confortement comme l'installation de drains peuvent permettre de réduire les probabilités de rupture. Cependant, l'accélération soudaine de l'instabilité reste difficile à prédire à l'heure actuelle et les solutions proposées consistent en général à mesurer le déplacement superficiel du glissement pour estimer une date de rupture potentielle.

Depuis une dizaine d'années, la sismologie environnementale connaît un essor continu et s'impose progressivement comme un nouveau domaine d'étude. Celle-ci s'intéresse aux sources sismiques générées par les processus de surface (i.e. volcans, glaciers, rivières, glissements de terrain) ou encore les constructions humaines (i.e. ponts, barrages, immeubles). En effet, la sismologie est une méthode d'observation non-invasive, sensible aux processus de surface ou de sub-surface et permettant une mesure à haute fréquence (> 50Hz) et par conséquent, une résolution temporelle très précise (et difficilement égalée). Un intérêt grandissant est porté sur les signaux sismiques générés à l'échelle globale et locale par les instabilités gravitaires. La théorie et les expériences de laboratoires montrent l'existence possible de signaux sismiques précurseurs à l'activation des glissements de terrain. Des réseaux et des campagnes de mesures comportant des sismomètres se sont développés ces dernières années pour la surveillance des instabilités gravitaires à l'échelle locale (< 1km). L'analyse des signaux haute fréquence (> 1 s) a permis de documenter de nombreux signaux mais la caractérisation des sources à l'origine de ces signaux reste difficile. Ce type de signaux a déjà été observé mais pour un nombre encore restreint de cas à distance du versant (Caplan-Auerbach and Huggel, 2007a, Yamada et al., 2016a, Poli, 2017, Schöpa et al., 2017) et pour une seule fois par un réseau installé sur et à proximité du massif effondré (Amitrano et al., 2007). Par conséquent, les observations sismologiques peuvent constituer un observable supplémentaire et pertinent, pour comprendre les mécanismes de déformations, mais aussi, dans certains cas, pour intégrer des système d'alerte.

Dans ce travail, nous proposons de développer des méthodes sismologiques appliquées à la surveillance des glissements de terrain à l'échelle locale des pentes instables. Les travaux portent sur l'analyse des sources sismiques induites par les glissements de terrain de roches molles caractérisées par des matériaux meubles non consolidés. Ils sont souvent classés comme glissements de terrain à déplacement lent (vitesse < 10 m.month^{-1}), bien qu'ils puissent être soumis à une fluidisation soudaine du sol et évoluer à mesure que les débris coulent citep Malet2005, Vanasch2006, Mainsant2012a . Leur réactivation et / ou leur accélération sont actuellement très difficiles à prévoir car ils sont fortement sensibles aux petites fluctuations du champ de contraintes et aux légers changements du réseau de contact sur la surface de glissement. L'augmentation de la pression de l'eau interstitielle est le facteur le plus commun contrôlant l'activité de ces glissements de terrain. Par conséquent, des méthodes ont été développées pour prédire le déplacement de surface par des modèles hydrogéomécaniques, la mesure des précipitations et / ou de la pression interstitielle, afin de contrôler la circulation de fluide à partir de la tomographie par résistivité électrique citepuhlemann2017 ou pour détecter le début de la liquéfaction à partir de la corrélation sismique du bruit ambiant citep Mainsant2012b, Mainsant2012a. Cependant, des défaillances ou une réactivation de glissements de terrain argileux peuvent également résulter de la présence d'arcs de force à travers le réseau de contact entre les grains, ce qui conduit à des hétérogénéités de contraintes à une échelle nettement plus grande que celle des grains eux-mêmes. Cette caractéristique peut entraîner une forte avalanche d'activité précurseur justifiant la surveillance sismique de ces pentes.

Différentes études ont porté sur les sources sismiques endogènes générées par les glissements de terrain de roches molles. Étonnamment, de nombreuses sources ont été enregistrées tandis que le fluage asismique était le principal comportement supposé. cite Gomberg1995 est parmi les premières études à avoir installé des sismomètres sur le glissement de terrain de Slumgullion (États-Unis). Des signaux sismiques ont été enregistré et ont été associés à des ruptures fragiles le long des surfaces de cisaillement limitrophes. Ils ont répété cette expérience avec un réseau sismique plus dense et une période d'acquisition plus longue plusieurs années plus tard et ont confirmé la présence d'une activité sismique riche de cette pente citep Gomberg2011. Cependant, ils ont souligné la difficulté d'analyser l'ensemble de données et en particulier de localiser précisément les sources et de comparer les taux de déplacement discrets avec la distribution de la sismicité. Par conséquent, le lien entre le fluage à l'état d'équilibre du glissement de terrain et les signaux analogues à des tremblements n'a pu être confirmé. Des recherches similaires de courte durée ont été menées sur les pentes de Heumoes (Autriche), Super-Sauze (France) et Valoria (Italie) citep Walter2011, Walter2013, Tonnellier2013. Ils ont confirmé la présence de signaux de rupture fragiles sur les glissements de terrain de roches tendres et ont tenté d'analyser leur occurrence spatio-temporelle. Sur le plan spatial, les fractures fragiles sont supposées se produire soit aux surfaces latérales du glissement de terrain (Slumgullion et Super-Sauze), soit à la surface de glissement basale (Heumoes). En fonction du glissement de terrain, ils sont corrélés à la zone qui se déplace le plus rapidement (Super-Sauze, Slumgullion) ou plus lente (Heumoes). Au fur et à mesure que survient une rupture fragile, les sources sismiques sont associées à la localisation des zones non saturées des glissements de terrain formés principalement par la géométrie du substrat rocheux citep Walter2012, Walter2013, Tonnellier2013. Les ruptures fragiles augmentent après de fortes pluies citep Walter2012, Tonnellier2013 mais la corrélation avec le déplacement de surface reste faible. De fortes accélérations du glissement de terrain sont observées avec une augmentation des événements de rupture fragiles citep Gomberg2011, Tonnellier2013 mais, lors de régimes cinématiques plus lents, aucune corrélation n'est trouvée alors qu'une légère accélération est observée citep Tonnellier2013. Comme le soulignent les études, les sources sismiques générées lors de la déformation des glissements de terrain restent difficiles à interpréter en raison: a) de l'emplacement incertain de la source empêchant l'interprétation des sources et / ou l'inversion des mécanismes focaux; b) de la courte durée des campagnes de mesure (quelques mois), c) l'absence de jeux de données de surface distribués pour corréler l'occurrence de la source à des modèles de déformation spécifiques. De plus, un cadre général de classification et d'analyse des sources sismiques générées par les instabilités des pentes fait actuellement défaut et empêche la comparaison entre les sites et la compréhension des mécanismes à l'oeuvre.

En prenant en compte, le nombre actuel de réseaux sismologiques installés et le nombre croissant de publications sur le thème, mes travaux de thèse consiste à développer des méthodes de traitement adaptées au suivi sismologique des instabilités gravitaires à l'échelle locale. En particulier, nous nous sommes intéressés à documenter et analyser les sources sismiques générées par les glissements de terrain argilo-marneux caractérisés par des matériaux meubles et non consolidés. Ces glissements évoluent le plus souvent avec des vitesses lentes (< 10 m.mois^{-1}) bien qu'ils soient aussi sujets à des liquéfactions soudaines pouvant évoluer en laves torrentielles. Leur réactivation/accélération est actuellement très difficile à prévoir car leur stabilité est très sensible à de faibles variations du champ de contrainte et à de légères modifications des propriétés mécaniques des matériaux. Plusieurs processus mécaniques contrôlant la cinématique des glissements de terrain peuvent ainsi être à l'origine des ondes sismiques. En combinant observations sismologiques et géodésiques, nous souhaitons apporter des éléments de réponse aux questions suivantes :

- Quels sont les processus physiques "d'origine gravitair" associés à l'émission d'ondes sismiques ?
- Quelles informations peut-on tirer de leur distribution spatiale et temporelle sur les modes de déformations des glissements argilo-marneux ?
- Est-ce que l'augmentation du nombre de signaux sismiques d'origine gravitaire est un signe précurseur fiable pour prédire l'accélération et/ou la rupture d'un glissement argilo-marneux ?

Afin de répondre à ces questions, les objectifs de la recherche sont les suivants :

- Proposer une nomenclature standardisée de la sismicité endogène des mouvements de terrain.
- Développer une méthode de classification automatique des signaux sismiques enregistrés afin d'accélérer et d'objectiver la construction de catalogues instrumentaux.
- Développer une méthode de localisation des sources sismiques afin d'associer les sources sismiques à la déformation observée.
- Documenter la déformation de glissements de terrain par des campagnes de mesures de déplacement de surface à haute fréquence spatiale et temporelle (par radar interférométrique terrestre) et l'installation de réseau dense de sismomètres.
- Analyser de manière jointe des jeux de données sismologiques et géodésiques pour améliorer la compréhension du lien entre l'occurrence de signaux sismiques et la déformation observée.

Les recherches ont été menées à l'Université de Strasbourg à l'Institut de Physique du Globe de Strasbourg (IPGS, UMR 7516 CNRS-UNISTRA), sous la supervision du Dr. J.-P. Malet et Dr. C. Doubre. Il a été réalisé dans le cadre des projets français financés par SAMCO, HYDROSLIDE et TIMES, et certaines des méthodes développées seront utilisées pour calculer des produits avancés pour Observatoire français des glissements de terrain - OMIV. Les méthodes développées durant cette thèse ont principalement été testé sur des données acquises sur le glissement de Super-Sauze (Alpes-de-Haute-Provence, France) par l'Observatoire Multi-disciplinaire des Instabilités Gravitaires (OMIV). Le glissement de Super-Sauze a commencé à se développer dans les années 1960 dans les marnes noires charactéristiques de la vallée de l'Ubaye. Sa longueur et sa largeur actuelles sont de 1 km et 200 m respectivement et le glissement de terrain est orienté dans la direction nord-sud. Sa longueur et sa largeur actuelles sont respectivement de 1 km et 200 m et le glissement de terrain est orienté nord-sud. Sa profondeur est estimée à 15-20 m citep Travelletti2012b pour un volume total de 750 000 m ^{3}. Il est classé comme un glissement de terrain actif lent, mais les taux de déplacement sont très variables (de 0,01 à 0,40 m.j $^{-1}$). Ce site a été activement étudié et surveillé depuis les années 1990. En tant que sites permanents de l'Observatoire des multi-disciplinaires des instabilités de Versants, plusieurs instruments ont été installés tels que le GPS, les piézomètres, les inclinomètres et, depuis 2013, deux antennes sismiques. Les données acquises sur d'autres sites et par d'autres groupes de recherche ont aussi été analysées afin de comparer les signaux sismiques.

Cette thèse s'articule en quatre chapitres: le premier proposent, dans un premier temps, une revue des études sismologiques menées précédemment sur les glissements de terrain et dans un second temps, proposent une typologie générale de classification des signaux sismiques associé à la déformation des glissements de terrain. Une fois ce cadre posé, les chapitres 2 et 3 présentent les développements réalisés pour automatiser la construction de catalogues de sismicité. En particulier, une méthode de classification générique et une méthode de localisation sont proposées dans les chapitres 2 et 3 respectivement. Enfin, le chapitre 4 applique ces méthodes sur les données permanentes de Super-Sauze et le catalogue de sismicité ainsi réalisé est comparé aux données de déformations, météorologiques et piézométriques.

Le **Chapitre 1** propose une revue de l'ensemble des sites équipés ou ayant été équipés avec des sismomètres à travers le monde. Le type d'instrumentation ainsi que les stratégies de déploiement y sont développés. Les jeux de données de 14 sites ont pu être rassemblés et analysés. L'étude comparée de ces signaux a permis de proposer une typologie standard des sources sismiques endogènes de processus gravitaires. Le but de cette typologie est de proposer un cadre à l'analyse des signaux sismiques enregistrés lors de la déformation d'instabilités gravitaires permettant la construction de catalogues standardisés et la comparaison des signaux obtenus sur différents sites afin de converger vers des interprétations fiables de la sismicité générées par les instabilités gravitaires.

Ce chapitre est basé sur l'article cité et résumé ci-après:

Provost, F., Malet, J.-P., Hibert, C., Helmstetter, A., Radiguet, M., Amitrano, D., Langet, N., Larose, E., Abancó, C., Hürlimann, M., Lebourg, T., Levy, C., Le Roy, G., Ulrich, P., Vidal, M., and Vial, B. (2018). Towards a standard typology of endogenous landslide seismic sources, Earth Surf. Dynam. Discuss., https://doi.org/10.5194/esurf-2018-23 (in review).

***Résumé**: L'objectif de ce travail est de proposer une classification standard des signaux sismiques générés par des pentes instables et détectés à courte distance (< 1 km). Nous examinons d'abord les différentes études où des instruments sismiques ont été installés à l'échelle de la pente. Le choix des instruments sismiques et des géométries de réseau est présenté et discuté. Pour construire la typologie proposée, les observations sismiques acquises sur 14 sites sont analysées. Les sites sont représentatifs de divers types de glissements de terrain (ie. Glissement, chute, renversement et écoulement) et de matériaux (ie. des sols non consolidés aux roches consolidées). Nous étudions la bande de fréquences 1-100 Hz où la plus grande partie de l'énergie sismique est enregistrée à ces distances entre capteurs et sources permettant de comparer les signaux sismiques enregistrés. Plusieurs propriétés du signal (durée, contenu spectral et forme du spectrogramme) sont prises en compte pour décrire les sources. Les propriétés des signaux sont corrigées à partir de la réponse du signal du capteur et sont calculées dans la même bande de fréquence pour permettre la comparaison. Nous observons que des processus similaires génèrent des signaux similaires sur différents sites. Trois classes principales sont proposées: les sources de rassemblement "Slopequake" potentiellement présentes dans le corps du glissement de terrain et les "Rockfall" et "Granular Flow" rassemblant les signaux sismiques générés par la déformation à la surface du glissement de terrain. Plusieurs sous-classes sont proposées pour différencier des propriétés de signaux spécifiques (par exemple, résonance, contenu harmonique, etc.). Nous décrivons les propriétés du signal de chaque classe et présentons plusieurs exemples de signaux de la même classe enregistrés sur différents sites et discutons de leurs sources potentielles. La typologie proposée vise à servir de cadre pour des comparaisons plus poussées de la micro-sismicité endogène enregistrée sur les glissements de terrain. Les signaux discutés dans le manuscrit sont distribués en tant que matériel supplémentaire.*

Le **Chapitre 2** se concentre sur les méthodes de création automatique de catalogues instrumentaux de sources sismique de processus gravitaires. La construction de ces catalogues est un point crucial de l'analyse des données sismologiques permettant d'analyser l'évolution temporelle de l'occurrence des sources de sismicité. Le développement de réseaux sismologiques denses conduit à une multiplication du nombre de données à traiter. La construction manuelle de ces catalogues représente un temps de travail important tant pour traiter les données que pour former les opérateurs à reconnaître les différentes classes de signaux. De plus, l'interprétation d'un signal peut fortement varier d'un opérateur à un autre et ainsi générer des biais important dans l'analyse de la sismicité des glissements de terrain. La mise en place de méthodes de classification permet de réduire à la fois les temps de traitement de ces données et de fournir des catalogues génériques et objectifs. Nous proposons une méthode de classification automatique fondé sur un algorithme d'apprentissage machine dit « Forêt Aléatoire ». Une liste d'attributs a été établi afin de décrire le plus précisément possible les signaux sismiques pour le site experimenal du glissement de Super-Sauze. Au final, 71 attributs ont été retenus pour décrire la forme d'onde, le contenu spectral, l'évolution du contenu spectral et les caractéristiques des signaux en fonction de la localisation du capteur d'enregistrement. La méthode proposée permet d'obtenir des taux de classification « correcte » élevés, supérieure à la variance entre deux personnes classifiant les mêmes signaux.

Ce chapitre est basé sur l'article cité et résumé ci-après:

Provost, F., Hibert, C. and Malet, J.-P. (2017). Automatic classification of endogenous landslide seismicity using the Random Forest supervised classifier. Geophysical Research Letters, 44, 113–120, doi:10.1002/2016GL070709.

***Résumé**: La déformation des glissements de terrain lents se développant dans les argiles induit une sismicité endogène d'événements de faible magnitude (*$M_L < 1$*). Des enregistrements sismiques longs et des catalogues complets sont nécessaires pour identifier le type de sources sismiques et comprendre leurs mécanismes. La classification manuelle des enregistrements longs prend du temps et peut être subjective. Nous proposons une méthode de classification automatique basée sur le calcul de 71 attributs sismiques et l'utilisation d'un classificateur supervisé. Aucun attribut n'a été sélectionné à priori afin de créer une méthode de classification générique multi-classes applicable à de nombreux contextes de glissements de terrain. La méthode peut être appliquée directement sur les résultats d'un détecteur simple. Nous avons développé l'approche du réseau sismique de 8 capteurs du glissement de terrain riche en argile de Super-Sauze (Alpes du Sud françaises) pour la détection de quatre types de sources sismiques. L'algorithme automatique récupère 93% de sensibilité par rapport à un catalogue interprété manuellement considéré comme référence.*

Le **Chapitre 3** décrit le développement d'une méthode de localisation automatique des sources sismiques générées par la déformation des glissements de terrain. Cette étape est cruciale (lorsqu'elle est possible) pour interpréter les sources et pour identifier les zones actives des glissements. La méthode développée est fondée sur le pointé automatique des premières arrivées. Celui-ci est réalisé en plusieurs étapes : 1) un premier pointé est déterminé à l'aide de la fonction kurtosis, 2) le pointé est progressivement amélioré en corrélant les signaux des différentes traces. Afin d'améliorer la localisation et de réduire le temps de calcul, l'amplitude des signaux est aussi considérée pour déterminer de façon grossière la zone de recherche. La méthode est testée sur le glissement de Super-Sauze où un modèle de vitesse des ondes P en 3D a aussi été construit à partir d'une campagne de tomographie sismique. La méthode couplée à l'utilisation d'un modèle de vitesse sismique d'ondes P en 3D permet d'améliorer significativement la localisation des sources en réduisant par deux l'erreur sur l'épicentre de tirs de calibration.

Ce chapitre est basé sur l'article cité et résumé ci-après:

Provost, F., Malet,J.-P., Helmstetter, A., Gance, J., and Doubre, C. (2018). Automatic approach for increasing the location accuracy of slow-moving landslide endogenous seismicity: the *APOLoc* method, *Geophysical Journal International* (accepted, in press).

Résumé: *Les observations sismologiques offrent des indications précieuses sur les états de contrainte-déformation, les mécanismes physiques et les éventuels signes précurseurs de l'activation de divers processus de superficiels (volcans, glaciers, glissements de terrain). Les catalogues complets de la sismicité des glissements de terrain endogènes, c'est-à-dire correspondant aux sources sismiques générées par la pente instable d'origine mécanique ou hydrologique, devraient inclure la typologie et une estimation des paramètres sources (emplacement, magnitude) de l'événement. Ces catalogues avancés constituent une base solide pour mieux décrire la déformation de la pente et son évolution temporelle et mieux comprendre les facteurs de contrôle. Étant donné que le nombre d'événements sismiques dans les catalogues de glissements de terrain est généralement important, des approches automatiques doivent être envisagées pour définir à la fois la typologie et l'emplacement des sources. Nous proposons ici une nouvelle approche de localisation appelée textit Optimisation de la sélection automatique et méthode de localisation - textit APOLoc pour localiser les sources sismiques endogènes des glissements de terrain à partir de réseaux sismologiques situés à proximité. L'approche est basée sur le prélèvement automatique des arrivées d'ondes P en optimisant les corrélations inter-traces. La méthode est testée sur des coups de calibrage réalisés au glissement de Super-Sauze (Alpes du Sud-Est) et comparée à d'autres approches de localisation. En utilisant un modèle de vitesse réaliste obtenu à partir d'une campagne de tomographie sismique, textit APOLoc réduit les erreurs de l'épicentre à 23 m (en moyenne) par rapport à ca. 40 m pour les autres approches. textit APOLoc est ensuite appliqué pour documenter la sismicité endogène du glissement de terrain étudié (c'est-à-dire les "slopequakes" et les chutes de pierres).*

Finalement, le **Chapire 4** documente l'analyse de trois années d'observations sur le glissement de Super-Sauze (Alpes de Hautes Provence, France) où deux antennes sismologiques ont été installées depuis 2013. Les catalogues de sismicité sont créés à l'aide des méthodes développées dans le Chapitre 2 et Chapitre 3. La distribution temporelle et spatiale des catalogues correspondants aux sources associées à la déformation du glissement (i.e. chute de blocs, « slopequake ») sont ensuite analysées. Des corrélations sont calculées entre la série temporelle des sources sismiques et a) les données de précipitation enregistrées par la station météorologique localisées à 500 m du glissement b) les données de déplacement trois stations GPS situés sur le glissement pour les données permanentes ou du GB-SAR pour les données temporaires. Les cartes de sismicité sont aussi calculées et comparées aux données de déplacement distribuées (LiDAR) disponibles sur cette période pour les données permanentes et aux données GB-SAR pour les données de la campagne temporaire. Les résultat préliminaires de cette partie semble confirmer l'existence de signaux sismiques précurseurs à l'accéleration du glissement. On observe également une diminution de signaux de type "slopequake" lorsque la vitesse du glissement devient constante et que le niveau de la nappe atteind un maximum local. Une augmentation du nombre de "slopequake" est de nouveau observée lors de la décélération du glissement alors que le niveau de la nappe d'eau décroît. Ces résultats suggèrent que la possibilité d'enregistrer de signaux sismiques précurseurs à l'accélération des glissements argilo-marneux dépend fortement de la teneur en eau du sol. L'analyse de la répartition spaciale et temporelle des chutes de blocs montrent des variations saisonnières dans la localisation des chutes de blocs detectées mais aussi, un changement de localisation de la zone active de l'escarpement principal. Les chutes de blocs sont majoritairement déclenchées sur quelques heures voires quelques jours (i.e. > 80 chutes de blocs par jour) lors des périodes de fortes précipitations en automne et de la fonte des neiges au printemps.

Ce chapitre est basé sur l'article cité et résumé ci-après:

Provost, F., J.-P. Malet, C. Hibert, J. Point, C. Doubre. Patterns of landslide endogenous seismicity and their relationships with environmental forcings and motion, *(submitted)*

Abstract: *L'activation des instabilités gravitationnelles reste difficile à prévoir efficacement car elles peuvent être déclenchées par une combinaison de forçages externes et de processus internes. En particulier, les glissements de terrain argileux présentent une transition solide à fluide entraînant une accélération soudaine et difficilement prévisible. Nous avons analysé les sources sismiques générées par l'accélération de la pente au lanslide argileux de Super-Sauze. Trois années de données sismiques ont été analysées en utilisant un traitement automatique pour construire un catalogue de sismicité pour les séismes et les signaux de chutes de pierres. Ces dernières sont corrélées aux données météorologiques, au niveau des eaux souterraines et au mouvement des pentes. Nous avons constaté que la présence de sources sismiques était significativement corrélée aux précipitations et cessait rapidement lorsque la pluie s'arrêtait pour les chutes de pierres, tandis que le temps de relaxation était plus long pour les "slopequakes" (ie. microséismes générés par la déformation de l'instabilité). La présence de cycles de sismicité associés à l'accélération et à la décélération de la pente est observée. En effet, toutes les accélérations de la pente sont précédées par une augmentation du taux de "slopequakes" qui diminue lorsque le mouvement de la pente atteint une vitesse constante pendant le maximum local du niveau de la nappe phréatique. La décélération de la pente est alors associée à la décélération de la pente. Ceci suggère que le taux de sources sismiques générées par le mouvement de la pente n'est pas linéairement proportionnel à la vitesse de la pente, mais fortement contrôlé par la teneur en eau du sol.*

Le **Chapitre 5** propose une discussion et une conclusion générale des précédents chapitres et propose des pistes d'améliorations pour les parties méthodologiques. En effet, les méthodes séismologiques proposées dans cette thèse nécessitent encore des développements pour être intégrées dans des outils opérationnels de surveillance des instabilités gravitaires mais sont prometteuses pour la compréhension des mécanismes à l'oeuvre lors de l'activation des instabilités de versant.

CONTENTS

LIST OF FIGURES

LIST OF TABLES

INTRODUCTION

Research context: micro-seismicity of Earth surface processes

On April 18, 1889, an earthquake occurs in Tokyo (Japan) and is recorded for the first time at ca. 8000 km distance in Postdam (Germany) by two horizontal pendulums (Von Rebeur-Paschwitz, 1889). This revolutionary discovery lead to the development of Seismology, a new domain of Earth Sciences dedicated to the understanding of earthquakes and of the structure of the Solid Earth with seismic waves. Significant steps in the comprehension of the physical processes acting on the Earth have been enabled during the 20th century by the development of the seismological instrumentation, the multiplication of instruments worldwide as well as a continuous effort in data processing, diffusion and interpretation. Progressively, the scientific community focused its research to the analysis of other, less energetic (lower magnitude) sources of seismic waves such as tremors, low-frequency earthquakes in subduction zones, reservoir induced micro-seismicity and more recently surface processes.

In the recent years, a growing attention has been dedicated to Environmental Seismology. This field of seismology aims to investigate the natural seismic sources generated by Earth surface processes (i.e. volcanoes, glaciers, rivers, landslides) but also human-made structures (i.e. dams, buildings). This is explained by the advantage of seismic monitoring being non-invasive, sensitive to physical processes occurring at the surface or in depth and the high sampling frequency (>50 Hz) of the acquisition providing an accurate (and hardly equaled) time resolution. On volcanoes, eruptions and fluid migrations are detected and analyzed efficiently with seismic sensors (Chouet et al., 1994, Ferrazzini et al., 1991, Benoit and McNutt, 1997, Massin et al., 2011); more recently, cryo-seismology investigated the seismic sources generated during glacier deformation (e.g. calving, glacier sliding, moulin fluid circulation) with significant results (Podolskiy and Walter (2016) and references therein).

Since the 1990s, a growing number of studies have investigated the seismic radiations generated by landsliding at both global and local scales. Large landslides generate seismic radiations that can be detected at large disances (> 20 km) distances. Increasing the density of regional seismic networks worldwide hence presents a significant interest to construct exhaustive instrumental catalogs (Dammeier et al., 2016) and complements field testimonies and remote sensing inventories. Moreover, the recorded low-frequency radiations (> 10 s) can be inverted to estimate the landslide force history Ekström and Stark (2013), Yamada et al. (2013), Allstadt (2013), Hibert et al. (2014b,c) and retrieve critical landslide properties such as duration, mass, basal friction, and run-out trajectories. As predicted by theory and laboratory experiments, possible precursory events are also expected before mass collapse but have been recorded only a few times (Yamada et al., 2016a, Poli, 2017, Schöpa et al., 2017). Local seismic networks have also started to be installed around specific unstable slopes. At this scale, seismic monitoring is expected to be a reliable and complementary observable for landslide monitoring mainly to identify some precursors of a main rupture. A large variety of seismic events are documented from the analysis of high-frequency signals (>1 s). However, the characterization of the seismic sources from the seismic radiation remains challenging because of high attenuation in landslide media and of the complexity of high-frequency radiations.

Research objectives

In this work, we propose to develop seismological methods applied to landslide monitoring at the local scale of unstable slopes. The work focuses on the analysis of the micro-seismic sources induced by soft-rock landslides, which are characterized by loose, unconsolidated material. They are often classified as slow-moving landslide (velocity < 10 m.month^{-1}) although they may be subjected to sudden soil fluidization and may evolve as debris flows (Malet et al., 2005, van Asch et al., 2006, Mainsant et al., 2012a). Their reactivation and/or acceleration are currently very difficult to predict because they are strongly sensitive to small fluctuations of the stress field and to slight changes of the contact network at the slip surface. Increase of pore water pressures is the most common factor controlling the activity of these landslides. Consequently, methods have been developed to predict the surface displacement through hydro-geomechanical models, precipitation and/or pore pressure measurement (Bernardie et al., 2015), to monitor fluid circulation from electrical resistivity tomography (Uhlemann et al., 2017, Lebourg et al., 2005, Travelletti et al., 2012, Gance et al., 2016) or to detect liquefaction onset from seismic ambient noise correlation (Mainsant et al., 2012b,a). However, failures or reactivation of clayey landslides may also arise naturally from the presence of force arches exerted through the contact network between the grains that leads to stress heterogeneities at a scale significantly larger than the scale of the grains themselves. This feature may results in a high avalanche of precursor activity justifying seismic monitoring of these slopes.

Different studies investigated the endogenous micro-seismic sources generated by soft-rocks landslides. Surprisingly, numerous sources were recorded while aseismic creep was the main assumed behavior. Gomberg et al. (1995) is among the first study to have installed seismometers on a landslide. At the Slumgullion earthflow (USA), they recorded “slide quakes” events that they associated to brittle failures along side bounding shear surfaces. They repeated this experiment with a denser seismic network and longer period of acquisition several years later and confirmed the presence of a rich seismic activity of this slope (Gomberg et al., 2011). However, they pointed out the difficulty to analyze the dataset and in particular to locate accurately the sources and compare the discrete displacement rates with the distribution of the seismicity. Hence, the link between the landslide steady-state creep and the recorded tremor-like signals could not be confirmed. Similar short-time investigations were pursued at the Heumoes (Austria), Super-Sauze (France) and Valoria (Italy) slopes (Walter et al., 2011, 2013b, Tonnellier et al., 2013). They confirmed the presence of brittle fracture signals on soft-rock landslides and attempted to analyze their spatio-temporal occurrence. Spatially, the brittle fractures are assumed to occur either at the side-bounding surfaces of the landslide (Slumgullion and Super-Sauze) or at the basal slipping surface (Heumoes). Depending on the landslide, they correlate to the area moving the faster (Super-Sauze, Slumgullion) or the slower (Heumoes). As brittle failure occurs, the seismic sources are associated to the location of unsaturated zones of the landslides mostly formed by bedrock geometry (Walter et al., 2012a, 2013b, Tonnellier et al., 2013). Brittle failures are found to increase after heavy rainfall (Walter et al., 2012a, Tonnellier et al., 2013). The correlation with the surface displacement is less significant. Strong accelerations of the landslide are observed with an increase in brittle failure events (Gomberg et al., 2011, Tonnellier et al., 2013) but during slower kinematic regimes no correlation is found while slight acceleration is observed (Tonnellier et al., 2013). As pointed out by the studies, the seismic sources generated during soft-rock landslide deformation remain difficult to interpret due to a) uncertain source location preventing source interpretation and/or focal mechanisms inversion, b) short durations of the seismic campaign (often only a few months), c) the lack of distributed surface datasets to correlate the source occurrence to specific deformation patterns. Moreover, a general framework for classifying and analyzing seismic sources generated by slope instabilities is currently missing and prevents comparison between the sites and further comprehension of the mechanisms at works.

Research questions

The objective of our research is to investigate the relation between external forcing, surface displacement and seismic sources occurrences in soft-rock (clayey) landslides in order to answer the following questions:

- When and where do the seismic sources occur? What kind of physical processes generate these seismic sources?
- What information on the deformation can we deduce from the spatial and temporal distribution of the seismic events? Are seismic events possible precursors of the deformation and/or do they occur simultaneously?

To try to answer to these questions, we propose 1) to construct relevant catalogs with a standardized description of the sources, 2) to locate accurately the sources, 3) to correlate the seismic activity rate to the surface deformation rate and to forcings parameters in space and time. More precisely, the work carried out in this thesis consisted in:

- Field data acquisition at several sites in order to document at high frequency seismicity and surface displacement, by combining earth/spatial geodesy and seismology. Different sites have been instrument, all located in the European Alps (France, Austria). The same procedure has been applied and consisted in maximizing the number of seismic sensors installed on the slopes and on documenting the surface deformation with several techniques (ground-based radar, terrestrial LiDAR, GNSS and photographs) Especially, ground-based radar offers a distributed and high frequency acquisition (every 2 mins) of the surface displacement field.
- Developing data processing methods: robust processing chains adapted to landslide seismic signals for automatic classification and localization of the sources have been tailored. The methods are developed to build generic catalogs of seismicity including location of the sources.
- Data analysis and interpretation: spatio-temporal correlation between the occurrence of the seismic sources, precipitation, groundwater circulation, and surface motion are established. Dataset acquired on both permanent seismic networks and campaign networks are analyzed.

Study sites

The dataset of three soft-rock landslides (Figure 1) located in the European Alps (France and Austria) are used in the present work:

- Super-Sauze (French Alps), located in the Ubaye valley, started to develop in the 1960's in weathered black marls. Its current length and width are 1km and 200m respectively and the landslide is oriented in the North-South direction. Its depth is estimated to 15 to 20m (Travelletti and Malet, 2012b) for a total volume of 750,000 m^3. It is classified an active slow-moving landslide but the displacement rates are highly variable (from 0.01 to 0.40 m.day^{-1}). This site has been actively studied and monitored since the 1990's. As a permanent sites of OMIV (Observatoire des Multi-disciplinaires des Instabilités de Versants), several instruments have been installed such as GPS, piezometers, inclinometers and since 2013, two seismic arrays.
- Pechgraben (Austria), located in the in Austria, is a complex landslide that reactivated as a mudslide in 2013 after heavy rainfall. Displacement rates vary in space and time from mm.day-1 to m.day^{-1} (Lindner et al., 2016). It developed in clayey colluvium and shales over an area of 0.848 km^2 and a superficial depth of 8 m (Baron et al., 2017). Most of the landslide stopped moving

after several drainage countermeasures (Baron et al., 2017). However, some part of the area were not stabilized and remain active. Several measures and campaign have been carried out on the site since 2013. In particular, we installed two broad-band seismometers and one short-period seismic array during one month in 2016.

- Aiguilles – Pas de l'Ours (French Alps), located in the Queyras valley, is paleo-landslide that reactivated with high displacement rates (> 0.5 m.day^{-1}) in Spring 2017. It developed in unconsolidated schists and moraines. The current moving area is roughly 1 km × 1 km for a total estimated volume of 10 millions cubic meters. The landslide is threatening a road the only access to two villages and the supply of hydroelectric dam downstream. Consequently, numerous instruments have been installed on the site among them the GB-SAR and four seismometers since may 2017.

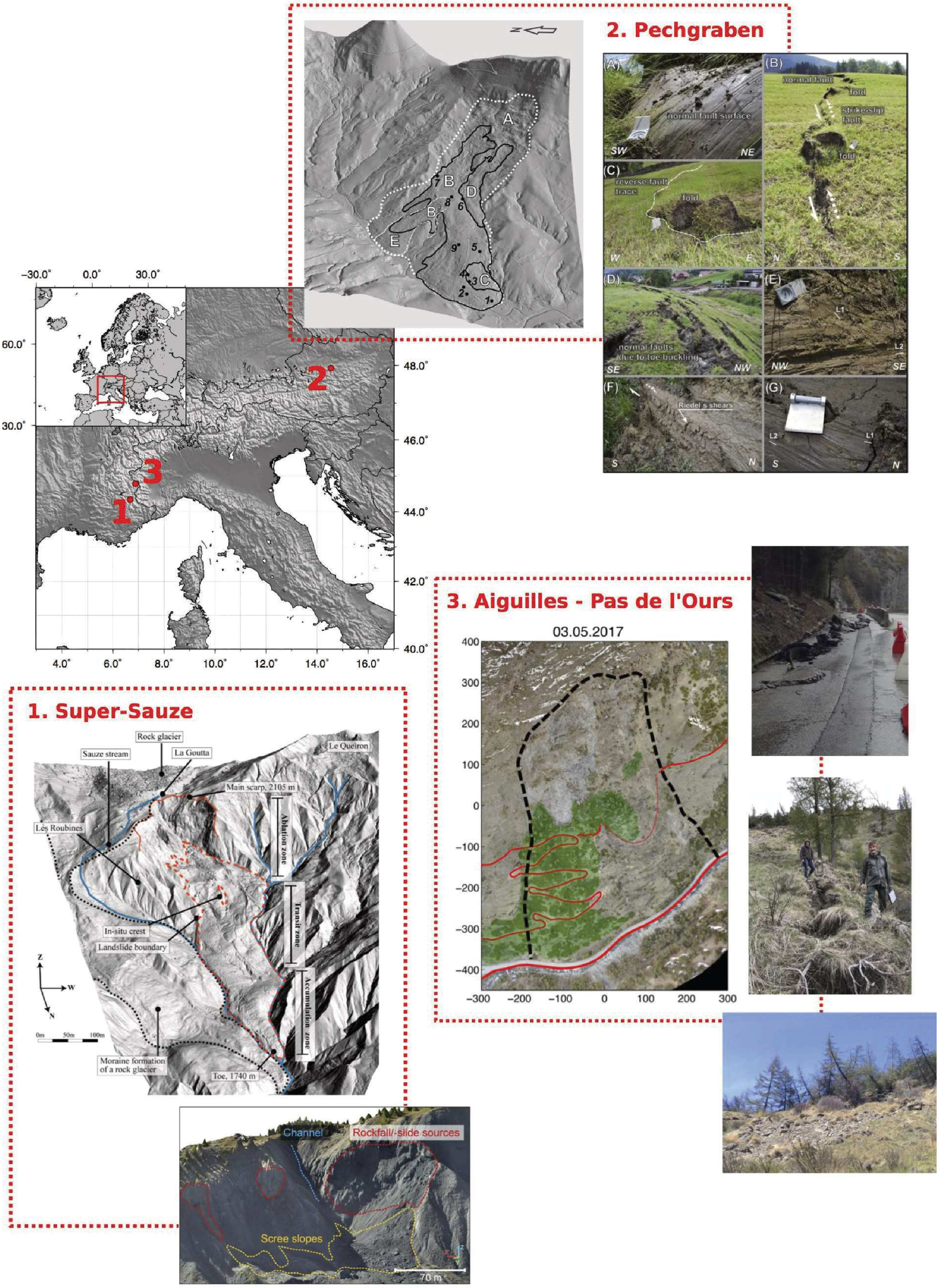

Figure 1: Map of instrumented unstable slopes. Modified photographs of the Pechgraben landslide from (Baron et al., 2017).

Outline of the thesis

The thesis manuscript is divided in four chapters (Figure 2). The **Chapter 1** provides a review the physical processes susceptible to generate seismic radiations on unstable slopes. The datasets of 14 sites are compared in order to propose a standard typology of the endogenous seismic signals recorded at proximity of unstable slopes. The possible sources of the recorded signals are also discussed.

In the **Chapter 2**, catalogs of seismicity are built in order to understand when do seismic sources occur. One of the goals of this chapter is also to propose automatic and robust method to build the catalogs. The recent development of Machine Learning algorithms offers different types of classifier such as Neural Networks or Decision Trees. The latter is chosen and tested for the case of landslide-induced seismicity. The classifier requires describing the signals as a vector of attributes. The latter were defined taking into account the criteria analyzed by human operator to determine a signal class.

The **Chapter 3** focuses on the location of the sources from the seismic signals. Indeed, this step is crucial to interpret the sources of the signals and better understand the occurrence of the seismic radiation recorded. This problem is challenging as soft-rock landslides are highly attenuating and may present complex underground structure. A location procedure is proposed based on the picking of the first arrivals and the use of the travel-time tables computed from a 3D velocity model. The latter is built from a seismic campaign realized on the Super-Sauze landslide in August 2014. The location procedure is tested and used on the seismic signals recorded at the Super-Sauze landslide.

Finally, **Chapter 4** the goal is to understand the spatio-temporal occurrence of the seismic sources. Correlations between the catalog of seismicity of the permanent stations on the Super-Sauze landslide and the precipitation and the displacement of two GPS stations are computed. The occurrence of the seismic events in space and time are analyzed and related to landslide motion and hydro-meteorological forcings.

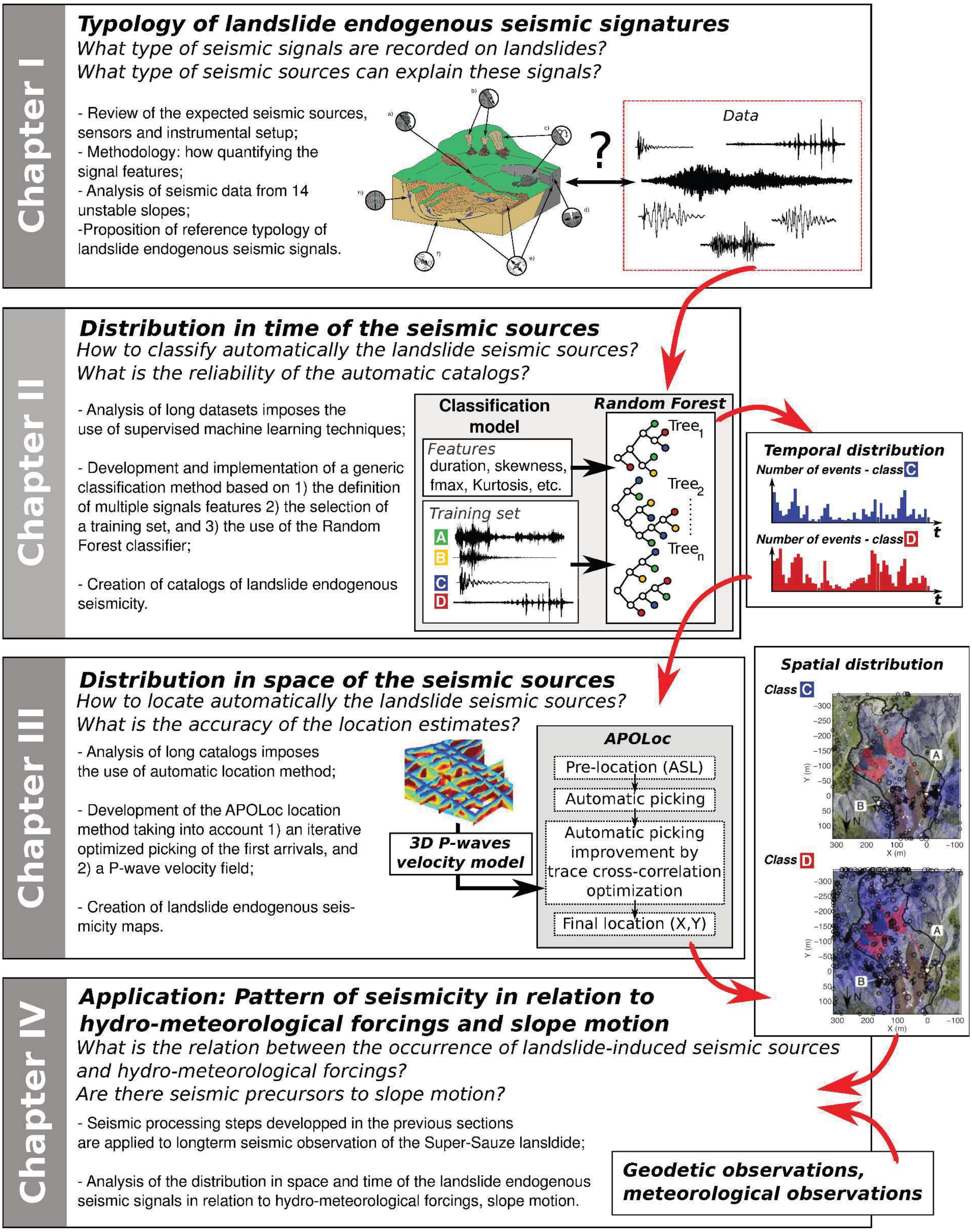

Typology of landslide endogenous seismic signatures
What type of seismic signals are recorded on landslides?
What type of seismic sources can explain these signals?

- Review of the expected seismic sources, sensors and instrumental setup;
- Methodology: how quantifying the signal features;
- Analysis of seismic data from 14 unstable slopes;
-Proposition of reference typology of landslide endogenous seismic signals.

Distribution in time of the seismic sources
How to classify automatically the landslide seismic sources?
What is the reliability of the automatic catalogs?

- Analysis of long datasets imposes the use of supervised machine learning techniques;

- Development and implementation of a generic classification method based on 1) the definition of multiple signals features 2) the selection of a training set, and 3) the use of the Random Forest classifier;

- Creation of catalogs of landslide endogenous seismicity.

Distribution in space of the seismic sources
How to locate automatically the landslide seismic sources?
What is the accuracy of the location estimates?

- Analysis of long catalogs imposes the use of automatic location method;

- Development of the APOLoc location method taking into account 1) an iterative optimized picking of the first arrivals, and 2) a P-wave velocity field;

- Creation of landslide endogenous seismicity maps.

Application: Pattern of seismicity in relation to hydro-meteorological forcings and slope motion
What is the relation between the occurrence of landslide-induced seismic sources and hydro-meteorological forcings?
Are there seismic precursors to slope motion?

- Seismic processing steps developped in the previous sections are applied to longterm seismic observation of the Super-Sauze lansldide;

- Analysis of the distribution in space and time of the landslide endogenous seismic signals in relation to hydro-meteorological forcings, slope motion.

Figure 2: Outline of the thesis.

Framework

The research was conducted at the University of Strasbourg at the Institut de Physique du Globe de Strasbourg (IPGS, UMR 7516 CNRS-UNISTRA), under the supervision of Dr. J.-P. Malet and Dr. C. Doubre. It has been carried out in the framework of the french funded projects SAMCO, HYDROSLIDE and TIMES, and some of the methods developed will be used to calculate advanced products for the French Landslide Observatory - OMIV.

CHAPTER 1| Typology of endogenous seismic sources generated by gravitational slope movements

The objective of **Chapter 1** is to propose a standard typology of the seismic signals generated by gravitational instabilities and propose or discuss their sources mechanisms.

Several studies have presented examples of seismic signals generated by landslides emphasizing their variety and their complexity. If the processes occurring at the surface (rockfall, debris flow, etc.) can easily be confirmed by other instrumental techniques (e.g. cameras, LiDAR surveys , the seismic signals generated by internal sources are more complex to understand; they are however important for understanding the landslide deformation pattern and could help for anticipating mass acceleration or forecast failure. One can assume that the same mechanical processes occur at different unstable slopes and, consequently, that the seismic signals share some common features. Proposing a generic and standard classification scheme of landslide endogenous seismic sources will help to correlate the seismic signals to mass movement activity (motion for landslides, number and size of falls for rockfalls) and hence to propose an interpretation for the source mechanism. Proposing a standard classification is also relevant for comparing the seismic activity recorded at several sites and propose relationships with the landslide forcing factors.

The first part of the chapter proposes a review of the previous results and methodologies developed for the seismic monitoring of landslide (Section 1.1), a description of the expected seismic sources for the landslide types (Section 1.2), and a review of the instrumented sites and monitoring strategies (sensors, array) worldwide (Section 1.3).

The second part of the chapter presents the classification scheme (Section 1.6) and the methodology to quantify the features of the signals (Section 1.5). Datasets of 14 sites have been analyzed to establish the classification. The sites are representative of the variety of soils/rocks and movements observed for landslides Hungr et al. (2014).

The chapter is based on:

Provost, F., Malet, J.-P., Hibert, C., Helmstetter, A., Radiguet, M., Amitrano, D., Langet, N., Larose, E., Abancó, C., Hürlimann, M., Lebourg, T., Levy, C., Le Roy, G., Ulrich, P., Vidal, M., and Vial, B. (2018). Towards a standard typology of endogenous landslide seismic sources, Earth Surf. Dynam. Discuss., https://doi.org/10.5194/esurf-2018-23 (in review)

Abstract: *The objective of this work is to propose a standard classification of seismic signals generated by unstable slopes and detected at close distances (< 1 km). We first review the different studies where seismic instruments have been installed at the slope scale. The choice of the seismic instruments and the network geometries are presented and discussed. To construct the proposed typology, seismic observations acquired at 14 sites are analyzed. The sites are representative of various landslide types (i.e. slide, fall, topple, and flow) and material (i.e. from unconsolidated soils to consolidated rocks). We investigate the 1-100Hz frequency band where most of the seismic energy is recorded at these sensor to source distances allowing comparison of the recorded seismic signals. Several signal properties (i.e. duration, spectral content and spectrogram shape) are taken into account to describe the sources. The signals properties are corrected from the sensor signal response and are computed in the same frequency band to enable comparison. We observe that similar processes generate similar signals at different sites. Three main classes are proposed:"Slopequake" gathering sources potentially occurring within the landslide body and "Rockfall" and "Granular Flow" gathering the seismic signals generated by deformation occurring at the surface of the landslide. Several sub-classes are proposed to differentiate specific signals properties (e.g. resonance, harmonic content,etc.). We describe the signal properties of each class and present several examples of signals of the same class recorded at different sites and discuss their potential sources. The proposed typology aims to serve as a framework for further comparisons of the endogenous micro-seismicity recorded on landslides. The signals discussed in the manuscript are distributed as supplementary material.*

1.1 Introduction

Seismology can be used to record (remotely and in a non-invasive way) ground deformation processes and to measure stress/strain conditions through the hydro-mechanical interactions occurring in the media. Seismology is widely used to understand the physical processes taking place on tectonic faults or volcanoes, to investigate fluid reservoir circulation, and more recently to analyze the dynamics of Earth surface processes such as glaciers (Podolskiy and Walter, 2016), snow avalanches (Leprettre, 1996, Sabot et al., 1998, Surin et al., 2000, Lacroix et al., 2012, Pérez-Guillén et al., 2016) and landslides (Deparis et al., 2008, Ekström and Stark, 2013, Gomberg et al., 1995, Rouse et al., 1991). In this manuscript, the term landslide describes a wide variety of processes resulting from the downslope movement of slope-forming materials by falling, toppling, sliding or flowing mechanisms (Hungr et al., 2014). Thus, landslides cover a large range of deformation processes, that can be differentiated in terms of sizes and volumes (smaller than 1 m^3 up to more than 10^7 m^3), in terms of displacement rates (mm.$yr^{-}1$ to m.$s^{-}1$), and in terms of mobilized material (hard/soft rocks, debris, poorly consolidated soils, and artificial fills).

With the increasing number of seismic sensors deployed worldwide and to the development of automatic seismological processing chains, the construction of landslide catalogs using seismology is now possible, especially at the regional scale (e.g. Switzerland, Hammer et al. (2013), Dammeier et al. (2016); France, Deparis et al. (2008)). However, the forecast of a particular landslide rupture or acceleration is still challenging at the slope scale, which is the focus of this work. In the 1960s, Cadman and Goodman (1967) observed an increase of Acoustic Emissions (AE) generated by slopes tilted towards failure at both laboratory and field scales. AEs are high frequency (10-1000 kHz) body waves generated by the release of strain energy through grain rearrangement (Michlmayr et al., 2012). Further studies confirmed these results for several slopes (Rouse et al., 1991, Smith et al., 2014, Dixon et al., 2015, 2018) where correlations between AE, surface displacement and heavy rainfall were documented. AEs record deep deformation processes before signs of displacement are identifiable at the surface. However, AEs are rapidly attenuated with the distance to the sources. The location of the sensors and the type of waveguide are also critical to capture the slope behavior. Recent developments of Fiber Optic Distributed Acoustic Systems (FO-DAS) offer the opportunity to overcome attenuation limitations and deploy measures over long distances (Michlmayr et al., 2017).

More recently, several studies focused on the analysis of the micro-seismicity (MS) observed on unstable slopes. MS studies analyze the seismic waves generated by the release of strain energy in the ground at larger scale than the grain to grain interactions in the frequency range of 1 to 500 Hz. The method offers the opportunity to remotely record the spatial distribution of the deformation through time (McCann and Forster, 1990, BRGM, 1995) and is less sensitive to attenuation than AE methods. Gomberg et al. (1995) installed seismometers on the Slumgullion slow-moving landslide (Colorado, USA) in order to understand the mechanical processes taking place during landslide deformation. Further studies used the same method for several slope configurations (hard/soft rocks, soils, very slow to rapid movements) but also investigated the possible links between the displacement rate and the seismic energy release (Spillmann et al., 2007, Helmstetter and Garambois, 2010, Walter et al., 2012a, 2013b, Tonnellier et al., 2013). Helmstetter and Garambois (2010) correlated the seismic response of the Séchilienne rockslide with the surface displacement rate and the rainfall amount. The analysis of the seismic waves generated by landslides allows monitoring spatio-temporal changes of the stress-strain field in the material from the scale of microscopic internal damage (Dixon et al., 2003, Michlmayr et al., 2012, Smith et al., 2017) to the initiation (e.g. pre-failure) of large ruptures (Amitrano et al., 2005, Yamada et al., 2016b, Poli, 2017, Schöpa et al., 2017). Both the failure and surface processes (e.g. rockfall, debris flow) generate seismic waves. Physical properties (mass, bulk momentum, velocity, trajectory) of the landslide can be inferred from the analysis of the seismic signals (Kanamori et al., 1984, Brodsky et al., 2003, Lacroix and Helmstetter, 2011, Ekström and Stark, 2013, Tang et al., 2015, Hibert et al., 2014a, Levy et al., 2015). On clayey landslides, drops of shear wave velocity have been observed before acceleration episodes. This shear wave variation through time has been documented using noise correlation techniques for laboratory experiments (Mainsant et al., 2012b), and for a few cases in the field at Pont-Bourquin landslide (Switzerland, Mainsant et al. (2012a)), at Harmaliére landslide (France, Bièvre et al. (2017)) and at Just-Tegoborze landslide (Poland, Harba and Pilecki (2017)). Precursory seismic signals are also expected and documented before large failures. Precursory increase in micro-seismic activity (in terms of event rates and/or average amplitudes) has been observed first before the fall of a coastal cliff (Mesnil-Val, France, Amitrano et al. (2005)) and was interpreted as the propagation of a fracture. More recently, repeating events have been detected before the Rausu landslide (Japan, Yamada et al. (2016b)) and the Nuugaatsiaq landslide (Greenland, Poli (2017)). These events are likely associated with the repeated failure of asperities surrounded by aseismic slip, driven by the acceleration of the slope displacement during the nucleation phase of the landslide rupture. Schöpa et al. (2017) recorded harmonic tremors that started 30 min before the failure of the Askja caldera landslide (Iceland) with temporal fluctuations of resonance frequency around 2.5 Hz. This complex tremor signal was interpreted as repeating stick-slip events with very short recurrence times (less than 1 s) producing a continuous signal. However, the characterization of the size of the asperity and the velocity of the ruptures associated to these precursory signals are difficult to invert mostly because of the lack of dense seismic network at close proximity of the slope instability (Schöpa et al., 2017). Therefore, the monitoring of endogenous MS may represent a promising approach especially, with the advent of robust, cheaper and portable seismic sensors and digitizers. It is now possible to install dense sensor networks close to the unstable slopes and record low amplitude signals in broad frequency bands. A wide variety of unstable slopes are currently monitored (i.e. through permanent or campaign installation) with seismic networks of different sizes and instruments (Table 1.1).

Understanding the possible mechanisms generating these seismic signals needs to be achieved. The discrimination of the endogenous landslide seismic signals is difficult and need to be established. The objective of this paper is thus to propose a typology of the landslide micro-seismic signals recorded in the field. The proposed typology is based on the analysis of observations from 14 monitored sites. The typology includes all the seismic sources recorded at near distances (< 1 km) and in the frequency range of MS studies (1-500 Hz), and generated by landslides 1) developed in hard/soft rocks and soils, 2) characterized by fragile (i.e. rupture) and ductile (i.e. viscous) deformation mechanisms.

In our work, we first discuss all the physical processes that occur on landslides and may generate seismic signals. We further present the available seismic sensors, the most commonly used network geometry and the instrumented sites. Then we establish a classification scheme of the landslide seismic signals from relevant signal features based on the analysis of the datasets of 14 sites. We further discuss the perspectives and remaining challenges of monitoring landslide deformation with MS approaches. The seismic signals associated with very large rock/debris avalanches and slides observed at regional distances are out of the scope of this work.

Table 1.1: Table of the instrumented sites. The bolded names correspond to the sites investigated in the present paper to establish the typology.

#	Site	Location	Type	Material	Sensor	Duration	Reference/Research Group
1	Randa	Switzerland	Slide	Hard rock	G	SC	Spillmann et al. (2007)
2	**Séchilienne**	France	Slide	Hard rock	G, SP	P	RESIF/OMIV (2015), Helmstetter and Garambois (2010), Lacroix and Helmstetter (2011)
3	**La Clapière**	France	Slide	Hard rock	SP(?)	P	RESIF/OMIV (2015), Palis et al. (2017)
4	**Aaknes**	Norway	Slide	Hard rock	G,BB	P	Roth et al. (2008)
5	Peschiera Spring	Italy	Slide	Hard rock	A	SC	Lenti et al. (2013)
6	Gradenbach	Austria	Slide	Hard rock	SP	P(?)	Brückl et al. (2013)
7	Alestch-Moosfluh	Switzerland	Slide	Hard rock	BB	P	Helmstetter et al. (2017b), Manconi and Coviello (2018)
8	Torgiovannetto, Assisi	Italy	Slide	Hard rock	SP	SC	Lotti et al. (2015)
9	Akatami landslide	Japan	Slide	Hard rock	(?)	(?)	-
10	Akkeshi landslide	Japan	Slide	Hard rock	SP	P	Doi et al. (2015)
11	Rausu landslide	Japan	Slide	Hard rock	BB	P	Yamada et al. (2016a)
12	Fergurson slide / Mercel River	USA / California	Slide	Hard rock	(?)	(?)	Harp et al. (2008)
13	Turtle Mountain - Frank slide	Canada	Slide	Hard rock	G	P	Chen et al. (2005)
14	**Aiguilles-Pas de l'Ours**	France	Slide	Soft rock / Earth	BB	SC	RESIF/OMIV (2015)
15	Harmalière	France	Slide	Soft-rock	SP,BB	P	Bièvre et al. (2017)
16	Utiku	New Zealand	Slide	Soft rock / Earth	(?)	P	Voisin et al. (2013)
17	Villerville	France	Slide	Soft rock / Mud	BB	SC,P	RESIF/OMIV (2015)
18	**Super-Sauze**	France	Slide	Soft rock / Mud	SP	P, RC	RESIF/OMIV (2015), Walter et al. (2012a), Tonnellier et al. (2013), Vouillamoz et al. (2017)

Continued on next page

Table 1.1 – continued from previous page

#	Site	Location	Type	Material	Sensor	Duration	Reference/Research Group
19	**Pont Bourquin**	Switzerland	Slide	Mud	SP(?)	P	Mainsant et al. (2012a), Larose et al. (2015)
20	Valoria	Italy	Slide	Mud	SP	SC	Tonnellier et al. (2013)
21	**Pechgraben**	Austria	Slide	Mud	SP,BB	RC	Vouillamoz et al. (2017)
22	US highway 50, CA	USA	Slide	Earth	G	P	USGS
23	**Slumgullion**	USA	Slide	Earth	G	RC	Gomberg et al. (1995, 2011)
24	Millcoma Meander, Oregon	USA	Slide	Earth	G	P	USGS
25	Xishancun	China	Slide	Earth	BB	SC	-
26	Chambon Tunnel	France	Slide	Earth	SP	P	-
27	Maca	Peru	Slide	Soft rock / Earth	SP	P(?)	Larose (2017)
28	Heumoes	Germany	Slide	Soft rock / Earth	SP	RC	Walter et al. (2011)
29	Mission Peak landslide	USA / California	Slide	Soft rock / Earth	BB	P	Hartzell et al. (2017)
30	Char d'Osset	France	Slide, Fall	Soft rock / Mud			-
31	Mesnil-Val	France	Fall	Hard rock	G	SC	Amitrano et al. (2005), Senfaute et al. (2009)
32	North Yorkshire coast	United Kingdom	Fall	Hard rock	BB	P	Norman et al. (2013)
33	Matterhorn peak	Italy	Fall	Hard rock	G	RC	Amitrano et al. (2010), Occhiena et al. (2012)
34	Madonna del sasso	Italy	Fall	Hard rock	SP	P(?)	Colombero et al. (2018)
35	**Chamousset**	France	Fall	Hard rock	SH	RC	Lévy et al. (2010), Bottelin et al. (2013b)
36	Mont-Granier	France	Fall	Hard rock	BB	P	-
37	Les Arches	France	Fall	Hard rock	SP	P(?)	Bottelin et al. (2013a,b)
38	La Praz	France	Fall	Hard rock	SP	P(?)	Bottelin et al. (2013b)
39	Rubi	France	Fall	Hard rock	SP	P(?)	Bottelin et al. (2013b)
40	La Suche	Switzerland	Fall	Hard rock	SP	P(?)	Bottelin et al. (2013b)
41	**St. Eynard**	France	Fall	Hard rock	SP	P(?)	Le Roy et al. (2017, 2018)
42	Cap d'Ailly	France	Fall	Hard rock			-

Continued on next page

Table 1.1 – continued from previous page

#	Site	Location	Type	Material	Sensor	Duration	Reference/Research Group
43	Lauterbrunnen valley	Switzerland	Fall	Hard rock	BB	SC	Dietze et al. (2017a,b)
44	Three Brothers	USA	Fall	Hard rock	SP	SC	Zimmer and Sitar (2015)
45	Mount Néron	France	Fall (triggered)	Hard rock	BB	SC	Bottelin et al. (2014)
46	**Riou Bourdoux**	France	Fall (triggered)	Hard rock	SP,BB	SC	Hibert et al. (2017a)
47	Montserrat	Spain	Fall (triggered)	Hard rock	SP	SC	Vilajosana et al. (2008)
48	**Piton de la Fournaise**	France	Fall, Flow	Volcanic rock	BB	P	OPVF/IPGP, Hibert et al. (2011, 2014a), Levy et al. (2015), Hibert et al. (2017c)
49	Bolungavík - Oshlíðslope	Iceland	Fall, Flow	Hard rock	A	P	Bessason et al. (2007)
50	**Rebaixader**	Spain	Flow	Debris	G	P	Abancó et al. (2012, 2014), Hürlimann et al. (2014), Arattano et al. (2014)
51	Manival torrent	France	Flow	Debris	G	P	Navratil et al. (2012)
52	Réal torrent	France	Flow	Debris	G	P	Navratil et al. (2012)
53	Marderello torrent	Italy	Flow	Debris	G	P	Arattano et al. (2016)
54	Acquabona torrent	Italy	Flow	Debris	G	P(?)	Berti et al. (2000), Galgaro et al. (2005)
55	Moscardo torrent	Italy	Flow	Debris	SP	P	Arattano and Moia (1999)
56	Gadria torrent	Italy	Flow	Debris	G	P	Arattano et al. (2016)
57	Mt. Yakedake volcano - Kamikamihorizawa Creek	Japan	Flow	Debris			Suwa et al. (2009)

Continued on next page

Table 1.1 – continued from previous page

#	Site	Location	Type	Material	Sensor	Duration	Reference/Research Group
58	Lattenbach torrent	Austria	Flow	Debris	G	P(?)	Schimmel and Hübl (2016), Kogelnig et al. (2014)
59	Illgraben torrent	Switzerland	Flow	Debris	G	P	Burtin et al. (2014), Walter et al. (2017b)
60	Farstrine torrent	Austria	Flow	Debris	G	P(?)	Schimmel and Hübl (2016)
61	Wartschenbach torrent	Austria	Flow	Debris	G	P(?)	Schimmel and Hübl (2016)
62	Dristenau torrent	Austria	Flow	Debris	G	P(?)	Schimmel and Hübl (2016)
63	Shenmu creek	Taiwan	Flow	Debris	G	P	Yin et al. (2011)
64	Ai-Yu-Zi creek	Taiwan	Flow	Debris	G	P	Huang et al. (2007)
65	Fong-Ciou creek	Taiwan	Flow	Debris	G	P	Huang et al. (2007)
66	Chenyoulan creek	Taiwan	Flow	Debris	G	SC	Burtin et al. (2013)
67	Mt. Sakurajima Volcano - Nojiri Torrent	Japan	Flow	Debris	G	P	Itakura et al. (2000)
68	Mount Pinatubo	Philippines	Flow	Debris	G	P	Marcial et al. (1996)
69	Colima volcano	Mexico	Flow	Debris	LP	P	Zobin et al. (2009), Vázquez et al. (2016)
70	Merapi volcano	Indonesia	Flow	Debris	G	P	Lavigne et al. (2000)
71	Nevado del Huila volcano	Colombia	Flow	Debris	G	P?	Worni et al. (2012)
72	Cotopaxi volcano	Ecuador	Flow	Debris	BB	P	Kumagai et al. (2009)
73	Mount Ruapehu	New-Zeland	Flow	Debris	BB	P	Lube et al. (2012)
74	Sawatch Range, Colorado	USA	Flow	Debris	G	P	Kean et al.

G: Geophone (f = [0.1-10] kHz); SP: Short-Period (f = [0.1-100] Hz); BB: Broad-Band (f = [10^{-2}-100] Hz); A: Accelerometer;
P: Permanent monitoring; RC: Repetitive Campaigns; SC: Single Campaign.
OPVF/IPGP: Volcanological Observatory of the Piton de la Fournaise / Institut de Physique du Globe de Paris.

Continued on next page

Table 1.1 – continued from previous page

#	Site	Location	Type	Material	Sensor	Duration	Reference/Research Group

USGS: United States Geological Survey (https://landslides.usgs.gov/monitoring/).

1.2 Description of landslide endogenous seismic sources

This section describes the possible hydro-mechanical processes observed on landslides and susceptible to generate seismic sources (Figure 1.1). We present the conditions controlling their occurrences (type of material, topography), their sizes, and their mechanical properties.

1.2.1 Fracture related sources

The term fracture denominates any discontinuous surface observed in consolidated media and originating from the formation of the rocks (i.e. joint) or the action of tectonic (i.e. schistosity), gravitational or hydraulic loads. In the case of slow-moving landslides, the propagation of the material also creates fractures on the edge and at the base of the moving material. Fractures occur in all type of materials at different scales from grain rupture to metric faults. The term fissure is sometimes used to describe fractures affecting the surface of the ground and for fractures affecting poorly consolidated material. We here include all these surface discontinuities under the general term “fracture”. Fractures are generated in three basic modes (I: opening, II: sliding and III: tearing) depending on the movement of the medium on the sides of the fracture plane. They result from either brittle failure of the media or from dessication effects forming polygonal failures during soil drying. On landslides, most of the fractures occur in a tensile mode because of the low tensile toughness of the landslide material and the shallow depth (Stumpf et al., 2013). The formation of fractures can also be generated in depth by progressive degradation of the rock through ground shaking and/or through weathering and long-term damage due to gravitational load. At the base and on the edges of the landslide, the movement is assumed to develop fractures in shear mode, creating sliding surfaces. Shearing on the fracture plane and tensile fracture opening/closing generate seismic signals. Shearing takes place at different scales from earthquakes on tectonic plates to grain friction and generates a variety of seismic signals (Zigone et al., 2011). Unstable regime leads to stick-slip behavior where the stress is regularly suddenly released generating impulsive seismic events. Tremor like signals or isolated impulsive or emergent events are also generated during plate motions. This variety of signals are observed during glacier motion. Deep icequakes are usually associated to basal motion (Winberry et al., 2011, Pratt et al., 2014, Helmstetter et al., 2015a,b, Röösli et al., 2016a, Podolskiy and Walter, 2016). Tremor like signals are also recorded during glacier motion (Lipovsky and Dunham, 2016). They are characterized by long duration signals of low amplitudes with no clear phase onsets. They are associated with repetitive stick-slip events on the fracture plane. Tensile fracture opening/closing generate similar signals on glacier at the surface and at depth (Walter et al., 2013a, Helmstetter et al., 2015b, Podolskiy and Walter, 2016). Focal mechanism and location of the source allow to differentiate between tensile and shear mechanism.

1.2.2 Topple and fall related sources

On vertical to sub-vertical slopes, mass movement occurs as the topple of rock columns or as the free-fall (and possibly bouncing and rolling) of rocky blocks (Hungr et al., 2014). In the case of toppling, the movement starts with a slow rotation of the rock blocks under the effects of water infiltration or ground shaking and ends with the free fall of larger blocks. Rockfalls, during the propagation phase, impact the ground at some location along their trajectory. These impacts generate seismic waves that can be recorded remotely by seismometers. The range of rockfall volumes can be very large, varying from less than one cubic meter to thousand cubic of meters.

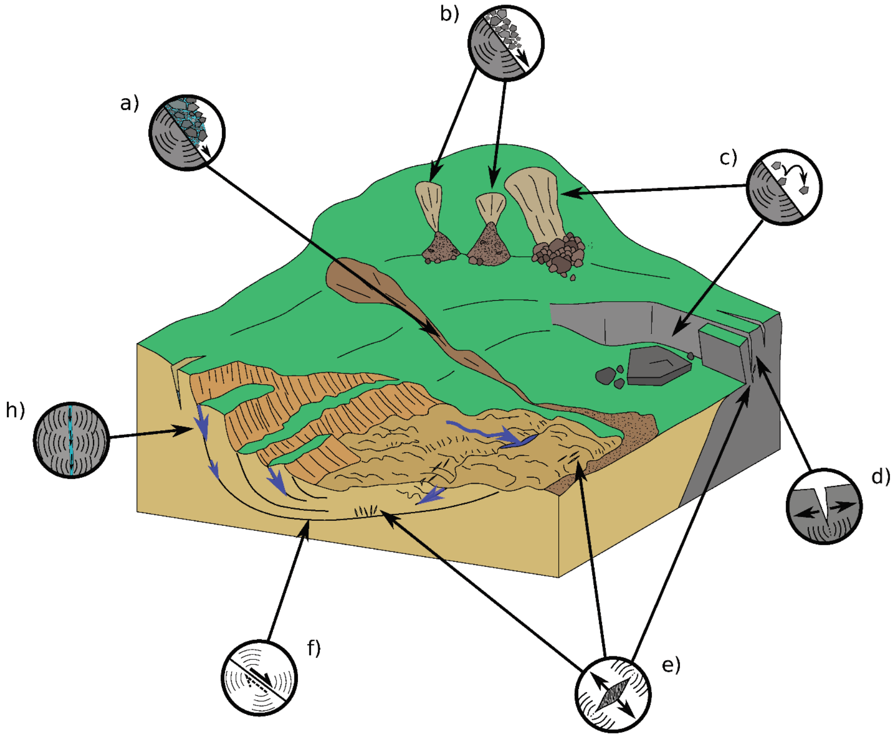

Figure 1.1: Conceptual scheme of the landslide endogenous seismic sources with a) wet granular flow, b) dry granular flow, c) rockfall, d) tensile fracture opening, e) tensile cracks opening, f) shearing and h) fluid migration in fracture.

1.2.3 Mass flow related sources

Mass flows gather different run-out processes of debris or of a mixture of water and debris. They cover a large range of volumes from large rock avalanches of several millions cubic meters to small (hundreds cubic of meters) debris falls and flows (Hungr et al., 2001). They can occur in wet or dry conditions. The contacts of the rock/debris fragments with the bedrock and in the mass flow generate seismic radiations (Suriñach et al., 2001, Burtin et al., 2009, Schneider et al., 2010, Hibert et al., 2011, Abancó et al., 2012, Burtin et al., 2013, Levy et al., 2015, Kean et al., Vázquez et al., 2016, Hibert et al., 2017b). The seismic signal is hence a combination of grain contacts within the granular flow and of grain to ground surface contacts and hence generate a complex seismic signal.

1.2.4 Fluid related sources

Hydrological forcing (e.g. precipitation, snow-melt) is one of the most common landslide trigger. The presence of fracture networks, water pipes and the heterogeneity of the rock/soil media result in the development of preferential water flow paths (Richards and Reddy, 2007, Hencher, 2010). These preferential flows induced local saturated area where the increase of pore water pressure may destabilize shallow or deep shear surfaces. In soils, the dissolution of material into finer granular debris creates weak zones prone to collapse either by suffusion (i.e. non cohesive material wash out under mechanical action) or by dispersion (i.e. chemical dissolution of fractured clay soils; Richards, Jones, 1981). In rocks, pipes may develop by erosion. In these saturated fracture networks, hydraulic fracturing can occur creating earthquakes and harmonic tremors related to flow migration in the fractures (Chouet, 1988, Benson et al., 2008, Tary et al., 2014a,b, Derode et al., 2015, Helmstetter et al., 2015b).

1.3 Landslide seismic investigation

1.3.1 Sensors used in landslide monitoring

Body and surface mechanical waves may be generated by the sources described in Section 2. Body waves (Primary -P-, Secondary -S-) radiate inside the media. P-waves shake the ground in the same direction they propagate while S-waves shake the ground perpendicularly to their propagation direction. Surface waves only travel along the surface of the ground and their velocity, frequency content and intensity change with the depth of propagation. Acoustic waves can be generated by the conversion of body waves at the surface. These waves travel in the air at a velocity of about 340 $m.s^{-1}$, slightly varying with temperature and air pressure. Acoustic waves are often generated by anthropogenic or atmospheric sources (e.g., gun shots, explosions, storms...), but can also be generated by rockfalls, debris flows or shallow fracture events. All these mechanical waves are subject to attenuation with the travel distance; the high frequency waves are attenuated faster than the low frequency waves. The relatively low energy released by the landslide related sources makes the choice of the seismic instruments to deploy very important. Four types of instruments are used to record ground motion for different frequency ranges and sensitivities. For landslide monitoring, Short-Period (SP) seismometers and geophones, Broad-Band (BB) seismometers, accelerometers, and AE sensors are commonly installed in the field.

- Broad-Band seismometers are force-balanced sensors with very low corner frequency (< 0.01 Hz) that can record the ground motion with a flat response in a large frequency range [0.01-25] Hz. They require a careful mass calibration during their installation and are sensitive to temperature and pressure variations. They are mostly used to record very weak ground motion and ambient noise;

- SP-seismometers are passive or force-balanced instruments with high corner frequency (> 1Hz). They measure the velocity of the ground with high sensitivity and a flat response in the [1-100] Hz frequency band. They are recommended for volcanic and glacier monitoring among other applications. They are less sensitive to air temperature and pressure variations and do not require mass calibration. They are hence particularly suitable for landslide monitoring. Geophones are similar to SP-seismometers but usually cover higher frequencies [1-600]Hz with lower sensitivity. They are mainly used for active seismic campaigns but may also be installed for the same purposes as SP-seismometers;

- Accelerometers are strong motion sensors able to record high amplitudes and high frequencies seismic waves. They can resolve accelerations in the frequency bands from 0.1 to 10 kHz. The response of the sensor is proportional to ground acceleration for all frequencies (there is no corner frequency). But the noise level is important for low frequencies and the sensitivity is not as good as for velocimeters. They are used to record strong ground motion in particular when installed close to epicenters (< 100 km) of large earthquakes where seismometers usually saturate. For landslide, they are usually used as inclinometers;

- AE sensors can record ground vibrations at very high frequencies (10 kHz-10 MHz) and low amplitudes. There are two types of AE sensors: the first type is very sensitive to a narrow frequency band only while the second type is sensitive to a broader frequency band (Michlmayr et al., 2012). In the field, a waveguide is often installed together with AE sensors in order to counteract the attenuation of the signal. They are used in combination with accelerometers for structural monitoring and for laboratory experiments (e.g. loading, shear, flume tests) and can be used on landslide to monitor very low magnitude sources at the grain-to-grain interactions (Dixon et al., 2003, Michlmayr et al., 2012, Smith et al., 2017);

- in addition, microphones or infrasound sensors can be useful to detect, locate and classify landslides seismic signals (Kogelnig et al., 2014, Schimmel and Hübl, 2016, Helmstetter and Janex, 2017). The detection of acoustic waves and body waves at one point, because they propagate at different velocities, can be used to estimate the distance from the source. The relative amplitude of seismic and acoustic waves can also provide information on the depth of the source, because shallow sources generate more acoustic waves than deeper ones.

It must be noted that AE sensors only record acoustic emissions generated at very high frequencies (> 10kHz) and consequently are very sensitive to attenuation. Indeed, attenuation factor Q is estimated to range between 10^{-2} and 10^{1} dB.cm^{-1} (Michlmayr et al., 2012). Even with a waveguide, they must be collocated with the cracks or the sliding surfaces observed on the slope (Dixon et al., 2015). BB, SP seismometers and geophones record seismic signals in the common band of 10^{0}-10^{2} Hz and hence offer a solution to monitor more distant sources. The detection of a seismic sources by MS sensors depends on the seismic energy released by the source, the sensor to the source distance and the attenuation of the media. Installation of MS sensors at the proximity of the geomorphological features of interest (e.g. scarp, faults, sliding surfaces, superficial crack networks, etc.) optimize the detection of the seismic signals generated by those processes but distant sources (> 1 m) can also be recorded by MS sensors. The latter do not need to be co-located with the geomorphological features of interest. After correcting the sensor response, the signals generated by these sensors can be analyzed and compared in their common frequency range. Installation of BB seismometers can complete SP network and enable to investigate the low-frequency signals generated by the slope while geophones are more adapted to explore very high frequency content (> 100 Hz). Dense networks of the latter instruments are recommended to investigate the seismicity induced by landslide deformation while the installation of one unique BB seismometer is enough to investigate the low-frequency radiations of the landslide.

1.3.2 Network geometry

Several network configurations have been tested in different studies. It must be noted that the network geometry in the case of landslides is constrained by the site configuration. Indeed, the maintenance of seismic sensors is very challenging when installed on the moving parts of the landslide; therefore, an installation on the most stable parts of the landslide or at its vicinity is often preferred for permanent monitoring (Spillmann et al., 2007, Helmstetter and Garambois, 2010, Walter et al., 2017b). During field campaigns, maintenance of sensors installed on the unstable slopes is possible and often realized (Gomberg et al., 2011, Walter et al., 2012a, Tonnellier et al., 2013). Therefore, the main challenges for seismic sensor installation at this scale is 1) to locate the sensor at close distance to the sources, 2) to maximize the number of stations and to locate the sensor close to each other to record the same event at different seismic station and 3) minimize the azimuthal gap between the sensors. The number of deployed sensors plays an important in the magnitude of completeness (M_c) of the seismic network. While the geometry of the network (i.e. inter-sensor distances, azimuthal gap) mostly control the accuracy of source locations.

Seismic sensors can be deployed in network of single sensors or network of sensor arrays. The difference between seismic network and seismic arrays is related to the distance at which the signals recorded by two sensors can be correlated. In the case of seismic arrays, the distance between the sensors is reduced to maximize the correlation of the signals recorded by each sensor. Otherwise the installation is called a seismic network Podolskiy and Walter (2016). Although the inter-sensor distance is often small (< 1 km) in the case of landslide monitoring, decorrelation of the signals is often observed even at small distances due to the complexity of the underground structure especially at high frequencies. The use of the “seismic array” approach in landslide monitoring often refers to specific geometries of collocated sensors (inter-sensors distances < 50 m) organized with a central sensor (often a three-component seismometer) and several satellite sensors (often vertical sensors). This kind of installation presents many advantages such as enhancing the Signal-to-Noise (SNR) ratio and allowing the computation of the back-azimuth of the source with beam-forming methods.

For the majority of the instrumented landslides, seismic networks are organized with single sensors located on or at close distance of the unstable slopes. The inter-sensors distance and the azimuthal gap are often controlled by the location of easily accessible or stable portions of the slopes. However, specific geometry can be adopted such as (almost) linear geometry. This is particularly the case for the monitoring the propagation of debris flows in stream channels. Dense networks (number of sensors > 50) can also be deployed. In this case the sensors are installed using a grid geometry with regular inter-sensor distances. This kind of installation is probably the most optimal but is currently mostly realized during short acquisition campaigns due to the difficulty to maintain a large number of sensors over long periods (battery, data storage, possible movement of the sensor), especially when installed directly on the unstable zones of landslides. Finally, the installation of sensors at depth (> 1 m) is challenging for landslide and it has currently only been realized on hard-rock slopes (e.g. Randa, Spillmann et al. (2007) or Séchilienne, RESIF/OMIV (2015)). This kind of installation are however very valuable to constrain the depth of the sources.

1.3.3 MS processing chains

One of the current challenge for landslide MS analysis is the development of dedicated processing chains able to analyze the unconventional seismic signals observed on landslides. The three steps of MS processing are successively: the detection, the classification and the location of the endogenous seismic events. The development of robust and versatile processing chains for analyzing landslide micro-seismicity is challenging because of 1) the low magnitude of the events and the attenuation of the media that results in emergent and low Signal-to-Noise Ratio (SNR) records, 2) the seismic source radiation patterns that may be single centroid source, double couple source or volumetric source, and, 3) the heterogeneity and variation in time (i.e. topography, water table levels, fissures) of the underground structure preventing the construction of precise velocity models and hence, accurate source locations.

First, for detecting automatically or manually the seismic events, the use of spectrograms is common. Spectrograms represent the evolution of the frequency content in time by computing the Fourier Transform on small moving time windows (e.g. < 1 s). Automatic detection is usually carried out with the STA/LTA (Short-Term Average/Long-Term Average) detector (Allen, 1982) applied on the summed energy of the spectrogram (Spillmann et al., 2007, Helmstetter and Garambois, 2010, Tonnellier et al., 2013).

Second, classifying the detected signals can be carried out automatically by discarding exogenous events with simple criteria (i.e. threshold on the signal duration, inter-trace correlation, apparent velocity) but the determination of the threshold to differentiate the class of signals may be difficult. Machine learning algorithms offer nowadays the possibility to automatize and improve this step. Dammeier et al. (2016) developed a Hidden Markov Model (HMM) that can detect automatically in the time series the occurrence of one particular type of events. The success rate of HMM is reasonable and this technique has the advantage of requiring only one single example to scan the time series. The Random Forest algorithm has proven its efficiency for volcanic and landslide signals classification with higher success rate and versatility (Provost et al., 2017, Hibert et al., 2017c). New signals are successfully classified in multiple pre-defined classes and changes in the source properties may be detected by change on the uncertainties (Hibert et al., 2017c). It must be noticed that this approach requires a training set with sufficient examples to build the model. Good success rates (i.e. > 85 %) are rapidly reached with 100 elements or more per class. Template-matching filters have also been used in many studies of landslide collapse and glaciers (Allstadt and Malone, 2014, Yamada et al., 2016a, Poli, 2017, Helmstetter et al., 2015a,b, Bièvre et al., 2017, Helmstetter et al., 2017a) in order to detect and classify seismic signals. This method consist in scanning continuous data to search for signals with waveforms similar to template signals. It can detect seismic signals of very small amplitude, smaller than the noise level. Seismic signals are grouped in clusters of similar waveforms, implying similar source locations and focal mechanism.

Finally, the location of the sources is the most challenging step. Common location methods (such as NonLinLoc; (Anthony et al., 2000, Lomax et al., 2009)) were used in combination to 3D-velocity models for locating impulsive micro-earthquakes occurring at the Randa rockslide (Spillmann et al., 2007). However, a certain number of recorded signals do not exhibit impulsive first arrivals and clear P- and S-waves onsets. For this kind of signal, location methods based on the inter-trace correlation of the surface waves (Lacroix and Helmstetter, 2011) or on the amplitude (Burtin et al., 2016, Walter et al., 2017b) are more suitable and easier to automatize. Other methods such as HypoLine (Joswig, 2008) aim at integrating different strategies (i.e. first arrival picking, inter-trace correlation and beamforming) to locate accurately the epicenter under the control of an operator. (Provost et al., 2018) developed a method combining Amplitude Source Location (ASL) and inter-trace correlation of the first arrivals in an automatic scheme. This strategy showed accurate location of impulsive events while the error on the epicenter of emergent events is reduced by the use of ASL to constrain the location. Many studies approximate the media attenuation field and/or the ground velocity, or do not take into account the topography, leading to mis-location of the events that prevents for accurate interpretation of certain sources and leads to false alarms (Walter et al., 2017b).

1.3.4 Instrumented sites

In the last two decades, seismic networks have been installed on several unstable slopes worldwide. Table 1.1 synthesizes the unstable slopes or debris flow prone catchments instrumented with seismic sensors worldwide. The sites are classified in terms of landslide types (i.e. slide, fall and flow) according to the geomorphological typology of Cruden (1996) (Cruden and Varnes, 1996). Studies on snow avalanches (Lawrence and Williams, 1976, Kishimura and Izumi, 1997, Sabot et al., 1998, Suriñach et al., 2001, Biescas et al., 2003) are not integrated. Most of the instrumented sites are located in the European Alps (France, Italy and Switzerland). Short-Period (SP) seismometers and Geophones (G) are the most common type of instruments. Their installation and maintenance is easy as they do not require mass calibration in comparison to Broad-band (BB) or long-period (LP) seismometers.

1.4 Data

Seismic observations from 14 sites are used to propose the typology. The sites are representative of various types of slope movements and lithology (Table 1.1) with four slides occurring in hard rocks, four slides occurring in soft rocks, three rockfall-prone cliffs occurring in hard and soft rocks and one catchment prone to debris flows. The seismic instruments installed on these sites are recording the seismicity generated by the slope deformation and are installed either permanently or were acquired during short campaigns (Table 1.1). The Riou-Bourdoux catchment is the only site where the seismic signals were manually triggered as rock blocks were thrown down the cliff and monitored with cameras, LiDAR and seismic sensors (Hibert et al. (2017a)).

The dimension of the unstable slopes range from 60 m × 30 m for the Chamousset cliff to 7 km × 300 m for the St.-Eynard cliff (Table 1.2). The seismic networks are deployed with various geometry depending on the configuration of the slope, its activity and the duration of the installation. For most of the sites, at least one seismic sensor is deployed on the active zone or very close to (Table 1.2). The maximal distance to the slope instabilities is 500 m for the St.-Eynard cliff being the largest investigated site of our study.

Table 1.2: Characteristic of the seismic network for the 13 sites analyzed in the present parer. The landslide dimensions are given for the most active area of the slope instabilities (as presented in the published studies). The total number of the seismic network are given as well as its minimal and maximal inter-sensor distance and distance to the active zone. In the case a fewer number of the sensors have been investigated in the present study, we indicate the number of the sensors as well as the name of the use station in parenthesis.

Site	Sensor	Network	Number of sensors		Inter-sensor distance		Distance to the landslide		Landslide
	type	geom.	in tot.	analyzed	min	max	min	max	dim.
Séchlienne	SP	SA	41	11 (THE)	25 m	85 m	< 50 m	< 200 m	600 m × 200 m
La Clapière	SP	SN	18	9 (CL4)	30 m	77	0 m		900 m × 700 m
Aaknes	G	SN	8		< 50 m	250 m	0 m		1 km × 1 km
Aiguilles-Pas de l'Ours	BB	SN	4		205 m	690 m	0 m	200 m	500 m × 500 m
Super-Sauze	SP	SA	8		30 m	150 m	0 m	< 100 m	800 m × 150 m
Pont Bourquin	SP	SN	2		30 m		0 m		240 m × 35 m
Pechgraben	SP	SA + SS	5		5 m	40 m	0 m		500 m × 100 m
Slumgullion	SP	D-SN	88		11 m	450 m	0 m		1 km × 500 m
Chamousset	SP	SN	7		15 m	50 m	0 m	40 m	60 m × 30 m
St. Eynard	SP	SN	4	3*	500 m	1.7 km	0 m	500 m	7 km × 300 m
Riou Bourdoux	SP,BB	SA + SS	5		50 m	200 m	20 m	30 m	length: 200 m
Piton de la Fournaise	BB	SN	10	1 (BOR)	-	-	< 50 m		1 km × 300 m
Reibaxader	G	SN	9		< 20 m	200 m	0 m		700 m × 50 m

G: Geophone (f = [0.1-10] kHz); SP: Short-Period (f = [0.1-100] Hz); BB: Broad-Band (f = [10^{-2}-100] Hz);
SN: Seismic Network; D-SN: Dense-Seismic network;
SA: Seismic Array; L-SA: Linear-Seismic Array; SS: Single Sensor;
* investigated stations: FOR, MOL, GAR.

The seismic network geometry of the majority of sites are distributed seismic network where sensors location are regularly installed over the active zone or at its vicinity. In the case of the Rebaixader catchment, the seismic network is installed at the border of the stream channel almost linearly. At the Slumgullion landslide, a dense network has been installed with regular spacing of the seismic sensors. Seismic arrays are installed at the other sites. The geometry of the seismic arrays are triangular shape with the exception of the Séchilienne landslide where an hexagonal shape is used.

The instruments are mostly SP seismometers with natural frequencies of 1 Hz to 5 Hz and 50 to 100 Hz. Fewer geophones and BB seismometers are installed at the sites. The instrument response is corrected for all the dataset. To be consistent with the sensitivity of all the sensors, we do not investigate the data below 1 Hz for BB seismometers and above 100 Hz for SP seismometers and geophones.

The dataset being analyzed is composed of either published seismic events or published catalogs. The comparison of these events and catalogs enable to compare the signals and to compose the classes of the typology. In the case that no published events or catalogs are available, we analyzed manually the dataset to complete the number of examples for each proposed class (see Section 5 for detailed information).

1.5 Methodology

The seismic signals recorded at different sites are compared in order to identify common features. Seismic signals result from the convolution of both the wave propagation and of the seismic source mechanism. Consequently, the observation of common signal features in signals recorded at different sites can only be explained by similar source mechanisms. The proposed typology is hence based on the analysis of these common features. We then selected nine signal features in order to quantify the differences and similarities between the different classes. The nine parameters are chosen because they correspond to the criteria used by experts to analyze and classify a seismic signal and also because they can be used in automatic classification algorithms (Fäh and Koch, 2002, Langer et al., 2006, Curilem et al., 2009, Hammer et al., 2012, 2013, Hibert et al., 2014a, Ruano et al., 2014, Maggi et al., 2017, Provost et al., 2017, Hibert et al., 2017c). They can be computed for any signal types and present a robust framework for future comparison. The selected signal features are:

- the duration of the signal T (expressed in second), computed on the stacked spectrogram of the traces (Helmstetter and Garambois, 2010).
- the dissymetry coefficient of the signal (expressed in percent), computed as:

$$s = \frac{t_m - t_1}{t_2 - t_1} \times 100 \tag{1.1}$$

  with t_1, t_2 and t_m the time of the signal onset, ending and maximum respectively.

- the number of peaks of the signal envelop N_{peaks}, computed as the number of local maximum above 50% of maximal value of the signal envelop. The envelop of the signal is computed as the absolute value of the Hilbert transform of the signal. The envelop is smoothed by a computing the average of on a moving window of length: $\delta t = \frac{100}{f_s T}$.
- the duration of the signal auto-correlation, defined as:

$$A_{max} = \frac{t_c}{T} \tag{1.2}$$

  with,

$$t_c = \max_t (C(t) < 0.2 * max(C)) \tag{1.3}$$

with C equal to the signal auto-correlation. A_{max} is expressed in percent (%) and represents the duration of the signal correlating with itself. As an example, a signal with a rapid and abrupt change in frequency content will rapidly be uncorrelated (low A_{max}) while a signal with a constant frequency content will have a long auto-correlation (high A_{max}).

- the mean frequency (expressed in Hertz), computed as:

$$F_{mean} = \frac{\sum_{i=1}^{N} PSD(f_i) f_i}{\sum_{i=1}^{N} PSD(f_i)} \tag{1.4}$$

  with the Power Spectral Density (PSD) defined as:

$$PSD(f) = \frac{2|FFT(y)|^2}{N f_s} \tag{1.5}$$

  with f_s and N being the sampling frequency of the signal and the number of samples respectively. The mean frequency is chosen here as it more representative of the signal spectrum energy and less sensitive to noise than the frequency of maximum energy. (Farin et al., 2014).

- the frequency corresponding to the maximal energy of the spectrum F_{max} (expressed in Hertz).

- the frequency bandwidth F_w defined as:

$$F_w = 2\sqrt{\frac{\sum_{i=1}^{N} PSD(f_i) f_i^2}{\sum_{i=1}^{N} PSD(f_i)} - F_{mean}^2} \tag{1.6}$$

- the minimal frequency of the signal spectrum, computed as:

$$f_{min} = \min_f (PSD(f) < 0.2 \times \max(PSD)) \tag{1.7}$$

- the maximal frequency of the signal spectrum, computed as:

$$f_{max} = \max_f (PSD(f) < 0.2 \times \max(PSD)) \tag{1.8}$$

  the maximal frequency of the signal spectrum f_{max} (not to be confused with parameter F_{max} defined above).

The signal features are always computed on the trace with the maximal amplitude band-passed in the range [f_c-50] Hz (f_c: natural frequency). This enables to limit the influence of the wave propagation and to compare signals with different sampling frequencies (i.e 120 Hz to 1000 Hz).

Based on already published events and further interpretations, we propose a standard classification of landslide endogenous seismic sources. The non-published datasets are used to investigate the presence of these signals at other sites and to increase the number of examples for different contexts. Numerous signals were analyzed to draw the proposed classification and selected examples are further presented to describe the different classes.

1.6 Seismic description of the signals - typology

The typology of the signals is based on the duration and the frequency content of the seismic signals. The signals are classified in three main classes: “Slopequake” (SQ), “Rockfall” (RF) and “Granular flow” (GF). For “Slopequake”, sub-classes are proposed and discussed based on the frequency content of the signals. Several examples of signals recorded at different sites are presented and the sources are discussed in the corresponding section.

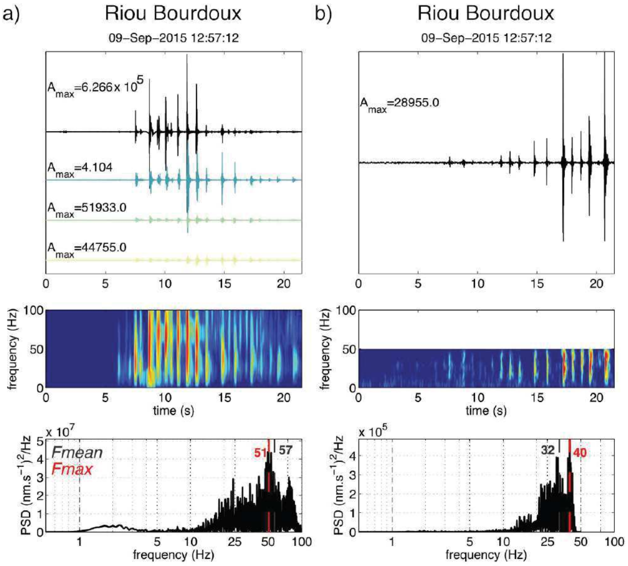

Figure 1.2: Example of one controlled rockfall (mass= 430kg) at the Riou-Bourdoux catchment (Hibert et al., 2017a) recorded by SP seismometer located at 50 m of the rock departure (left) and recorded by BB seismometer near the rock arrival (right). The waveforms of the vertical traces are plotted on the upper part of the figure. The amplitude are normalized on the trace with the maximal amplitude (black), the signal recorded by the other sensors (when available) are represented in color below. The maximal amplitudes (A$_{max}$) of all the traces are plotted on the sub-plot. The spectrogram is plotted on the middle part of the figure and normalized to the maximal energy. The lower part of the figure represents the PSD of the most energetic trace and the frequency corresponding to the maximum and the mean of the PSD are plotted in red and gray respectively.

1.6.1 Rockfall (RF)

Fig 1.2 displays the seismic waves recorded for a single block fall at the Riou-Bourdoux catchment (French Alps). The block was manually launch in the catchment and recorded with seismic sensors and cameras (Hibert et al., 2017a). The signal is characterized by successive impacts visible both on the waveform and on the spectrograms and lasts around 20 s. The spectral content contains mostly frequencies above 10 Hz but energy below 10 Hz is present for certain impacts (Fig 1.2a). At closer distance, very high frequencies can be recorded up to 100 Hz (Fig 1.2a). The auto-correlation remains large over time due to the similitude of the individual impacts signals (T_{corr} > 10%). P- and S- waves are hardly distinguishable on the record and the signals recorded at the seismic sensors are dominated by surface waves (Dammeier et al., 2011, Helmstetter and Garambois, 2010, Hibert et al., 2014a, Levy et al., 2015).

Seismic signals of natural masses detaching from cliffs are presented in Fig 1.3. They present similar characteristics to the artificially triggered rockfall. Depending on the height of the cliff, the signal lasts between 5 and tens of seconds. The symmetry of the signal ranges from 0 to 80 % depending on the cliff configuration. In general, the most energetic impacts are recorded at the middle or after the middle of the signal (skewness > 50%). The highest measurable frequency depends on the source-to-sensor distance and can be very high (> 100 Hz). The spectral energy is concentrated in frequencies above 5 Hz, with the largest PSD values ($F_{m}ax$) ranging from 20 to 40 Hz. Generally, the Power Spectral Density energy is low below 10-15 Hz with the exception of some case (Fig 5.c) where spectral energy can be observed. The initial falling masses can themselves break into smaller units during propagation. In this case, the signal does not return to the noise level between the impacts due to developing granular flow (Fig 1.3b,e,f) leading to the decrease of the duration of the auto-correlation of the signal. When several blocks are falling at the same time, impacts may overlap, so do the peaks of the signals.

In certain cases, the first rock free-fall is preceded by a signal that can be associated with the rock detachment. An example of this precursory signal can be observed in Fig 1.3a,f and in (Hibert et al., 2011, Dietze et al., 2017b). The seismic signals of rockfalls contain information on the physics of the process. The seismic energy of rockfall signals is proportional to the volume (Hibert et al., 2014a, Farin et al., 2014). Scaling laws are also established between seismic energy, momentum, block mass and velocity before impacts (Hibert et al., 2017a). The frequency content is mainly controlled by the block mass. The frequency of the spectral maximum energy decreases when the block mass increases (Farin et al., 2014, Huang et al., 2007, Burtin et al., 2016). If the rockfalls are well isolated, each impact generates impulsive waves. In the case of multiple rockfalls or short distances between the seismic sources and the sensors, the first arrivals may be emergent due to simultaneous arrivals of waves generated by impactors of different sizes impacting the ground at closely spaced time intervals (Levy et al., 2015, Hibert et al., 2014a).

1.6.2 Granular Flow (GF)

Granular flows are characterized by cigare-shape signals lasting between tens to thousands of seconds. They are subdivided in two classes:

- **Dry granular flow** (Fig 1.4): These signals are characterized by cigare-shape waveforms of long duration (< 500 s). Due to the absence of water, the source generally propagates over small distances. The duration of auto-correlation is very weak (T_{corr} ≈0%) and no seismic phase can be distinguished. No distinguishable impacts can be observed in the waveform nor in the spectrogram at the opposite of rockfall signals. The signal onsets is emergent and P- and S- waves are hardly distinguishable and the signal is dominated by surface waves (Deparis et al., 2008, Dammeier et al., 2011, Helmstetter et al., 2011, Hibert et al., 2014b, Levy et al., 2015). The dissymetry coefficient of the signal varies between 30% and 75% and depends on the acceleration and the volume of mass involved in the flow through time (Suriñach et al., 2001, Suriñach et al., 2005, Schneider et al., 2010, Levy et al., 2015, Hibert et al., 2017b). The frequency ranges from 1 to 35 Hz. The maximal frequency of the PSD varies between 5 and 10 Hz and can be larger (up to 20 Hz) when the seismic sensors are located close to the propagation path. The PSD values are significantly low below 3 Hz and incrase rapidely between 3 and 20 Hz.

- **Wet granular flow** (Fig 1.5): These signals last several thousands of seconds to several hours and correspond to debris flows. They occur during rainfall episodes when fine material and boulders propagates downstream over long distances (> 500 m). Like dry granular flow, the duration auto-correlation is very weak (T_{corr} =0%) and no seismic phase can be distinguished. The seismic sensors are often installed at very close distance to the flow path so high frequencies up to 100 Hz may be recorded (Abancó et al., 2014, Burtin et al., 2016, Walter et al., 2017b). Little energy is present in the low-frequencies (< 10 Hz) depending on the amount of water and the size of the rocky blocks integrated in the flow (Burtin et al., 2016). The signal is emergent and the amplitude variation depends on the mass involved in the flow passing in the vicinity of the sensor. Debris flows are very often divided in a front with the largest boulders and the highest velocity followed by a body and a tail where the sediment concentration and the velocity decreases (Pierson, 1995). The seismic signal amplitude hence increases progressively as the front is passing at the vicinity of the sensor (Abancó et al., 2012, Hürlimann et al., 2014, Burtin et al., 2016, Walter et al., 2017b) and decreases progressively, as the front is moving away from the sensor (skewness > 50%). Large spikes and low-frequencies may be observed in the seismic signal corresponding to the front of the debris flow generated by large boulders impacts. The frequency content also changes and, progressively, energy in the lower frequencies decreases (Fig 1.5.a).

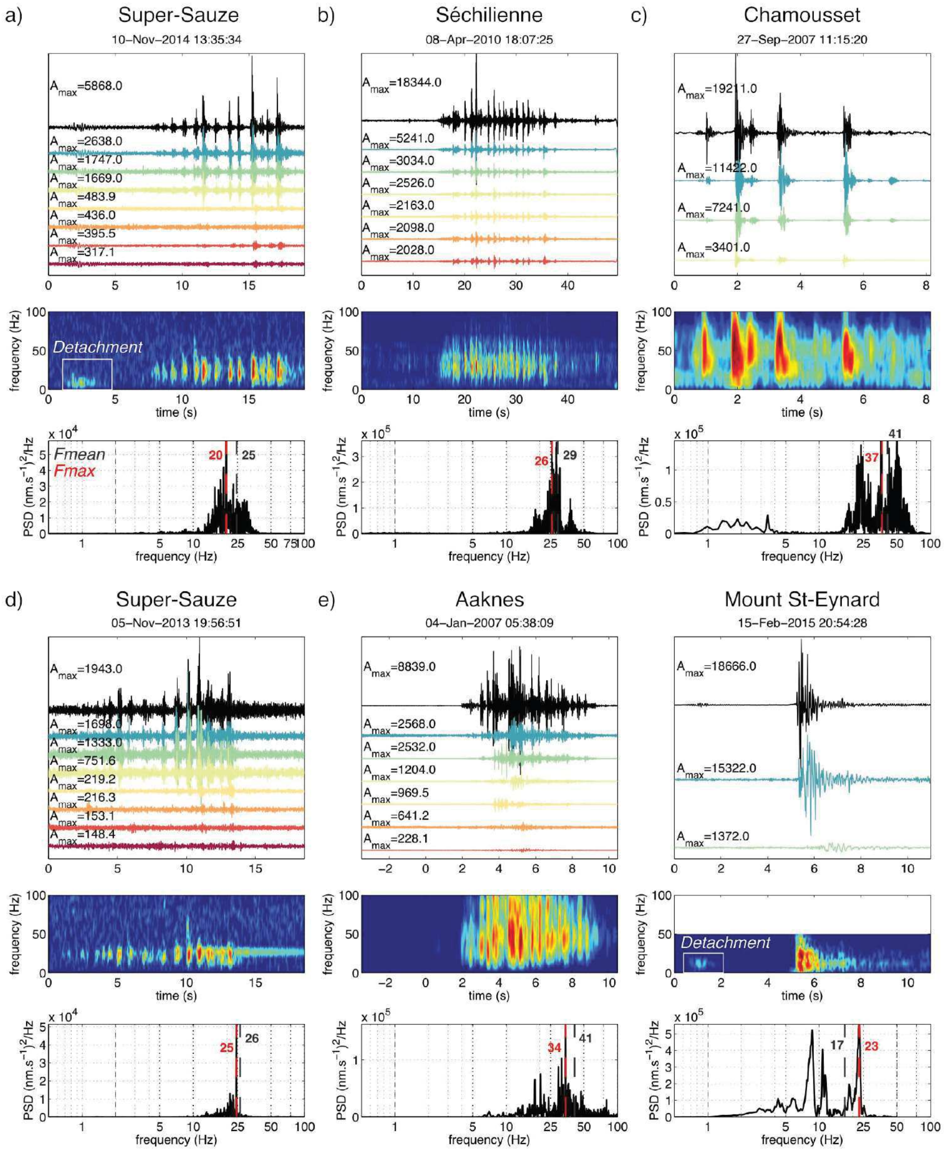

Figure 1.3: Rockfall events recorded at a) and d) Super-Sauze (France) (Provost et al., 2017), b) at the Séchilienne (France, Helmstetter et al. (2011), RESIF/OMIV (2015)), c) Chamousset (Levy et al., 2011), e) Aaknes and f) Mount Saint-Eynard slopes (Le Roy et al., 2018). See Fig 1.2 for description of the figure.

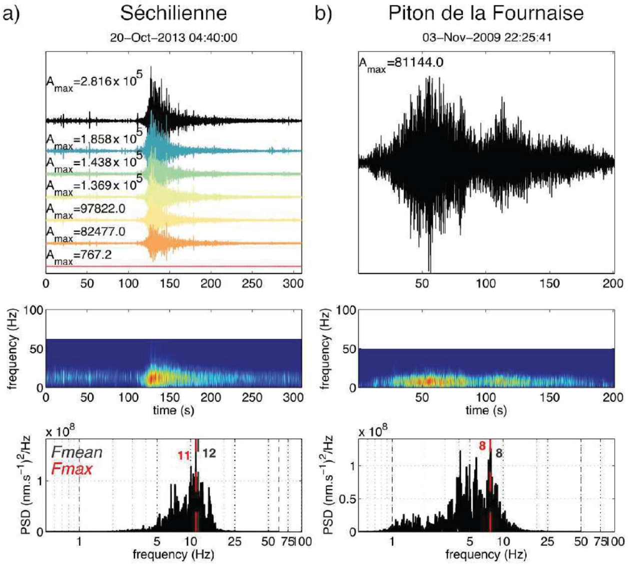

Figure 1.4: Dry granular flow events recorded at a) Séchilienne and b) the Piton de la Fournaise Caldera. See Fig 1.2 for description of the figure.

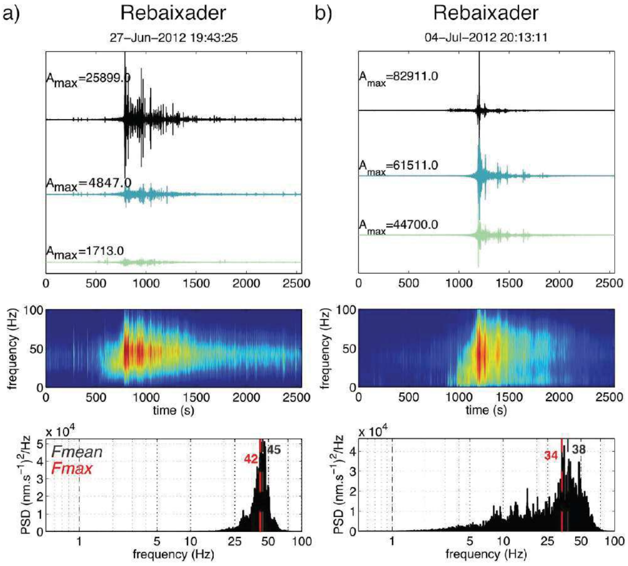

Figure 1.5: Wet granular flow events recorded at Rebaixader torrent (Abancó et al., 2012, Hürlimann et al., 2014, Arattano et al., 2016). See Fig 1.2 for description of the figure.

1.6.3 Slopequake (SQ)

The "Slopequake" class gathers all the seismic signals generated by sources located within the slope at the sub-surface or at depth such as fracture related sources or fluid migration (cf. section 2). Different names have already been proposed for this kind of signals: "slidequakes" (Gomberg et al., 2011), "micro-earthquake" (Helmstetter and Garambois, 2010, Lacroix and Helmstetter, 2011), "quakes" (Tonnellier et al., 2013, Vouillamoz et al., 2017) or "Landslide Micro-Quake (LMQ)" (Brückl, 2017). We here proposed the term "Slopequake" as a general name for these events. They are characterized by short duration (< 10 s) and are sub-divided into two classes "Simple" and "Complex".

Simple Slopequake

"Simple Slopequake" signals are of short (< 2 s) to very short duration (< 1 s) signals. Their main feature is the triangular-shape of the spectrogram with largest amplitudes being recorded in the first part of the signal (skewness < 50%). The first arrivals contain the highest frequencies of the signal and are followed by a decrease of the frequencies. Depending on the frequency content, these signals can be sub-divided into three classes:

- **Low-Frequency Slopequake (LF-SQ)** (Fig 1.6): The signal lasts between 1 and 5 s. The maximal amplitude of the signal waveform occurs at the beginning or at the center of the signal (15% < skewness < 50%). The waveform presents only one peak and most of the first arrivals are emergent. Phase onsets are difficult to identify. The signals are mostly dominated by surface waves. Consequently, the duration auto-correlation of the signals is large (> 10%). The largest PSD values are observed between 5 and 25 Hz with a mean frequency ranging between 10 and 15 Hz.

- **High-Frequency Slopequake (HF-SQ)** (Fig 1.7)): The signal lasts between 1 and 5 s. The maximal amplitude of the signal waveform occurs close to the beginning of the signal (skewness < 30%). The waveform presents only one peak and the first arrivals are mainly impulsive. Different phases may be observed (Spillmann et al., 2007, Lévy et al., 2010): P-arrivals are detected at the beginning of the signal and correspond to the high frequency waves, surface waves are then observed at the time the frequency decreases. However, in general the short sensor to source distance makes difficult the differentiation between the different seismic phases. The auto-correlation these signals is hence lower than for LF-SQ (< 10 %). In most of the cases, the picking of the different waves onset is made difficult because of the sensor-to-source distances and the low frequency sampling. The largest PSD values are observed between 3 and 45 Hz with a mean frequency ranging between 20 and 30 Hz.

- **Hybrid Slopequake (Hybrid-SQ)** (Fig 1.8)): The signal lasts between 1 and 2 s. It presents the characteristics of the two precedent signals. The brief first arrivals are very impulsive and last less than one second. They are followed by a low-frequency coda similar to the LF-SQ. The maximal amplitude of the signal waveform occurs close to the beginning of the signal (skewness < 40%). The waveform presents only one peak and the first arrivals are impulsive.

These signals are suspected to be associated with boundary or basal sliding (Helmstetter and Garambois, 2010, Gomberg et al., 2011, Walter et al., 2013b, Tonnellier et al., 2013) or fracturing of the slope (Helmstetter and Garambois, 2010, Colombero et al., 2018). Currently, only few studies have proposed inversion of the source tensor (Lévy et al., 2010). To the best of our knowledge, for soft-rock landslides, no source mechanism was modeled. Therefore, it remains difficult to set if the observation of LF- and HF-slopequakes is due to attenuation of the high frequencies with the distance or to the source mechanism. Indeed, the rupture velocity may explain the difference of frequency content

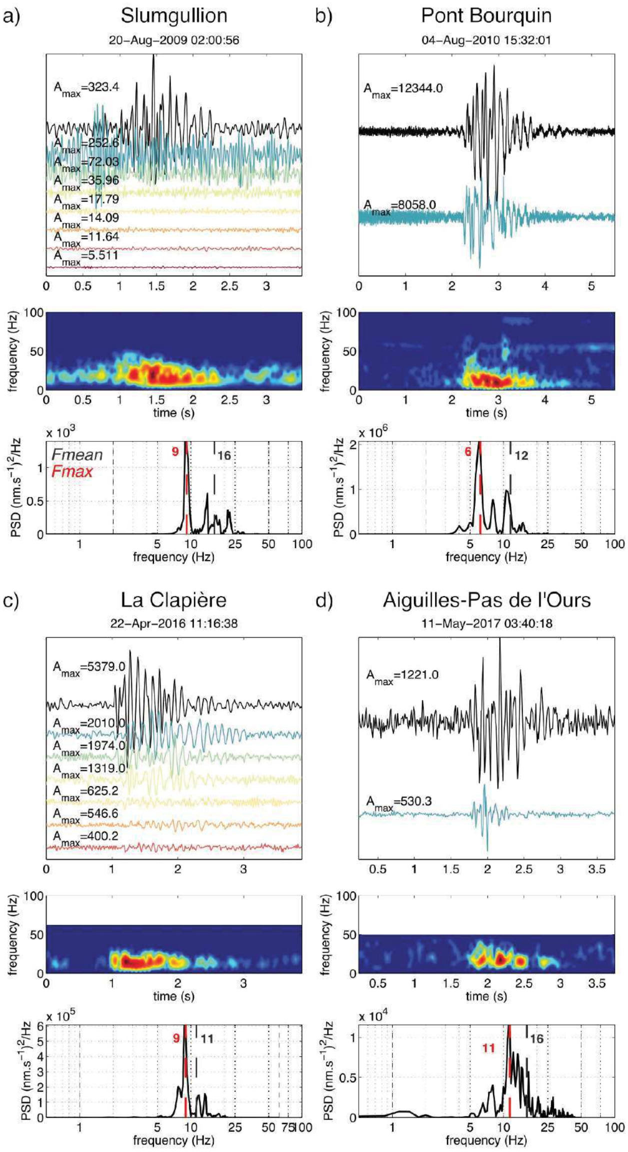

Figure 1.6: Low-Frequency Slopequakes recorded at the a) Slumgullion (Gomberg et al., 2011), b) Pont-Bourquin, c) La Clapière and d) Aiguilles-Pas de l'Ours slopes. See Fig 1.2 for description of the figure.

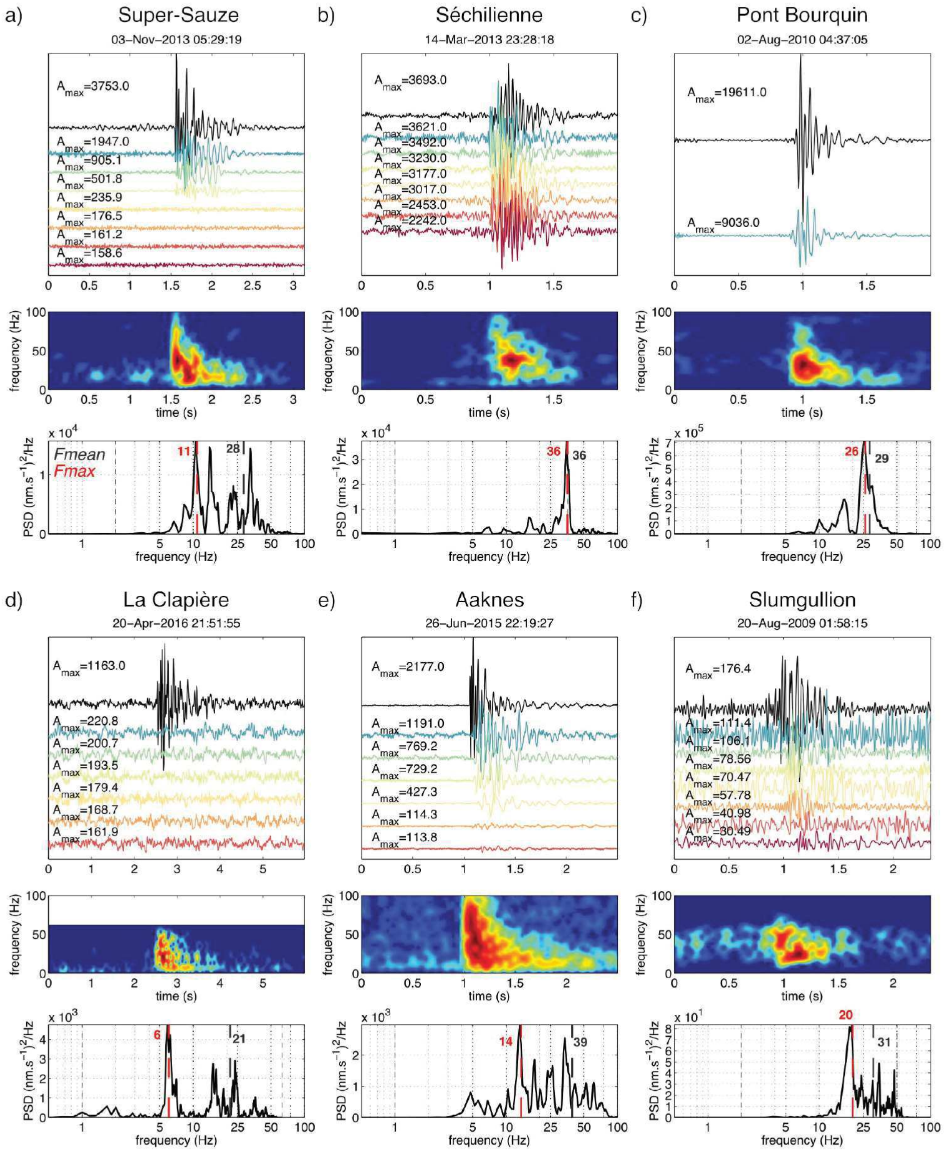

Figure 1.7: High-Frequency Slopequakes recorded at the a) Super-Sauze (Provost et al., 2017), b) Séchilienne (Helmstetter et al., 2011, RESIF/OMIV, 2015), c) Pont-Bourquin, d) La Clapière, e) Aaknes, and f) Slumgullion (Gomberg et al., 2011) slopes. See Fig 1.2 for description of the figure.

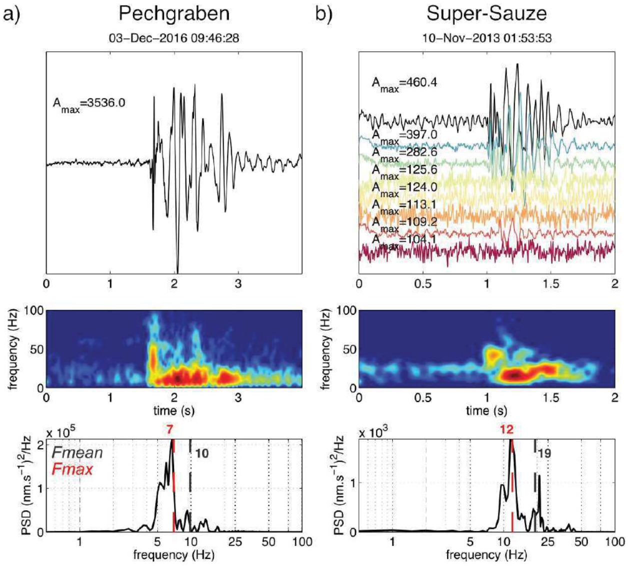

Figure 1.8: Hybrid-Slopequake recorded at the a) Pechgraben and b) Super-Sauze landslide. See Fig 1.2 for description of the figure.

and low-frequency earthquakes are observed on tectonic faults (Shelly et al., 2006, Brown et al., 2009, Thomas et al., 2016). They are characterized by low magnitude ($M_w < 2$) and short duration (< 1 s) and constitute at least part of the seismic tremor signal. Therefore, the main assumption for the source of these events are slow rupture (Thomas et al., 2016). Another interpretation for the low frequency quakes dominated by surface waves is crevasse opening (at the surface) as observed in glacier (Deichmann et al., 2000, Mikesell et al., 2012). (Colombero et al., 2018) analyzed AE at laboratory scales generated during thermal fracturing. During this experiment, high-frequency AEs are recorded during the heating stage up to the failure of the rock sample and are interpreted as thermal cracking events (Colombero et al., 2018). Low-frequency AEs are recorded during cooling stage (after failure) and are associated with stick-slip events (Colombero et al., 2018).

Hybrid slopequakes are very similar to the events recorded on volcanoes and glaciers with the presence of fluids in conduits or crevasses (Chouet, 1988, Helmstetter et al., 2015b). The sources of these events are assumed to be related to hydro-fracturing. The first high-frequency events corresponding to a brittle failure is followed by water flow into the newly opened cracks (Chouet, 1988, Benson et al., 2008).

The frequency content depends on the sensor to source distance and on the source mechanism. Observation of LF- and HF-SQ may be the signature of on-going processes taking place within the slope instabilities justifying the three proposed classes for simple slopequakes.

Complex Slopequake

The second class of short duration signals has the same general properties than the simple slopequakes but exhibits particular frequency content or precursory events. These additional characteristics change the possible interpretation of the sources. Consequently, these signals are gathered in the class “Complex Slopequake”. Three different sub-classes are proposed:

- **Slopequake with precursors** (Fig 1.9): The third class of short duration signals are similar to the slopequake signals but are preceded by a precursory signal of smaller amplitude (Fig 1.9). The content of the precursory signal ranges from 5 to 100 Hz depending on the site and is slightly lower than the highest frequency generated by slopequake-like event. The precursory arrival

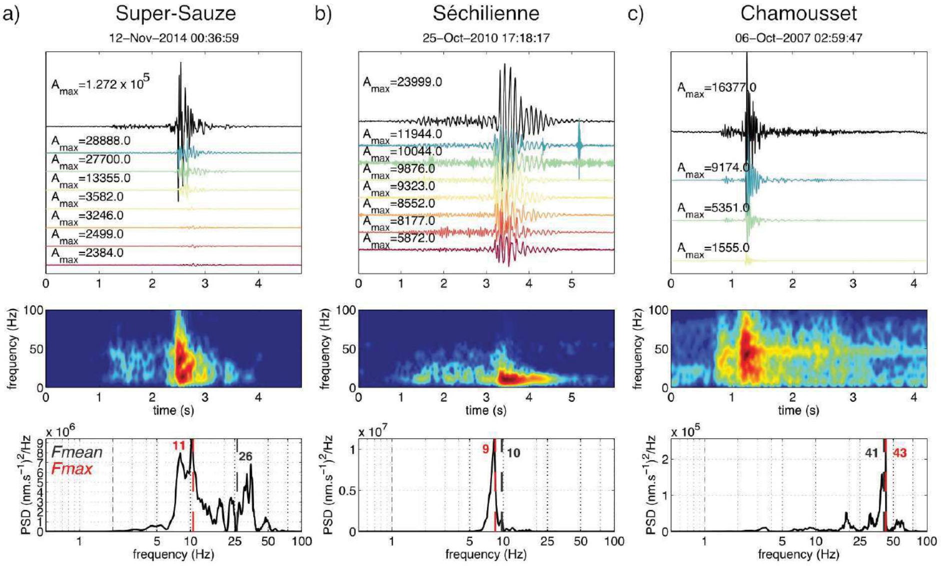

Figure 1.9: Examples of Slopequakes with presursory event recorded at the a) Super-Sauze, b) Séchilienne and c) Chamousset slopes. See Fig 1.2 for description of the figure.

last up to 1.2 s in the presented examples and no clear phases are detected. The frequency content ranges from 5 to 100 Hz but varies significantly at each site. At all sites, the amplitude of the signal is significantly higher for one of the sensor (3 to 50 times higher) when considering vertical traces. The precursory signal is buried in the noise at the sensors with lowest amplitudes and the signal is similar to a LF-slopequake. Such events have never been documented to our knowledge. They are likely to be generated by a strong and local source located at the very close vicinity of one of the sensor (< 10 m) due to the maximal amplitude (> 10^5 nm.s^{-1}) and the rapid decrease of the amplitude recorded by the other sensors. Although the signal is similar to certain earthquakes (the precursory signals interpreted as P-waves arrivals and the strong arrivals as surface waves), no earthquake location can explain the signal recorded at the time these events are recorded. Their occurrence in the night time also prevent any human activity to be the source. The most probable source would then be the detachment of a single block and its fall in the vicinity to one of the sensor. This kind of precursory signals are observed for some rockfalls (Fig 1.3.a) and at a the Saint-Martin-le-Vinoux quarry (France; Helmstetter et al. (2011)). At the Saint-Martin-le-Vinoux underground quarry, the duration between the detachment and the signal impact is well correlated to the room height. This interpretation is coherent with the drop of amplitude before the more energetic event at the Chamousset rock column (Fig 1.9.c) where a progressive decrease of the precursory signal is observed. However, on the other sites (Fig 1.9.a,.b) such decrease is not present. The one second lasting precursory signal has a constant amplitude and frequency content. Another interpretation could be that these precursory signals are a succession of overlaping slip or fracture events. The interpretation of these signals cannot be established with certainty and further analysis (i.e. location, time of occurrence) and other examples are needed to discriminate the mechanism at work.

- **Tremor-like slopequake** (Fig 1.10): The last class of short duration signals often last between 1 and 5 seconds (Fig 1.10). They present a symmetrical waveform (S=50%) with emergent arrivals and slow decrease of the amplitude to the noise level. The frequency ranges from 5 Hz to 25 Hz. High-frequencies may be briefly recorded in certain events (Fig 1.10.c) . The maximal energy of the PSD corresponds to a frequency of 8 to 13 Hz while the mean energy corresponds to a frequency of 13 to 17 Hz. No seismic phases are identified. The signal is not recorded by all the sensors even when the sensors are organized in small arrays with short inter-sensor distances (< 50 m). Their waveforms and frequency content are similar to the one of the granular flows (Fig 1.4). Small debris flows have been observed at La Clapière and Super-Sauze landslides and are likely to generate seismic waves; however, small debris flows are not observed at the Pas de l'Ours landslide when these kinds of seismic signals are recorded. Another possible source mechanisms for such events may also be a very rapid succession (< 1 s) of shear events along the basal or the side bounding strike-slip faults (Hawthorne and Ampuero, 2017). Further investigations are needed to analyze their occurrences over time and their location to confirm one or the other assumptions.

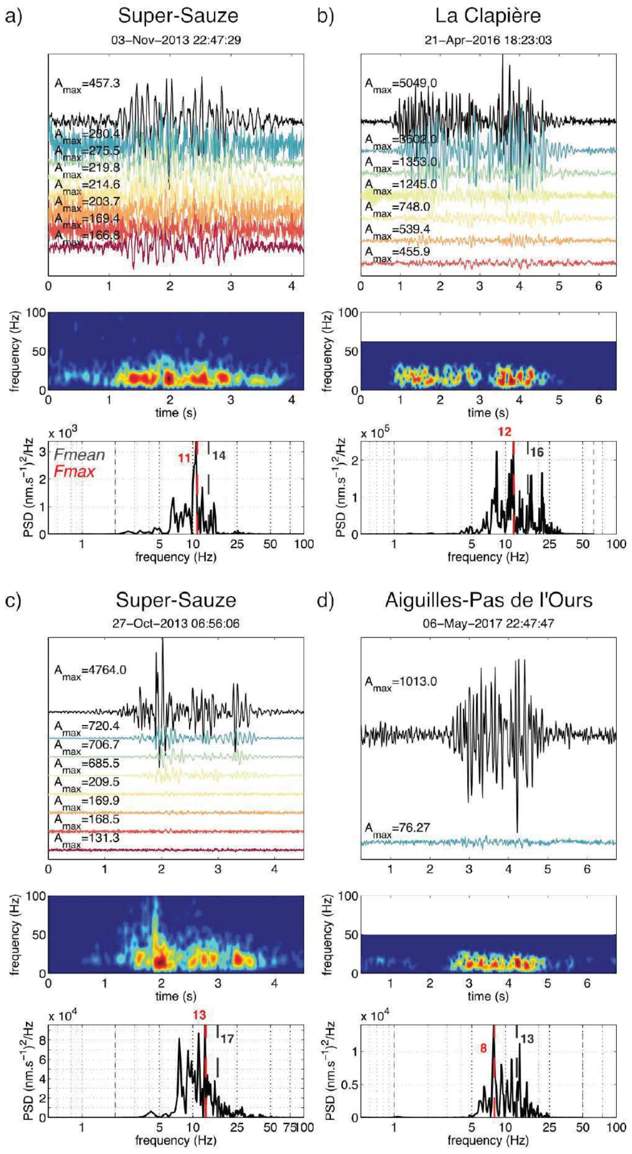

Figure 1.10: Examples of repetitive Slopequakes recorded at the a),c) Super-Sauze, b) La Clapière and d) Aiguilles-Pas de l'Ours slopes. See Fig 1.2 for description of the figure.

1.7 Discussion

The proposed typology is summarized in Fig 1.11. The approach consisted in comparing the datasets of different sites in order to identify the common features of the recorded seismic signals. Figure 1.11 show that the three main classes can be differentiate mainly from the length of the signals, the number of peaks and the duration of the auto-correlation. Figure 1.12 shows more example of the signal variability for the sites where long seismic catalogs have been recorded (e.g. Aaknes, Chamousset, Séchilienne, Super-Sauze and La Clapière). Only the signals classified as Rockfall, LF- and HF-slopequake are presented because fewer events of the other classes are present in the investigated datasets. The signal features are in good agreement with the defined classes proposed in the present classification (Fig 1.11). Similar feature and in general, narrow variability is observed on the feature values among the different sites and consequently, the observed features are likely associated to the source mechanism and not to propagation effects.

Our analysis does not allow at this stage, to conclude whether the frequency content of simple slopequake is associated to source mechanism because complete catalogs differentiating these two classes are not yet available. (Colombero et al., 2018) suggested that HF-slopequake are the dominant class of slopequake at the Madonna del Sasso cliff (hard-rock) and were generated by thermal cracking while LF-slopequake associated to frictional sliding are less frequent. Although we did not investigate the whole datasets, no LF-slopequakes were provided at two hard-rock cliffs: Aaknes and Chamousset (Fig 1.12) while LF-slopequake are recorded at hard-rock slides: La Clapiè re and Séchilienne (Fig 1.12). This observation seems to confirm the results of (Colombero et al., 2018). However, further comparison of the occurrence of the different slopequakes at specific sites in space and time must be done to improve the comprehension of these sources and confirm this statement.

Some variability exist for rockfall events due to the large variability of this source but also to the site geometry. Indeed, the volume of the blocks and possible break-up control the frequency content and the auto-correlation duration while the height of the scarp will play a significant role in the duration of the event. Depending on the site, rockfall signal can be very similar (e.g. Séchilienne, Fig 1.12) suggesting a constant source mechanism or very variable (e.g. Super-Sauze, 1.12). In the case of the Super-Sauze datasets, rockfall are characterize by a lack of energy in high frequencies due in this case to the distance between the seismic network and the scarp. Installation of additional sensors could be the easiest way to get rid of this variability. It must also be noted that, the differentiation between flow and fall signals may be challenging. Indeed, some of the events are very likely a mix of these two sources. Rockfalls of various blocks may generate granular flows with metric block impacts, both overlapping in the recorded seismic signals. Presence of metric rocks is also observed in debris flow prone torrents; for this type of events, the block impacts within the mass flows are recorded in the seismic signals (Burtin et al., 2016).

Harmonic signals have been also been documented recorded at the Pechgraben and Super-Sauze landslides Vouillamoz et al. (2017). These signals last from 1 to 5 s and repeat during minute-lasting sequences. The proposed interpretation includes hydro-fracturing or repetitive swarms of micro-earthquakes (Vouillamoz et al., 2017). The same signals are recorded at the La Clapière and the Aiguilles landslides with a fundamental frequency of 8 ± 1 Hz (Fig 1.13.b,c). At Séchilienne landslide, harmonic signals are also detected (Fig 1.13.d), mostly during the day, with different resonant frequencies between 2 and 12 Hz, simultaneously or for different time periods. Similar signals are observed at the Slumgullion and Super-Sauze but without clear harmonics in the PSD (Fig 1.13.e,f). Gomberg et al. (2011) hypothesizes that the waves were trapped along the side-bounding strike-slip fault generated by shear events. The presence of pipes and drains on or in the vicinity of these sites could also explain the origin of these signals. It justifies why these signals are not included in the Slopequake class because they are likely not generated by a slope deformation process. The location of the source, the distribution of the amplitude, the stability of the fundamental frequency and the daily temporal

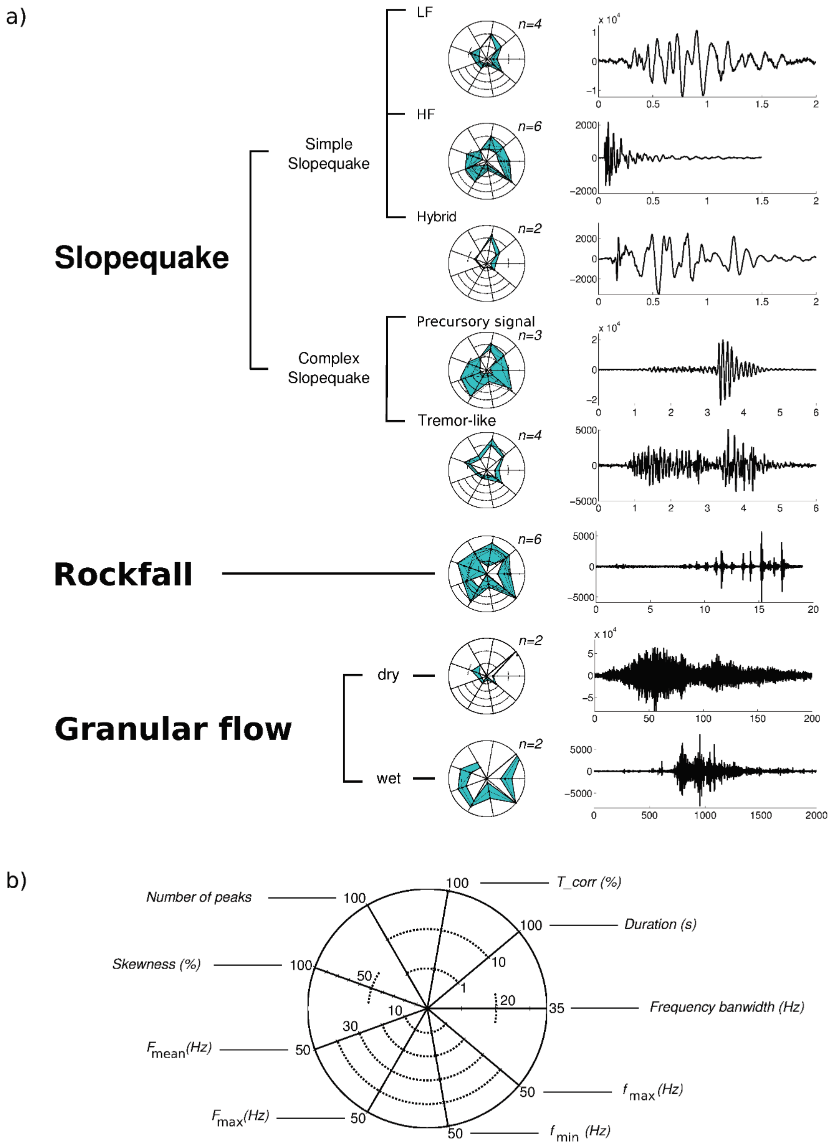

Figure 1.11: a) Summary of the proposed classification with plot of the attributes for the examples presented in the precedent figures and an example of waveform for each class. The convention for the attribute plot is presented in b).

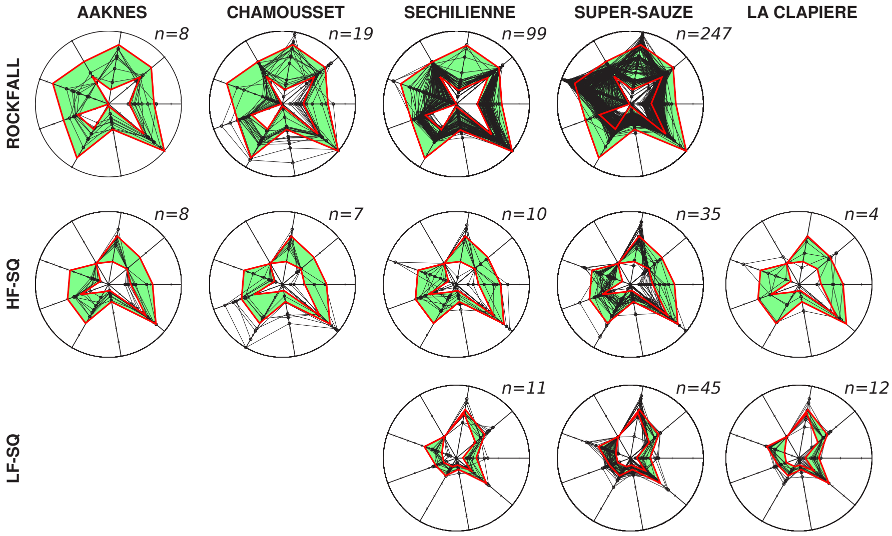

Figure 1.12: Variability of the signal features of classes “Rockfall”, “HF-slopequake” and “LF-slopequake” for five different sites: Aaknes, Chamousset, Séchilienne, Super-Sauze and La Clapière. The axes of the star diagram are the same as in Fig. 1.11.

occurrence of the source supports this assumption or result from wave propagation. More precise location of these events are needed to determine if they must integrated or not in the general typology in the case they are generated by fluid resonance in fractures.

Harmonic coda are also observe for certain signals (Fig 1.3d, Fig 1.9c) at high frequencies (i.e. 20 and 43Hz). The resonance is not present before the beginning of the signal and hence can not be due to anthropogenic noise (i.e. motors). In the case of Chamousset cliff, Levy et al. (2011) explained the presence of this monochromatic coda by the resonance of the rock column after the occurrence of the rock bridge breakage. At the Super-Sauze, similar resonant coda are observed at the end of certain rockfalls (Figure 4.d). Considering the distance between the main scarp and the seismic arrays (> 300 m) and the absence of large fracture on the scarp, the occurrence of this kind of resonance is very surprising in this case. This signals feature could also result from the wave propagation (i.e. trapped waves).

No long-lasting tremors are presented in this study. Schöpa et al. (2017) recorded a tremor with gliding before the occurrence of the Askja caldera landslide. Similar tremors are found on the Whillans ice stream in Antarctica during slow slip events (Paul Winberry et al., 2013, Lipovsky and Dunham, 2016), which repeat twice a day with a slip of about 10 cm lasting for about 20 minutes. Therefore, such signals may also occur during the nucleation phase of landslide failure. The question remains unclear if they are not observed because landslide acceleration is aseismic due to high pore fluid pressure (Scholz, 1998) or low normal stress at the sub-surface of the slope.

Difficulties still arise in providing an exhaustive description and interpretation of all the sources, particularly those generating short-duration signals. Several limitations currently prevent such analysis. First, the location of the sources remains difficult to establish due to the complexity of some of the signals, the size of the instrumented sites and the geometry (number, location) of the sensors installed close to the unstable slopes. The location of the epicenter of most of the events seems coherent with the instabilities deformation although resolving dispersion and 3-D heterogeneities of the velocity fields currently prevents to infer the depth of the events and their focal mechanisms. Secondly, a complementary approach to explain the origin of the sources is the analysis of their occurrence with respect to surface or basal displacement and monitoring of the water content and pore fluid pressures. It requires both exhaustive catalogs of landslide seismicity over long time periods and continuous and

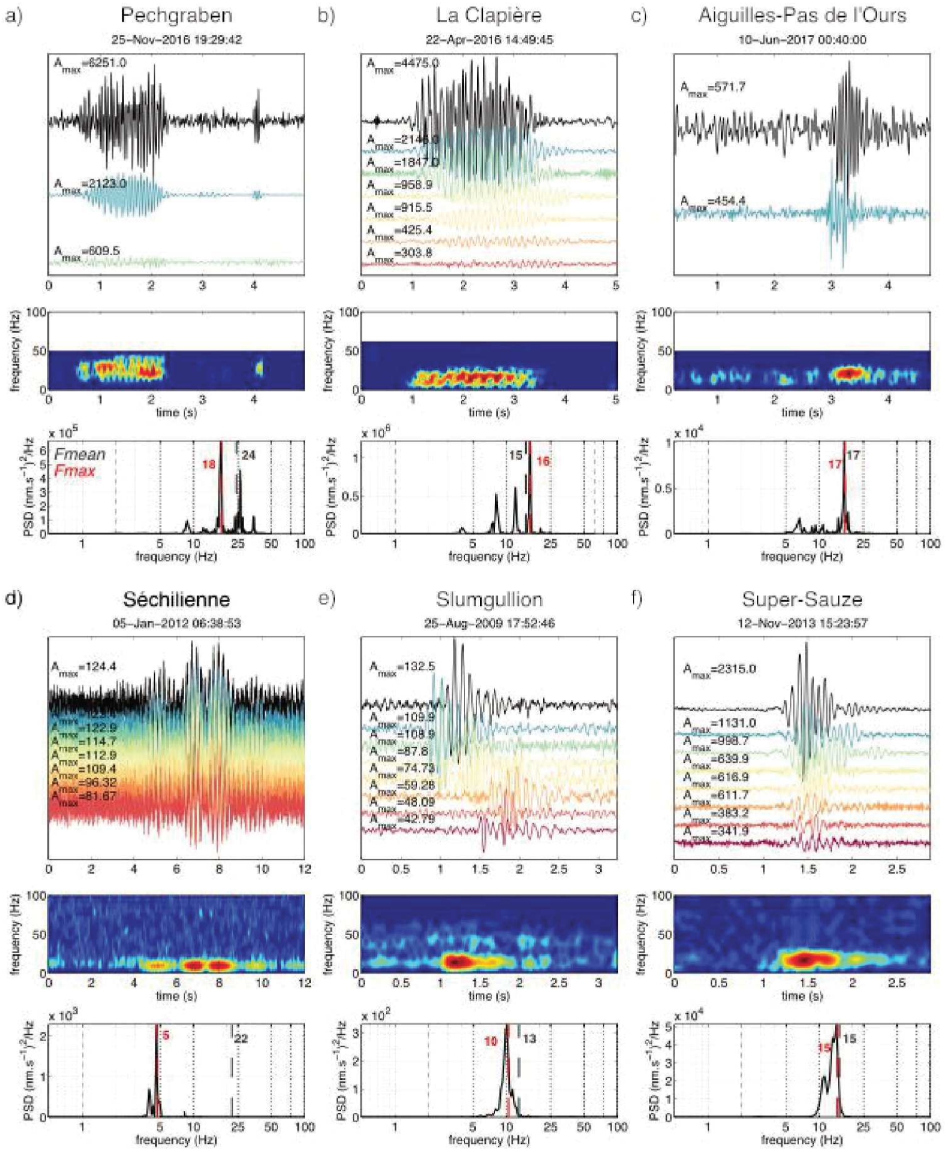

Figure 1.13: Examples of pure harmonic signals recorded at the a) Pechgraben, b) La Clapière and c) Aiguilles-Pas de l'Ours, d) Séchilienne, e) Slumgullion (Gomberg et al., 2011) and f) Super-Sauze slopes. See Fig 1.2 for description of the figure.

distributed datasets of displacements and pore fluid pressures which remains challenging to acquire. Finally, on addition to the characteristics of seismic signals, further information on the sources processes can be obtained from the distribution of the events in time, space and size. Events that occur regularly in time with similar amplitudes are likely associated with the repeated failure of an asperity surrounded by aseismic slip, for instance, at the base of a glacier (Helmstetter et al., 2015a) or of a landslide (Yamada et al., 2016a, Poli, 2017). Signal amplitudes and recurrence times often display progressive variations in time. In contrast, events that are clustered in time and space, with a broad distribution of energies, are more likely associated with the propagation of a fracture (Helmstetter et al., 2015b). The daily distribution of events time can also be helpful to identify anthropic sources, that occur mostly during the day. In contrast, natural events are more frequently detected at night, when the noise level is smaller.

Simulations and models are also required to explain the current observations. Indeed, experimental results suggest an increase of acoustic emissions correlated with the increase of the slope velocity (Smith et al., 2017) or an increase of acoustic emission due to the creation of the rupture area (Lockner et al., 1991). Acceleration of pre-existing rupture surface(s) seems to be the mechanism responsible for the seismicity recorded before large rockslide collapse. Yamada et al. (2016a), Poli (2017) argued that the high correlation between the repetitive events could only be explained by stick-slip movement of the locked section(s), while a cracking process would imply a migration of the location of the events and a change in the events waveforms. Schöpa et al. (2017) argued that the presence of gliding frequencies could only be produced by similar sources and hence close location. On the contrary, in the case of the Mesnil-Val column, Senfaute et al. (2009) interpreted the evolution from high frequency to low frequency events as the progressive formation of the rupture surface followed by the final rupture process immediately before the column collapse where both tensile cracks and shearing motion on the created rupture are generated.

1.8 Conclusions

Over the last decades, numerous studies have recorded seismic signals generated by various types of landslides (i.e. slide, topple, fall and flow), for different kinematic regimes and rock/soil media. These studies demonstrated the added-value of analyzing landslide-induced micro-seismicity to improve our understanding of the mechanisms and to progress in the forecast of landslide evolution.

In this work we propose a review of the endogenous seismic sources generated by the deformation of unstable slopes. A dataset of fourteen slopes is gathered and analyzed. Each of the source is described by nine quantitative features of the recorded seismic signals. Those features provide distinct characteristics for each type of source. A library of relevant signals recorded at relevant site is shared as supplementary material. We propose three main class “slopequake”, “rockfall” and “granular flow” to describe the main type of deformation observed on the slopes. Slopequakes are related to shearing or fracturing processes. This family exhibits the most variability due to the complexity of the sources. These variations are likely to be generated by different source mechanisms. “Rockfall” and “granular flow” classes are associated to mass propagation on the slope surface. They are distinguishable by the number of peaks clearly identified in the seismic signals.

Presently, several descriptions of the seismic sources are proposed for each study case. We believe that a standard typology will allow to discuss and compare seismic signals recorded at many unstable slopes. We encourage future studies to use and possibly enrich the proposed typology. This also requires publication of the datasets and/or catalogs to progress towards a common interpretation. Recently, organizations such as the United States Geological Survey (USGS) or the French Landslide Observatory (OMIV) have started this work (RESIF/OMIV, 2015, Allstadt et al., 2017).

A better understanding of the different sources endogenous to unstable slopes can also be achieved through the development of new adapted processing strategies to classify, locate and invert focal mechanism. Those developments must also be associated with the deployment of denser seismic networks, by taking advantage of the recent arrival on the market of relatively cheap and autonomous seismometers (eg. ZLand node systems, Raspberry-Shake systems). Moreover, the recent operational applications of Ground-Based SAR (Synthetic Aperture Radar) and terrestrial LiDAR technologies for monitoring purposes shows their relevance to monitor distributed surface displacements. On-going monitoring on several landslides combining those innovative approaches will certainly help to associate SQ events to deformation processes (Dietze et al., 2017b, RESIF/OMIV, 2015).

The proposed typology will help to constrain the design of new models to confirm the assumptions on the nature and the properties of the seismic sources. This will be particularly important for 1) explaining the variability of the SQ sources observed at the sites, 2) progressing in the physical understanding of the SQ sources, and 3) ascertaining the spatio-temporal variations of the seismic activity observed at some unstable slopes in relation with their deformation as well as, with external forcings such as intense rainfalls and earthquakes.

Acknowledgements

This work was carried with the support of the French National Research Agency (ANR) through the projects HYDROSLIDE "Hydrogeophysical Monitoring of Clayey Landslides", SAMCO "Society Adaptation to Mountain Gravitational Hazards in a Global change Context", and TIMES "High-performance Processing Techniques for Mapping and Monitoring Environmental Changes from Massive, Heterogeneous and High Frequency Data Times Series". Additional support by the Open Partial Agreement "Major Hazards" of Council of Europe through the project "Development of Cost-effective Ground-based and Remote Monitoring Systems for Detecting Landslide Initiation" was available. The continuous seismic data were provided by the Observatoire Multi-disciplinaire des Instabilités de Versant (OMIV) (RESIF/OMIV, 2015). Some seismic signals analyzed were acquired with seismometers belonging to the French national pool of portable seismic instruments SISMOB-RESIF. The authors thank J. Gomberg for the access to the data of the Slumgullion slope, constructive discussions and review of the early version of this paper as well as Nick Rosser and Emma Vann Jones for the access to the data of the North Yorkshire cliff. The author also thank Naomi Vouillamoz (University of Stuttgart) and Pascal Diot (ONF-RTM) for helping in the data acquisition at, respectively, the Pechgraben site and the Aiguilles-Pas de l'Ours site.

Synthesis: A standard typology of landslide endogenous seismic signals

Main results: We investigated the seismic signals generated by the deformation of a large number and variety of unstable slopes. Although we have not processed the complete datasets available at certain sites, we demonstrate that the seismic signals recorded in the vicinity of unstable slopes share common features suggesting similar source mechanisms. We proposed a generic classification of these signals as well as an interpretation for their associated sources. We also quantified the signal properties and proposed nine main features to discriminate the classes of seismic events.

Perspectives: Further catalogs of landslide endogenous seismicity could be established on the basis of the proposed typology allowing for the statistical comparison of the seismic events occurrence at different sites. This kind of studies may help validating the proposed assumption made on the physical processes associated with the seismic signals. Standard catalogs will also help to understand the relation between the endogenous seismicity, the landslide activity and the external forcings. This is important in order to investigate both the hydro-mechanical processes taking place during landslide deformation and the long-term seismic regime of the slopes. Indeed, as precursory seismic signals have been recorded before certain large failures, knowledge of the creeping regime is needed to differentiate it from the acceleration phase. The source to sensor distances play a critical role in the recorded signal features, in particular on the recorded frequency content.

However, the source may also generate certain frequencies which currently prevents to interpret the source of certain signals. The comparison of catalogs from different sites could help to resolve this ambiguity.

The identification of the main signal features discriminating the endogenous seismic events enables the implementation of supervised classification techniques which have the advantages of 1) proposing a less subjective analysis of the signals, and 2) being automatic. The machine learning method is presented in Chapter 2.

CHAPTER 2| Classification of seismic signals for the automated creation of seismicity catalogs

This chapter aims at developing a fully automatic classification method of seismological datasets using machine learning techniques. This development is relevant for many types of applications as the number of seismic networks, operating sensors and datasets is growing. Moreover, human interpretation is likely subjective introducing possible bias in the construction of the seismicity catalogs. The proposed methodology is expected to be robust, versatile and easy to use for any type of seismic datasets and classes of seismic signals.

The machine learning method has been developed on the datasets acquired at the Super-Sauze landslide. After some trial tests Hibert et al. (2017) we implemented the *Random Forest* supervised classifier which is based on multiple decision trees. This classifier has been chosen because it does not require any tuning (except the number of built trees) and because it intrinsically selects the most pertinent features during the training and provides an estimation of their importance. Its performance has been demonstrated for several application fields but has never been tested on seismic signals classification. Two inputs are required to built the classification trees: a set of attributes describing the signal properties and a training set (i.e. a set of example signals).

The attributes describe the seismic signal (e.g. waveform, frequency content and polarity). The list of attributes has been established by analyzing seismic datasets recorded on unstable slopes and on volcanoes. We present in this chapter the implementation of the method, and its application to the classification of the seismicity recorded at the Super-Sauze landslide. The training set has been elaborated for some selected periods, and the influence of the training set size on the sensitivity of the classification is discussed.

The chapter is based on:

Provost, F., Hibert, C. and Malet, J.-P. (2017). Automatic classification of endogenous landslide seismicity using the Random Forest supervised classifier. Geophysical Research Letters, 44, 113–120, doi:10.1002/2016GL070709.

Abstract: *The deformation of slow-moving landslides developed in clays induces endogenous seismicity of mostly low magnitude events* ($M_L < 1$)*. Long seismic records and complete catalogs are needed to identify the type of seismic sources and understand their mechanisms. Manual classification of long records is time consuming and may be highly subjective. We propose an automatic classification method based on the computation of 71 seismic attributes and the use of a supervised classifier. No attribute was selected a priori in order to create a generic multi-class classification method applicable to many landslide contexts. The method can be applied directly on the results of a simple detector. We developed the approach on the seismic network of 8 sensors of the Super-Sauze clay-rich landslide (South French Alps) for the detection of four types of seismic sources. The automatic algorithm retrieves 93% of sensitivity in comparison to a manually interpreted catalog considered as reference.*

2.1 Introduction

Recent studies have demonstrated the presence of endogenous seismicity induced by the deformation of slow-moving clay-rich landslides whereas aseismic creeping was previously assumed (Gomberg et al., 1995, Tonnellier et al., 2013, Walter et al., 2013b). Slide-quakes have been recorded on these unstable slopes proving the presence of material failures and shearing at the contact with the bedrock or directly within the moving mass. Locally, rockfalls can also be recorded on steep slopes (Tonnellier et al., 2013). Tremor-like signals have also been observed (Gomberg et al., 2011) and may be linked to fluid transfer or transient-slip. In the case of clay-rich landslides, analysis of the microseismicity is a challenging task because the signals are of low magnitude ($M_L < 1$), low amplitude (< 10000 nm.s^{-1}) and are generally highly attenuated at short distances (< 200 m). Dense seismic arrays should therefore be installed over long observation periods to obtain numerous signals with high Signal to Noise Ratio (SNR). Analysis of long seismological records (> 2 years) have been realized (Spillmann et al., 2007, Helmstetter and Garambois, 2010) resulting in the detection of several thousands of landslide seismic events. In these studies, the seismic events are classified manually after detection and rely on the personal experience of the human operator which can be subjective and time consuming.

Automatic classification methods have been developed for detecting the sources in volcanic areas (Langer et al., 2006, Curilem et al., 2009), to differentiate earthquakes and blasts (Fäh and Koch, 2002, Laasri et al., 2015) or for characterizing large rockslides (Dammeier et al., 2016). For multi-class problems, many classifiers were used such as Hidden Markov Models (HMM), Artificial Neural Networks (ANN) and Support Vector Machines (SVM), mainly on a reduced number of seismic attributes (Curilem et al., 2009, Hibert et al., 2014, Ruano et al., 2014). Recently, some studies (Beyreuther and Wassermann, 2008, Ruano et al., 2014, Quang et al., 2015) focused on the classification of continuous seismic records discriminating the background noise from the signal of interest. HMM was modified to detect one type of signal from few to one single example which is interesting for the detection of rare seismic sources (Hammer et al., 2012, 2013, Dammeier et al., 2016). However, the use of a unique seismic signal as reference lacks to capture the influence of the travel-path effects on the waveform and the frequency content of the recorded signal (Hammer et al., 2013). The authors hence suggested to use one example for different source-receiver distances. Finally, (Ruano et al., 2014) applied SVM for the discrimination of earthquake and explosion from background noise but the method requires a further interpretation of the detected events.

We propose a generic (applicable to various objects) and automatic (no fine tuning required) method to classify the endogenous seismicity of slow-moving landslides.The Super-Sauze landslide dataset is used as an example to test the method. We decided to use the Random Forest (RF) supervised classifier (Breiman, 2001) on a large training set. Four classes of seismic events are identified: two classes are related to events associated with the landslide deformation (e.g. quakes and rockfalls) and two classes of external sources (e.g. regional/global earthquakes, natural and anthropogenic noise). To train the model, 71 seismic attributes are computed (waveform, spectral content, spectrogram content, polarization and attributes related to the seismic network geometry). We here focused on the results of the classification method on a sample dataset and discuss possible improvement for its implementation as a near real-time classifier.

2.2 Data

The seismic records are acquired by two permanent arrays of the French Landslide Observatory OMIV (Observatoire Multi-disciplinaire des Instabilités de Versants) installed at the East and West sides of the Super-Sauze landslide (Southeast France) developed in weathered black marls (Malet et al., 2005). The seismic stations consist of short period seismometers (Noemax and Sercel L4C) with a flat response in the range 5-100 Hz; the signals are recorded with two broadband seismic recorders (RefTek 130S-01) at a 250 Hz sample frequency. The seismometers are arranged as tripartite array of 40 m layout around one three-component (3C) center site and three vertical one-component (1C) organized as equilateral triangle. The array thus forms a six-channels seismic recorder. The experiment dataset consists of 3 acquisition periods from October 11 to November 19, 2013, from November 10 to November 30, 2014 and from June 09 to August 15, 2015. The investigated dataset consists of 418 “Rockfall” events, 239 “Quake” events, 407 “Earthquake” events (EQ) and 395 “Natural/Anthropogenic noise” events (“N & A” noise) (Figure 2.1).

1. The “Rockfall” events take place mostly in the landslide main scarp where rigid blocks fall from steep slopes (> 100 m high). The block impacts are visible both in the signal waveform and in the stacked spectrogram for most of the events but can also present cigar-shapes when finer material is falling.
2. The “Quake” events are likely to be triggered by material failures, surface fissure openings and shear stress release at the landslide boundaries or at the contact with the bedrock. They are usually strongly attenuated and not recorded by all the seismometers and last less than 5 seconds.
3. The “Earthquake” events cluster all the regional seismic events triggered in the region (Jenatton et al., 2007) and teleseisms. Their pseudo-spectrograms have typically a triangle shape with a decrease of high frequency content with time.
4. The “Natural/Anthropogenic noise” events cluster all the anthropogenic (footsteps, car and helicopter motors, ski lifts, etc.) and environmental (wind, storm, water streams, etc.) noise in the vicinity of the landslide. Those events usually last several tens of seconds and illuminate either several frequencies or only specific ones in the spectrogram.

For more details on the endogenous signals observed at Super-Sauze landslide, the reader may refer to (Helmstetter and Garambois, 2010, Walter et al., 2012a, Tonnellier et al., 2013). It must be noted that it can be difficult to differentiate certain signals such as a succession of quakes from small-volume rockfalls or to distinguish footsteps and small-volume rockfalls.

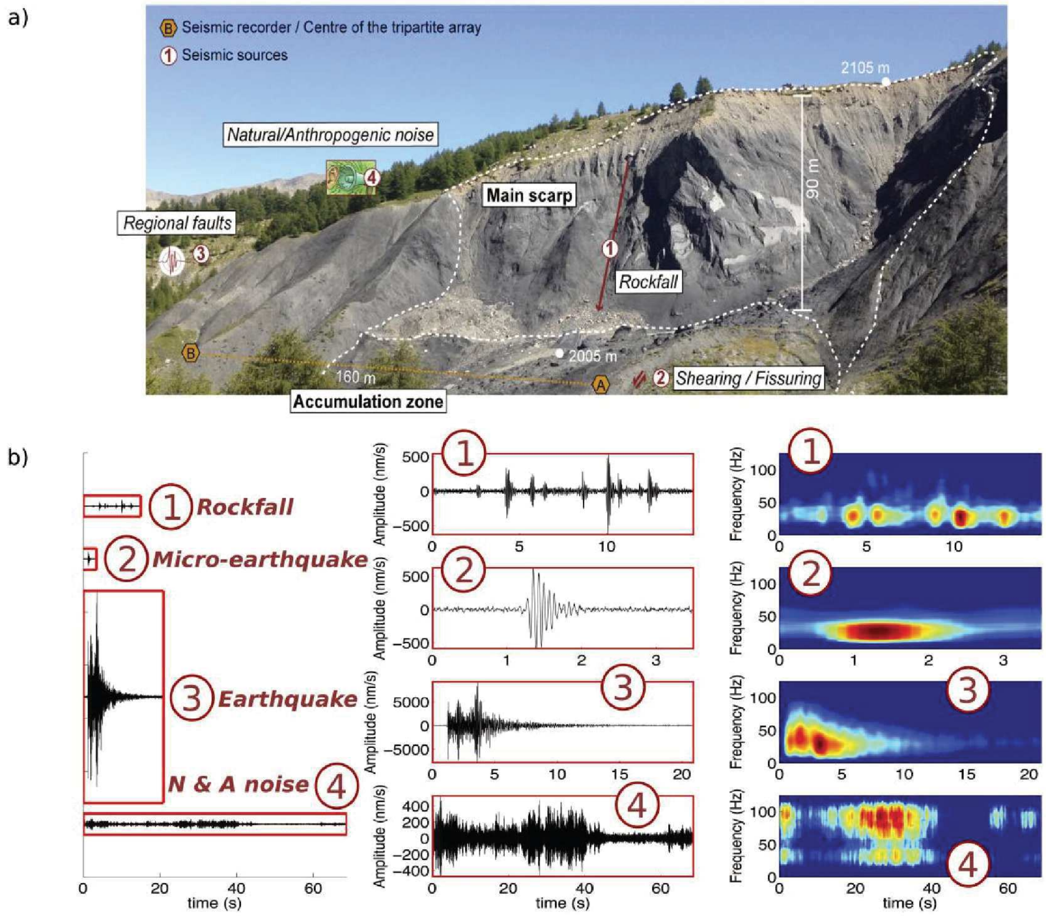

Figure 2.1: Seismic signals, sources and mechanisms observed on clay-rich landslides based on analyst interpretation: (a) Location of the micro-seismic arrays (A and B) and of the sources at the Super-Sauze landslide (South East France); (b) Examples of seismic signal for each class with the display of the waveform (trace with the higher SNR, first and second column) and stacked spectrogram (third column).

2.3 Methods

The processing chain consists in successive stages with (1) the detection of signals of potential interest, (2) the computation of the seismic attributes, and (3) the classification of the signals. The method relies on a detection algorithm that must be carefully chosen depending depending of the signals of interest and the study area. We used a spectrogram analysis (Helmstetter and Garambois, 2010) to detect the signals. The method is equivalent to a STA/LTA algorithm applied in the frequency domain. An event is detected when the seismic signal spectrum is larger than 1.5 times the noise spectrum level. The spectrogram is computed in the frequency range 5-100 Hz for each vertical sensor. Second, we calculated 71 seismic attributes (Table 2.1) to describe the signals in terms of signal waveform, signal frequency content, pseudo-spectrogram, polarity and some attributes related to the seismic network geometry. The signal waveform and the frequency content are computed on the trace with the highest SNR. The spectrogram attributes are computed on the summed spectrogram and the polarity attributes are computed separately on the three-component seismometers. Some of these attributes are commonly used in signal classification and have been described in previous studies (Bessason et al., 2007, Curilem et al., 2009, Hammer et al., 2012, Hibert et al., 2014). We explored here additional attributes related to the seismic network geometry. All the attributes are computed automatically on the raw signal window and do not require any human interpretation such as wave onset identification or location. Only the Kurtosis attribute requires setting manually various frequency bands (here 5-10Hz, 5-50Hz, 10-70Hz, 50-100Hz, 5-100Hz).

Table 2.1: Attributes table

#	Description	Formula
	Waveform attributes:	
1	Duration	$t_f - t_i$, with t_i and t_f: beginning and end of the signal
2	Ratio of the mean over the maximum of the envelop signal	–
3	Ratio of the median over the maximum of the envelop signal	–
4	Ratio between ascending and descending time	$\frac{t_{max}-t_i}{t_f-tmax}$, with t_max : time of the largest amplitude
5	Kurtosis of the raw signal (peakiness of the signal)	$\frac{m_4}{\sigma^4}$, with m_4: fourth moment, σ: standard deviation
6	Kurtosis of the envelop	see 5
7	Skewness of the raw signal	$\frac{m_3}{\sigma^3}$, with m_3: third moment
8	Skewness of the envelop	see 7
9	Number of peaks in the autocorrelation function	–
10	Energy in the first third part of the autocorrelation function	$\int_0^{\frac{T}{3}} C(\tau) d\tau$, with T: signal duration, C: autocorrelation function
11	Energy in the remaining part of the autocorrelation function	see 10
12	Ratio of 11 and 10	–
13-17	Energy of the signal filtered in 5-10Hz, 10-50Hz, 5-70Hz, 50-100Hz, 5-100Hz	$\int_0^T y_f(t) dt$, with y_f: filtered signal in the frequency range [f1-f2]
18-22	Kurtosis of the signal in 5-10Hz, 10-50Hz, 5-70Hz, 50-100Hz, 5-100Hz frequency range	see 5
23	RMS between the decreasing part of the signal and $l(t) = Y_{max} - \frac{Y_{max}}{t_f - t_m ax} t$	$\sqrt{\overline{Y(t) - l(t)}^2}$, with Y: envelop of the signal
	Spectral attributes:	
24	Mean of the DFT	DFT: Discrete Fourier Transform
25	Max of the DFT	–
26	Frequency at the maximum	–
27	Central frequency of the 1^{st} quartile	–
28	Central frequency of the 2^{nd} quartile	–
29	Median of the normalized DFT	–
30	Variance of the normalized DFT	–
31	Number of peaks ($> 0.75 DFT_{max}$)	DFT_{max}: maximum of the DFT

Continued on next page

Table 2.1 – continued from previous page

#	Description	Formula
32	Number of peaks in the autocorrelation function	–
33	Mean value for the peaks	–
34-37	Energy in $[0,\frac{1}{4}]Nyf$, $[\frac{1}{4},\frac{1}{2}]Nyf$, $[\frac{1}{2},\frac{3}{4}]Nyf$, $[\frac{3}{4},1]Nyf$	$\int_{f_1}^{f_2} \text{DFT}(f)df$ with f_1,f_2: the considered frequency range
38	Spectral centroid	$\gamma_1 = \frac{m_2}{m_1}$, with m_1 and m_2 are the first and second moment
39	Gyration radius	$\gamma_2 = \sqrt{\frac{m_3}{m_2}}$, with m_3 is the third moment
40	Spectral centroid width	$\sqrt{\gamma_1^2 - \gamma_2^2}$
	Spectrogram^{a} attributes:	
41	Kurtosis of the maximum of all Discrete Fourier Transforms (DFTs) as a function of time t	$Kurtosis\big[\max_{t=0,..,T}(\text{SPEC}(t,f))\big]$ with SPEC(t,f): the spectrogram
42	Kurtosis of the maximum of all DFTs as a function of time t	see 41
43	Mean Ratio between the maximum and the mean of all DFTs	$mean(\frac{max(\text{SPEC})}{mean(\text{SPEC})})$
44	Mean Ratio between the maximum and the median of all DFTs	see 43
45	Number of peaks in the curve showing the temporal evolution of the DTFs maximum	–
46	Number of peaks in the curve showing the temporal evolution of the DTFs mean	–
47	Number of peaks in the curve showing the temporal evolution of the DTFs median	–
48	Ratio between 45 and 46	–
49	Ratio between 45 and 47	–
50	Number of peaks in the curve of the temporal evolution of the DTFs central frequency	–
51	Number of peaks in the curve of the temporal evolution of the DTFs maximum frequency	–
52	Ratio between 50 and 51	–
53	Mean distance between the curves of the temporal evolution of the DTFs maximum frequency and mean frequency	–
54	Mean distance between the curves of the temporal evolution of the DTFs maximum frequency and median frequency	–

Continued on next page

Table 2.1 – continued from previous page

#	Description	Formula
55	Mean distance between the 1st quartile and the median of all DFTs as a function of time	–
56	Mean distance between the 3rd quartile and the median of all DFTs as a function of time	–
57	Mean distance between the 3rd quartile and the 1st quartile of all DFTs as a function of time	–
58	Number of gaps in the signal	–
	Network attributes:	
59	SNR maximum	–
60	Station with maximum SNR	–
61	Station with maximum amplitude	–
62	Station with minimum amplitude	–
63	Ratio between attributes 62 and 61	–
64	Mean correlation	–
65	Maximum correlation	–
66	Mean correlation lag in between station	–
67	Standard deviation correlation lag in between station	–
	Polarity attributes:	
68	Rectilinearity	$1 - \frac{\lambda_{11}+\lambda_{22}}{2\lambda_{33}}$ with $\lambda_{33} >> \lambda_{22} >> \lambda_{11}$
69	Azimuth	$\arctan(\lambda_{23}/\lambda_{13}) \times 180/\pi$
70	Dip	$\arctan(\lambda_{33}/\sqrt{\lambda_{23}^2+\lambda_{13}^2}) \times 180/\pi$
71	Planarity	$1 - \frac{2\lambda_{11}}{\lambda_{33}+\lambda_{22}}$

[a] The spectrogram is the collection of the DFTs computed for signal windows of 1s with an overlap of 90%. The spectrogram is represented as a two-dimensional matrix representing the evolution of the frequency content (rows) through time (columns).

The selected supervised classifier is the *Random Forest* algorithm (RF), which is an ensemble learning method based on decision trees (Breiman, 2001). It is based on several (> 500) decision trees trained on the dataset. The class is assigned by the majority of the decision tree votes. RF has proven to be one of the most efficient algorithm for the classification of 121 complex datasets among 17 families of classifiers (Fernández-Delgado et al., 2014). Moreover it is simple to use and does not require any fine-tunning (Stumpf and Kerle, 2011). It also enables to compute which attributes are the most discriminant for the classification. This is done through the estimation of the *Variable Importance* as defined by (Breiman, 2001) and consists in randomly swapping the values of one attribute over all the samples of the training dataset. The *Variable Importance* is the variation in the Out-Of-Bag error computed before and after the permutation. The larger the error variation the more important is the attribute. We worked with the TreeBagger version of RF implemented in the Matlab Statistical Toolbox. For the tests, successively 10%, 30%, 50% and 70% of each class was randomly selected as training set for the classifier. The RF model was evaluated for each test on 70 events randomly chosen in each class in the events not used in the training set. One hundred models runs were performed for each test and the classification results are averaged.

2.4 Results

The sensitivity reaches 93% ± 1.5% and the specificity 97% ± 0.5% in average for 100 runs of Random Forest. Table 2.2 presents the confusion matrix that represents the comparison between the reference interpretation and the automated classification of the dataset. The “Earthquake” and “Rockfall” events are better classified with a sensitivity of 94% whereas the “Quake” and the “Natural/Anthropogenic noise” events have a sensitivity of 93% and 92% respectively.

The sensitivity increases with the number of examples in the training set (Figure 2.2). We observe that for above 50% of examples introduced in the training set for each class, the increase in sensitivity is not significant anymore (< 1%). However, it seems that the sensitivity of the classes “Earthquake” and “Natural/Anthropogenic noise” increases more than for the two others; thus more examples of these two classes may improve the sensitivity.

The importance of the attributes in the classification are presented in Figure 2.3. In our case, we observe that the most discriminant attribute is the ratio between the maximum and minimum amplitude recorded in the network (A63). The other most discriminant attributes are, successively, the ratio between the ascending and descending duration of the signal (A4), the signal duration (A1), the station with the maximum amplitude (A61), the median correlation (A65), the energy in the first third of the auto-correlation function (A10), the energy in the signal spectrum between 0 and 31.25 Hz (A34), the planarity (A71), the mean correlation lag in between traces (A66) and the energy of the signal filtered in 50-100 Hz (A16)). No attribute from the spectrogram analysis appears in the 10 most discriminant attributes. The less discriminant attributes are respectively the azimuth (A69, A73) and the ratio between the number of peaks in the pseudo-spectrogram function (A52).

Table 2.2: Mean confusion matrix for 100 runs of Random Forest. The classified (Class.) events are represented with respect to the events of the reference catalog (Ref.).

	Class. Rockfall	Class. Quake	Class. EQ	Class. N & A Noise
Ref. Rockfall	94%	1%	3%	2%
Ref. Quake	3%	93%	3%	1%
Ref. EQ	1%	2%	94%	3%
Ref. N & A Noise	2%	3%	3%	92%

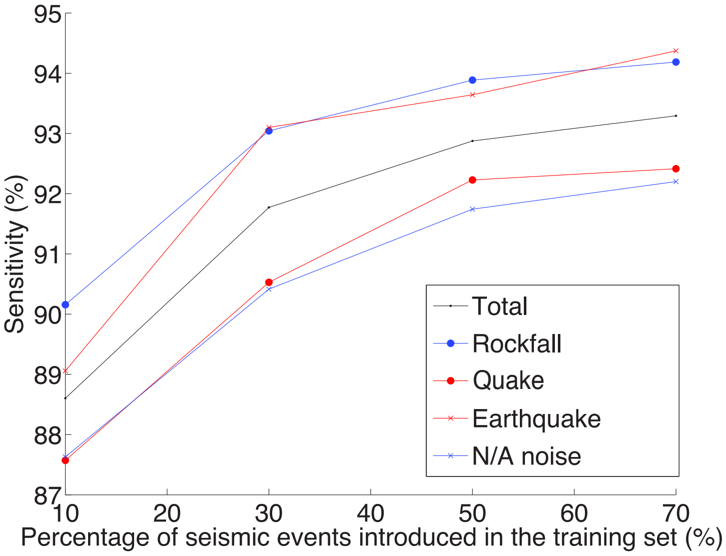

Figure 2.2: Sensitivity for different sizes of the training set: 10%, 30%, 50% and 70% of each class. The training set is randomly selected 100 times and the sensitivity is averaged for each run.

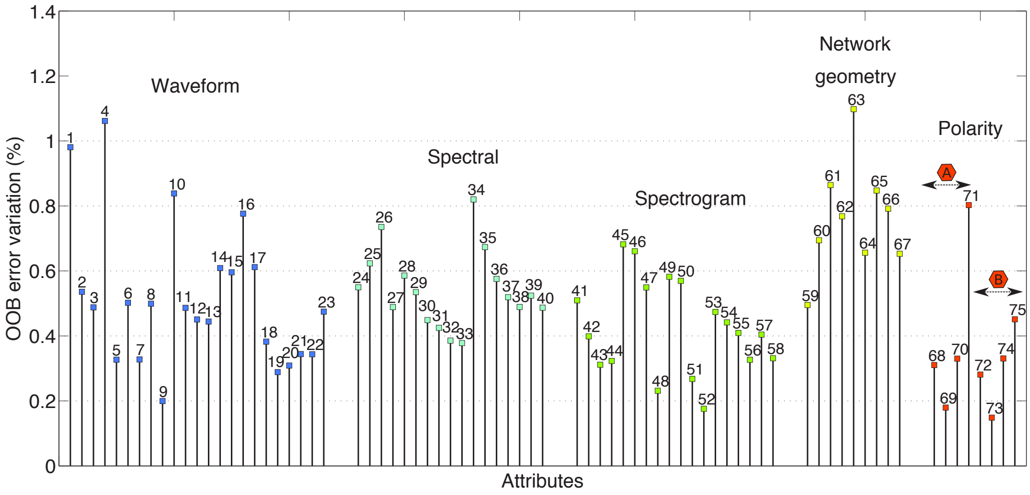

Figure 2.3: Mean variable importance for 100 runs of Random Forest. The attributes are presented with their respective numbers (Table1) and by category: Waveform, Spectral (attributes computed on the FFT of the signal), Spectrogram (attributes computed on the pseudo-spectrogram of the signal), Network geometry (attributes taking into account the geometry of the network) and Polarity. The polarity attributes of the three-component seismometers are represented successively for microseismic array A and B.

2.5 Discussion and conclusion

The more classes are discriminated by an attribute, the more important the attribute is. Therefore, all the seismic sources can be separated by attribute 63 ($A63_{EQ} >= A63_{N\&Anoise} > A63_{ROC} >= A63_{Q}$) because the waves created by the local sources travel through the subsurface and may be highly attenuated at short distances (< 100 m) while for the external sources, the waves travel in the consolidated bedrock and are thus less attenuated. In the same manner, the ratio between the ascending and descending phase can separate the highly non symmetrical sources (Rockfall and Earthquake) from the symmetrical signal generated by the quakes ($A4_{ROC} >= A4_{Q} > A4_{EQ}$). The duration finally discriminates mostly the “Natural & Anthropogenic noise” events ($A1_{N\&Anoise} > 20s$) and the quakes ($A1_{Q} < 5s$). Finally the next attributes in the order of importance mainly discriminate only one class: the "N & A noise” events are highly not correlated compared to the other signals (A65) and the rockfall events mainly occur in the scarp so the sensors with the maximum amplitude are the closer ones (A61).

The azimuth of the particle motion is, in theory, a useful information to discriminate the sources because it gives the source location direction. Here it seems that the station with the maximum amplitude (A61) gives more robust information on the source location by discriminating the rockfall events. The attributes implying the number of peaks are also not very discriminating here probably because it is rather difficult to set an efficient threshold above which a peak is considered relevant.

Considering only the 10 most discriminant attributes slightly deteriorates the classification with a sensitivity of 92% ± 1.5% while not reducing significantly the computing time (e.g. the attributes can currently be calculated from the raw signal in ca. 1 second). Therefore, no attribute should be removed from the model even the one with the lower discriminating rate. Moreover, the list of attributes enables the method to be easily applied to various contexts since they allow to fully describe each signal. The most discriminant attributes will probably be different at other landslides but this will not decrease the accuracy of the method. The number of attributes also enables the method to be adaptive to possible temporal variations of the source mechanisms.

Sensitivity is a common measure used to evaluate a classifier but this criteria requires a reference catalog constructed by one analyst. Because the human interpretation is subjective (Langer et al., 2006, Hibert et al., 2014, Laasri et al., 2015), the sensitivity may not reflect the complexity of the dataset. We thus tested the human subjectivity on a smaller dataset of 60 events with 20 human analysts and compared the results. The total of the analysts’ votes agrees fully with the reference interpretation thus validating the reference catalog used to compute the sensitivity. The mean sensitivity for the human interpretation is 82% (Table 2.3). It must be noted that the information given to the human analysts was slightly different to the one introduced in the statistical model as the seismic network geometry and the polarity attributes were not presented to the analysts. We ran the RF model with the same information as given to the analysts (A1 to A58) and obtained a mean sensitivity of 90% (Table 2.3). In both cases, the automatic method obtains higher or similar maximal sensitivity than the analysts (Table 2.3). The automatic method is hence comparable to the human analysis while a larger sensitivity of the automatic method would over-fit the interpretation of one particular analyst.

Table 2.3: Sensitivity results for the set of 20 human analysts, for the RF model with all attributes taken into account and for the RF model with A1 to A58. The RF model is tested 100 times using 70%of the dataset as training set and testing the model on the 30% of the dataset (not selected as training set).

	Human analysts	RF	RF (Attributes 1 to 58)
Mean Sensitivity	82%	93%	90%
Max. Sensitivity	95%	96%	94%
Min. Sensitivity	58%	90%	86%

We propose an automatic classifier based on RF and a large number of attributes to describe the seismic signals. The obtained sensitivity is 93% ± 1.5% for a complex multi-class problem (low magnitude events, intra-class heterogeneity). The method requires at least 150 examples for the different event types to train the model; it further allows separating the highly heterogeneous class (e.g. “N & A noise”) with the same success rate than the other classes. RF provides probability estimates on the classification that are useful to accept or reject a new classification and determines when the model needs to be retrained. The latter could also provide new insights to detect changes of the seismicity with time. In summary, the method is easily applicable to classify the seismicity of various objects (volcanoes, geothermal fields, earthquake detection) and can be used even for studies where only one single sensor is available. The implementation of the method for real-time applications is in progress.

Acknowledgements

This work was carried with the support of the French National Research Agency (ANR) through the projects HYDROSLIDE ’Hydrogeophysical Monitoring of Clayey Landslides’ and SAMCO ’Adaptation de la Société aux Risques Gravitaires en Montagne dans un Contexte de Changement Global’ and of the Open Partial Agreement Major Hazards of Council of Europe through the project ’Development of cost-effective ground-based and remote monitoring systems for detecting landslide initiation’. Continuous seismic data used here were provided by the Observatoire Multi-disciplinaire des Instabilités de Versant (OMIV) (RESIF/OMIV, 2015). The authors thank A. Stumpf (EOST) for constructive discussion on supervised classification algorithms, A. Helmstetter (ISTerre) for discussion on the classification of the event types and the volunteers at EOST who participated in our classification experiment. The authors also acknowledge the anonymous reviewers for their helpful remarks.

2.6 Appendix: Analysis of the classification uncertainty

Random Forest also provides an estimation of the uncertainty of the classification for each classified event. Each tree provides a vote meaning that each tree estimate the class of an event. The uncertainty is hence computed as the percentage of trees voting for a class. We want to analyze the reliability of this uncertainty and determine a threshold to consider an event correctly classified. We trained the Random Forest algorithm with 119 micro-earthquakes, 209 rockfalls, 203 earthquakes and 197 natural/anthropogenic noise examples. The trained model was then used to classify a set of 400 landslide seismic events (100 events per class). We analyzed the set of events for each class and analyze the distribution of the votes obtained with Random Forest (Figure 2.4). For “Rockfall” and “N & A noise” classes, more than 60% of the classifications are made with 90% of tree voting for the correct class. For “slopequake” and “Earthquake” classes, around 40% of the events are classified with more than 90% of votes. However, above the threshold value of 65%, the tree vote gives the correct classification for all the classes. Hence, we set a threshold of 0.65 to validate the classification of an event meaning at least 65% of the grown decision trees must vote for one class to accept this class. When the threshold is set, 59 of the 400 event classifications were rejected (7 micro-earthquakes, 13 rockfalls, 20 earthquakes, and 16 natural/anthropogenic noise). The rest of the events are perfectly classified with the exception of one natural/anthropogenic noise event (electrical transient) that was misclassified as a micro-earthquake.

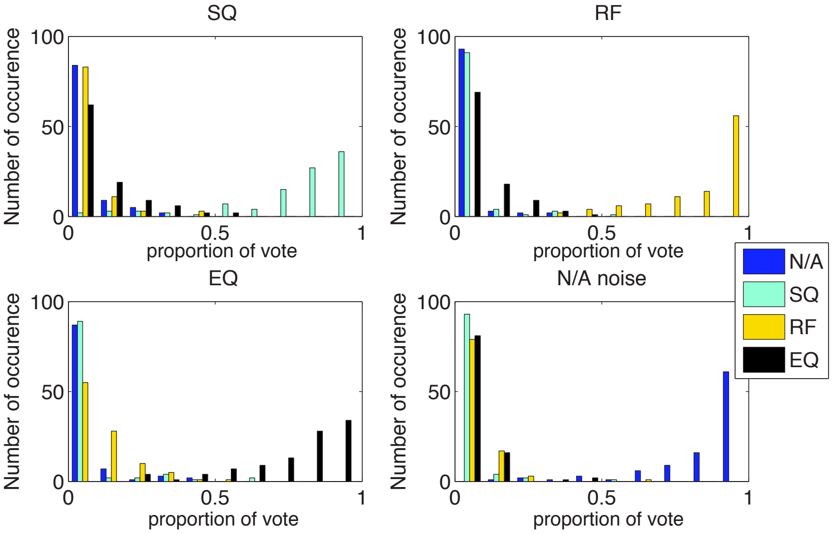

Figure 2.4: Distribution of votes obtained with Random Forest for each all the events of the training set classified as a) slopequake, b) Rockfall, c) Earthquake and d) "N & A" events.

Synthesis: Classification of seismic signals for the automated creation of seismicity catalogs

Main results: We proposed and implemented a supervised classification method of seismic signals based on a the calculation of a large number of signals features and on the *Random Forest* algorithm. We applied and tested the method on the seismic datasets of the Super-Sauze landslide. We obtained a sensitivity > 90% for the classification of four types of seismic events . We show that this sensitivity is equivalent or event larger than human sensitivity. The sensitivity depends on the number of examples used in the training sets. Introducing a large number of examples improved the value of the sensitivity. This can be a limitation to explore the occurrence of seldom events. The methodology was also applied on the Piton de la Fournaise volcano (Maggi et al., 2017, Hibert et al., 2017c). These studies demonstrated the efficiency of this approach as the authors obtained a sensitivity > 90% with 2 or more classes. The ranking of the attributes is different for these two studies, demonstrating the pertinence of calculating the complete set of attributes to construct the statistical model.

Perspectives: We demonstrated in Chapter 1 that similar signals are observed for several gravitational slopes. The construction of a general catalog with examples of signals from several unstable slopes may be a solution to provide large training sets even for the more seldom events. Further tests must be carried out to determine if the training set identified on one site is adequate and usable for another site. The question also remains on the suitability of the training set through time. Hibert et al. (2017c) show that changes in the rockfall dynamics observed at the Piton de la Fournaise could be observed by a decrease of the sensitivity. The implementation of the semi- and unsupervised version of the Random Forest would help to address these issues and to refine the classes.

CHAPTER 3| Location of seismic signals for understanding the landslide deformation pattern

Location of seismic sources is a crucial step in seismology to interpret the physical processes. The objective of **Chapter 3** is to propose a robust and automatic location method adapted to the specific context of landslides. Accurate locations require a proper interpretation and/or processing of the signal and a realistic estimation of the ground properties.

In the case of landslides, the limited number of sensors, the often poorly constrained geometry of the networks, the complexity of the ground structure and of the surface topography (possibly rapidly evolving in time) as well as the properties of the recorded seismic signals make the location of the sources very challenging. In order to implement an accurate and automatic method, we need:

- to take into account the topography and the heterogeneity of the underground velocity structure,
- to implement an automatic processing of the seismic signals to retrieve the different information needed for source location (i.e. seismic wave arrivals, amplitude, polarization, etc.),
- to integrate these information in a location scheme and estimate their uncertainties.

We propose a method based on the analysis of the seismic wave amplitude and the picking of the P-wave arrivals. Seismic wave tomography has been realized to create a realistic and high spatial resolution P-wave velocity model taking into account the topography and the heterogeneity of the ground. The location method consists in maximizing the inter-trace correlation of the P-wave arrivals. The analysis of the amplitude is used as a prior information to reduce the search area. Due to the complexity of the seismic signals, we propose an optimization step to improve the determination of the P-wave window.

This chapter is based on:

Provost, F., Malet,J.-P., Helmstetter, A., Gance, J., and Doubre, C. (2018). Automatic approach for increasing the location accuracy of slow-moving landslide endogenous seismicity: the *APOLoc* method, *Geophysical Journal International* (accepted, in press).

Abstract: *Seismological observations offer valuable insights on the stress-strain states, the physical mechanisms and the possible precursory signs of activation of various Earth surface processes (i.e. volcanoes, glaciers, landslides). Comprehensive catalogs of the endogenous landslide seismicity, i.e. corresponding to seismic sources generated by the unstable slope from either mechanical or hydrological origins, should include the typology and an estimate of the source parameters (location, magnitude) of the event. These advanced catalogs constitute a strong basis to better describe the slope deformation and its time evolution and better understand the controlling factors. Because the number of seismic events in landslide catalogs is generally large, automatic approaches must be considered for defining both the typology and the location of the sources. We propose here a new location approach called Automatic Picking optimization and Location method - APOLoc for locating landslide endogenous seismic sources from seismological arrays located at close distance. The approach is based on the automatic picking of the P-waves arrivals by optimizing the inter-trace correlations. The method is tested on calibration shots realized at the Super-Sauze landslide (Southeast French Alps) and compared to other location approaches. By using a realistic velocity model obtained from a seismic tomography campaign, APOLoc reduces the epicenter errors to 23 m (on average) compared to ca. 40 m for the other approaches. APOLoc is then applied for documenting the endogenous seismicity (i.e. slopequakes and rockfalls) at the landslide.*

3.1 Introduction

The term landslide refers to a large range of gravitational instabilities of various sizes, rheologies and dynamics. They may be triggered by internal causes, such as changes of pore-fluid pressure due to gravitational load and/or external causes such as heavy and prolonged rainfalls or earthquakes. Current forecasting methods are based on a prediction of the failure or acceleration of the mass from geodetic (Saito, 1969, Petley, 2004), hydrologic and/or meteorological data (Bernardie et al., 2015). In most cases, these statistical methods fail in providing an accurate timing of the failure (Intrieri and Gigli, 2016) as many physical mechanisms can also interact and initiate slope acceleration and slope failure depending on the geomechanical properties of the mass. Slope acceleration towards failure results from fracture propagation at depth (Amitrano et al., 2005, Crosta and Agliardi, 2003, Petley et al., 2005, Poli, 2017, Yamada et al., 2016) or from rheological solid-fluid transition (Van Asch, 1984, Malet, 2003, van Asch et al., 2006, Mainsant et al., 2012b, Carrière et al., 2018). These processes generate seismic signatures that can be investigated.

Two main approaches exist to analyze the seismic signals recorded on unstable slopes: micro-seismic or seismic noise correlation monitoring (Amitrano et al., 2005, Larose, 2017). Seismic noise correlation monitoring computes the variation of the shear waves velocity in the medium through time. The shear waves are related to the shear modulus of the medium and their variation may reflect changes in the mechanical properties of the mass. The method seems to be particularly efficient for the monitoring of soil fluidization. A drop in the shear waves velocity has been observed before acceleration of the Pont-Bourquin mudflow (Switzerland; Mainsant et al. (2012b)) and have been reproduced in laboratory experiments for clayey soils (Mainsant et al., 2012a, 2015). Micro-seismic monitoring aims at detecting and classifying the seismic sources generated by landslide deformation. The analysis of the space and time distribution of the sources allows retrieving the mechanism of the seismic sources in order to improve the knowledge on the mechanical state of the landslide. It is also a valuable information to understand the temporal response of the slopes to external forcings. Catalogs of landslide seismic activity constitute an efficient corpus of information to forecast the evolution of slope deformation, and to understand the temporal response of the slopes to external forcings. As precursory events have been detected before a few large failures, the creation of automatic catalogs documenting the long-term landslide seismic activity is needed to improve the prediction of slope deformation. Seismological precursory signals have been recorded on a coastal cliff before its collapse (Amitrano et al., 2005) and before some major landslides (Caplan-Auerbach and Huggel, 2007b, Poli, 2017, Yamada et al., 2016, Schöpa et al., 2017) demonstrating the potential of seismology as an input for warning systems. Detection and location of the seismic signals in real-time has demonstrated its efficiency on volcanoes to provide alarms before eruption (Chouet et al., 1994, García et al., 2014). Thus, one of the challenge for developing robust landslide monitoring and warning systems integrating seismic observations is the automatic creation of advanced seismic catalogs including the detection, the location and the characterization of the endogenous seismic signals.

Previous analyses of landslide micro-seismicity revealed the occurrence of endogenous seismic sources in both brittle (e.g. rockslides; Amitrano et al. (2005), Spillmann et al. (2007), Helmstetter and Garambois (2010), Levy et al. (2011), Walter et al. (2012b), Brückl et al. (2013), Provost et al. (2018)) and ductile medium (e.g. earth/mudslides; Rouse et al. (1991), Gomberg et al. (1995), Tonnellier et al. (2013), Walter et al. (2013b), Provost et al. (2018)). However the mechanisms controlling the generation of these seismic signals remain poorly understood, mainly because of the poor accuracy of the seismic source location with respect to the landslide dimensions. Accurate source location for landslides is complex due to:

- the difficulty in constructing reliable velocity models taking into account the spatial and temporal variations of the petrophysical properties of the medium;
- the complexity of the seismic signals, particularly for the identification of P- and S-waves (Spillmann et al., 2007, Lacroix and Helmstetter, 2011) , due to low Signal-to-Noise Ratios (SNR) resulting from low energy sources ($M_L < 0$), high attenuation of the seismic waves in unconsolidated and cracked media (Rouse et al., 1991, Gance et al., 2012), and the short propagation distances and possible scattering;
- the field conditions (steep slopes, rapidly evolving surface topography, often in mountain areas with difficult meteorological conditions) rendering the maintenance of seismic instruments difficult for long-term observations and potentially modifying signal polarities (Neuberg et al., 2000).

The objective of this work is to propose an accurate location procedure for the automatic analysis of landslide endogenous seismic sources. The proposed method consists in a new coupled picking and location procedure: *APOLoc* (which stands for *Automatic Picking Optimization and Location*). After building a realistic velocity model for P-waves from seismic tomography profiles, the *APOLoc* workflow consists in three steps: first, the search area is constrained by applying an Amplitude Source Location analysis (ASL); second, the onset of the signal is automatically identified using a Kurtosis-based function; third, the picking of the signal onset is refined by recursively optimizing the inter-trace correlation. *APOLoc* is tested on a set of 15 calibration shots and compared to other location methods: Amplitude Source Location (ASL; Taisne et al. (2011)), Probabilistic location (NonLinLoc; Anthony et al. (2000)) and Beam-Forming (BF; Lacroix and Helmstetter (2011)). The effect of the velocity model on the location accuracy is also tested and discussed for the calibration shots. These tests prove the efficiency of *APOLoc* combined to a realistic P-wave velocity model. Finally, this approach is applied to natural events (i.e. slopequakes and rockfalls) and its suitability is discussed.

3.2 Study site: the Super-Sauze landslide

The study site is the Super-Sauze landslide located in the Southeast French Alps. The landslide is composed of reworked clay shales (black marls) of the Jurassic age. Triggered in the early 1960's, it has propagated progressively downslope and has reached a volume of 750 000 m^3 and a size of 800 ×

300 m^2 with an average thickness of 15 m. The landslide is one of the permanent monitoring sites of the French Landslide Observatory OMIV (Observatoire Multi-disciplinaire des Instabilités de Versant: www.ano-omiv.cnrs.fr). Three categories of observations are monitored since 2007 using different sensors: the surface deformation monitored using permanent GPS, terrestrial optical cameras and repeated terrestrial laser scanning campaigns; the sub-surface hydrology using a network of pore water pressure sensors installed in shallow piezometers and soil humidity probes; the seismic activity of the slope using two permanent arrays of seismometers. Geophysical and geotechnical investigation campaigns helped to constrain the underground structure (Malet, 2003, Schmutz et al., 2009, Gance et al., 2012, Travelletti and Malet, 2012b). Dynamic penetration tests and inclinometric measurements showed the presence of two main units above the bedrock (Malet, 2003). The first and shallow unit, with an average thickness of 5 to 9 m, can be subdivided into two sub-layers depending on the water saturation of the medium. The top sub-layer, with an average thickness of less than 5 m, is the vadose (unsaturated) zone, mostly dry, and characterized by a brittle behavior; the lower - 4 m-thick - sub-layer is the saturated zone characterized by a visco-plastic behavior (Malet, 2003, Travelletti and Malet, 2012b). A shear surface is identified at the bottom of this unit and is corresponding to the lower limit of the groundwater table (Malet, 2003). The second and deep unit, not observed throughout the whole landslide (with an average thickness of 5 to 10 m), is an impermeable and very compact medium with a brittle behavior (Malet, 2003). Underneath, the bedrock is composed of intact black marls (Malet et al., 2005, Travelletti and Malet, 2012b). From GPS and remote sensing geodetic measures, the average surface displacement rates are in the range of 0.01-0.03 $m.d^{-1}$ but velocities up to 3.5 $m.d^{-1}$ can be reached during acceleration phases in springtime (Malet et al., 2005, Stumpf and Kerle, 2011, Stumpf et al., 2014). The upper part of the landslide is the most active part of the slope in terms of surface deformation (Stumpf et al., 2014, 2015) as well as for seismic activity (Walter et al., 2012b, Tonnellier et al., 2013). Most of the deformation occurs around a stable buried bedrock crest (i.e. a protrusion of the bedrock) along two shallow mudflows (Figure 3.1). Various modes of deformation are identified: a rigid deformation at the surface during the low velocity periods with the development of fissure networks in extension and shearing and at depth along the shear bands; a ductile deformation at the surface during periods of high velocity deformation with the progression of the material as a viscous fluid (e.g. shallow mudflows; Malet et al. (2005), van Asch et al. (2006)).

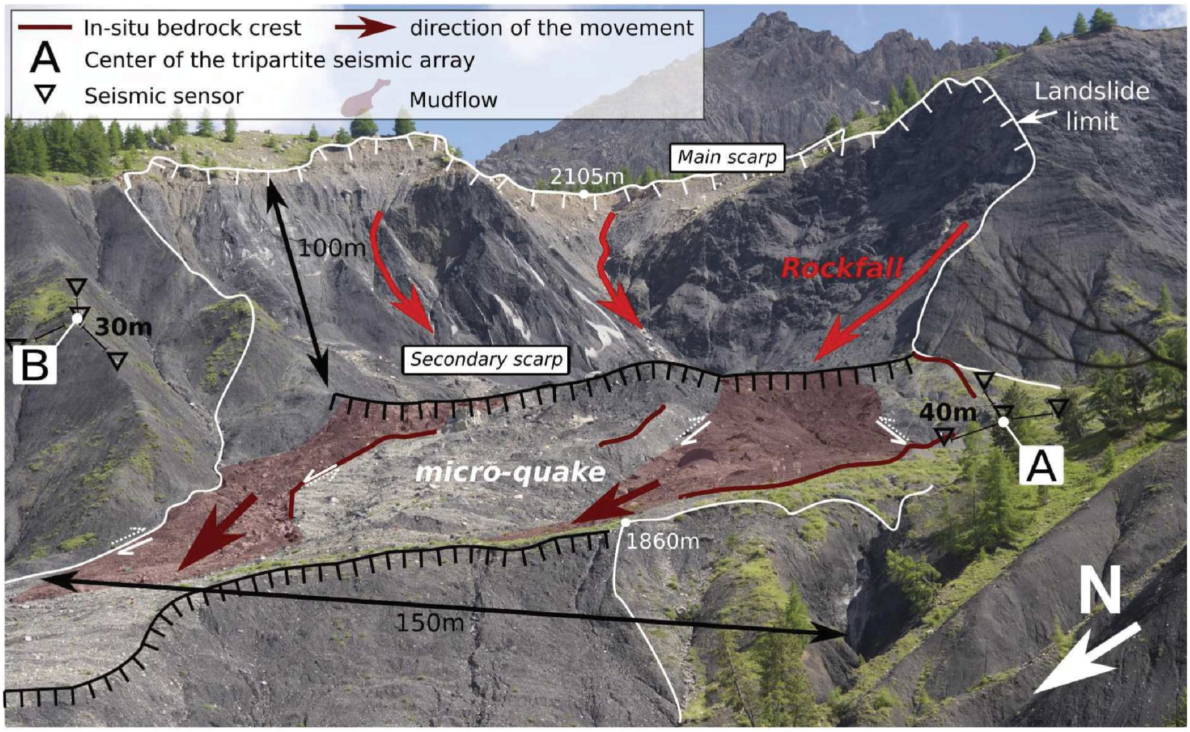

Figure 3.1: Morphology of the Super-Sauze landslide with indications on the dimensions, main geomorphological features and possible location of the endogenous seismic sources.

3.3 Data: geophysical structure of the landslide and seismological observations

3.3.1 Geophysical structure of the landslide: P-wave seismic model

Prior to this investigation, four seismic profiles were measured on the landslide. They showed a complex distribution of the seismic velocity (Grandjean et al., 2006, Tonnellier et al., 2013, Gance et al., 2012). A dense coverage seismic campaign has been conducted in August 2014 in order to estimate the velocity structure at high spatial resolution. During this campaign, the sensors were installed along twelve profiles spaced of ca. 30 m. and located in the upper part of the landslide (8 across-slope profiles and 4 along-slope profiles (Figure 3.2)). Along each profile, 48 vertical geophones were spaced by 5 m, and the sources were shot every two geophones.

The Quasi-Newton inversion approach developed by Gance et al. (2012) is used to estimate the P-wave velocity structure for each profile (Figure 3.3). It takes the first Fresnel zone as an approximation of the Hessian matrix and uses the full source spectrum to reduce the tomography resolution. Gance et al. (2012) show its efficiency to invert complex velocity structures in highly heterogeneous medium. The final model is obtained by inverting only the picks with less than 5 ms of travel-time residuals (Gance et al., 2012). The RMS error ranges from 1.6 to 3.5 ms.

A 3D seismic model is built by a cubic interpolation of the 2D profiles on a regular grid of 5 x 5 x 5 m^3 in order to keep low lateral velocity gradient. The model is then oversampled to cells of 1 x 1 x 1 m^3. Outside of the seismic tomography area, the P-wave velocity is set to 2700 $m.s^{-1}$ in the bedrock and to 600 $m.s^{-1}$ in the landslide body (Figure 3.4). P-wave travel-time grids are computed with the Fast Marching Method (Podvin and Lecomte, 1991) implemented in the software NonLinLoc (Anthony et al., 2000). The Fast Marching Method (FMM) is a 3D solver of the eikonal equation providing a

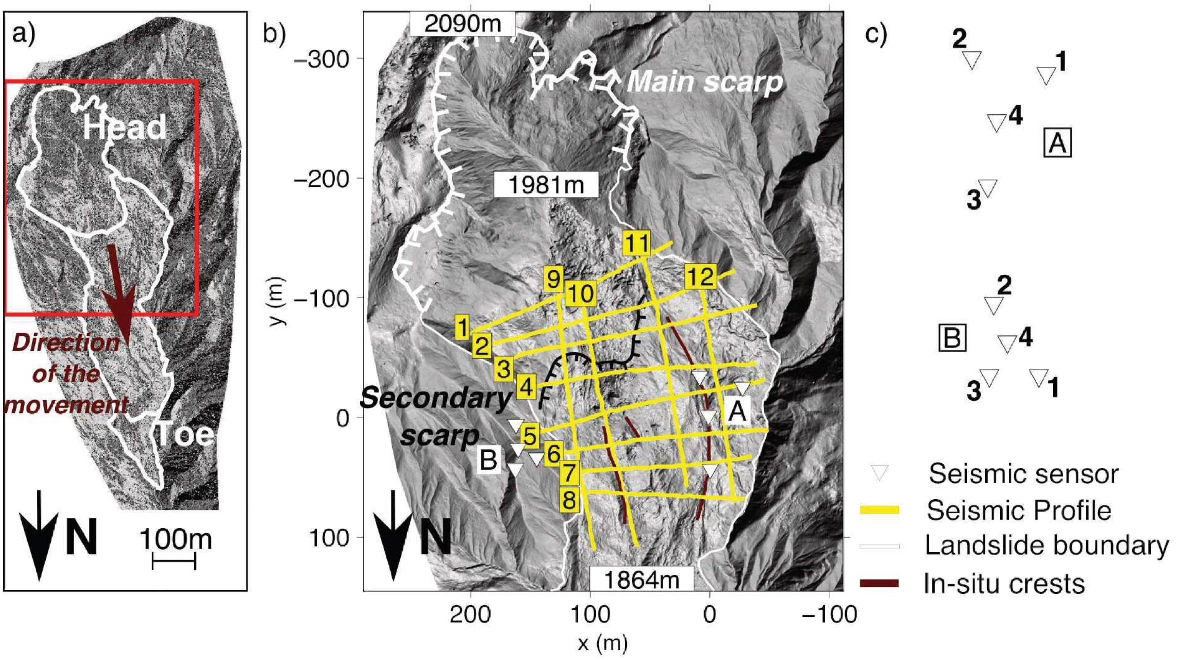

Figure 3.2: Location of the permanent seismic network (e.g. seismic arrays A and B), and of the seismic tomography profiles: (a): Investigated area within the landslide, (b): Location of the sensors and seismic tomography profiles, (c): Number and geometry of the sensors for the two arrays A and B.

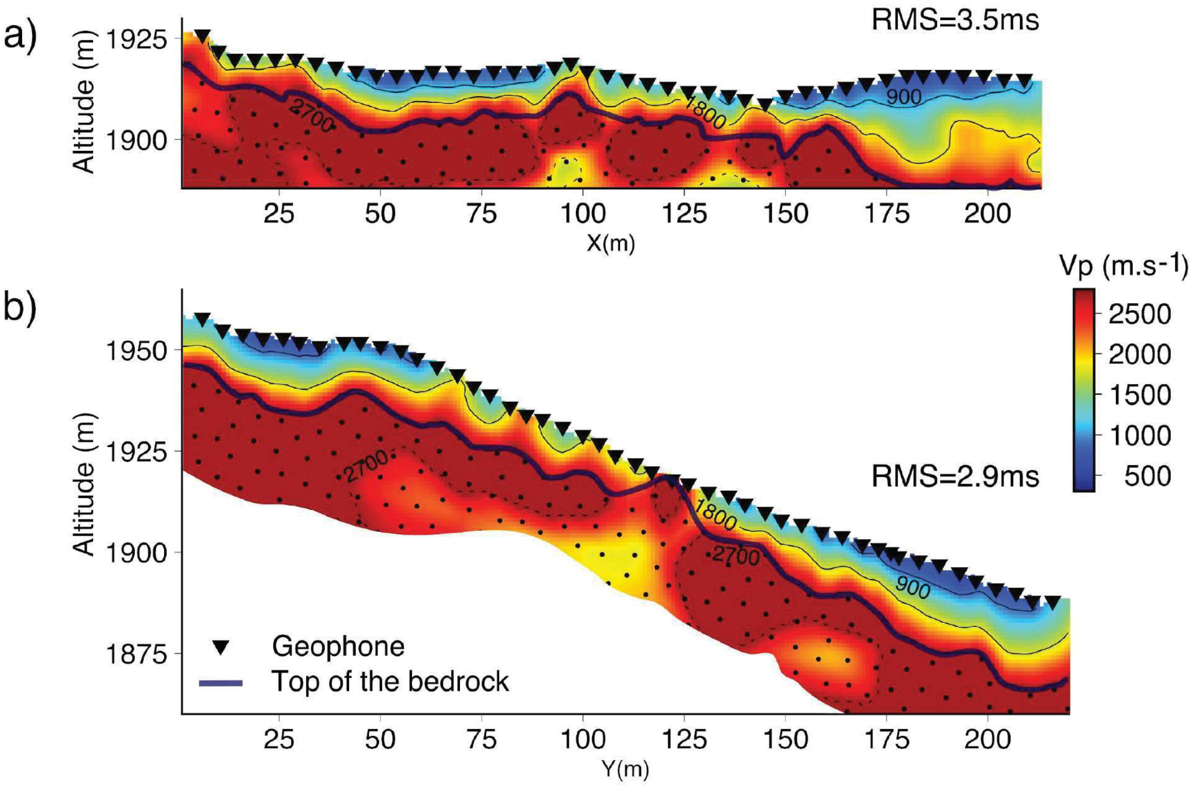

Figure 3.3: Inverted P-wave seismic velocity field for (a) profile 5 and (b) profile 11. In the bedrock (areas with the dots), the velocity is assumed to be homogeneous (v_P=2700 m.s^{-1}).

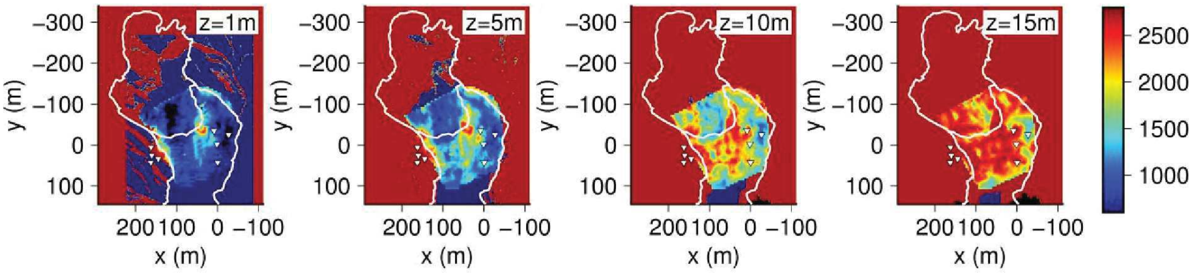

Figure 3.4: P-wave seismic velocity model at 4 depths (Z = -1 m, Z = -5 m, Z = -10 m, Z = -15 m). The reference Z = 0 m is the topographic surface.

solution of the seismic wavefront propagation through a given velocity model. Grids of travel times are computed and further used for the location of the seismic sources.

3.3.2 Micro-seismic monitoring and seismic signal description

Seismological data are provided by OMIV - the French Landslide Observatory (RESIF/OMIV, 2015). The seismicity of the landslide is continuously recorded by a single seismic array since 2009 (i.e seismic array A, Figure 3.1) and by two arrays since 2013 (i.e seismic array B, Figure 3.1). Each array corresponds to an equilateral triangle with three vertical seismometers distant from the central 3-component sensor of 40 m and 30 m for the array A and the array B, respectively. The seismic array A is instrumented with Agecodagis Noemax sensors (natural frequency: 4.5 Hz), the seismic array B is instrumented with Sercel L4C sensors (natural frequency: 1 Hz). The sampling frequency for all sensors is 250 Hz.

The seismic events can be classified in four main types (Walter et al., 2012b, Tonnellier et al., 2013, Provost et al., 2017): 1) rockfalls, 2) slopequakes, 3) regional earthquakes/teleseisms and 4) anthropogenic/natural noise (i.e. car, engine, rainfall, water discharge in torrent, wind, thunderstorm). Most of the regional earthquakes recorded at the Super-Sauze slope originate from the active Sérennes fault located 10 km far from the landslide (Jenatton et al., 2007). The two first classes are considered as endogenous as they are generated by the slope deformation.

The first type of endogenous signal is generated by rockfalls of various sizes, from decimeter-scale debris to meter-scale large blocks. Their seismic signals present a series of impacts that are easily recognizable in the waveform as well as in the frequency content. The recorded signals last from five to tens of seconds and usually contain dominant frequencies in the 5-50 Hz range (Figure 3.5). Most of these events are recorded by the two seismic arrays. Some P-waves onsets could be recognized if the successive impacts are clear and separated through time (Vilajosana et al., 2008). On the contrary, when the signals of the different impacts are overlapping, surface waves appear to dominate the recorded signals (Levy et al., 2015, Hibert et al., 2014, Bottelin et al., 2014). For some clear and separated impacts, P-waves are observed (Figure 3.5c). However, the interpretation of the wave polarization remains difficult. Indeed, horizontally polarized P-waves are expected for shallow sources in complex topography (Neuberg et al., 2000) as observed at the seismic array B (Figure 3.5c.). The second type of endogenous signals is generated by slopequakes; these sources are assumed to result from stress release by both fracture opening or shearing (Helmstetter and Garambois, 2010, Walter et al., 2013b, Tonnellier et al., 2013, Vouillamoz et al., 2017). The recorded signals last less than 5 s and different waveforms and frequency content may be observed. It must be noted that some events are only recorded by one of the seismic array (Walter et al., 2012b, Tonnellier et al., 2013, Vouillamoz et al., 2017) and that the inter-trace correlation of the whole signal is low due to scattering and dispersion of the seismic waves (Walter et al., 2012b, Tonnellier et al., 2013). P-wave arrivals of most of the slopequakes are identifiable on the seismic signal vertical component (Figure 3.5). The observation dataset

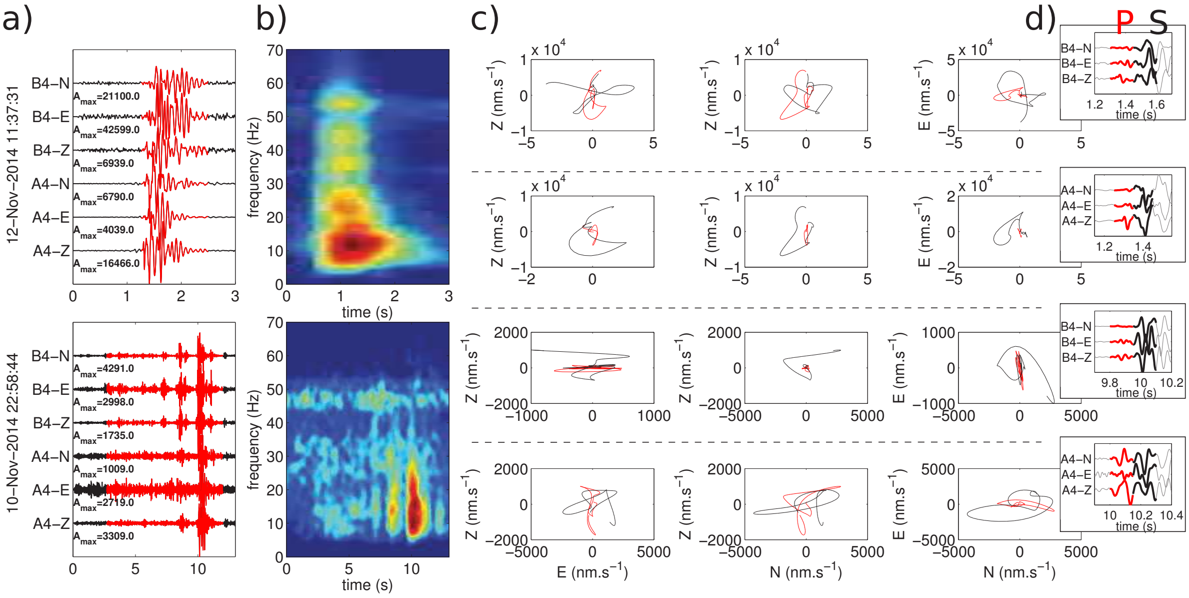

Figure 3.5: Example of endogenous seismic sources recorded at the Super-Sauze landslide: typical slopequakes with high-frequency content (top) and typical rockfall event (bottom). The figure displays (a) the waveform recorded at the three component sensor of each seismic array with the maximal amplitude (A_{max} in nm.s^{-1}), (b) the spectrogram of the signal, (c) the polarization of the P-waves (red) and surface waves (black) and (d) the waveforms of the signal onset with the corresponding P- and surface waves windows.Their polarization is vertical at seismic array A and horizontal at seismic array B for the example displayed in Figure 3.5.

consists of three acquisition periods from 11 October to 19 November 2013, from 10 to 30 November 2014, and from 9 June to 15 August 2015. The investigated data set consists of 418 rockfall events and 239 slopequake events that have been classified manually. The original purpose of this catalog was to train an automatic machine learning classifier (Provost et al., 2017). The duration of this dataset is too short to analyze the dynamics of the landslide but allows us to test the suitability of the proposed location method on natural events.

3.4 Method: *APOLoc, Automatic Picking Optimization and Location*

The picking of the phase onsets is a critical part of the location and is very challenging in the case of landslides because of the proximity of the sources to the sensors and the attenuation of the media. Prior investigation of the problem underlines the importance of the picking error for seismic source location at the Super-Sauze landslide (Appendix A). The proposed location method is based on a robust and automatic processing of the signal to obtain the picking time of the P-wave arrivals taking advantage of the 3D velocity model constructed from the seismic profiles. The strategy consists in 1) a pre-location of the source with the Amplitude Source Location (ASL) approach to reduce the grid search extension, 2) an automatic picking of the signal onset with a Kurtosis-based algorithm to broadly identify the onset of the signal, and 3) an iterative improvement of the picking based on the inter-trace correlation maximization through picking time perturbation. The workflow of the method is presented in Figure 3.6; the successive steps are detailed below.

3.4.1 Initial location with signal amplitude analysis

The grid search area is reduced by determining a rough location of the seismic source using the ASL method. The ASL method is classically used in volcanic environments to determine the location of

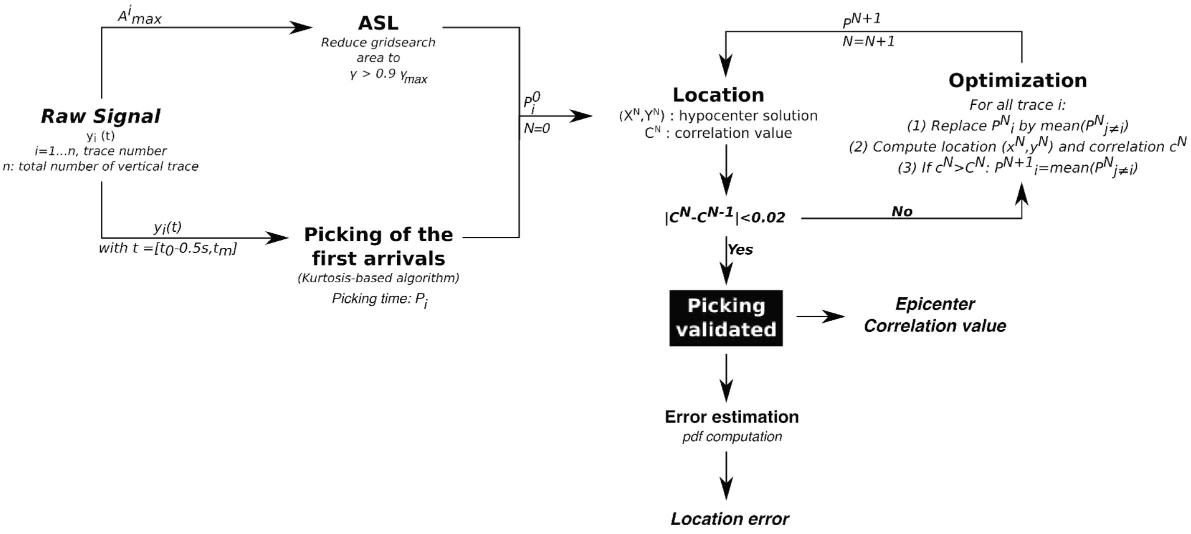

Figure 3.6: Flowchart of the proposed methodology.

seismic swarms during eruptions (Battaglia and Aki, 2003, Taisne et al., 2011) and has been more recently implemented for the location of debris-flows (Walter et al., 2017a). The surface waves are used because they are more energetic than the P-waves and are likely recorded by most of the sensors. The amplitude of the seismic signals is modeled by a simple attenuation law (Battaglia and Aki, 2003):

$$A(r) = A_0 \frac{e^{-\alpha r}}{r^n} \tag{3.1}$$

where A_0, α, r are the amplitude of the seismic waves at the source, the attenuation coefficient depending of the media properties and the source-sensor distance, respectively. The exponent n is equal to 0.5 for surface waves and equal to 1 for body waves (Taisne et al., 2011). The amplitude ratios are computed for each sensor pairs (i, j) and compared to the observed amplitude ratios. A misfit function (Taisne et al., 2011) is used:

$$\gamma = 1 - \sqrt{\sum_i \sum_{j>i} \left(\frac{A_i^{mod}}{A_j^{mod}} - \frac{A_i^{obs}}{A_j^{obs}}\right)^2} \tag{3.2}$$

The grid search area is reduced to the points satisfying the condition : $\gamma > 0.9\gamma_{max}$.

3.4.2 Initial picking of the signal onset

The picks of the first arrivals (P_K) are identified using the Kurtosis method (Baillard et al., 2014, Hibert et al., 2014) which is the most suitable method for picking emergent arrivals of micro-seismic sources. As demonstrated for rockfalls at the Piton de la Fournaise volcano (Hibert et al., 2014), differences between manual and automatic picks are in the range of 0.05 s to 0.30s for SNR > 10 and SNR < 5, respectively.

3.4.3 Location procedure

The location is determined by maximizing the inter-trace correlation of the P-wave arrivals. The initial picking times determined by the Kurtosis function (P_{Kurt}) define the center of the time window used for the computation of the inter-trace correlation. We work with a time window of ± 0.16 s around the Kurtosis picked times (P_{Kurt}). To determine the epicenter location, the inter-trace correlation is computed on this time window for each cell of the grid search area (cf. section 5.1.1). The inter-trace correlation values are calculated in the cell (X, Y):

$$C(X,Y) = \frac{1}{N^2}\sum_{i,j} c_{ij} c_{ij}^{max} \tag{3.3}$$

c_{ij}^{max} is the maximum correlation of the traces i and j:

$$c_{ij}^{max} = \max_{\tau}\left(\frac{1}{\sigma_x\sigma_y}\int_{t_0-\delta_t/2}^{t_0+\delta_t/2} y_i(t)\, y_j(t-\tau)\,\mathrm{d}t\right) \tag{3.4}$$

The epicenter location is given by the point where the sum of the inter-trace correlations is maximized. The inter-trace correlation value differs from the one proposed by (Lacroix and Helmstetter, 2011) since the weight values are not set as a function of the sensor to sensor distances but as a function of the maximum cross-correlation of the traces for the selected window. The weight of the traces for which the signals correlate are hence increased. A first location (X_0,Y_0) and a new piking time $P_0 = P_{Kurt} + \tau_{c_{max}}$ is determined at the end of this step.

3.4.4 Iterative improvement of the picking time

The initial picking time (P_{Kurt}) can be incorrect for two reasons: 1) the Kurtosis-based algorithm may detect the first onset but may not pick the same part of the onset phase, and/or 2) the Kurtosis-based algorithm may significantly fail to detect the signal onset.

In order to pick the same part of the signal onset and reduce outliers, the center of the time window (P^N) for each trace is iteratively improved. The picking time center of the trace i is successively replaced by the mean of the other picked times center ($j \neq i$). The previous location procedure is computed on the new window. If the inter-trace correlation increases by changing the picking time of trace i, the picking time is replaced by the mean picked time of the other traces.

$$P_i^{N+1} = mean_{j\neq i}(P_j^N), \text{ if } c^N > C^N \tag{3.5}$$

with c^N, the maximum inter-trace correlation value for the tested change of piking time reference and C^N, the maximum inter-trace correlation value obtained at the previous step N. This is repeated until the $|C_N - C_{N-1}|$ becomes lower than 0.02 with N the number of iterations. At the end of this step, the epicenter location (X,Y) and the final picking times P^{fin} are determined by maximizing the inter-correlation on the last optimized time window (i.e. centered on P^N).

3.4.5 Error estimation

The location error is computed by estimating the Posterior Density Function (PDF) of the final picked arrival times. The errors on the location are computed with (Tarantola and Valette, 1982):

$$PDF(X,Y) = \sum_{m=1}^{M} \exp\left(-\frac{1}{2\sigma_m^2}(\Delta t_m^{obs} - \Delta t_m^{mod})^2\right) \tag{3.6}$$

where M is the number of sensor pairs, $\Delta t_m = P_N^i - t_N^j$ is the final picking time difference between the sensors i and j, and σ_m is the uncertainty of the picking. The choice of σ_m is discussed in the next part. The prior probability is taken uniform and we do not estimate velocity model uncertainties.

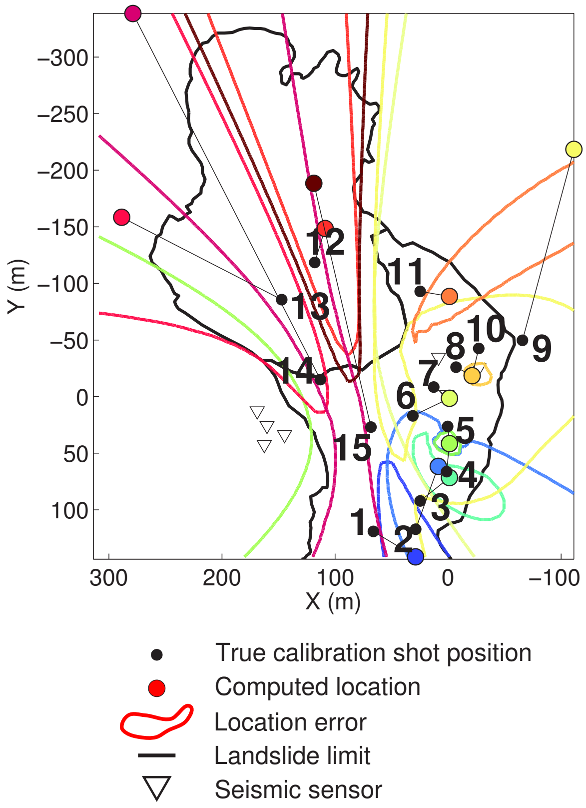

Figure 3.7: Location of the calibration shots with the ASL method and an attenuation coefficient $\alpha = 0.008\ \mathrm{m}^{-1}$.

3.5 Results

3.5.1 Validation of *APOLoc*

The methodology is tested for the location of 15 air-gun calibration shots. The timing of the shots was recorded with an accuracy of 1 s and their locations were measured with a GPS survey with an accuracy of 5 cm. The locations of the shots cover the study area (Figure 3.7). The data are filtered in the range of [5-100] Hz and the Kurtosis-based algorithm is computed on a time window ranging from [t_0-0.5 s - t_m], t_0 and t_m corresponding to the beginning of the signal defined by the spectrogram analysis and to the time of the maximum energy of the spectrogram, respectively. The amplitude analysis is carried out with the maximum amplitudes and the exponent is fixed equal to 0.5 assuming that the surface waves are the most energetic ones. The attenuation coefficient α used in the ASL pre-location method is assumed uniform. It is determined by analysis of the results for different values of α ranging from 0 to 0.05 m^{-1} with an increment of 0.001 m^{-1}. We found that a value between 0.007 and 0.011 provided similar and reliable estimation of the location of the calibration shots. We choose to work with $\alpha = 0.008\ \mathrm{m}^{-1}$. The location of the calibration shots with the ASL method and the grid search areas for each shot are displayed Figure 3.7. Most of the pre-location areas include the true shot location or are very close (<10 m) except for shot 17.

The locations of the calibration shots obtained with *APOLoc* are plotted in Figure 3.8a. The computed source locations are consistent with the real locations of the calibration shots: the mean epicenter error is 27±29 m. Shots located within the seismic network are the most accurately located with a mean epicenter error of 7±4 m. Outside the seismic network, the location errors are larger with a mean epicenter error of 37±31 m. Except for the shots 15 and 7, the first arrivals of the shots are recorded by only one of the seismic arrays with a high SNR. Despite the relatively small number of sensors used for the location (< 5), the epicenter errors are very small (<10 m) in the western part of the landslide (shots 2 to 11) while they are larger ([20-50] m) for shots located in the eastern part of the landslide (shots 1 and 12 to 14). The amplitude of the shot sources follows the attenuation law (Figure 3.9) with R^2 value of 0.9741. The attenuation coefficient is lower ($\alpha = 0.002 \pm 0.03\ m^{-1}$) than the one used in pre-location step ($\alpha = 0.008\ m^{-1}$). However, the attenuation coefficient is not well constrained since the lower and upper bound values are significant (-0.033; +0.038).

The location results for the *APOLoc* method and for the manual picking are shown in Figure 3.8b,c and examples of the corresponding picked times are plotted in Figure 3.10. A Root-Mean-Square method is used to locate the shots from manual picked times; the epicenter of the source is the point that minimizes:

$$\mathrm{RMS} = \sqrt{\sum_{n=1}^{N} \frac{1}{N} (\delta t_n^{obs} - \delta t_n^{mod})^2} \tag{3.7}$$

with N the number of pairs of sensors, δt^{obs} and δt^{mod} the travel time difference between the two sensors computed for manually picked and modeled arrival times respectively. The shots in the center of the seismic array are all located precisely with the three approaches. Outside the network, *APOLoc* provides better or equivalent results than the manual picking and the initial picking (i.e. *APOLoc* without optimization of the picking) except for shot 12. The correlation values increase with the iterative optimization (mean correlation value of C=0.22 and C=0.29, without and with optimization, respectively) indicating a more robust estimate of the quality of the arrival times. The optimization step demonstrates its efficiency to correct the initial picks (Figure 3.10) and consequently, improves some source locations (Figure 3.8a,b).

The larger errors are observed for the shots outside the seismic array. The question is to determine whether this is due to picking errors or to velocity model errors. For shots 1, 3, 12, 13 and 14, the difference between the final picking error and the model is larger than 0.01 s suggesting a velocity model error on these ray paths. A way to correct the velocity model inaccuracy is to add station correction (Spillmann et al., 2007, Lacroix and Helmstetter, 2011). This option was not tested here as the station correction is correlated to the azimuth and the distance of the shots preventing the estimate of a robust correction.

3.5.2 Influence of the velocity model

We tested the influence of the seismic velocity model. The shots are located with 1) a homogeneous velocity model ($v_p = 2500\ m.s^{-1}$), 2) a 2-layers velocity model, 3) a gradient model, and 4) a 3D velocity model. For each of these models, travel time tables are computed with the FMM algorithm. The results are plotted in Figure 3.11. Among all the velocity models tested, the 3D velocity model significantly decreases the mean epicenter error (Table 3.1).

The 3D velocity model constructed from the seismic tomography is thus considered as an accurate approximation of the velocity heterogeneity of the underground surface. We further carried out simulations to estimate the sensitivity of the location for the velocity models (Appendix A). The synthetic simulations show that the four seismic models are very similar to each other in terms of location of the synthetic sources; for real observations, they differ significantly when they are used as inputs to improve the picking of the P-wave. This last point demonstrates the difficulty to estimate the location error due to the velocity model uncertainties.

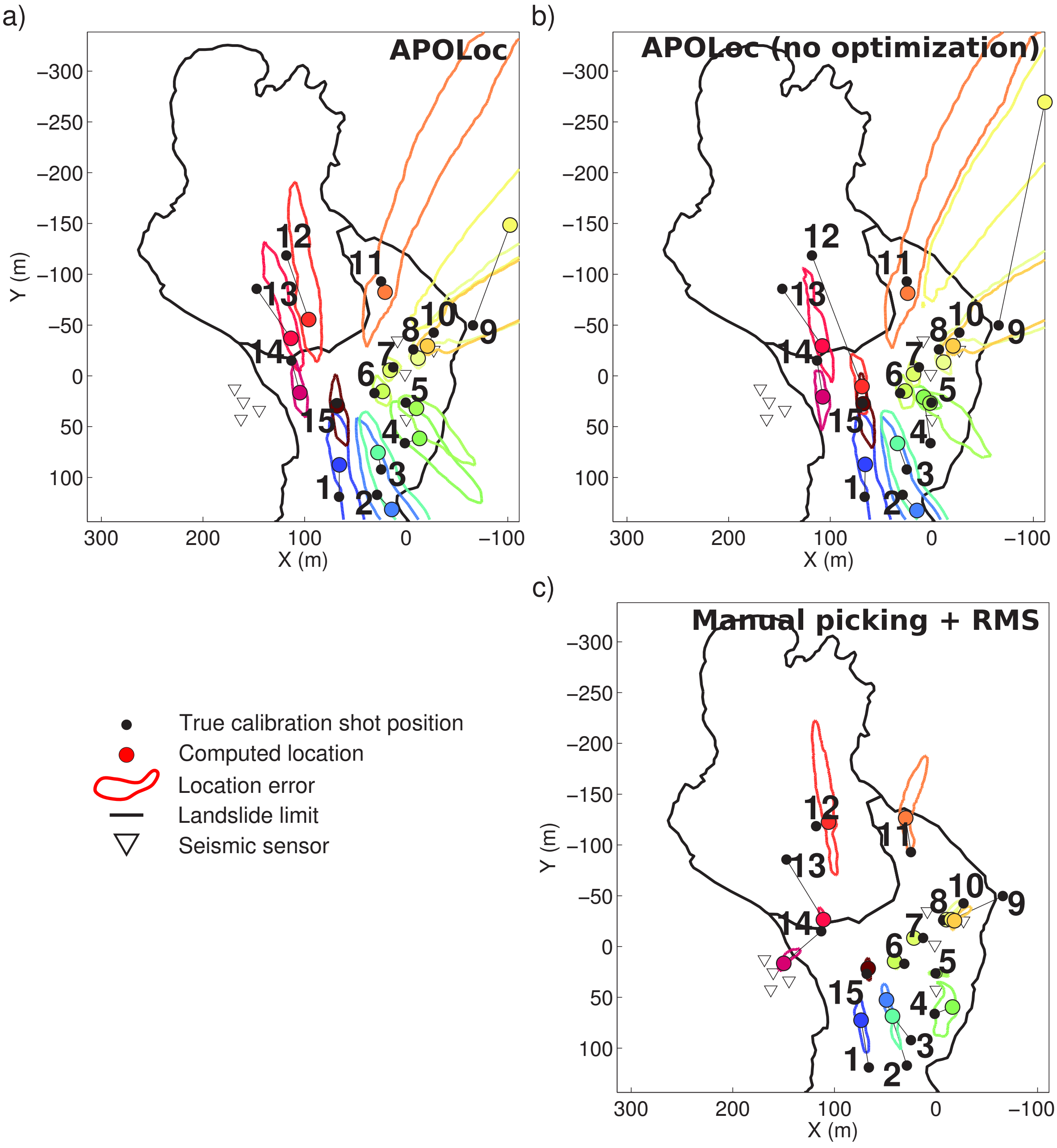

Figure 3.8: Location of the calibration shots with (a) the *APOLoc* method, (b) the *APOLoc* method without the optimization step and (c) the RMS location method with manually picked arrival times. For all the locations, the 3D velocity model is used.

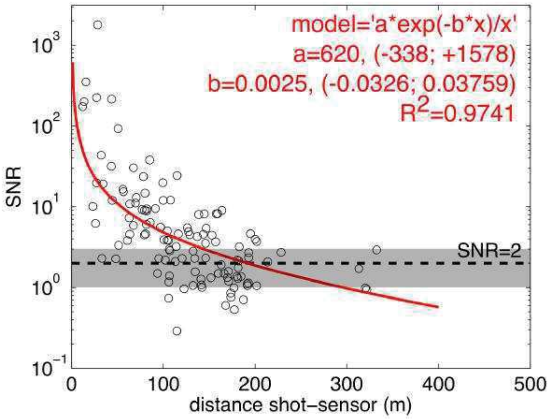

Figure 3.9: Signal-to-Noise Ratio (SNR) of the P-wave onset as a function of the source-sensor distance for the calibration shots. The red curves represent the regression function best fitting the data. The equation of the model , the inverted coefficient with their upper and lower values and the regression coefficient are indicated in the upper right corner with “x” the source -sensor distance.

Table 3.1: Summary of the epicenter errors obtained for the different tests using three location methods: ASL, NonLinLoc, Beam-Forming and *APOLoc*. The latter is tested with and without the optimization of the picking and for several velocity models.

Method	ASL	NonLinLoc	BF	Proposed methodology:Inter-trace correlation of P-wave				
Picking	/	Manual	/	Kurtosis	Kurtosis+picking optimization			
Model	/	3D	V_{app}	3D	V_P=2500m.s^{-1}	2L	Gradient	3D
mean	94	65	48	43	74	47	44	**27**
std	112	65	36	61	61	67	37	**29**
min	15	2	6	**1**	5	6	2	3
max	395	202	147	224	207	279	141	**105**

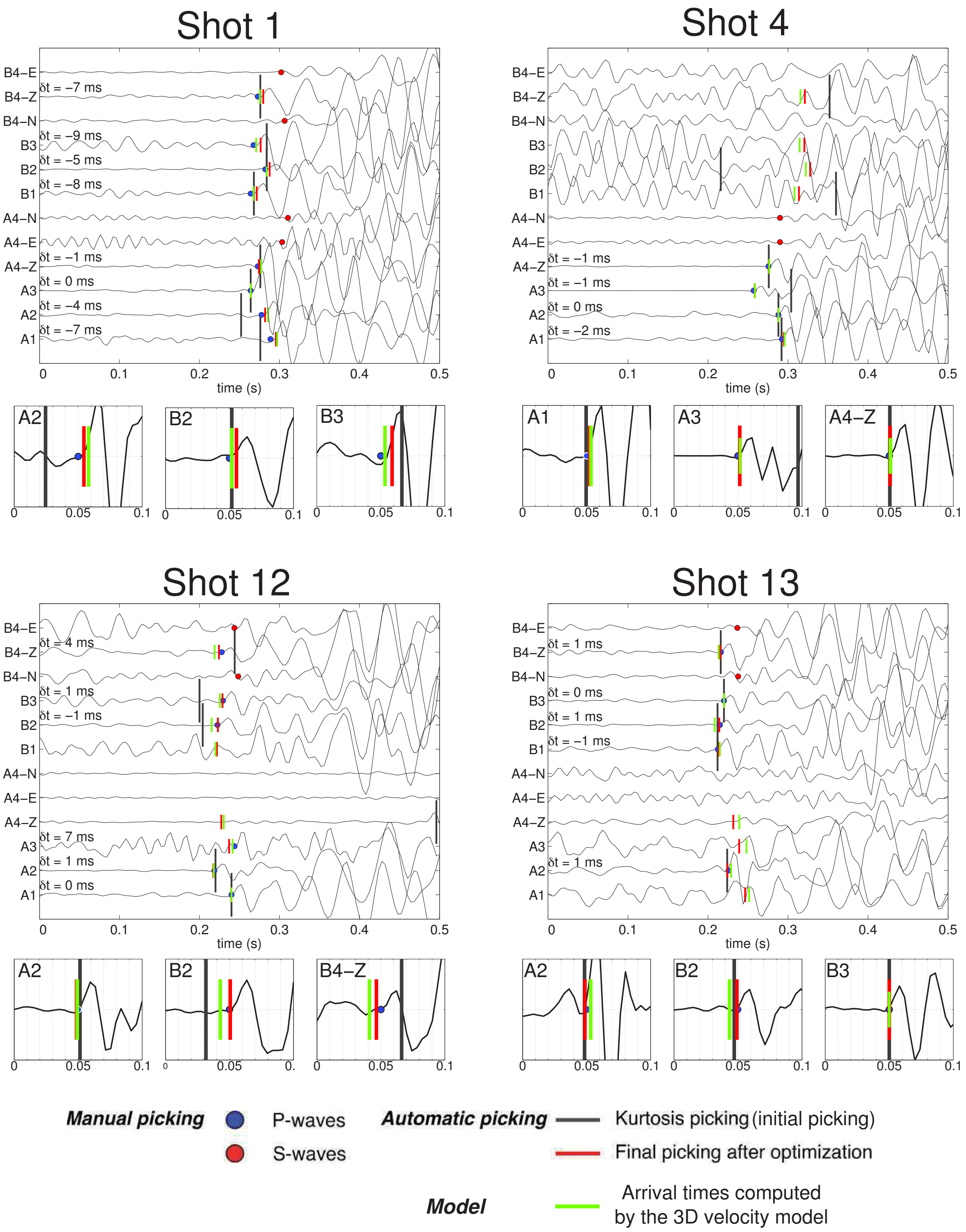

Figure 3.10: Comparison of the P-wave pick (i.e. manual, Kurtosis and the final picking obtained after the optimization) for shots 1, 4, 12 and 13. The S-wave time arrivals are plotted on the horizontal traces. The arrival times computed with the 3D velocity model are also presented.

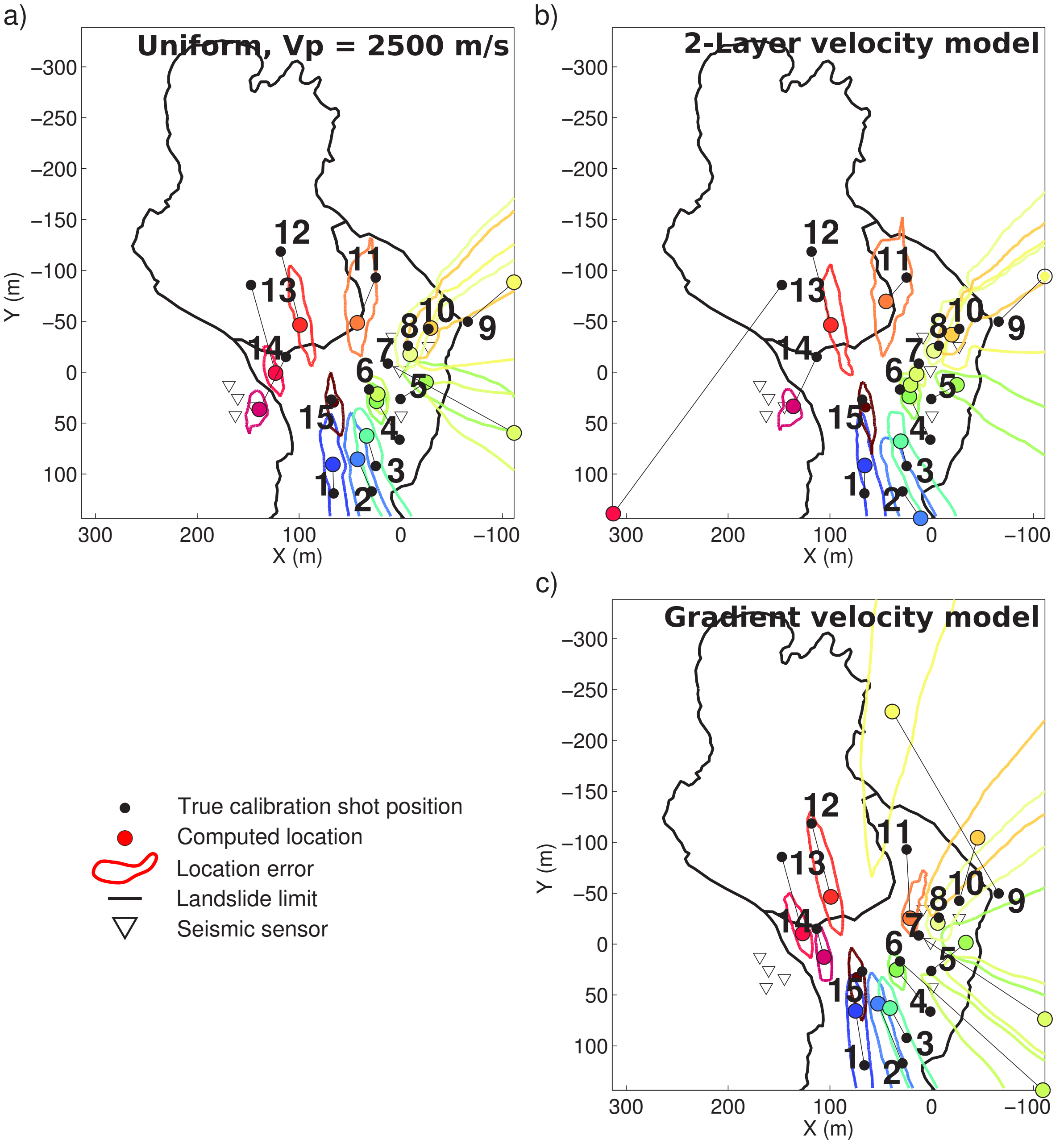

Figure 3.11: Location of the calibration shots with the *APOLoc* method using (a) a uniform velocity model taking into account the topography with v_p = 2500 m.s^{-1}, (b) a two-layers velocity model composed of a superficial layer (above the bedrock limit) with a uniform velocity of v_p = 800 m.s^{-1} and a deeper layer (bedrock) with a uniform velocity of v_p = 2500 m.s^{-1} and (c) a gradient velocity model where the velocity in the superficial layer varies linearly from v_p = 800 m.s^{-1} at the surface to v_p = 2500 m.s^{-1} in the bedrock.

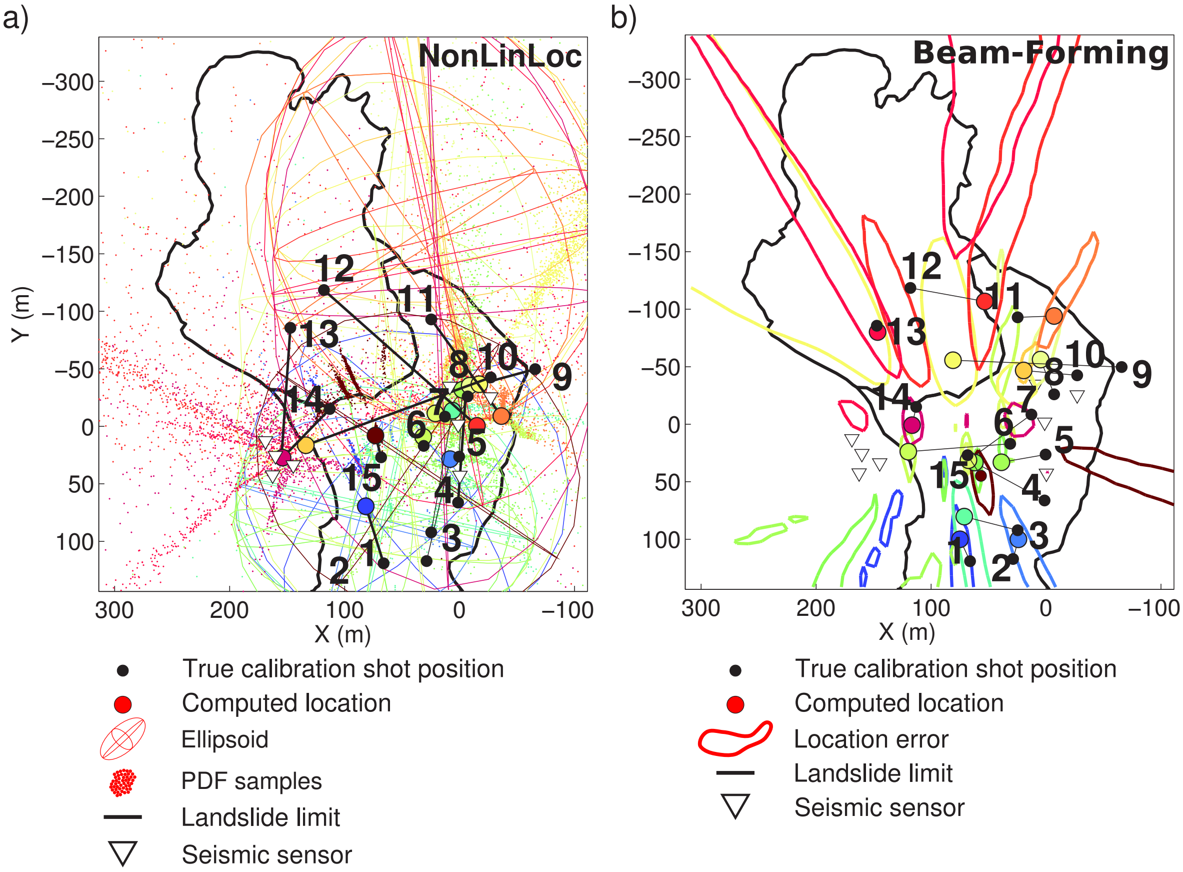

Figure 3.12: Location of the calibration shots with*APOLoc* using (a) the L2-RMS likelihood function implemented in NonLinLoc and (b) the Beam-Forming approach. The location errors are represented by PDF samples and the 68% confidence ellipsoids for locations (a) and by the contour delimiting the area where the correlation function is larger that 95% of the maximal correlation (i.e. $C > 0.95C_{max}$ for locations (b).

3.5.3 Comparison to other location approaches

Two other approaches are tested to locate the calibration shots: 1) the NonLinLoc approach (Anthony et al., 2000) with a manual picking and 2) the full waveform Beam-Forming approach with an inversion of the velocity (Lacroix and Helmstetter, 2011). Probabilistic estimation of the location from the manual picking of the P-waves provides large epicenter errors (mean epicenter error : 65 m; Table 3.1, Figure 3.12a). Most the epicenter locations are shifted towards the seismic array A. The location errors are large and fail at delimiting the areas where the shots were triggered. It shows that the location of seismic sources in the landslide is highly uncertain and that considering uniform prior information leads to unconstrained locations. In the contrary, the pre-location step in *APOLoc* has a prior information on the source location thus improving the determination of the source locations.

The waveform Beam-forming approach provides larger epicenter errors than *APOLoc* (mean epicenter error 48 m; Table 3.1, Figure 3.12b). Shots located inside the seismic network (except shot 15) are shifted towards the seismic array B while those located outside the seismic network in the eastern part of the landslide are more accurately located than with *APOLoc* (shots 1, 12, 13 and 14) with a mean epicenter error of 27 m (48 m with *APOLoc*). It is likely due to the fact that surface waves are more energetic and hence recorded by the two seismic arrays.

3.6 Discussion

3.6.1 Relevance of *APOLoc* for landslide endogenous sources

The *APOLoc* method is used to locate the 239 slopequake and 418 rockfall events observed at Super-Sauze landslide. The slopequakes are located with the same criteria as for the calibration shots; the rockfalls are located using a different strategy as several impacts of blocks are observed and the first one is rarely the most energetic. To determine the time window, the maximum energy of the spectrogram is detected. The part of the signal used for the picking optimization is in the window t_m-1s to t_m (with being t_m the time of the spectrogram maximum). The results are presented in Figure 3.13 and Figure 3.14. The mean correlation values for the location of, respectively, the slopequakes and the rockfalls, are respectively, 0.23±0.12 and 0.19±0.1; these values are slightly smaller than the correlation values obtained for the calibration shots.

Most of the slopequakes are located inside the seismic network (Figure 3.13). Some clusters are located in the vicinity of sensors A1 and A3 (< 10m). Few sources are located in the upper part of the landslide. The shapes of the location error are elongated, as for the calibration shots, in the North-South direction for the sources located inside the seismic network. The two clusters of seismicity located around sensors A1 and A3 present location errors elongated along the East-West direction. The location of these signals is in accordance with the geomorphological observations. We probably record only the sources occurring in the vicinity of the sensors or inside the seismic network where *APOLoc* demonstrated the most accurate location. If we analyzed the SNR distribution versus the distance to the source for each sensors, slopequake locations respect the attenuation law with coefficient of regression of 0.98 (Figure 3.15a). This tends to confirm the reliability of the location for this kind of sources although we cannot confirm these locations.

The rockfalls are mostly located at the main scarp (Figure 3.14). The shapes of the location errors are elongated along the North-South direction and cover the whole area of the main scarp due to the geometry of the network and the distance of the source to the seismic network. The SNR distribution poorly respects the attenuation law (regression coefficient of 0.84; Figure 3.15b). However, this might be due to the heterogeneity of the attenuation coefficient in the landslide but also due to source mislocation. Indeed, numerous sources are located at the boundary of the grid search area. This may be explained by the use of a P-wave velocity model while rockfalls signals may be dominated by surface waves (Helmstetter and Garambois, 2010, Lacroix and Helmstetter, 2011, Hibert et al., 2014) especially when they occur at large distances from the sensors. A 3D velocity model for surface wave propagation would probably be more adequate for the location of this kind of signals. A cluster of seismicity is also located in the vicinity of the seismic array B. This cluster may be explained either by mislocation of the sources or by the fact that numerous small rockfalls may occur at close distance (<10 m) of these sensors whereas only rockfall emitting large energy are recorded at large distances (>10 m). Some locations are coherent with the geomorphological observations. In particular, on the main scarp where all location are correlated to the rockfall paths (Figure 3.14). The secondary scarp at the East appears to be also active (Figure 3.14), which is in agreement with previous observations (Stumpf and Kerle, 2011, Stumpf et al., 2014). A better discrimination between rockfalls dominated by emergent surface waves and rockfalls with impulsive onsets may also improve the determination of the rockfall location and enable to select adequate velocity model (P-waves or surface waves) to locate each type of signal. The current catalog does not take into account this difference. Moreover, the polarization of the P-waves is expected to be complex and seems to be different for different location of the seismic sensors (Figure 3.5). This would imply that the use of vertical sensors is not always adapted to pick the P-waves arrivals for rockfalls. We did not investigate the polarization of all the sources present in the catalog. The development of robust and possibly automatic methods to estimate the nature of the first onset is needed to choose adequately the velocity model.

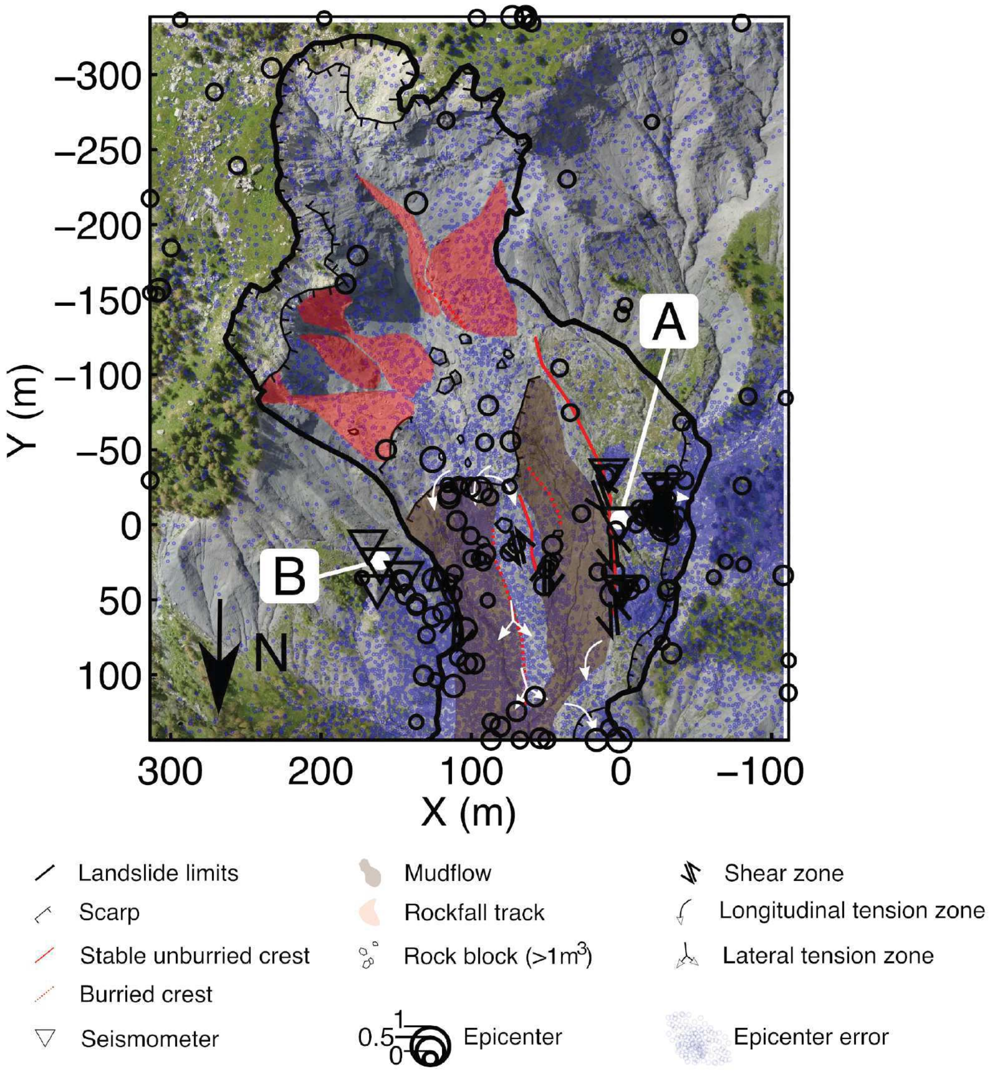

Figure 3.13: Location of the slopequakes and spatial correlation with the geomorphological structures. The size of the circles represents the final value of the inter-trace correlation. The map of the tension zones are reproduced after Stumpf et al. (2013)

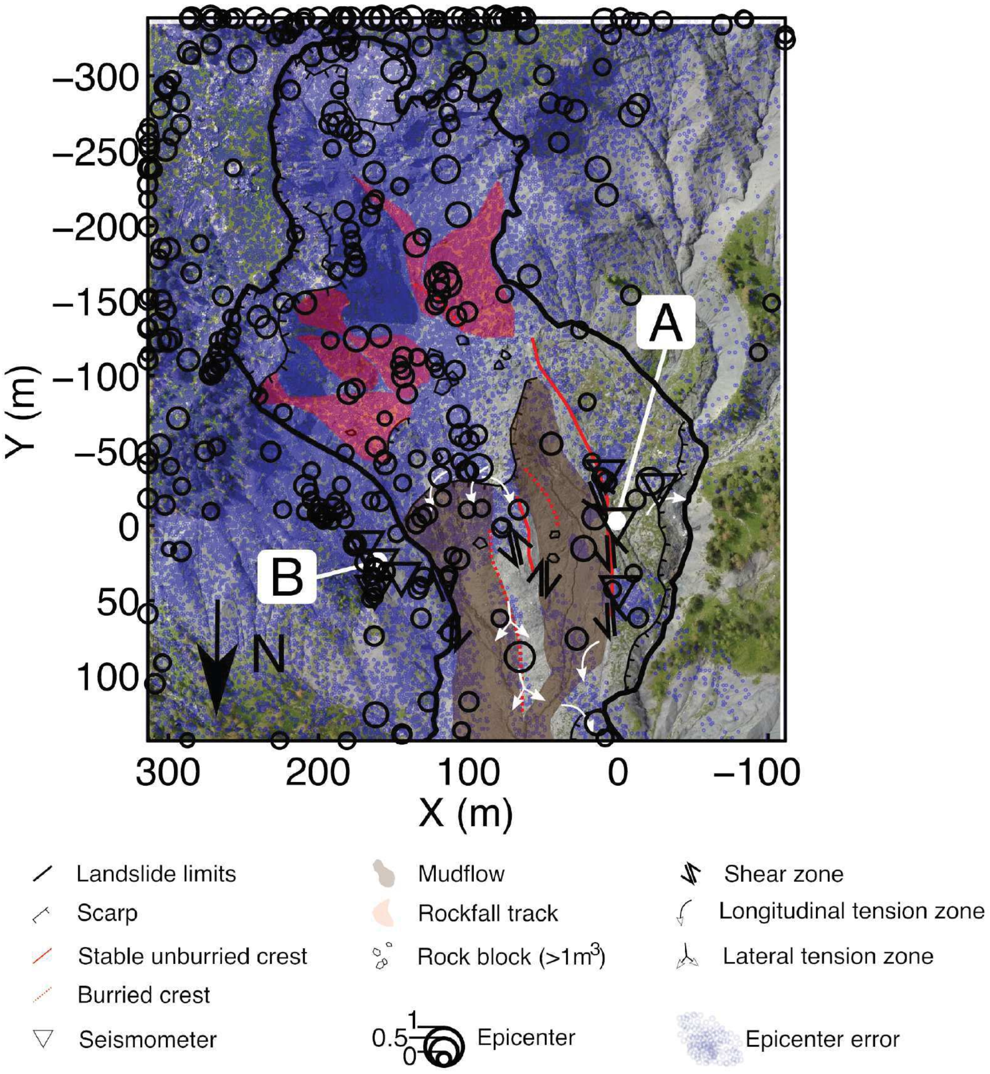

Figure 3.14: Location of the rockfalls and spatial correlation with the geomorphological structures. The size of the circles represents the final value of the inter-trace correlation. The map of the tension zones are reproduced from Stumpf et al. (2013)

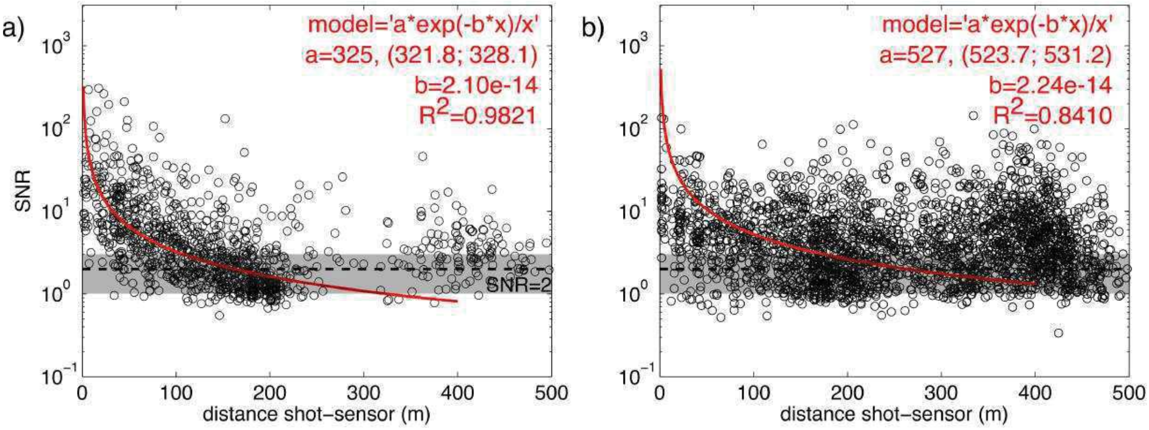

Figure 3.15: Signal-to-Noise Ratio (SNR) of the P-wave onset as a function of the source-sensor distance for (a) the slopequakes and (b) the rockfalls. The red curves represent the regression function best fitting the data. The equation of the model (f), the inverted coefficient with their upper and lower values and the regression coefficient are indicated in the upper right corner of the plot with “x” the source to sensor distance.

3.6.2 Estimation of the depth of the sources

The depths of the sources are currently not computed. In the synthetic tests, reasonable vertical errors (3±3 m) are obtained when no picking error are added to the simulated travel-times for the velocity model (Appendix A). This case is highly unrealistic. The synthetic tests indicate that the uncertainty on the depth is large and very sensitive to the velocity models and picking errors taking into account the small thickness of the landslide (e.g. mean depth to the bedrock interface of 20 m). The installation of buried sensors would improve the determination of the depth of the sources but their maintenance would be very difficult taking into account the high surface displacement rates (Malet et al., 2005). Further, the geometry of the seismic network is imposed by topographic and geomorphological constraints (e.g. elongated shape of the landslide, absence of stable parts within the landslide body, presence of lateral streams). One of the seismic arrays presents a wide aperture angle that reduces the precision of the azimuth inversion of the source. Installation of additional sensors in the North-South direction would improve the determination of the source epicenters and reduce the shape of the location error in that direction. One option is to install sensors at the top of the main scarp. This would improve the location of the rockfall events but would have only small impacts on the location of the slopequakes.

3.6.3 Estimation of the attenuation coefficient

We assumed a uniform coefficient of $\alpha = 0.008$ m^{-1}. The inversion of the attenuation law found that a smaller coefficient of 0.002 m^{-1} fits the data for the calibration shots and even, that anelastic attenuation could be neglected for the slopequake locations. The uncertainties on the attenuation coefficients inverted from the calibration shots (Figure 3.9) are also large : -0.033; +0.038 meaning that considering a uniform attenuation coefficient may be a too strong assumption. We thus inverted the attenuation coefficient for each shot (Table 3.2) and found very heterogeneous values ranging from 0.003 m^{-1} and 0.054 m^{-1} if we consider only the inversions with $R^2 > 0.9$. The values are significantly larger than our initial assumption with a mean attenuation coefficient of 0.026 m^{-1}.

The coefficient of regression varies also significantly. Very low coefficients of regression (< 0.9) are obtained for shots 1, 6, 9, 12, 13, 14 and 15. The attenuation coefficients of the shots on the eastern part of the landslide are less well resolved than for the shots of the western part. We investigated the

Table 3.2: Inversion of the attenuation coefficient for each shots with the attenuation law: $A(x) = A_0 \frac{e^{-\alpha x}}{\sqrt{x}}$. The minimum and maximum of the sensor to shot distances are indicated (d_{min} and d_{max} respectively).

Shot	A_0 ($nm.s^{-1}$)	δA_0 ($nm.s^{-1}$)	α (m^{-1})	$\delta\alpha$ (m^{-1})	R^2	d_{min} (m)	d_{max} (m)
1	$2.9\ 10^4$	$[-2.1\ 10^4; 8.0\ 10^5]$	0.010	[-0.004; 0.024]	0.44	100	166
2	$9.4\ 10^6$	$[4.1\ 10^4; 1.4\ 10^5]$	0.020	[0.014; 0.026]	0.96	80	180
3	$2.7\ 10^4$	$[1.3\ 10^4; 4.1\ 10^4]$	0.014	[0.007; 0.020]	0.91	55	170
4	$1.6\ 10^5$	$[1.4\ 10^5; 1.8\ 10^5]$	0.038	[0.034; 0.042]	0.99	25	182
5	$3.3\ 10^4$	$[2.4\ 10^4; 4.2\ 10^4]$	0.021	[0.009; 0.032]	0.99	15	175
6	$2.7\ 10^6$	$[-9.4\ 10^6; 1.5\ 10^7]$	0.129	[-0.009; 0.268]	0.84	30	144
7	$1.1\ 10^6$	$[1.1\ 10^6; 1.2\ 10^6]$	0.054	[0.050; 0.057]	0.99	15	164
8	$9.3\ 10^4$	$[-6.0\ 10^3; 1.9\ 10^5]$	0.042	[-0.009; 0.093]	0.94	19	186
9	$4.6\ 10^3$	$[1.7\ 10^3; 7.5\ 10^3]$	0.003	[-0.003; 0.008]	0.62	50	249
10	$3.0\ 10^5$	$[2.2\ 10^5; 3.9\ 10^5]$	0.030	[0.020; 0.040]	0.99	23	211
11	$1.0\ 10^4$	$[6.1\ 10^3; 1.5\ 10^4]$	0.008	[0.004; 0.013]	0.92	61	196
12	$1.8\ 10^4$	$[-2.9\ 10^4; 6.6\ 10^4]$	0.005	[-0.010; 0.022]	0.06	137	197
13	$5.6\ 10^4$	$[-9.5\ 10^4; 2.1\ 10^5]$	0.017	[-0.006; 0.039]	0.50	102	192
14	$8.6\ 10^3$	$[-2.4\ 10^3; 1.9\ 10^4]$	0.005	[-0.010; 0.020]	0.23	61	138
15	$1.5\ 10^4$	$[1.0\ 10^4; 2.0\ 10^5]$	$2.0\ 10^{-14}$	-	-0.35	67	108

possible site effects by analyzing the ratio of the seismic amplitudes for 30 earthquakes coda Aki and Chouet (1975). The amplification values range from 0.8 to 1.5. We obtained similar results by correcting the site effects. A possible explanation is thus that these shots are very distant from the two seismic arrays (minimal source to sensor distance d_{min} >60 m) and are located at approximately the same distance to both sensors (d_{max}-d_{min} <100 m). The recorded amplitudes are in the same order and the attenuation coefficient cannot be constrained. We hence cannot confirm that the attenuation is larger in the eastern part of the landslide. Although our initial assumption provides proper estimation of the pre-location areas of the source, a possible improvement of the method would be to invert the attenuation coefficient in order to take into account the spatial heterogeneity (and possibly temporal variation) of this coefficient. Increasing the density of the network of sensors is also needed to improve the reliability of the attenuation coefficient inversion and to decrease the picking errors and uncertainties in particular for the distant sources.

3.7 Conclusion

The *APOLoc* methodology is based on an automatic picking of the first arrivals and on the optimization of the initial picking. A location is estimated at each step, and is progressively refined. The ASL method is used to identify a pre-location area to reduce the size of the grid search. A realistic P-wave velocity model is then introduced in the methodology. The location procedure is fully automatic and demonstrated good performance on calibration shots reducing by a factor of two the mean epicenter error (27±29 m) compared to other location strategies. In particular, the prior information from ASL and the iterative optimization of the initial Kurtosis picks improve the determination of the location. The picking procedure provides satisfactory results for strong and emergent onsets of natural sources occurring inside the seismic network. Even if the slopequakes present lower SNR than the calibration shots, their SNR distribution respects the attenuation law and the slopequakes seem to be reliably located. One may anticipate lower location errors of slopequakes for landslides developed in other geological contexts especially in hard rocks mostly due to lower attenuation of the P-waves arrivals. Despite the limitations linked to the seismic network geometry and the material heterogeneity , the results of *APOLoc* are promising. We show that simple (uniform) assumption on the velocity model and attenuation coefficient do not provide good estimation of the location. Further improvements would be to build a realistic model for surface waves propagation taking account the strong topography of the site and the lateral velocity heterogeneities, to invert the attenuation coefficient and possibly implement joint inversion of the locations.

Acknowledgements

This work was carried with the support of the French National Research Agency (ANR) through the projects HYDROSLIDE “Hydrogeophysical Monitoring of Clayey Landslides” and SAMCO “Adaptation de la Société aux Risques Gravitaires en Montagne dans un Contexte de Changement Global” and of the Open Partial Agreement Major Hazards of Council of Europe through the project “Development of cost-effective ground-based and remote monitoring systems for detecting landslide initiation”. The continuous seismic data were provided by the Observatoire Multi-disciplinaire des Instabilités de Versant (RESIF/OMIV, 2015). The authors acknowledge Alexandre Remaître, Pierrick Bornemann, Benoit Carlier, Juliette Trautmann and Gaëlle Rigoudy who participated to the seismic tomography campaign in 2014, and Patrice Ulrich who installed the permanent seismometers. Finally, the authors thank Clément Hibert for constructive discussions and comments on earlier versions of the manuscript, and Joan Gomberg (USGS) and an anonymous reviewer for their helpful comments.

3.8 Appendix A

3.8.1 Sensitivity analysis: location accuracy vs. seismic velocity models and picking errors

In order to quantify the influence of the velocity model and of the picking error on the location accuracy, 180 seismic sources are simulated with the NonLinLoc package. The synthetic sources are placed at nine different horizontal (X-Y) locations in the upper part of the landslide; their depths range from 0 to 20 m below the surface for each (X-Y) locations. The current configuration of the Super-Sauze seismic network is used. Two tests are carried out in order to assess the sensitivity: 1) of the location for different velocity models and 2) of the location for different picking errors. For each tests, the synthetic P-wave arrival travel time tables computed with the 3D P-wave velocity model are taken as the reference time t_0 (cf. Section 3.1). It implies that for testing the velocity model influence, the location are estimated using the travel time tables of the tested model to locate reference arrival times t_0. For testing the picking error influence, an error of picking δt_0 is added to the reference picked times t_0. The error of picking is randomly drawn from a Gaussian distribution centered at 0 s with a variance corresponding to the tested picking error magnitude. The location is computed with the reference 3D P-wave velocity model for the pick times $t = t_0 + \delta t_0$.

The locations are computed with the NonLinLoc package using the L2-RMS likelihood. The hypocenters are plotted by determining the maximum likelihood (computed from the L2-norm misfit between observed and calculated travel-times) and the location uncertainty (computed from the hypocenter Posteriori Density Functions –PDFs-). The PDF gives the probability of the source location considering the uncertainty on the data and the model. The point density of the PDF sample is proportional to the PDF value of the cell; thus the more dense the points are, the higher the PDF value is (Anthony et al., 2000). Consequently, robust source locations correspond to dense and narrow PDF samples.

Sensitivity to the seismic velocity model

Four velocity models are tested: 1) a homogeneous model with a velocity of 1500 m.s^{-1}, 2) a homogeneous model with a velocity of 2500 m.s^{-1}, 3) a 2-layers velocity model with a velocity of 1500 m.s-1 above the bedrock and 2700 m.s^{-1} in the bedrock and 4) a gradient velocity model where the velocity increases from the surface (v_P=600 m.s^{-1}) to the bedrock interface (v_P=2700 m.s^{-1}). The homogeneous models are chosen as a low and high estimation of the apparent velocity of P-wave through the landslide. The synthetic source for P-wave arrival times are computed with the reference 3D velocity model presented in Section 3.1 and the location is calculated for all the velocity models. The results of the location with the four different velocity models are plotted in Figure 3.16.

The epicenter errors are larger (mean error 89 m) with the first velocity model ($\mathrm{v_P}$=1500 m.s^{-1}) than with the other models (mean error 11-14 m). The hypocenter errors are larger with a mean error of 115 m for the first model, 66 m for the second model (v_P=2500 m.s^{-1}) and 30 m for the 2-layers and the gradient models. The PDFs scatters of the location obtained for the first model are narrow with an extension of ca. 50 m in the horizontal plane and 100 m in depth. The PDFs scatters obtained for other models have a larger extension of ca. 100 m in the horizontal plane and ca. 200 m in depth. Their shapes are elongated along the Y-direction for the sources located at the same latitude as the seismic sensors and at further distances progressively elongate in the X-direction. In comparison, when the locations are calculated with the 3D velocity model, the hypocenter errors decrease to 2 m (Figure 3.16.a) but the shapes of the PDF scatters are similar to the ones obtained with the homogeneous velocity model (v_P=2500 m.s^{-1}), the 2-layer and the gradient models. The latter can be considered as reliable approximation of the 3D velocity model.

Sensitivity to the picking errors

The arrival times of the synthetic sources are computed with the reference 3D velocity model (Figure 3.17) and random picking errors of ±0 ms, ±5 ms, ±10 ms, ±50 ms are added to the arrival times respectively. The locations are computed with NonLinLoc using the L2-RMS likelihood and the results are presented in Figure 3.17. The mean epicenter and hypocenter errors progressively increase with the picking error (mean horizontal error of 3±2 m, 20±13 m, 29±21 m and 117±94 m and mean vertical error of 3±3 m, 46±45 m, 58±49 m and 131±98 m for the ±0 ms, ±5 ms, ±10 ms and ±50 ms added error respectively). The PDF scatters present similar shapes as the ones described in Section 4.1.1 when the picking error is lower than 10 ms. For a picking error of ±50 ms, the PDF scatters is widely spread and diffused and the source locations are poorly constrained.

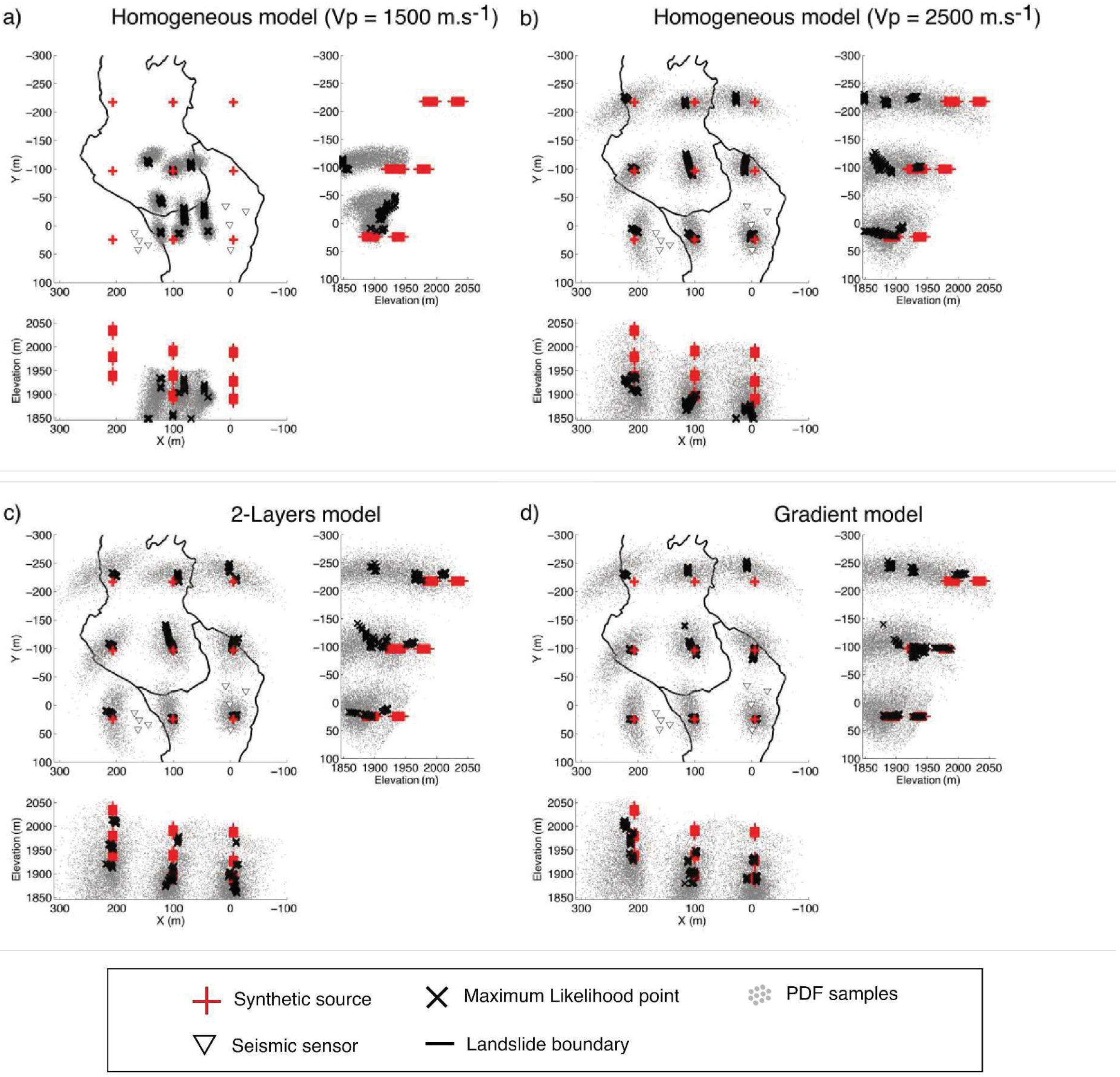

Figure 3.16: Influence of four velocity models on the location of synthetic sources: a) homogeneous P-wave velocity model of 1500 m.s^{-1}; b) homogeneous P-wave velocity model of 2500 m.s^{-1}; c) two-layers velocity model with constant P-wave velocities of 1000 m.s^{-1} in the landslide body and 2700 m.s^{-1} in the bedrock, d) "gradient" velocity model where the velocity varies linearly with depth from 500 m.s^{-1} in the top unit to 2700 m.s^{-1} in the bedrock. The L2-RMS likelihood function implemented in NonLinLoc is used to locate the synthetic events.

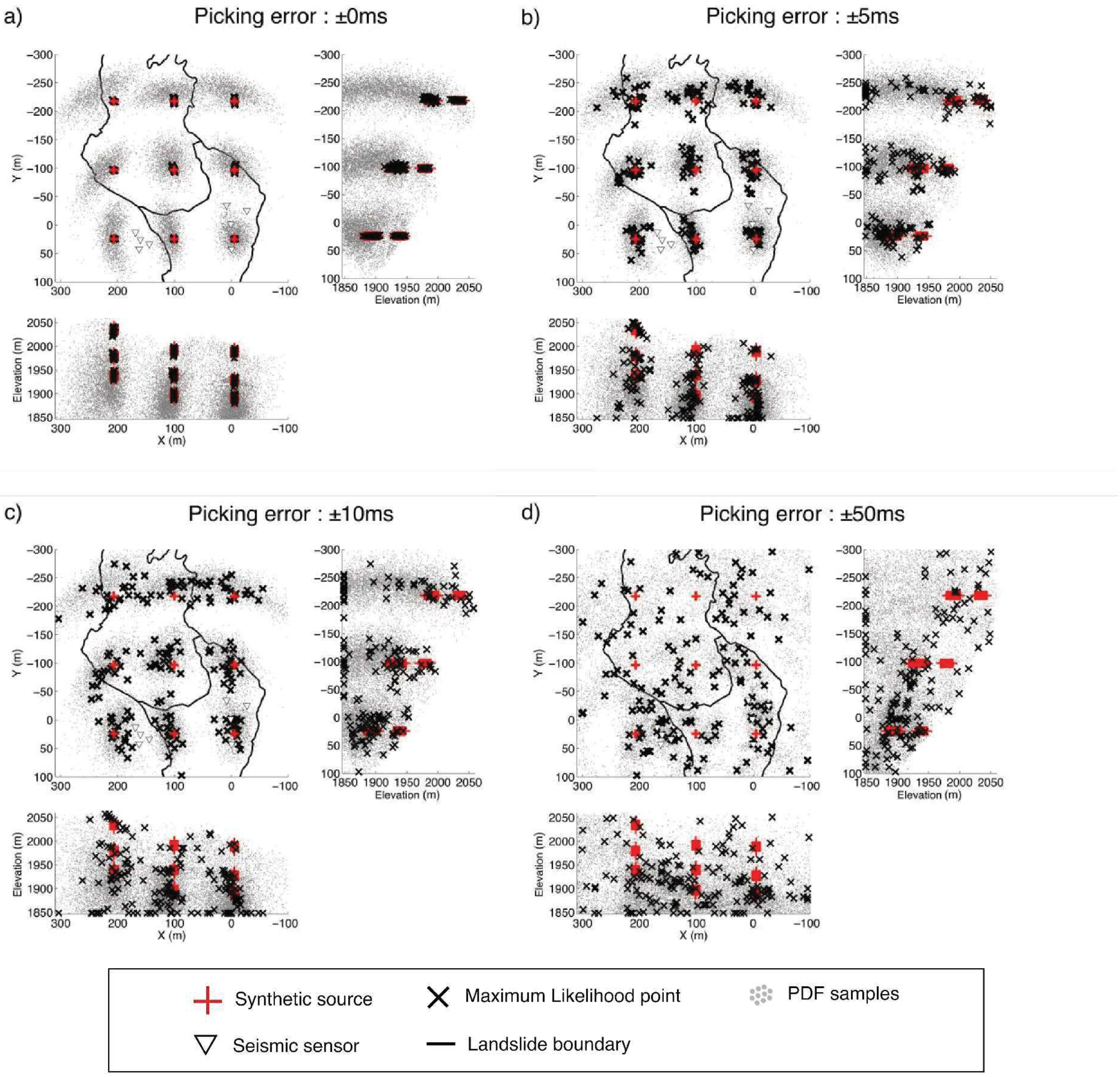

Figure 3.17: Influence of the picking error on the location of synthetic sources. Three picking error values are tested : (a) with no picking error; b) ±5 ms; c) ±10 ms; d) ±50 ms. The L2-RMS likelihood function implemented in NonLinLoc and the 3D velocity model is used to locate the synthetic events.

Synthesis: Location of seismic signals for understanding the landslide deformation pattern

Main Results: We developed an automatic seismic source location method adapted to the context of landslides. Our method is based on the inter-trace correlation of the P-wave arrivals, a realistic estimation of the P-wave velocity model from seismic tomography and on the use of the Amplitude Source Location as prior information. We demonstrate the importance of the picking resolution on the location accuracy and implemented an iterative strategy to optimize the quality of the initial picks. We also show the importance of determining a priori information on the location based on the signal. Finally, we show that introducing a realistic velocity model of the underground structure is crucial to obtain accurate locations. We tested our methodology on calibration shots and obtained epicenter errors of 27±29 m which is better than previous approaches used for similar contexts. The method is adapted to locate slopequakes occurring inside the seismic network but likely fails to locate most of the rockfall events located at far distances from the seismic sensor and outside the velocity model.

Perspectives: In our approach, we assumed that first arrivals onsets are P-waves. This assumption is reasonable for calibration shots and high-frequency slopequakes while low-frequency slopequakes and rockfalls may be dominated by surface waves. A detailed analysis of the signal polarization is needed to determine the suitability of the proposed method to locate the recorded events. This could either be implement at the classification step by defining polarization features or simply separating HF- and LF-slopequakes for instance, or at the location step by analyzing the polarization of the picked time window.

For the signals characterized by the very attenuated or even absence of P-waves, the same methodology could be used to pick the arrivals of the surface waves. The surface wave arrivals taking into account the topography and the heterogeneities of the sub-surface could be inverted from the data of the seismic tomography. The pre-location step is currently computed assuming a uniform attenuation coefficient. We show that this coefficient varies significantly in the landslide body. The inversion of the the coefficient from the seismic tomography shows its dependence to the presence of fractures. As the number of fractures varies significantly through time, an inversion of this coefficient in the pre-location step would be needed.

Finally, our results suggest that taking into account several estimations of the location improves the accuracy of the location. The current implementation propose to set as a prior information the location area obtained from the information with the simplest assumption (i.e. uniform attenuation coefficient) and compute the final location with the most robust model (i.e. 3D P-wave velocity model). A possible improvement would be to implement a joint inversion of the different information. However, this will require an effort to quantify more accurately the model and signal processing errors.

CHAPTER 4| Application: Landslide deformation pattern of clayey landslides

This chapter aims at investigating the distribution in space and time of the landslide endogenous seismic sources. The main objectives are to understand and potentially quantify the landslide dynamics in relation with hydro-meteorological forcings and to determine the presence of seismic precursors before or during slope acceleration. The seismic observations recorded during three years at the Super-Sauze landslide (French Alps) are studied. The methodology of the precedent chapters is applied to construct catalogs of landslide seismic sources for two classes: Slopequake and Rockfall.

The temporal relationship between recorded seismic signals and hydro-meteorological forcings (and slope motion) is first analyzed. The correlation between the seismic sources time series and the hydro-meteorological datasets and slope motion measures are computed. In case the correlation is significant, we also analyze the time delay and the relaxation time of the correlation function. The spatial variations of the seismic location is then described as well as the observed cycles of seismic occurrences.

This chapter is mainly based on the following scientific papers:

Provost, F., J.-P. Malet, C. Hibert, J. Point, C. Doubre. Patterns of landslide endogenous seismicity and their relationships with environmental forcings and motion, *(submitted)*

Abstract: *Activation of gravitational instabilities remains hard to predict efficiently as they may be triggered by a combination of external forcings and internal processes. In particular, clayey landslides exhibit solid to fluid transition leading to sudden and hardly predictable acceleration. We analyzed the seismic sources generated by slope acceleration at the Super-Sauze clayey lanslide. Three years of seismic dataset has been analyzed using automatic processing to construct catalog of seismicity for slopequakes and rockfall signals. The latter are correlated to meteorological data, ground water level and slope motion. We found that the seismic sources occurrence are significantly correlated with the precipitation and cease rapidely as the rain stops for rockfall while the relaxation time is longer for slopequakes. This traduces the presence of the cycles of seismicity associated to acceleration and deceleration of the slope. We observed that all the accelerations of the slope are preceded by increase of slopequake rates. The slopequake rates decrease as the slope motion reaches a constant velocity during local maximum of ground water level. The deceleration of the slope is then associated to the deceleration of slope. This suggests that the rate of seismic sources generated be slop motion is not linearly proportional to the slope velocity but highly controlled by the soil water content.*

4.1 Introduction

Landslides are a common natural hazard worldwide causing damage and causalities each year Petley (2004). Forecasting their failure (in the case of initially stable slopes) or their acceleration (in the case of continuously active slides) is still a challenge as they can be controlled by several mechanisms (Hungr et al., 2014) and can be triggered by various forcing factors (i.e. rainfall, snowmelt, change in air/soil temperature, earthquake). Influences of external forcings have been studied mainly at regional scales where landslide inventories are constructed from field or airborne/satellite observations. Although regional thresholds laws can be observed for the amount of landslides that can be expected above a certain rainfall threshold (Caine, 1980, Guzzetti et al., 2008) or after an earthquake (Keefer, 1994, 2000, Meunier et al., 2007, Marc et al., 2015), the activation of peculiar slopes cannot be forecast by these approaches. Hence the analysis of individual landslides to improve our understanding of their dynamics.

At the slope scale, the challenge is to anticipate when a movement suddenly occurs, and what are the causes. In order to model slope failure and/or acceleration, several approaches have been proposed. The most direct one consist in monitoring the surface deformation from in-situ (GNSS, extensometers) or remote (total stations, ground-based radar) sensors in order to detect changes in the velocity regime. When the acceleration has initiated, the time to failure might be predicted if the slip surface is sufficiently developed and that tertiary creep has initiated (Saito, 1969, 1979, Petley et al., 2002, Kilburn and Petley, 2003, Petley, 2004). This approach, although relatively simple as it does not require any geo-mechanical properties, is rather difficult to apply as a predictive tool because certain accelerations may not lead to failure (Hutchinson, 2001, Federico et al., 2012). Geo-mechanical models are also used to predict landslide displacement from meteorological and hydrological (pore fluid pressure) observations (Wilkinson et al., 2002, Corominas et al., 2005, François et al., 2007, Ferrari et al., 2011, Bernardie et al., 2015, Bru et al., 2018) but such approaches are very complex to implement operationally as geo-mechanical models are very demanding in terms of input parameters.

Recent observations suggest that precursory seismic signals can be recorded before collapse of different sizes. For instance repetitive micro-quakes have been recorded several hours before the onset of large landslides (Caplan-Auerbach and Huggel, 2007a, Poli, 2017, Schöpa et al., 2017) and/or small rockfalls (Amitrano et al., 2005). A progressive increase of their amplitude is observed and a decrease of the time delay between these seismic precursory events (Caplan-Auerbach and Huggel, 2007a, Poli, 2017, Bell, 2018), sometimes even leading to the generation of tremors (Schöpa et al., 2017). The seismic activity may also stop suddenly just before the rupture of the slope (Poli, 2017, Schöpa et al., 2017) These observations demonstrate the interest of the seismic monitoring to investigate the processes leading to the rupture. Seismic monitoring presents the advantages to record deformation processes at a very high time resolution (< 0.1 s) and with the ability to detect the occurrence of processes at some distances from the source. It has been used to delineate seismically active fracture zones (Spillmann et al., 2007, Lacroix and Helmstetter, 2011) but also to construct catalogs of seismic events with an accurate temporal resolution. Two main types of seismic signals are usually analyzed: “slopequakes” generated by internal sources and “rockfalls” affecting the surface of the instable slope. Few studies have attempted to investigate the dynamics of instabilities to hydro-meteorological forcings and slope motion (Helmstetter and Garambois, 2010, Lévy et al., 2010, Gomberg et al., 2011, Walter et al., 2012c, Tonnellier et al., 2013, Dietze et al., 2017b, Colombero et al., 2018).

The temporal precision of catalogs of rockfall built from seismic monitoring allows to precisely investigate the different meteorological conditions generating rockfalls. The strong influence of precipitation and temperature on the occurrence of rockfall is confirmed (Helmstetter and Garambois, 2010, Dietze et al., 2017b, Colombero et al., 2018) although these studies put in light the difficulty to apply rain threshold methodology to predict rockfall at this scale (Helmstetter and Garambois, 2010).

Signals characteristic of brittle failure were observed in several soft and hard rock landslide

(Gomberg et al., 1995, Helmstetter and Garambois, 2010, Levy et al., 2011, Walter et al., 2011, 2012b, 2013b, Tonnellier et al., 2013, Vouillamoz et al., 2017, Colombero et al., 2018). Helmstetter and Garambois (2010) observed an increase of slopequakes preceding the motion of the Séchilienne landslide suggesting an activation of fault network leading to the movement of this gravitational instability. On soft-rock landslides, the relation between slopequake occurrences and slope motion is more complex to establish (Walter et al., 2011, Tonnellier et al., 2013, Vouillamoz et al., 2017) mostly due to the fact that the monitoring periods are short preventing any robust interpretation.

The present paper investigates the time and space occurrence of the endogeneous (e.g. landslide-triggered) seismic sources observed at the Super-Sauze clayey landslide (South East French Alps). A catalog of seismic events is created for nearly three years of seismic monitoring. The catalog of endogeneous seismicity is rich for this landslide as both rockfall seismic sources (triggered from the main scarp of the landslide) and slopequake seismic sources (mostly generated by the landslide motion) are recorded from the same seismic network. The site, the dataset and the processing of the data is first presented. We then analyzed the correlation of the seismic signals occurrence and the meteorological and motion time series to seek for temporal response to forcings. The locations of the seismic sources are also computed. The anlysis of the spatio-temporal patterns of the seismic events enable to observe variations in the rockfall location as well as cycles in the slopequake occurrences. The latter shade in light a complex occurrence of slopequakes during slope acceleration and deceleration.

4.2 Study site

The study site is the Super-Sauze landslide located in the Ubaye valley (Southeast French Alps). The landslide is composed of reworked clay shales (black marls) of the Jurassic age. Triggered in the early 1960's, it has propagated progressively downslope and has reached a volume of nearly 800,000 m^3 and a size of 850 × 300 m^2 with an average thickness of 15 m. The landslide is one of the permanent monitoring site of the French Landslide Observatory OMIV (Observatoire Multi-disciplinaire des Instabilités de Versant: www.ano-omiv.cnrs.fr). Three categories of observations are monitored with several sensors: the surface deformation is monitored using permanent GNSS, terrestrial optical cameras and repeated terrestrial laser scanning campaigns; the sub-surface hydrology is investigated through a network of three pore water pressure sensors installed in shallow piezometers and through soil humidity probes; finally, the seismic activity of the slope is documented using 8 seismometers organized in two arrays.

Various modes of deformation are observed on the landslide (Figure 4.1). Rockfalls are triggered at the 100 m height main scarp and in the badland areas bordering the landslide to the East and the West (Figure 4.1). Many boulders are deposited in the two lateral streams delineating the landslide. These boulders are further eroded and transported downstream by the water flows. The landslide body behaves as an earth-flow like movement (Figure 4.1) with a changing rheology according to the degree of saturation of the material (Malet et al., 2005). During the lower pore water pressures and velocity periods, a rigid deformation is observed at the surface. The material behaves as a brittle media and fissure networks in extension and shearing are created (Stumpf et al., 2013). During the higher pore water pressures and velocity periods, a ductile deformation is observed and the material progresses downhill as a viscous fluid with the triggering of shallow mudflows (Malet et al., 2005, van Asch et al., 2006).

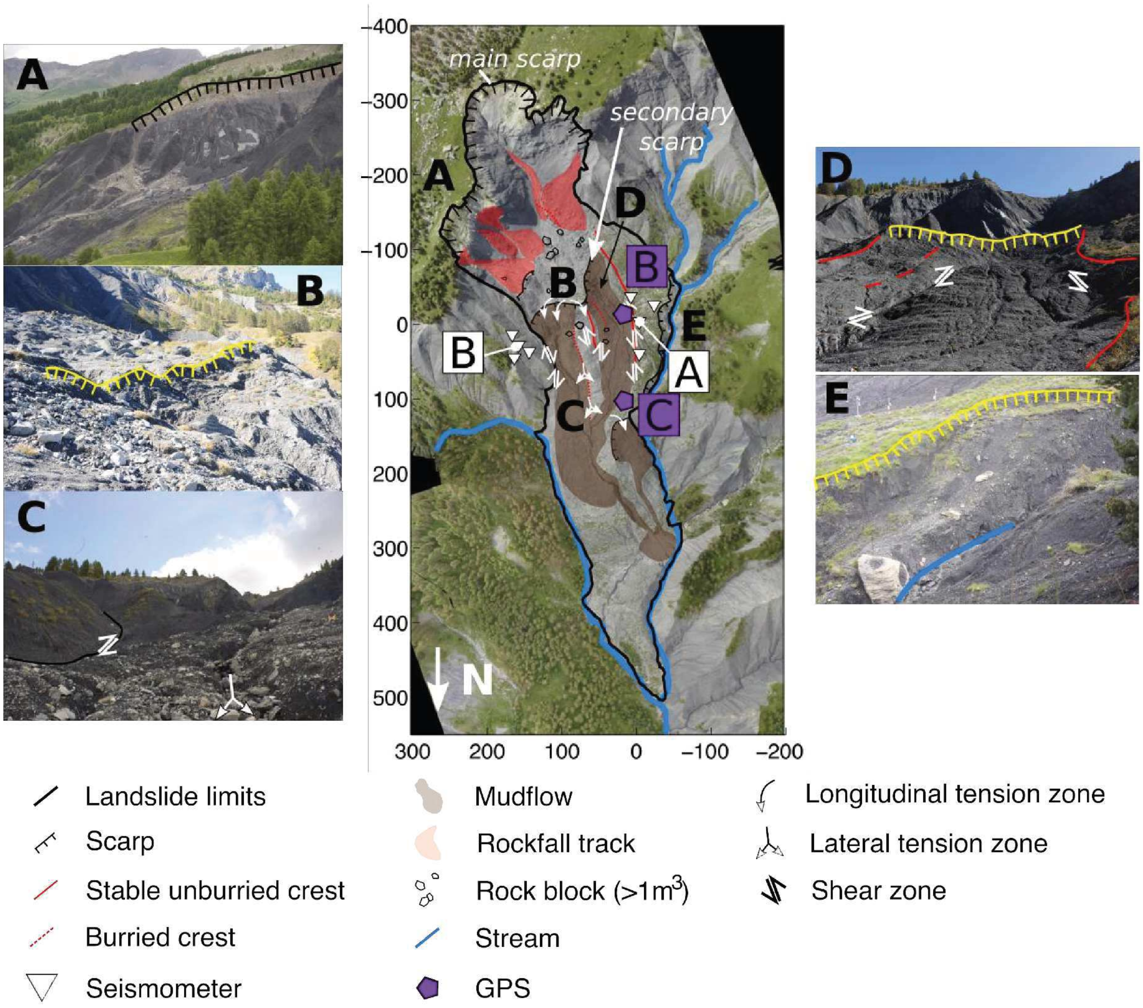

Figure 4.1: The Super-Sauze study site: Geomorphological structures and sensors are represented over an orthophotograph dated from July 2017. Photographs of the main geomorphological structures are also presented.

4.3 Observation data

All sensor observations are managed and disseminated publicly by the French Landslide Observatory - OMIV RESIF. The instruments are located in the upper part of landslide (Figure 4.1, at the vicinity of the most active zones of the Super-Sauze lanslide (Stumpf et al., 2014, 2015, Tonnellier et al., 2013).

4.3.1 Seismological observations

The seismological observations consist in 1) a long-term dataset covering the period October 2013 to June 2016 and 2) a short-term campaign experiment covering the period June to July 2016. The long-term dataset is acquired by 8 seismometers organized in two permanent seismic arrays (Figure 4.1). Seismic array A continuously is operated since 2009 while seismic array B was installed in 2013. Each array correspond to an equilateral triangle with three vertical seismometers distant from the central 3-component sensor of 40 m (array A) and 30 m (array B). The seismic array A is instrumented with Agecodagis Noemax sensors (natural frequency: 4.5 Hz), the seismic array B is instrumented with Sercel L4C sensors (natural frequency: 1 Hz). The sampling frequency for all sensors is 250 Hz.

4.3.2 Surface displacement monitoring

An array of three GPS receivers have been installed on the landslide since 2009 (Figure 4.1), with two receivers located in the landslide body (GPS-B, GPS-C) and one receiver located outslide the landslide. The GPS observations are acquired with TRIMBLE NetRS or TRIMBLE R9 geodetic dual-frequency receivers equipped with TRM41249.00 antenna and a TZGD radome. Every day, one 30-second daily file (i.e. 2880 sessions) and 24 1-second hourly files (i.e. 3600 sessions) are produced. The data are stored locally on the receiver memory boards and, within one day, the data are transferred to a network server. The GPS observations are processed using a double differencing solution (Malet et al., 2011).

The GAMIT/GLOBK package (Herring et al., 2003a,b), package is used to estimate the three-dimensional positions of the ground stations and the satellite orbits. A loosely constrained daily solution file of parameter estimates and covariances is the output of GAMIT. The GLOBK package combines the daily solutions to estimate station positions and velocities. Orbital and Earth-rotation parameters are also estimated. The processing algorithm is described and evaluated in Malet et al. (2013).

The accuracy of the sensor position is evaluated at ± 1.5 cm in the horizontal component (E-W) and ± 3.5 cm in the vertical component (Z).

4.3.3 Hydro-meteorological monitoring

The hydro-meteorological observation network consists of a permanent survey of ground water levels in shallow boreholes (BV, CV) located at close distance (< 5 m) from the GPS sensors, and of rainfall, air temperature net radiation measurements at 500 m from the landslide (Figure 4.1). The depth of the piezometers is 4.2 m for BV, and 4.6 m for CV. The groundwater levels are measured with Diver TD water level probes corrected from barometric air pressure. The probes are installed at a depth of -3.9 m in piezometer BV, and -4.2 m in piezometer CV, and the water levels are measured with a time step of 6 hours. The meteorological parameters are monitored with an ARG1000 raingauge, a CS215 sensor for the air temperature, a 03002 sensor for the wind velocity and direction, and a CS300 pyranometer for the net total radiation. The parameters are acquired at an hourly time step, except for the rainfall which is monitored at a 6 min timestep.

Effective precipitation (P_{eff}) is estimated daily by the difference between the daily cumulated rainfall and the net evapo-transpiration calculated with the Penman-Monteith equation (Beven, 1979).

4.4 Methodology

The seismic observations are used to construct catalogs of seismicity. The different steps of the seismic processing as well as the methodology to investigate the relationships between the spatio-temporal occurrences of the seismic signals, the hydro-meteorological forcings and the slope motion are summarized in a flowchart (Figure 4.2).

4.4.1 Seismic processing

Event detection

The detection is based on the ratio between short-term average and long-term average (STA/LTA) of a characteristic function computed from the spectrogram (Helmstetter and Garambois, 2010). The characteristic function is defined as geometric mean of the Power Spectral Density (PSD). The analyzed characteristic function is a stack of the spectrograms computed for each sensor to enhance the PSD of low SNR events. This method is sensitive to changes in the signal frequency content and hence is predominantly suitable to detect low amplitude signals. The threshold is set to 1.5 meaning that an event is detected if its PSD is 1.5 larger than the background noise. The characteristic function is computed in the [5-100] Hz frequency range. As we expect to record rockfalls, each individual impacts may be detected as a single event. Events detected within 10 seconds are merged into one event. The detection threshold is set at a low value in order to detect very weak endogenous seismic sources with the drawback of also detecting a significant number of noise events.

Event classification

The classification is based on the supervised machine learning method proposed by (Provost et al., 2017, Hibert et al., 2017c) using the Random Forest algorithm. Statistical classifiers require the definition of a training set (i.e. examples of signals) and of a set of attributes describing the signals. Several signal features are computed (i.e. signal waveform, frequency content, etc) as proposed by (Provost et al., 2017). The signal features are computed for the trace with the maximal amplitude. For the 2013-2016 dataset the spectral features are computed for the summed-up spectrogram; for the June-July 2016 dataset, only the spectrogram of the trace with the maximal amplitude is used. This choice was made to reduce the computation time. The principle of Random Forest then consists in the construction of several decision trees (> 500) from the initial training set and the random selection of the attributes.

The seismicity is classified into four general families: “Slopequake” (SQ), “Rockfall” (RF), “Earthquake” (EQ) and “Natural and Anthropogenic noise” (N & A) . For the 2013-2016 dataset, the training dataset consists of three acquisition periods from October 11 to November 19, 2013, from November 10 to November 30, 2014 and from June 09 to August 15, 2015. The investigated dataset consists of 418 “Rockfall” events, 239 “Quake” events, 407 “Earthquake” events (EQ) and 395 “Natural/Anthropogenic noise” events (“N & A” noise). For the June-July 2016 dataset, a catalog of seismicity has been produced manually.

Event location

The endogenous events (i.e. “rockfall” and “slopequake” classes) are then located automatically. The location method is based on a simpler version of the *APOLoc* method (Provost et al., 2018). It consists in using the Amplitude Source Location (ASL) method (Taisne et al., 2011) to pre-locate the area of the source and to locate the epicenter of the source by maximizing the inter-trace correlation using the method developed by (Lacroix and Helmstetter, 2011). The whole signal is correlated and apparent

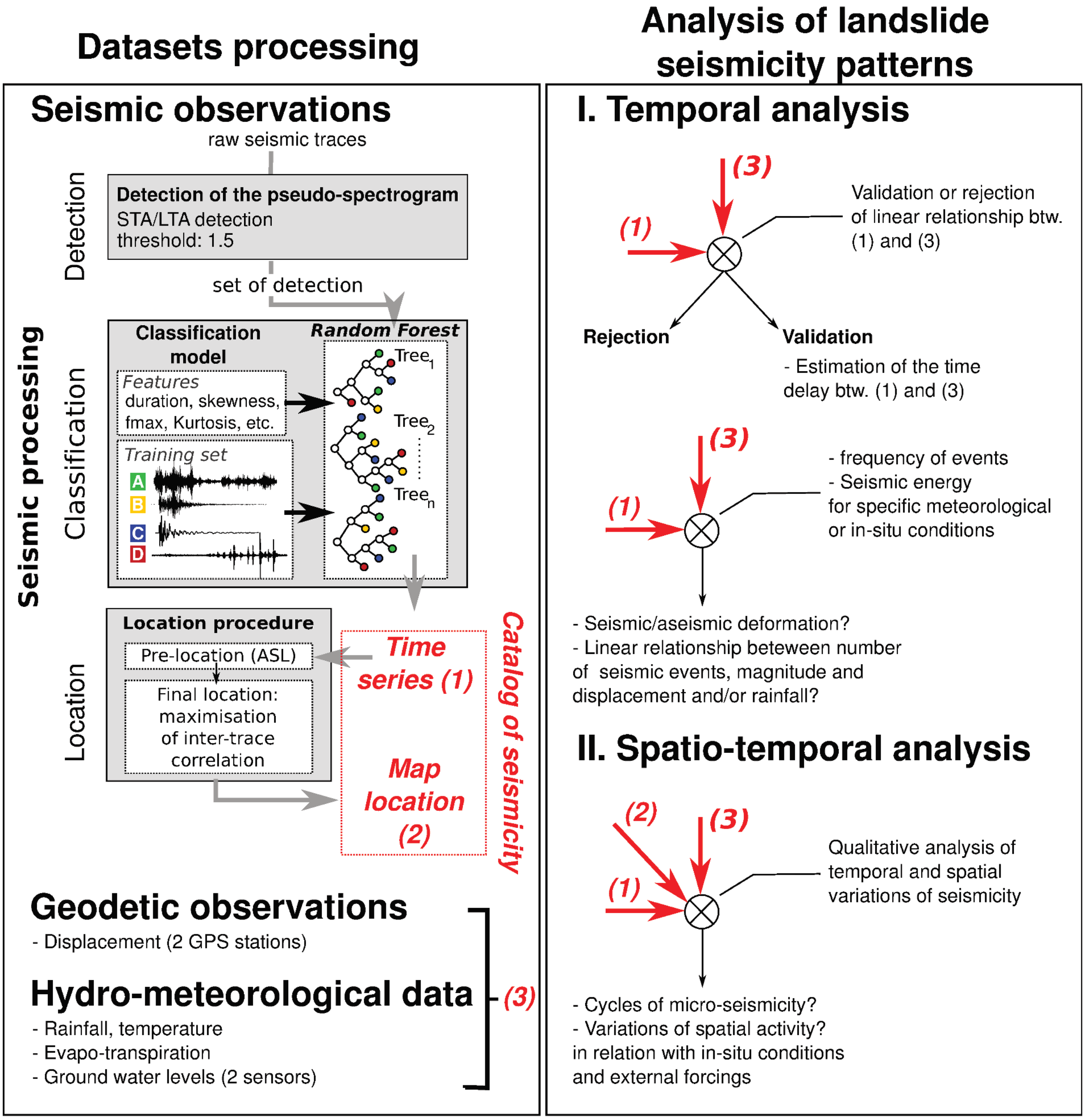

Figure 4.2: Processing flowchart indicating the source dataset, seismic processing and methodology used to analyze the advanced catalogs of endogenous seismic sources.

velocity is optimized with the source epicenter to maximize the correlation. An attenuation coefficient of 0.008 m^{-1} is used to compute the pre-location area with the ASL method. The apparent velocity is allowed to vary between 300 $m.s^{-1}$ and 4,000 $m.s^{-1}$.

Analysis of landslide endogeneous seismic catalog

We compute the correlation of the seismicity rates with the different meteorological time series in order to determine a time delay between them. The time series are corrected from their average value and normalized by their standard deviation. During the periods where no seismic data are recorded, the meteorological data are set to zero. We also model the increase and decrease of the correlation function to invert relaxation times around the maximal correlation.

We then compute the distribution of the events rate and seismic energy for specific meteorological conditions and/or slope velocity. The main objective of this analysis it to investigate if the number and the magnitude of the recorded events could be predicted. We compute the seismic energy for all the seismic sources as:

$$\mathrm{E}s = \int_{t1}^{t2} 2\pi r \rho h c u_{env}(t)^2 e^{\alpha r} dt \tag{4.1}$$

with r being the sensor to the source distance, ρ the density of the rocks ($\rho = 1300$ $kg.m^{-3}$), h the thickness of the layer through which the surface waves propagates (h = 5m), c the velocity of the surface waves (c = 1,000 $m.s^{-1}$), $u_{env}(t)$ the envelope of the seismic signal $u(t)$ computed from the Hilbert transform (Ht) as $u_{env} = \sqrt{u(t)^2 + \mathrm{H}t(u(t))^2}$ and α the coefficient of inelastic attenuation ($\alpha = 0.008$ m^{-1}).

Finally, we analyze the spatio-temporal occurrences of the seismic sources to detect specific variations during the period of acquisition.

4.5 Results

4.5.1 Quality of the seismicity catalog

Performance of the classification algorithm

The complete dataset consists in 95,647 events detected for the period 2013-2016. Among them 46,862 events are classified with a score higher than 0.6. In order to evaluate the results of the automatic classification, 1,000 events are randomly selected in the predicted set. They are manually inspected and classified to estimate a confusion matrix (Table 4.1).

The accuracy (i.e. the correctly classified events over the total number of events) is 79%. However the results vary significantly among the different classes. The "N & A" class is correctly classified at

Table 4.1: Confusion matrix for the long-term dataset. 1,000 event are randomly selected in each predicted class and manually classified.

		True class			
		N&A	EQ	SQ	RF
Predicted	N&A	998	2	0	0
	EQ	82	901	7	10
	SQ	256	4	729	11
	RF	415	45	0	540
Total		1669	950	849	561

Table 4.2: Values of the Kendall correlations and p-values estimated between rockfall and meteorological observations: effective precipitation (P_{eff}), daily rainfall, air temperature and daily air temperature gradient.

	Peff	Rainfall	Temperature	Temperature gradient
C_K	0.233	0.2344	0.1508	-0.1461
p-value	$1.5734\ 10^{-10}$	$4.2533\ 10^{-11}$	$1.8445\ 10^{-6}$	$3.8231\ 10^{-6}$

more than 99% while the “EQ”, “SQ” and “RF” classes obtain a precision rate of 90%, 73% and 54% respectively. Indeed, many “N & A” events are present in the other predicted classes. The low precision for rockfall can be explained by the fact that rockfall sources show heterogeneous features depending on their volumes, their fall height and the size of their blocks. The classification sensitivity of the slopequake events is higher (73% of correct classification) likely due to the fact that their short duration is a highly discriminant feature. The interpretation of these kind of signals is much more complex than rockfall events, and sometimes, rockfalls of small volumes maybe confused with slopequakes.

The catalogs are validated manually for further interpretation and consist in 2,312 rockfall and 2,601 slopequake events (Figure 4.3. Rockfalls mainly occur during day time while slopequake are more frequent in the morning between 5 and 11 am (Figure 4.4). Earthquake and “N & A” are not verified manually but their daily distribution is consistent with common observations: the noise progressively increases during daytime as human activity generates most of the high-frequency noise and the number of earthquakes is the same for all hours of the day (Figure 4.4).

Performance of the location algorithm

The spatial locations of the 2,312 rockfalls and 2,601 slopequakes are presented on Figure 4.5. Rockfalls are mostly located at the eastern part of the main scarp (Figure 4.5a). A few events are also located in the central and at the western part of the main scarp which are two less active areas. The inter-trace correlation associated to the final location is of 0.47 ± 0.05 for the rockfall events. The locations of the slopequakes are located in the central part of the slide mostly in the vicinity of seismic array A (Figure 4.5b). The mean inter-trace correlation for the slopequakes is 0.39 ± 0.05, corresponding to an expected location error of 50 m with the chosen location method (Lacroix and Helmstetter, 2011, Tonnellier et al., 2013, Provost et al., 2018). Some slopequakes are also located on the main scarp and on the western part outside of the landslide either due to fractures or mis-interpreted single block fall.

4.5.2 Analysis of the temporal pattern of seismic sources, hydro-meteorological forcings and motion

As a first approach, the existence of possible relationships between the seismic event occurrences, hydro-meteorological forcings and surface motion is verified. The rockfall and slopequake catalogs are analyzed separately and the most pertinent relationships are tested.

Rockfall

The main expected triggers are the rainfall rates and amounts and the temperature gradient per day. We thus only investigate the correlation with these parameters. We computed the Kendall correlation coefficient and its associated p-value. We choose to work with the Kendall correlation because it is a measure of the rank correlation. We found significant correlation ($p\text{-value} < 0.05$) between the rockfall rate (i.e. number of events per day) and effective precipitation (P_{eff}), rainfall rate per day, temperature and temperature gradient (Table 4.2). This confirms the expected correlation between rockfall, precipitation and temperature.

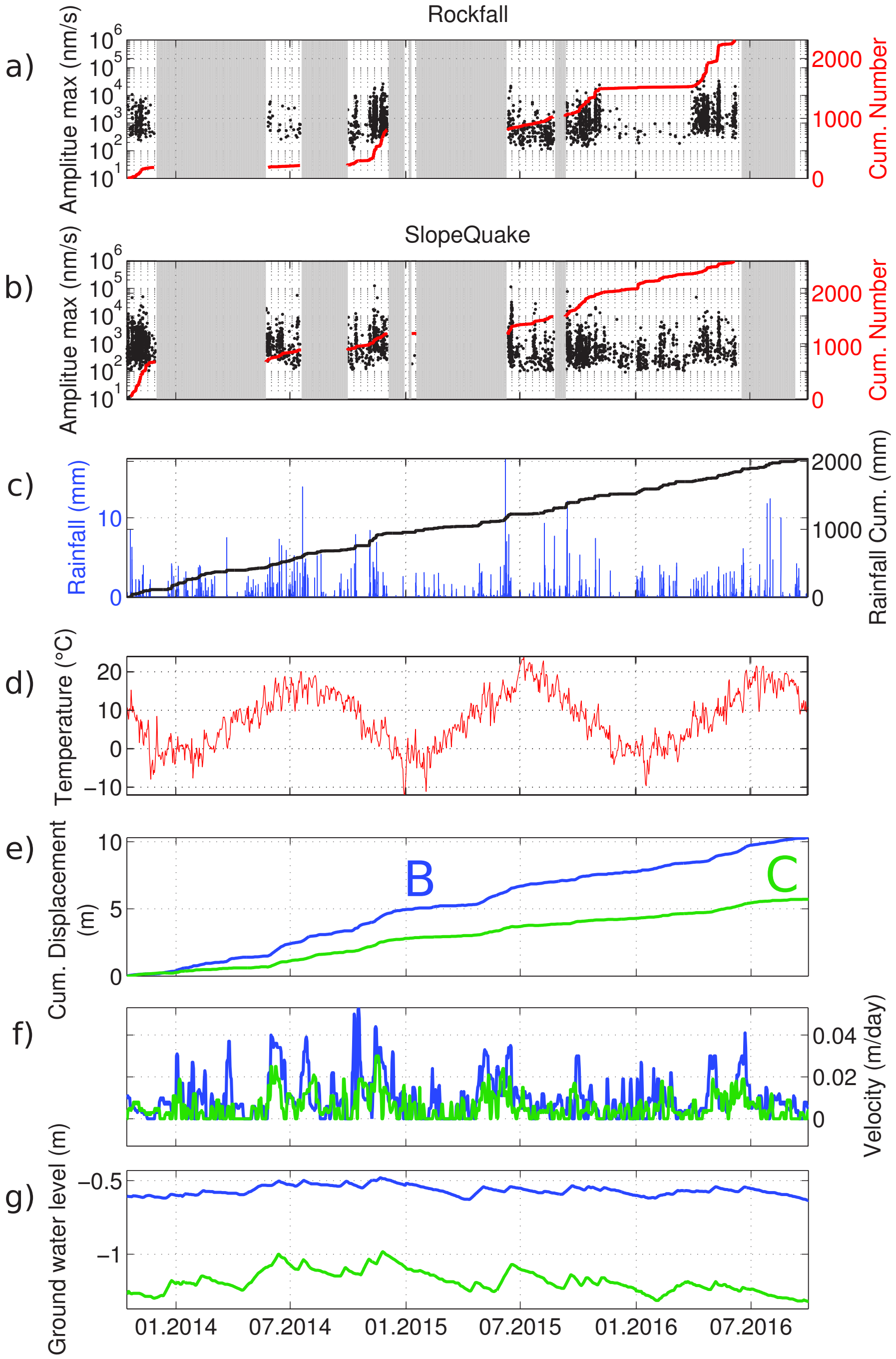

Figure 4.3: Time series of seismic observations: a) Rockfall and b) Slopequake; meteorological observations: c) rainfall, d) temperature; of geodetic observations: e) Cumulative displacement and f) velocity of GPS B and GPS C; g) ground water level variations.

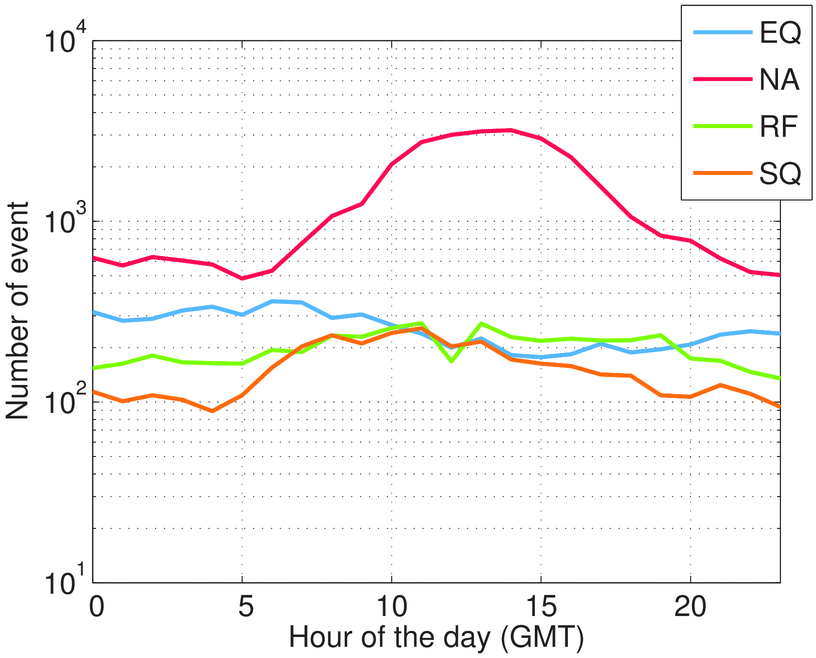

Figure 4.4: Number of events per hour of the day for the four classes of seismicity: earthquake, slopequake, rockfall and natural/anthropogenic noise.

In order to determine possible time delay and relaxation times between the meteorological forcings and the rockfall occurrences, we compute the linear correlation. A correlation value higher than 0.2 is found between rockfall rates and daily effective precipitation and hourly rainfall (Figure 4.6a,b). Although the correlation value is small, the peak is significantly above the background level.

The time delays are found at zero at a daily sampling rate but we found that rockfalls are slightly delayed from the rainfall initiation by 2 hours when the hourly rainfall rates are considered (Figure 4.6b). The correlation function can be fitted by an exponential law with a relaxation time tc. The latter is small for rockfall (tc_2 = 16-17 hours) meaning that rockfall ceases rapidly after the precipitation episodes. For the hourly datasets, a relaxation time is also found (tc_1 = 10 hours) probably due to the fact that several episodic rain events may occur in less than 16 hours before the previous one. The correlation with antecedent precipitation (i.e. cumulative precipitation over the past 10 days) is also significant. The relaxation times are respectively tc_1 = 4 days and tc_2 = 9 days.

No correlation is found with the temperature (Figure 4.6c) but a negative correlation is found for the temperature gradient. Rockfall rates are hence increasing during days with small amplitudes of air temperature. This can be explained by the fact that during rainy days the temperature gradient is lower. Consequently, the proposed triggers related to temperature (i.e. thaw-freezing, freezing-thaw or thermal dilatation) are not the main triggers of rockfall activity for this site.

The seismic energy of the rockfall is increasing slightly with the intensity of the rain episode (Figure 4.7a) and with the antecedent cumulative precipitation (Figure 4.7b). However, large rockfalls are mostly occurring during the days where no rain is recorded (Figure 4.6a) and 70% of the seismic energy is released during dry days while only 53% of rockfall events occur during those days. Less than 10% of the rockfall events occur during days with effective precipitation larger than 10 mm (Figure 4.7a). Considering cumulative antecedent rainfall (i.e. cumulative rainfall over the past 10 days), we identify that the energy and the rockfall activity are highly dependent of antecedent rainfall; indeed, less than 10% of the events occur on days with no antecedent rainfall (Figure 4.7b). The mean seismic energy released per day is slightly increasing with antecedent rainfall (Figure 4.7b).

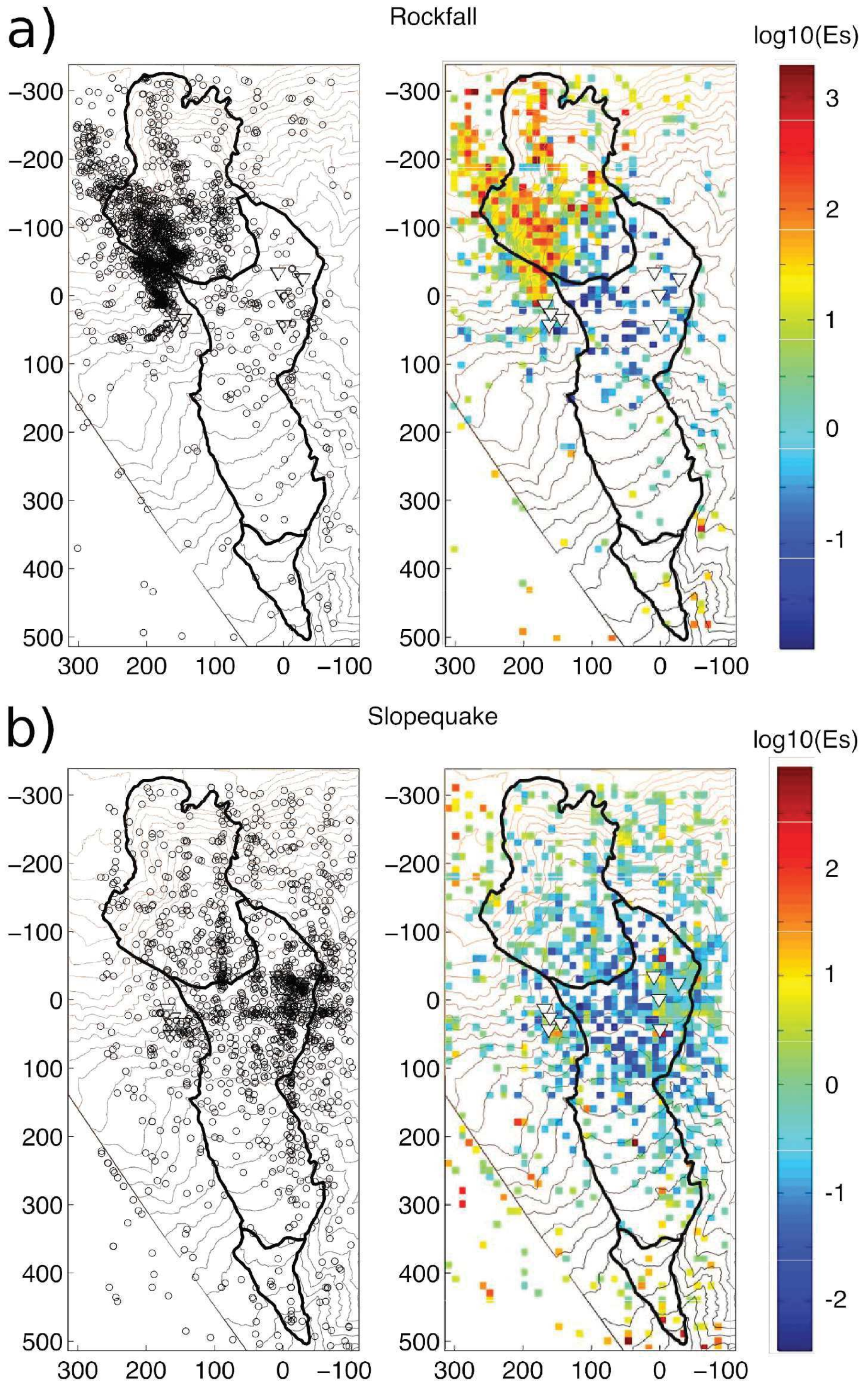

Figure 4.5: Location of the seismic events (left) and cumulative seismic energy for grid cells of 5 m × 5 m (right) for a) rockfall seismic sources and b) slopequakes seismic sources.

a) Peff

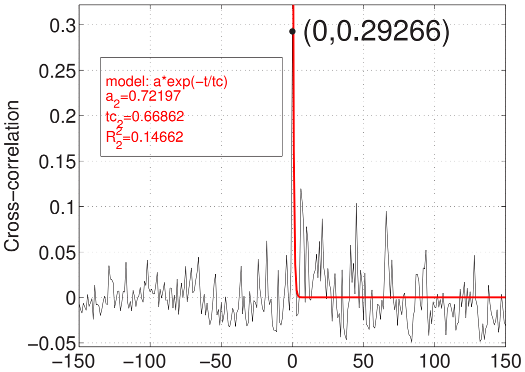

b) Rainfall (mm/hr)

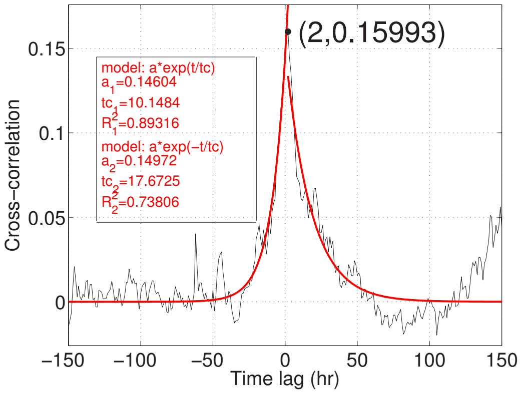

c) Pcum (mm)

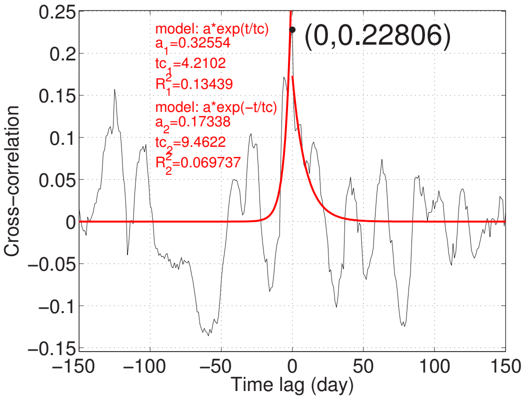

d) Temperature

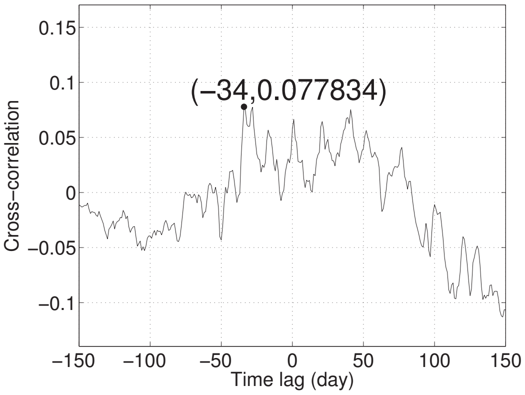

e) Temperature gradient (day)

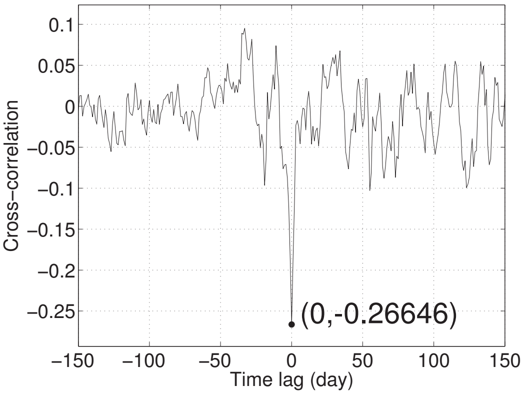

Figure 4.6: Cross-correlation between the rate of rockfall and a) daily effective precipitation (P$_{e}ff$), b) hourly effective rainfall rate, c) cumulative effective rainfall computed on the past 10 days (P$_{c}um$), d) air temperature and e) daily air temperature gradient (in black). The red curves represent the model fit for an exponential law: $a_1 * e^{t/tc_1}$ and exponential decay: $a_2 * e^{t/tc_2}$ with parameters a_1, a_2, tc_1 and tc_2 indicated on the size of the subplots in red for the best inversion.

a) Effective precipitation

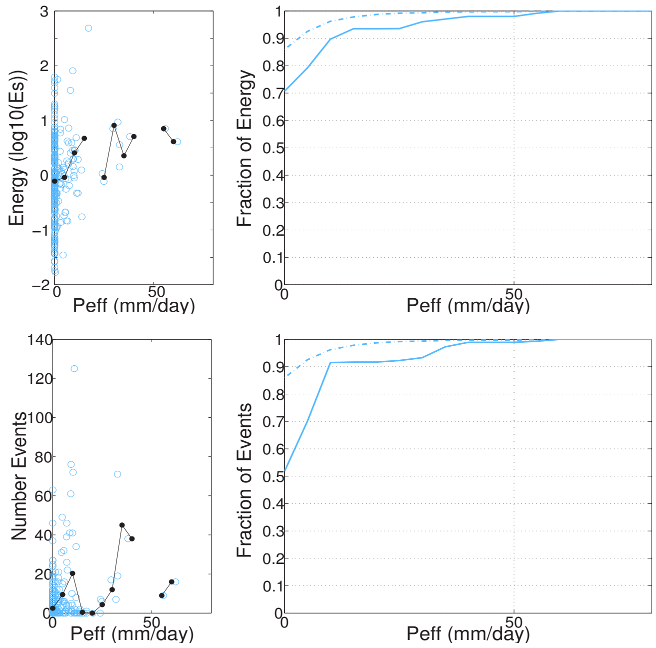

b) Cumulative precipitation

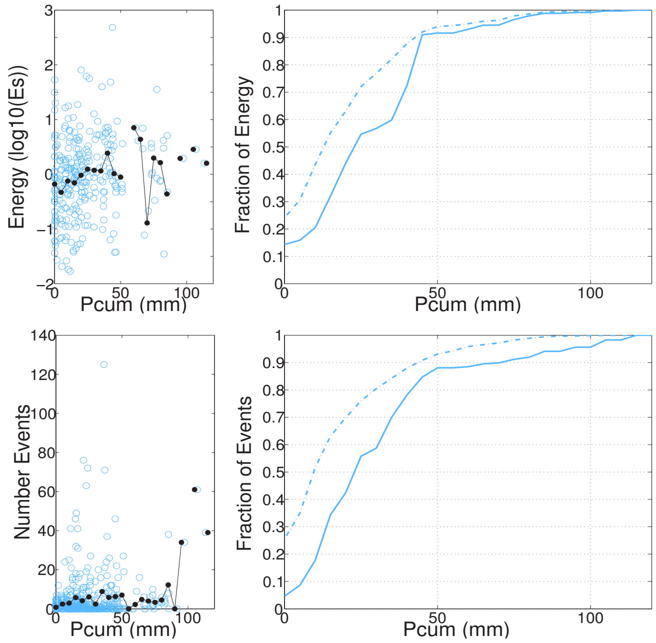

Figure 4.7: Number of rockfall per day and mean seismic energy released per day as a function of a) effective precipitation and b) cumulative effective precipitation. The number of rockfall per day (and repspectively, the mean seismic energy released per day) are plotted with respect to the amount of effective precipitation (or cumulative effective precipitation) on the left plots (in color). On these plots, the black curves represent the mean number of rockfall per day (and respectively, the mean seismic energy released per day) for ranges of precipitation amount (taken every 5mm). On the right, the dot curves represent the proportion of rockfall events (and respectively, the mean seismic energy released per day) with respect to the effective precipitation (or cumulative effective precipitation). The plain curves correspond to the proportion of days where the seismic monitoring system was active for each range of effective precipitation (or cumulative effective precipitation).

Table 4.3: Values of the Kendall correlations and p-values estimated between rockfall and meteorological observation: Effective precipitation (P_{eff}), daily rainfall, air temperature, daily air temperature gradient, slope velocity and ground water level (g.w.l)

	Peff	Rainfall	Temp	Temp. grad	Velocity		G.w.l		G.w.l	
					B	C	B	C	B	C
C_K	0.2982	0.2931	0.0377	-0.2172	0.0392	0.0950	0.1098	0.1026	0.0531	0.0307
p-value	$2.7566\ 10^{-17}$	$1.6209\ 10^{-17}$	0.2180	$1.3147\ 10^{-12}$	0.2100	0.0026	$0.3493\ 10^{-3}$	$0.8177\ 10^{-3}$	0.1087	0.3367

Slopequake

We expect slopequakes to be associated to the slide motion, we calculated correlation with the displacement recorded by the two GPS stations. The Super-Sauze landslide movement being strongly influenced by hydrological variations (Malet et al., 2005, Bernardie et al., 2015), we also analyzed the correlation between slopequake occurrences, rainfall rates and ground water level (g.w.l.).

For the slopequake rates, the Kendall correlation is significant for the effective precipitation, the rainfall rates, the displacement rate at GPS-C, and the ground water level. The correlation is not significant for the air temperature, the displacement rate of GPS B and the ground water level variation (p-value > 0.1; Table 4.3). A significant correlation is found for temperature gradient, displacement rate at GPS-C and the ground water level (Table 4.3).

Slopequakes are recorded at the same time of the rain episodes (time delay = 0; Figure 4.8a). The relaxation time tc_2 is longer (tc_2 = 41 hr; Figure 4.8b) than for the rockfalls (tc_2 = 17 hrs). An anti-correlation is found between slopequakes and temperature gradient (Figure 4.8d) like for the rockfalls. As slopequakes are well correlated to effective precipitation, the decrease of the temperature during rainy days should explain this negative correlation. A very weak correlation is found with the GPS displacement (Figure 4.8e,f). The correlation with the ground water level is weak ($C_K < 0.11$). The time delays are large for both displacement rates (GPS-B: 35 days; GPS-C: 50 days).

The seismic energy released in function of the displacement rate does not show clear trend (Figure 4.9a). However, around 50% of the seismic energy as well as 50% of the seismic events occurred during days where no displacement is measured (Figure 4.9a). This proportion is slightly lower for GPS-B than GPS-C. The latter shows slower velocity and smaller cumulative displacement; consequently more slopequakes are occurring during the periods of low velocity ($v < 0.001$ m.day^{-1}). The seismic energy of the slopequakes is slightly larger when the groundwater level is above its average level but a larger number of events occur during the periods when the G.w.l is below its average (Figure 4.9b). Low G.w.l seem to be associated to numerous and weak seismic while high G.w.l seem to be associated to less frequent by more energetic sources.

4.5.3 Analysis of the spatio-temporal distribution of seismic sources

Rockfall

Rockfalls are mainly located on the main scarp and few events occur on the secondary scarp (Figure 4.10). From the temporal analysis of the location, we observe that the activation of these different zones changes through time (Figure 4.10). Indeed, at the beginning of the acquisition period (i.e October and November 2013), the recorded rockfalls are mostly located on the western part of the main scarp. This observation is consistent with the rockfall dynamics measured with LiDar during summer 2013 (Stumpf et al., 2013). In the rest of the acquisition period the rockfall crisis occur principally in the eastern part and the center of

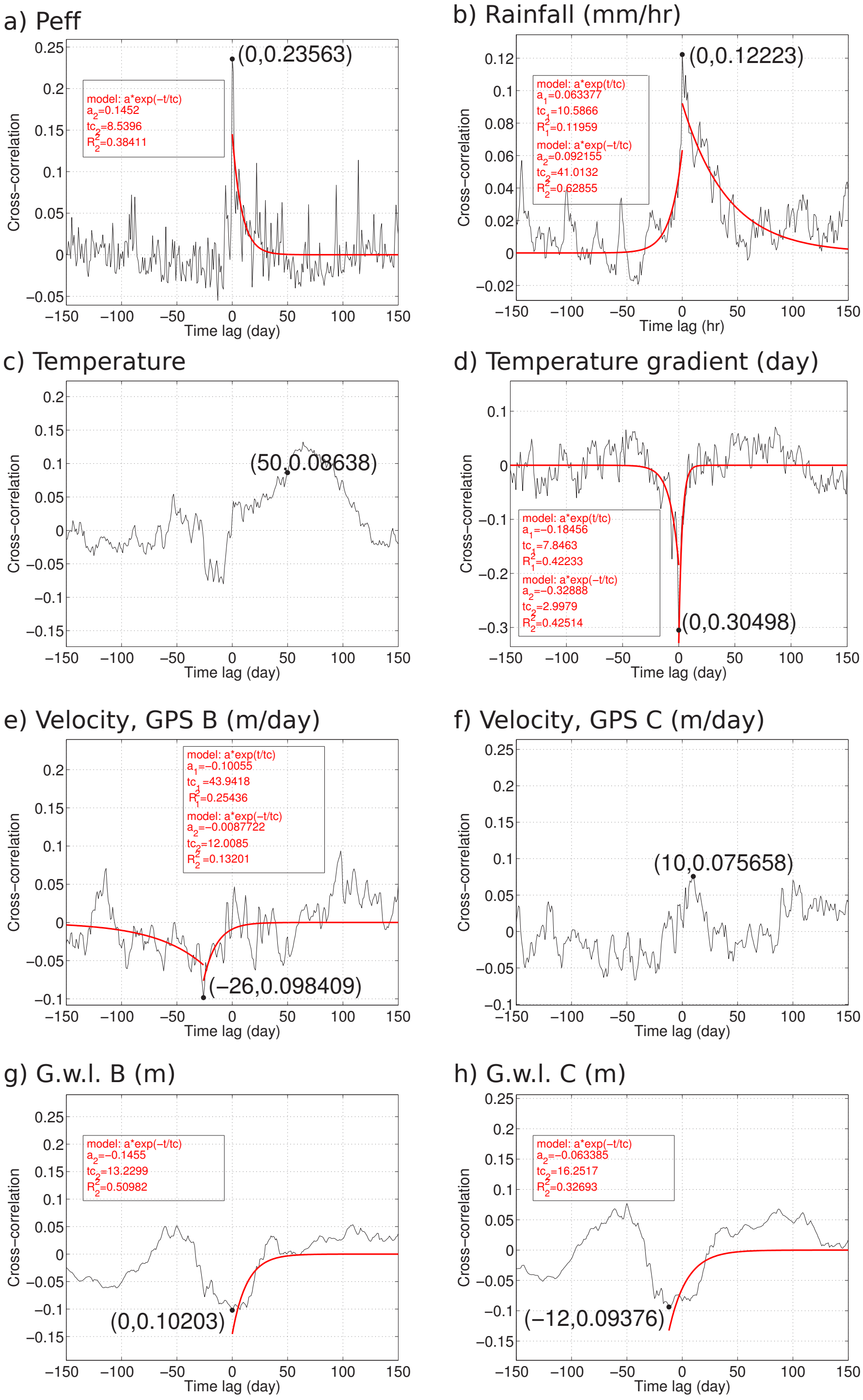

Figure 4.8: Cross-correlation between the rate of slopequake and a) daily effective precipitation (P_{eff}), b) hourly rainfall rate, c) air Temperature and d) daily air temperature gradient, e), f) slope motion expressed in terms of velocity at GPS-B and GPS-C, ground water level variations measured by piezometers B g), and C h). See Figure 4.6 for figure description.

a) Displacement rate

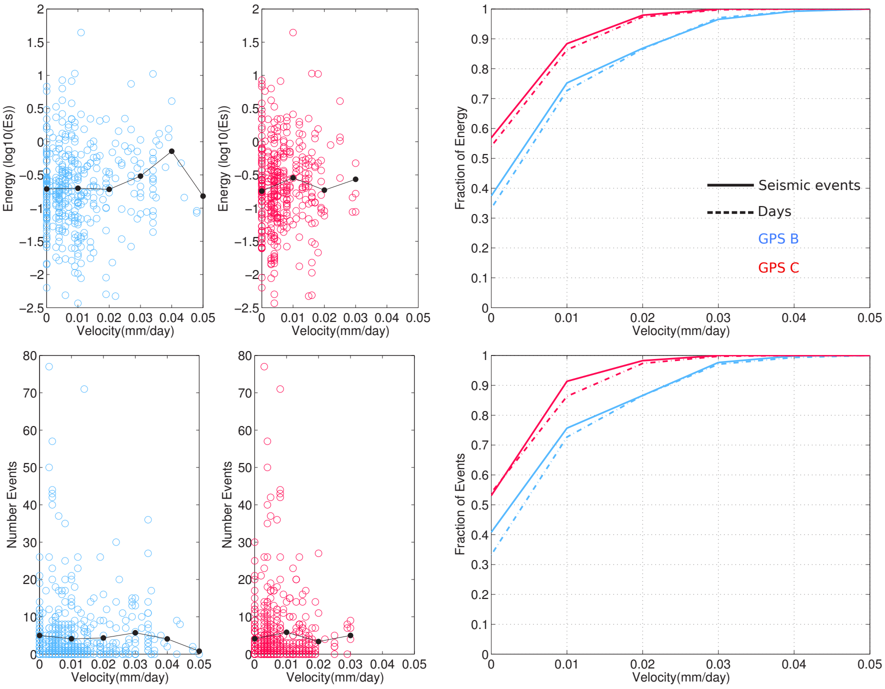

b) Ground water level

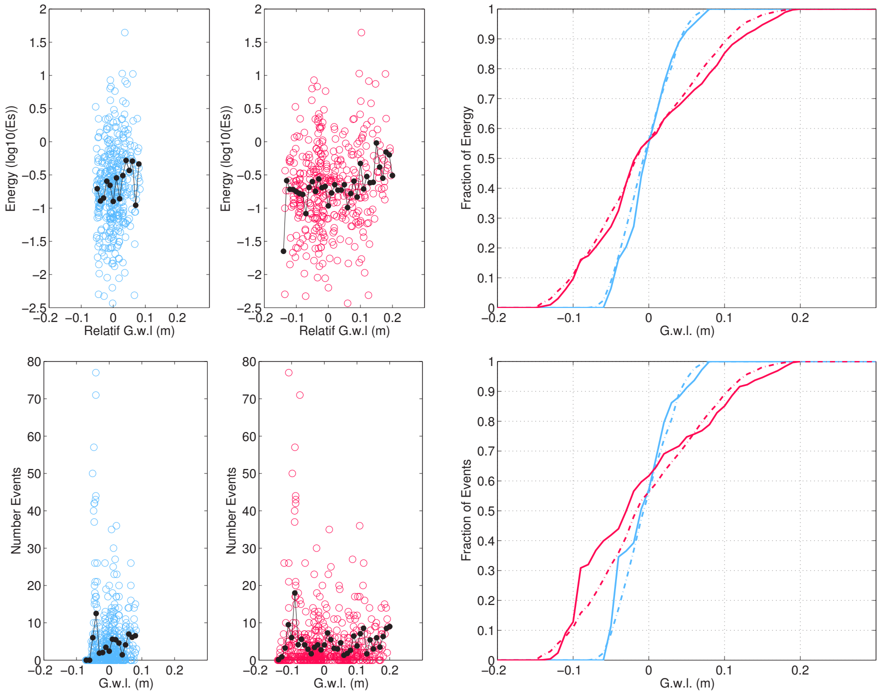

Figure 4.9: Number of slopequake per day and mean seismic energy release per day as a function of a) effective precipitation and b) cumulative antecedent effective precipitation (computed on the last 10 days) cumulative precipitation. See Figure 4.7 for figure description.

the main scarp (Figure 4.10). Very few rockfall are located in the secondary scarp during the large rockfall crisis occurring in spring and autumn. We observe that during summer time, rockfalls are located in the secondary scarp (Figure 4.10, summer 2015). During this period the activity of the main scarp decrease and we do not observe cluster of events.

The absence of rockfall in the secondary scarp during spring and autumn time can be explained by the fact that the rainfall episodes are much stronger during autumn hence increasing the level of seismic noise and decreasing the sensitivity of the seismic sensors to detect small rockfalls. The rockfalls occurring on the secondary scarps have smaller volume and do not fall from a high scarp hence releasing weak seismic energy so they can only be recorded when the seismic noise level is low.

The attenuation of the seismic waves with distance also implies that rockfall of small volume are not detected if occurring at large distance to the seismic network. Although the noise level is lower during summer time, it would be possible that the volume of the rockfall occurring on the main scarp decreases and is not detected by the permanent seismic network.

The rockfall activity is clustered in very few days and up to 110 events can be recorded in one day during spring time. We record the largest number of rockfall per day during spring 2016. During this period, the precipitation are significantly low (< 20 mm.day^{-1}) compare to autumn (> 25 mm.day^{-1}). This can be explained by the fact that snowmelt contributes to mobilize a larger volume of rocks and contributes to the fact that the number of rockfall is weakly proportional to the rainfall rate and to the cumulative rainfall (Figure 4.6).

Slopequake

The slopequakes location are spread on all the location gridsearch area with a cluster of events located at the vicinity of seismic array A (Figure 4.5b). To compare the slopequake activity to the GPS motion and Ground water level variations we only consider the slopequakes clustered in the central part of the slide (Figure 4.11). The slopequakes are mainly located on western border of western mudflow at the vicinity of GPS B. Some slopequakes also occur on the central part and on the eastern border of the eastern mudflow.

Despite the weak correlation of the slopequake occurrence with the displacement, different temporal clusters of slopequake events are identified. The first family of increase of slopequake rates occurs before slope accelerations of GPS-B (Figure 4.11, in blue and gray). These acceleration are associated to an increase of the ground water level (Figure 4.11 in blue) while few acceleration occur during a decrease of the ground water level (Figure 4.11 in gray). It suggests that seismic precursors can be recorded before the main accelerations of the slope ($v > 0.01$ m.day^{-1}). The slopequake rate increases during the slope acceleration but we record a small number of events per day (< 40) preventing us to observe decrease of the recurrence time and an increase of the amplitude during the slope acceleration. The second family of slopequake clusters occur during the deceleration of the slope (Figure 4.11, in red). They are always simultaneous with the ground water level decrease and occur after the first family of cluster. Between the two families of slopequakes increase, we observe a drop of slopequake rate as the slope velocity is constant and the ground water level reaches a local maximum.

Very high slopequake rates are recorded during the lower ground water levels (October-November 2013 and January 2016). In November 2013, the seismic signals are located along the western stream (Figure 4.12) and maybe generated by single block impacts due to the stream activity. In January 2016, the slopequakes are recorded at the vicinity of the main scarp (Figure 4.12) and maybe rather generated by fracture located in the main scarp or very

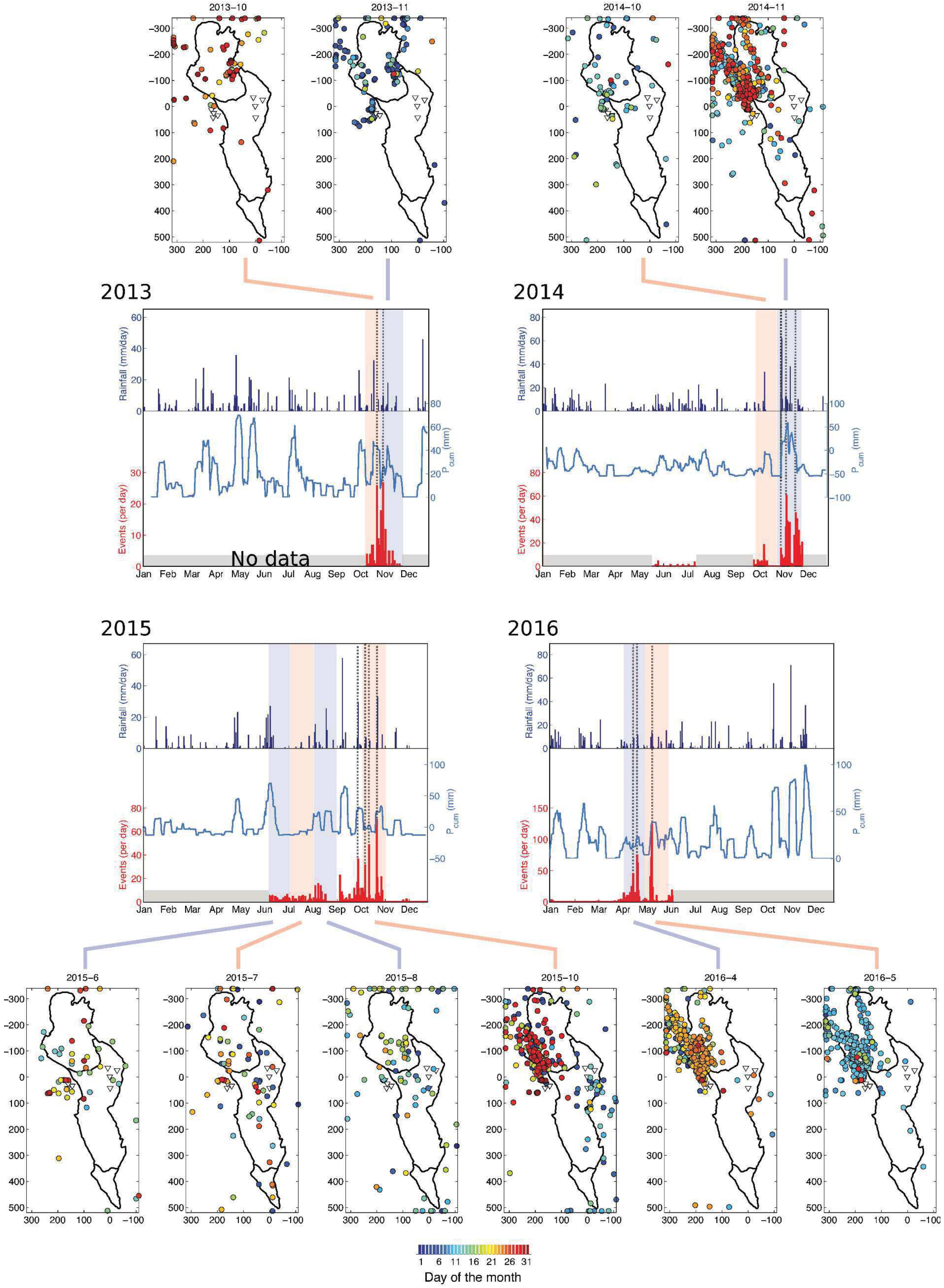

Figure 4.10: Rockfall occurrences in space and time. The number of rockfall per day is plotted for each year of the acquisition period together with daily effective rainfall rate and cumulative effective rain. The location maps of the seismic sources are presented.

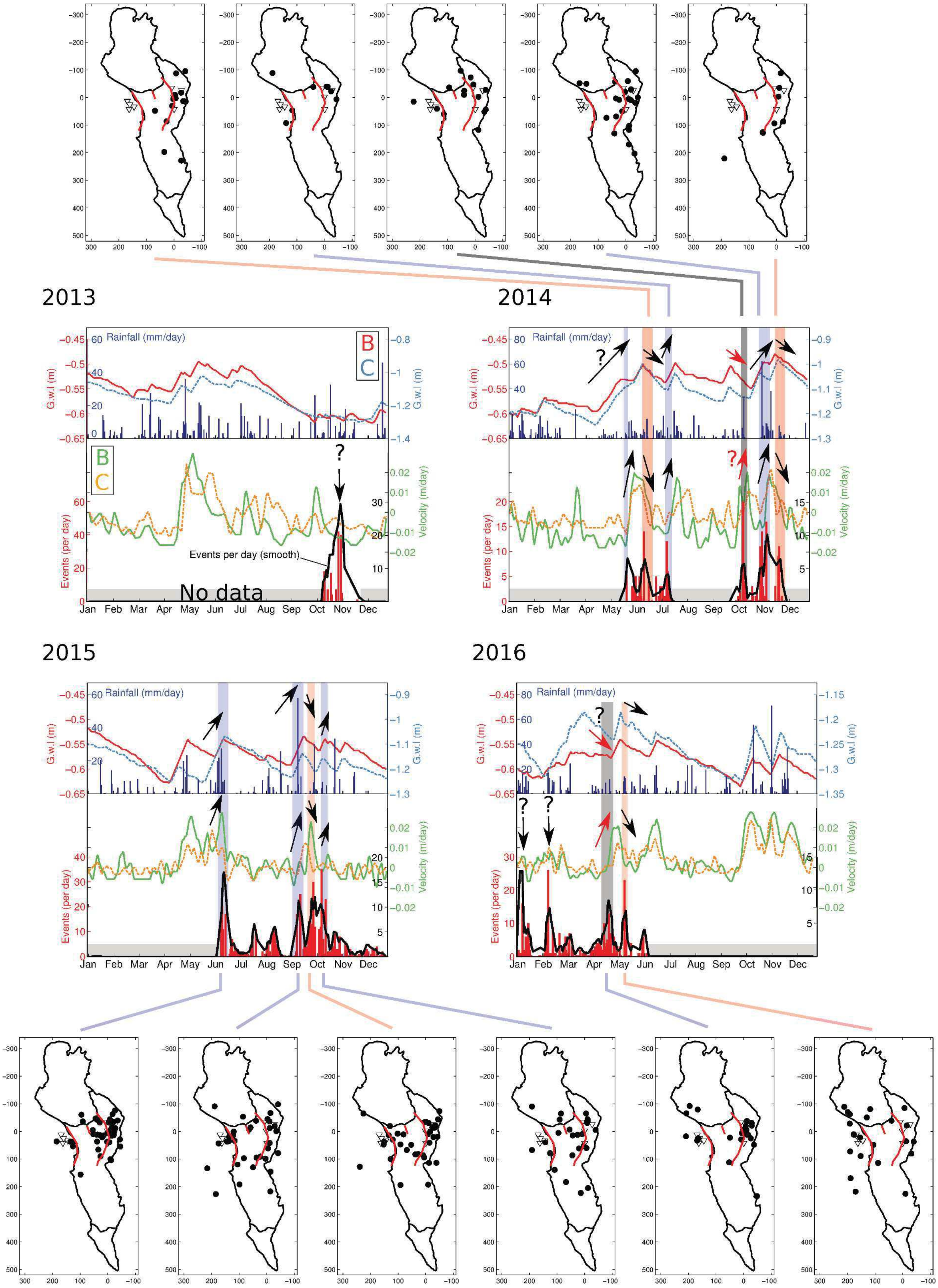

Figure 4.11: Slopequakes occurrence in space and time. The number of slopequake, the smoothed number of slopequakes is plotted for each year of the acquisition period together with daily effective rainfall rate, the smoothed velocity per day and the ground water level variations. The location maps of the seismic sources are presented. The smoothed time series are computed taking the average on a 7 days sliding window.

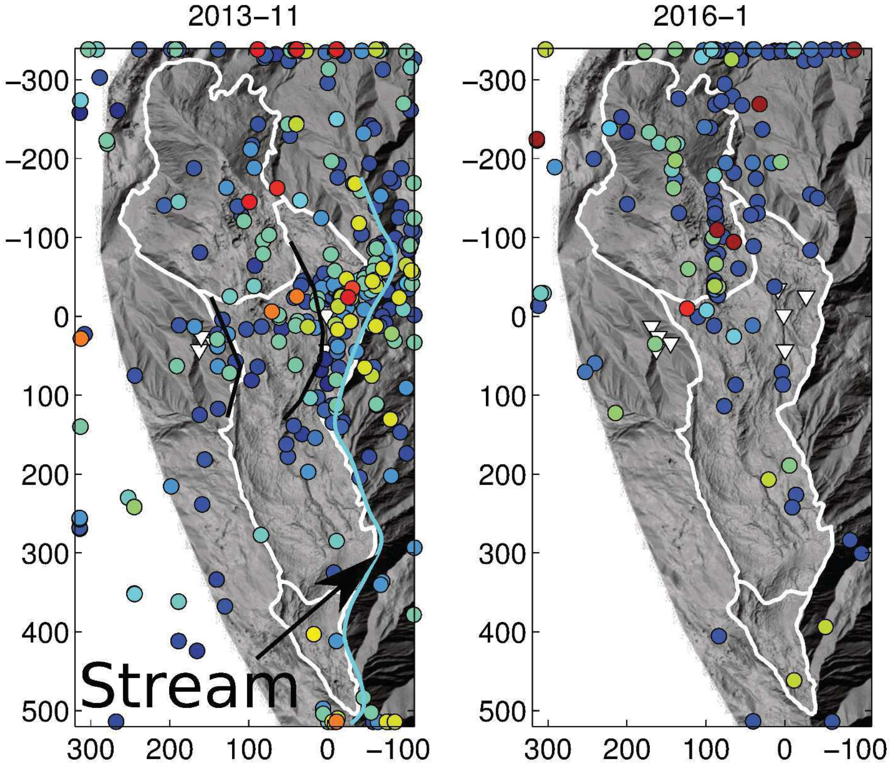

Figure 4.12: Location of the slopequakes recorded in November 2013 (left) and January 2016 (right).

small rockfall or granular flows sources.

4.6 Discussion

The locations of the rockfall are coherent and clustered on the main scarp while the location of slopequakes are spread over the slide. We analyzed the distribution of the sources in order to evidence possible space and time patterns of seismic activity, hydro-meterological forcings and landslide motion. We show that rockfalls are correlated to rainfall rate with a nearly immediate activation of the sources during rain episods. The rockfall activity is slightly delayed (2 hours) from the rainfall which could be explained by the time needed to infiltrate water in the scarp. The relaxation time is very short for rockfalls (16-17 hours) meaning that rockfall activity stops rapidly after the end of the rain event. Moreover, most of the rockfall activity occurs only over a few days of the year during the spring and autumn periods with up to more than 80 rockfalls events per day due intense rain in autumn (> 25 mm.day^{-1}) and snowmelt in spring. We observe very few rockfalls during winter time and could not correlate any rockfall occurrence to freeze-thaw cycles partly because the seismic acquisition stopped during most of the winters. We further identify a negative correlation with the temperature gradient which can be explained by the decrease of daily temperature amplitude during rainy days as suggested by Helmstetter and Garambois (2010). The spatial pattern of rockfall locations has changed during the acquisition period from the eastern part of the main scarp at the beginning of the acquisition to the western part of the main scarp during the rest of the acquisition. Rockfall volumes are estimated between 10^{-2} and 10^{2} m^{3} which is coherent with field observations. Due to the numerous gaps in the data acquisition we cannot compute the total eroded volumes for the four years of acquisition.

We find a significant correlation between rainfall and slopequakes. The slopequake activity starts immediately with the rainfall events but the time of relaxation is longer (41 hours) than for the rockfalls reflecting a more complex hydro-mechanical response of the slide motion to precipitation. No correlation among the slide velocity and the slopequake rate is found if we consider the whole time serie. However, we observed repetitive cycles of seismicity associated to: 1) an increase of the slopequake rate corresponding to an increase of the g.w.l triggering the acceleration of the slope, 2) followed by a steady-state movement where the g.w.l reaches a local maximum and no seismic sources are recorded and 3) a decrease of the g.w.l. with a simultaneous decrease of the slide velocity when a new increase of slopequake rate is recorded (Figure 4.10). The presence of these cycles explains the weak correlation as increases of slopequake rates may be associated to acceleration and deceleration of the slope. We observe hence two type of relationships between the slide velocity and the slopequake rate (Figure 4.13d and e,f). The first one corresponds to the expected relationship where the slopequake rate increases with the slope velocity (Figure 4.13d). This relationship is commonly observed in laboratory experiments (Smith et al., 2017, Amitrano and Helmstetter, 2006) and in the field when acoustic emission sensors are installed at the vicinity of the shear surface (Amitrano et al., 2005, Smith et al., 2014, Dixon et al., 2015). In our dataset, we also observe a second type of relationship between the slopequake rate and the slope motion (Figure 4.13b, c). This phenomenon could be explained by the fact that a threshold in ground water level is reached, acceleration of the slide motion starts but the moisture content of the slope remains sufficiently low to generate seismic signals at the surface. With the increase of ground water level, the friction decreases reducing the generation of brittle seismic events. The slide velocity is constant or is slightly decreasing during these periods. Then the slide rapidly decelerates as the ground water level decreases hence increasing again the friction and the slopequake rates. Another possibility would be a the transition of the clay from brittle to ductile behaviors as the ground water level increases (Iverson, 1997, 2005, Picarelli et al., 2004).

It must be noted that comparing the slopequake rates and the time series of slope motion and ground water levels is difficult as slopequake locations are distributed over the landslide area while the GPS and piezometers are local sensors representative of a small portion of the slide. We observe that the slope acceleration is slightly delayed for the two GPS stations. Consequently, some increase of the slopequake rates, which are not well correlated with the current measure slope acceleration, may be associated to the acceleration of another part of the landslide. Spatial measures of the displacement field at high temporal frequency is now possible from LiDAR or Ground-based Interferometric radar (Jaboyedoff et al., 2012, Caduff et al., 2015). This set of acquisition will allow associating better the slopequake occurrences. The catalog of slopequakes could also be refined by using matching filter processing to find repeaters. Increase of the number of seismic sensors on the slope could also be a perspective to improve the location accuracy and decrease the magnitude of completeness of the seismic network.

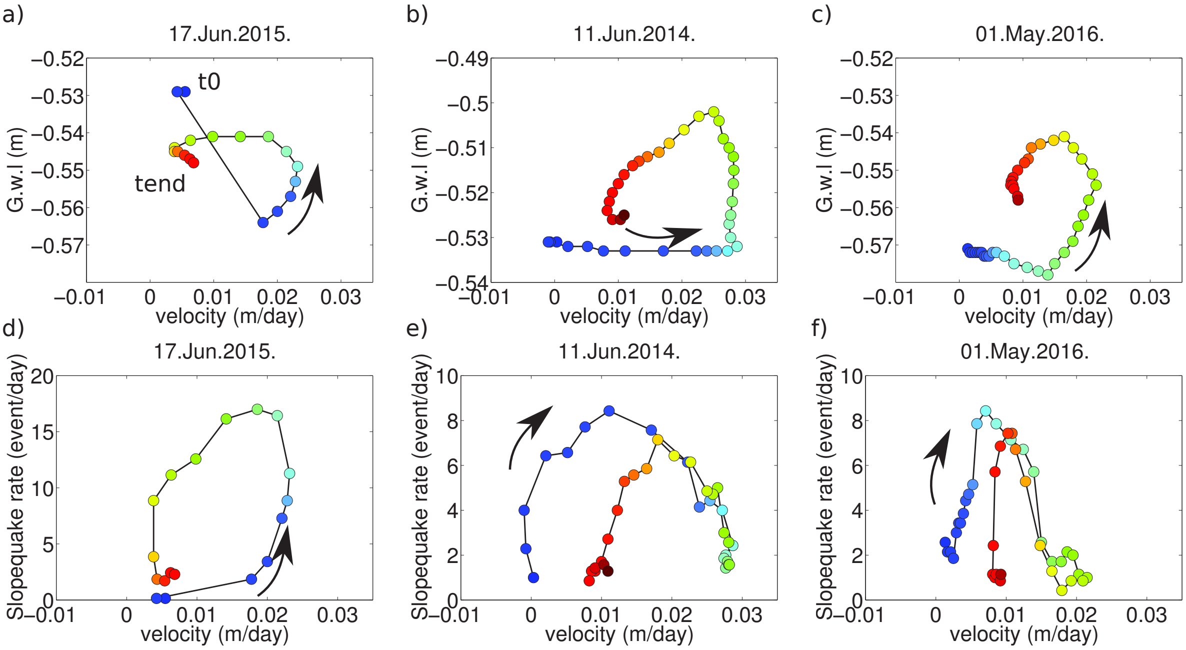

Figure 4.13: Ground water level as a function of slope velocity for three acceleration/deceleration periods: a) 17 June 2015, b) 11 June 2014 and c) 01 May 2016. The daily slopequake rate (smoothed) as a function of slope velocity for three acceleration/deceleration periods are presented: d) 17 June 2015, e) 11 June 2014 and f) 01 May 2016.

4.7 Conclusion

We analyzed the seismic signals generated by the activity of a clayey landslide. A methodology is developed to process long seismic datasets and applied to the data recorded at the Super-Sauze landslide. Advanced catalogs of endogeneous seismicity including the location of the sources are created. Two family of seismic signals are studied: rockfalls and slopequakes. Seismic monitoring allow us to identify variations in the location of the rockfall throughout the period of acquisition. Rockfall occurrences are clustered during few days of high activity in Spring and Autumn periods and are associated to hydraulic forcings (i.e. precipitation and snowmelt). We observe an increase of the slopequake rates before all the acceleration of slope. We also identify cycles of slopequake occurrences associated to acceleration and deceleration of the slope. A decrease of the slopequake rates is observed when the slope velocity becomes constant after the acceleration phase during local maximums of the ground water level. These results demonstrate that seismic monitoring provides valuable information to understand the response of gravitational instabilities to hydro-mechanical forcings and on the mechanical deformation of the slope.

Synthesis of the research findings on the analysis of the patterns of micro-seismicity in relation with landslide motion and hydro-meteorological forcings:

Main results: Investigation of the seismic catalogs realized for rockfalls and slopequakes enables to observe patterns of seismic occurrences in space and time. We observe a significant correlation between landslide endogenous seismic sources and daily effective precipitation and hourly rainfall rate. Rockfall activity initiates with rainfall and rapidly ceases as the rain episodes stop. Consequently, the number of rockfall per day can be large (> 80 events per day) during few days of the year. The periods of rockfall activity are clustered in the Spring and Autumn seasons. The zones affected by rockfall vary during the acquisition period. The main scarp is highly active during Spring and Autumn time while the lower part of the landslide is more active during summer time.
Slopequakes are also correlated to daily effective precipitation and hourly rainfall rate but a longer time of relaxation is observed (41 hours). We do not observe significant correlation between slopequake rate and slope motion when considering the whole time series. However, we observe an increase of the slopequake rates for all the main accelerations of the landslide (> 0.01 m.day^{-1}). The slopequake rate decreases as the slope reaches a constant velocity and the ground water level a local maximum. An increase of slopequake rate is also observed during slope deceleration. These results suggest that the rate of slopequakes is not continuously increasing with the the slope velocity and that soil water content (e.g. degree of saturation) controls the relation between seismic emissions and slope motion.

Perspectives: As discussed in Chapter 1, a large variety of signals are gathered under the term “slopequake”. The next step will be to refine the catalog of slopequakes to investigate the signal properties associated to slope motion and soil water content. Matching Filter processing could be used to verify if repeaters are also generated during the acceleration and deceleration periods and analyze their distribution (i.e. seismic energy and recurrence time). The location of these sources could also be improved using either the APOLoc method helping associating the recorded signals to geomorphological features. The volume loss due to rockfalls could also be estimated and compared to the geodetic measures in order evaluate the robustness of seismic monitoring to quantify short-term erosion rates. Additional observations at different sites are needed to confirm if slopequakes can be considered as a robust precursory signals to slope acceleration and to analyze the influence of soil water content on the rate of generated seismic signals. The non-linear relationship between slope velocity and slopequake rates could be also confirmed by experimental studies.

CHAPTER 5| Conclusion and perspectives

5.1 General conclusion

Understanding the hydro-mechanical properties controlling slope failure or slide acceleration is needed to improve models and forecasts of gravitational instabilities. This requires to measure directly or indirectly the variations of the geo-mechanical properties of the slopes in response to internal and/or external forcings in space and time. Our research aimed at improving our knowledge of these relationships through the analysis the landslide endogenous micro-seismicity. Our work consisted in developing generic and automatic processing tools to construct advanced seismicity; the tools have to be adapted to the specific conditions imposed by highly heterogeneous and attenuated medium

A large variety of landslide endogenous seismic signals have been documented. We thus proposed in **Chapter 1** a standard typology of the seismic signals generated by gravitational instabilities. The different families were constructed from the quantitative evaluation of different signal features allowing to compare signals from different sites and build homogeneous catalogs. The analysis of several datasets representative of the diversity of landslides demonstrated the existence of similar seismic signals for different sites. It enables us to propose and discuss the possible sources mechanisms associated to each family of signals.

Chapter 2 aimed at developing a fully automatic classification method of seismic signals using machine learning techniques. We proposed and implemented a supervised classification method of seismic signals based on a the calculation of a large number of signals features and on the *Random Forest* algorithm. We applied and tested the method on the seismic datasets of the Super-Sauze landslide. We obtained a good rate of correct classifications and a selection of the relevant features to discriminate the classes. We show that this sensitivity is equivalent or even larger than human sensitivity. The sensitivity depends on the number of examples used in the training sets. Introducing a large number of examples improved the value of the sensitivity.

Chapter 3 focuses on the construction of advanced catalogs integrating the location of the seismic sources. We developed an automatic seismic source location method adapted to the context of clayey landslides. Our method is based on the inter-trace correlation of the P-wave arrivals, the use of realistic P-wave velocity models from seismic tomography and the use of the Amplitude Source Location as prior information. We demonstrate the importance of the picking resolution on the location accuracy and implemented an iterative strategy to optimize the quality of the initial picks. We also show the importance of determining a priori information on the location based on the signal. Finally, we demonstrate that the use of a realistic velocity model of the underground structure is crucial to obtain accurate locations. We tested our methodology on calibration shots and obtained epicenter errors of 27±29 m which is better than previous approaches used for similar contexts. The method is well adapted to locate slopequakes occurring inside the seismic network but likely fails to locate most of the rockfall events located at far distances from the seismic sensor and outside the velocity model.

We further use the typology of Chapter 1 and the classification methodology developed in Chapter 2 to build a catalog of seismicity for the Super-Sauze seismic observations. **Chapter 4** presents the analysis of the patterns of seismic signals in time and space in relation to hydro-meteorological forcings and slope motion. We found that the number of rockfall and slopequake seismic sources is correlated to precipitation with different relaxation times. While the rockfall seismic sources are concentrated over few days during Spring and Autumn, the slopequake seismic sources present longer relaxation time traducing a complex hydro-mechanical response of the slide. Analysis of the time series allows us to distinguish cycles of increasing slopequake rates associated with the acceleration and the deceleration of the slope motion. We also observed that the slopequake rate decreases between the acceleration and deceleration phases at the moment the ground water level reaches a local maximum. This pattern of seismicity may be explained by the variation of the friction on the sliding surfaces controlled by pore water pressure. Another explanation would be a brittle to ductile transition of the deformation due to changes of water content (degree of saturation) in the clay. This preliminary result, if confirmed by further investigation of the catalog, might bring new insights in the mechanical deformation of the clayey landslide confirming the interest of seismic monitoring for landslides. It must also be noted that accelerations occurring during ground water level decrease were also preceded by slopequake increase making seismic monitoring a potential method to record precursors of the deformation.

5.2 Perspectives

Findings of our research give rise to new questions and perspectives

1 *How to improve the classification methodology to enable the construction of* ***generic catalogs of landslide seismicity*** *in order to enable further comparison of signals from different sites?*
The classification methodology was developed and tested successfully for the classification of seismic signals generated by volcanoes (local scale) (Maggi et al., 2017, Hibert et al., 2017c) and for the detection of large landslides (regional scale). These tests were realized using several years of seismicity to build the training set implying large variety of signal examples for each classes and a well constrained overview of the signals generated in these contexts. In the case of landslide endogenous seismicity, long and exhaustive catalogs remain seldom. As the classification highly depends on the training set, the choice of the signals must be made carefully to represent the diversity of seismic signals. The latter may be challenging in particular for short monitoring campaigns where rapid changes in daily seismicity can be observed. Construction of a general training set from different sites or the use of synthetic signals may be tested and evaluated to overcome this issue. Implementation of unsupervised classifier is also a possible way of development to improve the determination of classes of seismic signals occurring on landslides and possibly to detect changes in the seismic signals generated by slope instabilities.

2 *How to further improve the location algorithm by taking into account the **heterogeneity of the underground structure** and possibly implement joint inversion of the different part of the seismic signals?*
We show that taking into account the heterogeneity of the underground structure and the use of different part of signals (ASL and P-wave location) improved the accuracy of the source location. Joint inversion of the location of the P-wave picking, ASL and surface wave picking could be a strategy possibly adapted to the diversity of the properties of the recorded seismic signals. Realistic models of the inelastic attenuation coefficient (Figure 5.1) and of the surface wave velocity can be constructed from inversion of the seismic profiles as well. This strategy should enable to better adapt the location processing to the signals features. However, more work must be realized to estimate the uncertainties associated to velocity models in particular 3D velocity models.

3 *How to improve the **design of landslide monitoring** in order to link the variations of the hydrological regime of the slide, the surface motion and the occurrence of seismic signals in space and time?*
Landslide seismic monitoring is very challenging due to the difficult accessibility of the slopes, their rapid evolution that constrain the spatial location of instruments only on stable slopes, thus limiting the sensitivity of the detection and location. This usually leads to non-optimal seismic network geometry. Moreover, the setup of several sensors is needed to detect and locate the internal seismic sources due to their weak energy. The recent development of wireless seismic sensors (Fairfield nodes) or cheap seismometers (Raspberry Shake) present significant advantages to increase the number of instrumented sites and/or the density of the seismic networks. Simultaneous measures of the surface displacement and the ground water level at high space and time resolution are needed to associate the seismic signals to landslide deformation. The use of Ground-based interferometric radar (GB-SAR) as well as LiDAR can provide a distributed measure of the surface displacement a high temporal resolution (> 3 minutes). This kind of campaign was realized during our PhD thesis at the Super-Sauze, the Pechgraben (Austrian Alps) and the Pas-de-l'Ours (French Alps) landslides (Figure 5.2). This kind of maps would help to associate the recorded seismic sources to co-localized deformation improving the comprehension of the sources mechanism.

Comparative analysis of the recorded seismic signals on different sites is also needed to better understand the recorded seismic signals, in particular, in order to confirm the presence of precursory seismic signals before slope failure or acceleration. This work has started for the Pechgraben landslide where both a GB-SAR and a seismic network has been installed during two months. Preliminary results show the same cycle of seismicity during acceleration and deceleration of the slope (Figure 5.3). We also monitor the Pas-de-l'Ours landslide' with four seismometers and several geodetic measurements. The landslide underwent several periods of acceleration with the development of a complex deformation field. This dataset could allow us to investigate the difference between the seismic signals generated during the tertiary creep and its progressive evolution toward landslide failure.

Estimation of the volume loss could also be computed for both geodetic and seismological measures allowing to compare the two estimations and provide natural dataset to validate the physical laws developed recently for rockfalls (Farin et al., 2014, Hibert et al., 2017a).

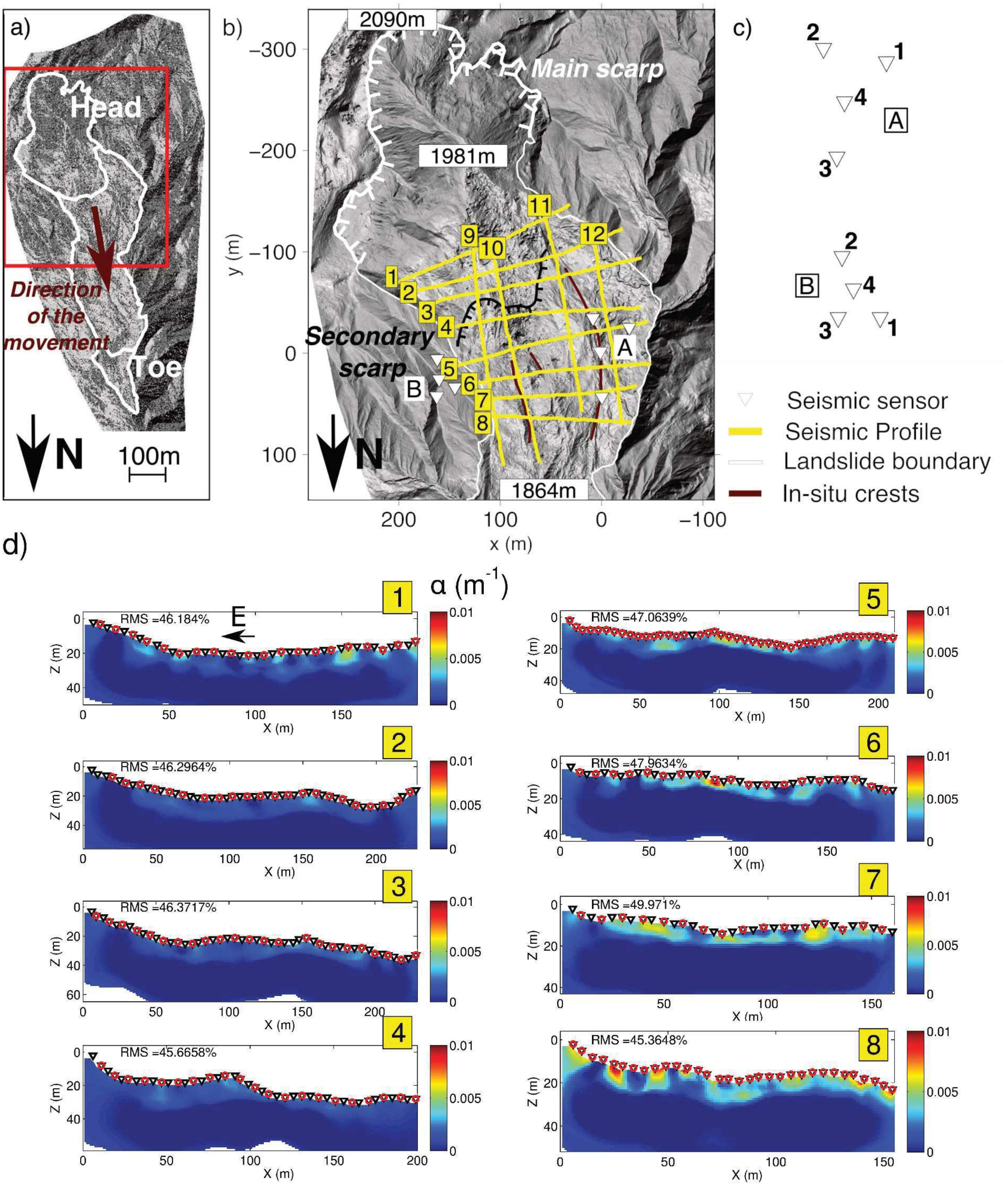

Figure 5.1: Inversion of the inelastic attenuation coefficient for P-wave propagation at the Super-Sauze landslide a),b),c). The inversion for the seismic profiles (1 to 8) are presented in d). The attenuation coefficient is inverted using the wavepaths computed from the P-wave velocity inversion Gance et al. (2012) used to built the 3D velocity model. The results are in good agreement with the values found in Chapter 3, with a low attenuation in the upper part of the landslide (Profiles 1-4) and higher values in the lower part of the landslide (Profiles 5-8).

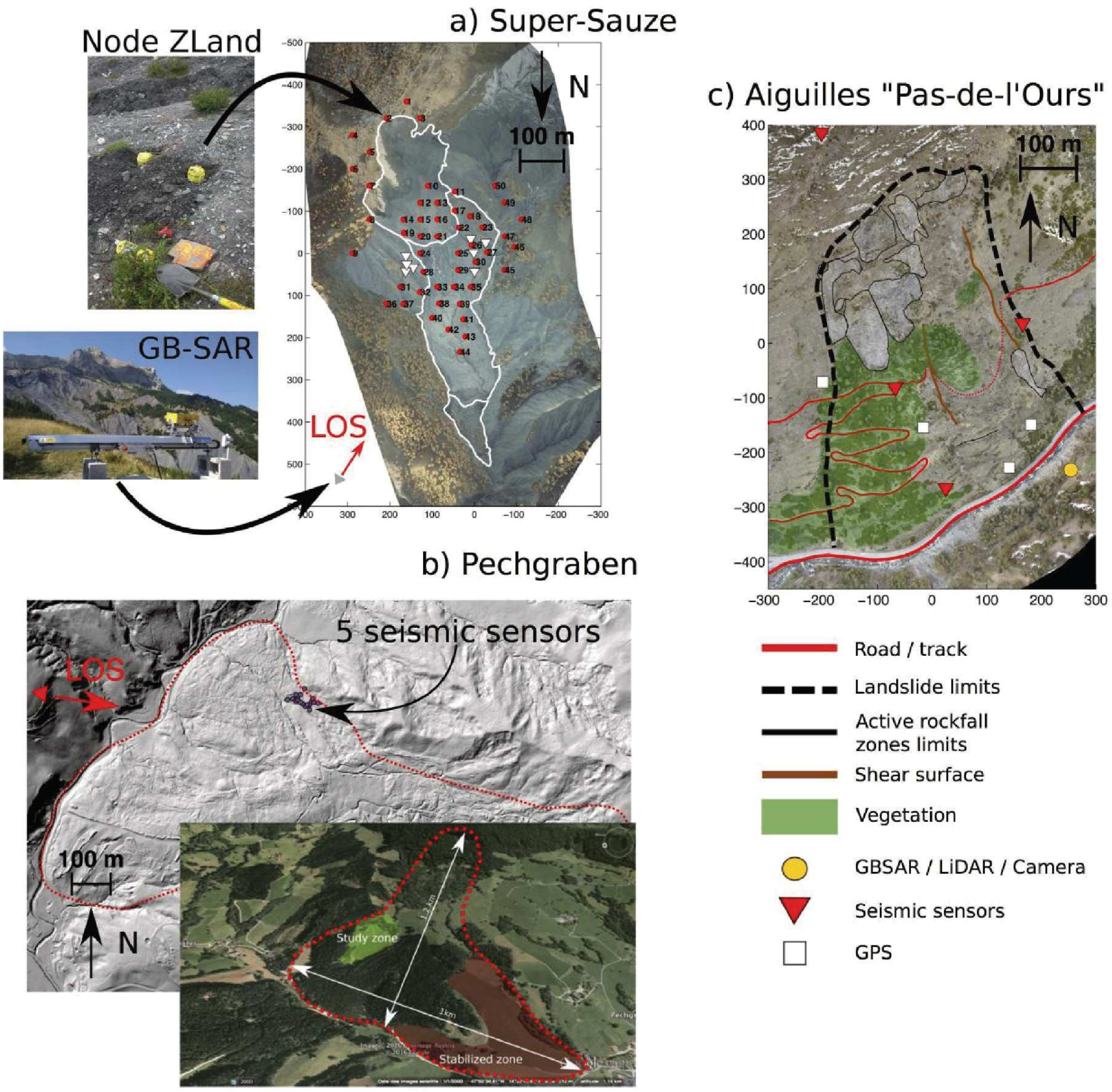

Figure 5.2: Monitoring campaigns realized at the a) Super-Sauze landslide (Southeast French Alps), b) Pechgraben landslide (Austria) and c) Aiguilles / Pas-de-l'Ours landslide (Southeast French Alps). At the Super-Sauze landslide, 50 portable seismometers (Fairfield Nodes) have been installed together with a GB-SAR during June-July 2016. At the Pechgraben landslide, one broadband seismometer and one seismic arrays of short-period seismometers have been installed on the most active zone as well as a GB-SAR during November-December 2016. At the Aiguilles / Pas-de-l'Ours landslide, numerous instruments have been installed in order to follow its evolution. Among them, four broadband seismometers, a GB-SAR, and 4 GNSS stations are permanently monitoring the landslide activity since May 2017.

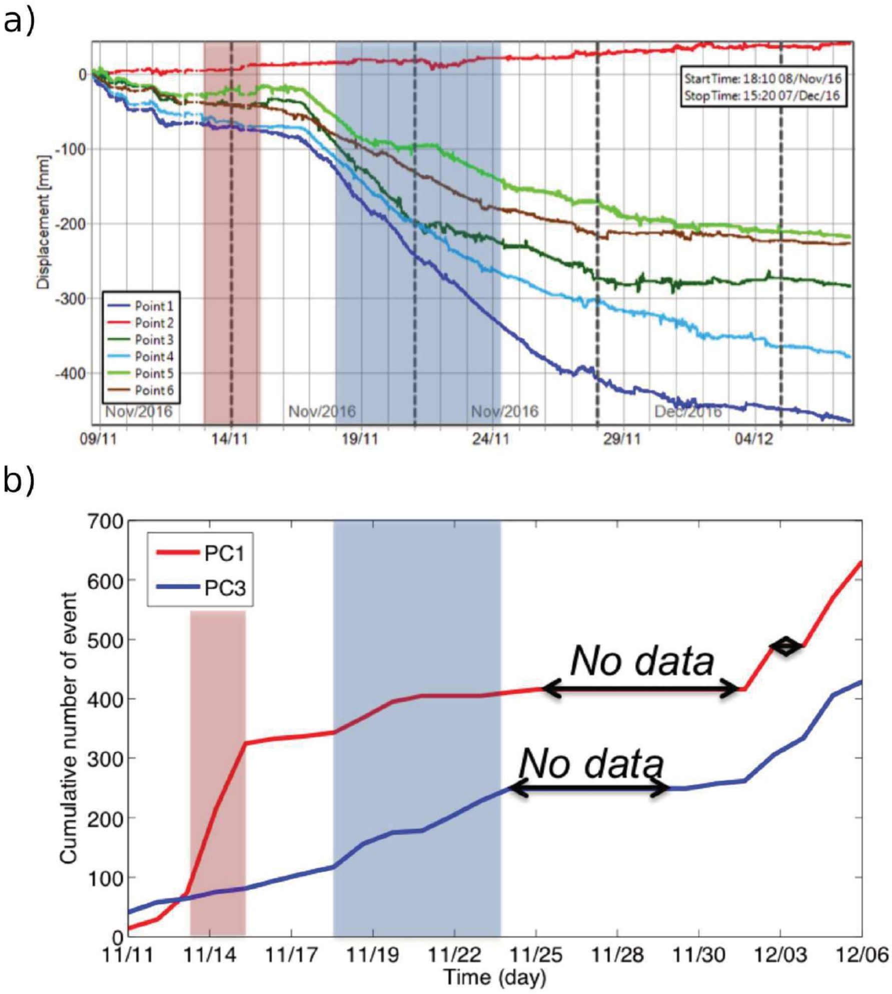

Figure 5.3: Time series of displacement (top) and slopequake (bottom) recorded at the Pechgraben landslide (Figure 5.2) during November-December 2016. An increase of the slopequake rate is observed at seismometer PC1 two days before the acceleration of the slope. The slopequakes decreases as the acceleration initiates and increases again as the velocity of the slope motion decreases at both PC1 and PC3 seismic sensors. Further investigation of this dataset in relation with the meteorological observation must be analyzed to confirm this observation.

4. *How to understand the sources of the seismic signals through* ***experimental studies****?*
   The origin of acoustic emissions generated by several types of landslide deformation mechanisms (creep, rupture, flow) for several hydrological conditions needs to be analyzed. Laboratory scale experiments (such as flume tests, (Okura et al., 2002, Olivares et al., 2009)) could be designed to record the seismic signals generated during the movement of the slope. This kind of experiments would enable to model several space and time variations of the stress-strain field for different rupture scenarios (i.e. water infiltration, loading mass, ground shaking), boundary conditions and initial rheology (i.e. media compaction, total solid fraction) and hence better understand the conditions to record seismic signals on clayey slides.

BIBLIOGRAPHY

Abancó, C.; Hürlimann, M., and Moya, J. Analysis of the ground vibration generated by debris flows and other torrential processes at the Rebaixader monitoring site (Central Pyrenees, Spain). *Natural Hazards and Earth System Sciences*, 14(4):929–943, 2014. doi: 10.5194/nhess-14-929-2014. URL `https://www.nat-hazards-earth-syst-sci.net/14/929/2014/`. 15, 28

Abancó, Claudia; Hürlimann, Marcel; Fritschi, Bruno; Graf, Christoph, and Moya, José. Transformation of ground vibration signal for debris-flow monitoring and detection in alarm systems. *Sensors*, 12(4):4870–4891, 2012. xvii, 15, 19, 28, 30

Aki, Keiiti and Chouet, Bernard. Origin of coda waves: source, attenuation, and scattering effects. *Journal of geophysical research*, 80(23):3322–3342, 1975. 80

Allen, Rex. Automatic phase pickers: Their present use and future prospects. *Bulletin of the Seismological Society of America*, 72(6B):S225–S242, 1982. URL `http://www.bssaonline.org/content/72/6B/S225.abstract`. 22

Allstadt, Kate. Extracting source characteristics and dynamics of the August 2010 Mount Meager landslide from broadband seismograms. *Journal of Geophysical Research*, 118(3):1472–1490, 2013. doi: 10.1002/jgrf.20110. 1

Allstadt, Kate and Malone, Stephen D. Swarms of repeating stick-slip icequakes triggered by snow loading at Mount Rainier volcano. *Journal of Geophysical Research: Earth Surface*, 119(5):1180–1203, 2014. ISSN 2169-9011. doi: 10.1002/2014JF003086. URL `http://dx.doi.org/10.1002/2014JF003086`. 2014JF003086. 22

Allstadt, K.E.; McVey, B.G., and Malone, S.D. Seismogenic landslides, debris flows, and outburst floods in the western United States and Canada from 1977 to 2017: U.S. Geological Survey data release. 2017. doi: https://doi.org/10.5066/F7251H3W. 42

Amitrano, D and Helmstetter, A. Brittle creep, damage, and time to failure in rocks. *Journal of Geophysical Research: Solid Earth*, 111(B11), 2006. doi: 10.1029/2005JB004252. URL `https://agupubs.onlinelibrary.wiley.com/doi/abs/10.1029/2005JB004252`. 108

Amitrano, D.; Grasso, J. R, and Senfaute, G. Seismic precursory patterns before a cliff collapse and critical point phenomena. *Geophysical Research Letters*, 32(8), 2005. ISSN 1944-8007. doi: 10.1029/2004GL022270. URL `http://dx.doi.org/10.1029/2004GL022270`. L08314. 11, 14, 60, 61, 88, 108

Amitrano, D.; Arattano, M.; Chiarle, M.; Mortara, G.; Occhiena, C.; Pirulli, M., and Scavia, C. Microseismic activity analysis for the study of the rupture mechanisms in unstable rock masses. *Natural Hazards and Earth System Sciences*, 10(4):831–841, 2010. doi:

10.5194/nhess-10-831-2010. URL `https://www.nat-hazards-earth-syst-sci.net/10/831/2010/`. 14

Amitrano, David; Gaffet, Stéphane; Malet, Jean-Philippe, and Maquaire, Olivier. Understanding mudslides through micro-seismic monitoring: the Super-Sauze (South-East French Alps) case study. *Bulletin de la Société Géologique de France*, 178(2):149–157, 2007. ISSN 0037-9409. doi: 10.2113/gssgfbull.178.2.149. URL `http://bsgf.geoscienceworld.org/content/178/2/149`. vii

Anthony, Lomax; Virieux, Jean; Volant, Philippe, and Berge-Thierry, Catherine. *Probabilistic Earthquake Location in 3D and Layered Models*, pages 101–134. Springer Netherlands, 2000. ISBN 978-94-015-9536-0. doi: 10.1007/978-94-015-9536-0_5. URL `http://dx.doi.org/10.1007/978-94-015-9536-0_5`. 23, 61, 63, 75, 81

Arattano, M.; Abancó, C.; Coviello, V., and Hürlimann, M. Processing the ground vibration signal produced by debris flows: the methods of amplitude and impulses compared. *Computers & Geosciences*, 73:17 – 27, 2014. ISSN 0098-3004. doi: https://doi.org/10.1016/j.cageo.2014.08.005. URL `http://www.sciencedirect.com/science/article/pii/S0098300414001915`. 15

Arattano, Massimo and Moia, Fabio. Monitoring the propagation of a debris flow along a torrent. *Hydrological Sciences Journal*, 44(5):811–823, 1999. 15

Arattano, Massimo; Covellio, Velio; Abancó, Claudia; Hürlimann, Marcel, and McArdell, Brian W. Methods of data processing for debris flow seismic warning. *International Journal of Erosion Control Engineering*, 9(3):114–121, 2016. xvii, 15, 30

Baillard, Christian; Crawford, Wayne C.; Ballu, Valérie; Hibert, Clément, and Mangeney, Anne. An automatic Kurtosis-`[U+2010]`based P`[U+2010]`- and S`[U+2010]`-phase picker designed for local seismic networks. *Bulletin of the Seismological Society of America*, 104(1): 394–409, 2014. doi: 10.1785/0120120347. URL `http://www.bssaonline.org/content/104/1/394.abstract`. 67

Baron, Ivo; Kernstocková, Marketa, and Melichar, Rostislav. Stress field reconstruction in an active mudslide. *Geomorphology*, 289:170 – 178, 2017. ISSN 0169-555X. doi: https://doi.org/10.1016/j.geomorph.2017.04.020. URL `http://www.sciencedirect.com/science/article/pii/S0169555X17301666`. Slope tectonics: inherited structures, morphology of deformation and catastrophic failure. xvii, 3, 4, 5

Battaglia, Jean and Aki, Keiiti. Location of seismic events and eruptive fissures on the piton de la fournaise volcano using seismic amplitudes. *Journal of Geophysical Research: Solid Earth*, 108(B8), 2003. ISSN 2156-2202. doi: 10.1029/2002JB002193. URL `http://dx.doi.org/10.1029/2002JB002193`. 2364. 67

Bell, Andrew F. Predictability of landslide timing from quasi-periodic precursory earthquakes. *Geophysical Research Letters*, 45(4):1860–1869, 2018. 88

Benoit, John P and McNutt, Stephen R. New constraints on source processes of volcanic tremor at Arenal Volcano, Costa Rica, using broadband seismic data. *Geophysical Research Letters*, 24(4):449–452, 1997. 1

Benson, Philip M; Vinciguerra, Sergio; Meredith, Philip G, and Young, R Paul. Laboratory simulation of volcano seismicity. *Science*, 322(5899):249–252, 2008. ISSN 0036-8075. doi: 10.1126/science.1161927. URL http://science.sciencemag.org/content/322/5899/249. 19, 34

Bernardie, S.; Desramaut, N.; Malet, J.-P.; Gourlay, M., and Grandjean, G. Prediction of changes in landslide rates induced by rainfall. *Landslides*, 12(3):481–494, Jun 2015. ISSN 1612-5118. doi: 10.1007/s10346-014-0495-8. URL https://doi.org/10.1007/s10346-014-0495-8. 2, 60, 88, 101

Berti, M; Genevois, R; LaHusen, R; Simoni, A, and Tecca, PR. Debris flow monitoring in the acquabona watershed on the dolomites (italian alps). *Physics and Chemistry of the Earth, Part B: Hydrology, Oceans and Atmosphere*, 25(9):707–715, 2000. 15

Bessason, Bjarni; Eiríksson, Gísli; Thorarinsson, Óð*inn; Thórarinsson, Andrés, and Einarsson, Sigurð*ur. Automatic detection of avalanches and debris flows by seismic methods. *Journal of Glaciology*, 53(182):461–472, 2007. doi: 10.3189/002214307783258468. 15, 48

Beven, Keith. A sensitivity analysis of the penman-monteith actual evapotranspiration estimates. *Journal of hydrology*, 44(3-4):169–190, 1979. 91

Beyreuther, Moritz and Wassermann, Joachim. Continuous earthquake detection and classification using discrete Hidden Markov models. *Geophysical Journal International*, 175 (3):1055–1066, 2008. ISSN 1365-246X. doi: 10.1111/j.1365-246X.2008.03921.x. URL http://dx.doi.org/10.1111/j.1365-246X.2008.03921.x. 46

Biescas, Berta; Dufour, François; Furdada, Glória; Khazaradze, Giorgi, and Suriñach, Emma. Frequency content evolution of snow avalanche seismic signals. *Surveys in Geophysics*, 24 (5):447–464, Nov 2003. ISSN 1573-0956. doi: 10.1023/B:GEOP.0000006076.38174.31. URL https://doi.org/10.1023/B:GEOP.0000006076.38174.31. 23

Bièvre, G.; Helmstetter, A.; Lacroix, P.; Baillet, L.; Langlais, M.; Vial, B.; Voisin, C.; Larose, E., and Jongmans, D. Réactivation du glissement-coulé d'Harmalière (Isère, France). Journées Aléas Gravitaires, Besançon, France, 2017. 11, 13, 23

Bottelin, P.; Jongmans, D.; Daudon, D.; Mathy, A.; Helmstetter, A.; Bonilla-Sierra, V.; Cadet, H.; Amitrano, D.; Richefeu, V.; Lorier, L.; Baillet, L.; Villard, P., and Donzé, F. Seismic and mechanical studies of the artificially triggered rockfall at mount néron (french alps, december 2011). *Natural Hazards and Earth System Sciences*, 14(12):3175–3193, 2014. doi: 10.5194/nhess-14-3175-2014. URL https://www.nat-hazards-earth-syst-sci.net/14/3175/2014/. 15, 65

Bottelin, Pierre; Levy, Clara; Baillet, Laurent; Jongmans, Denis, and Gueguen, Philippe. Modal and thermal analysis of Les Arches unstable rock column (Vercors massif, French Alps). *Geophysical Journal International*, 194(2):pp 849–858, January 2013a. doi: 10.1093/gji/ggt046. URL https://hal.archives-ouvertes.fr/hal-00933213. 14

Bottelin, Pierre; Jongmans, Denis; Baillet, Laurent; Lebourg, Thomas; Hantz, Didier; Levy, Clara; Roux, Olivier Le; Cadet, Heloise; Lorier, Lionel; Rouiller, Jean-Daniel; Turpin, Julien, and Darras, Lionel. Spectral analysis of prone-to-fall rock compartments using ambient vibrations. *Journal of Environmental and Engineering Geophysics*, 18(4):205–217, 2013b. doi:

10.2113/JEEG18.4.205. URL https://library.seg.org/doi/abs/10.2113/JEEG18.4.205. 14

Breiman, Leo. Random Forests. *Machine Learning*, 45(1):5–32, 2001. ISSN 1573-0565. doi: 10.1023/A:1010933404324. URL http://dx.doi.org/10.1023/A:1010933404324. 46, 53

BRGM, . Ecoute acoustique et microsismicité appliquée aux mouvements de terrain. etat de l'art. Rapport BRGM R38659 , BRGM, 1995. URL infoterre.brgm.fr/rapports/RR-38659-FR.pdf. Document annexe à la PG11. 11

Brodsky, E E; Gordeev, E, and Kanamori, H. Landslide basal friction as measured by seismic waves. *Geophysical Research Letters*, 30(24):2236, 2003. doi: 10.1029/2003GL018485. 11

Brown, Justin R.; Beroza, Gregory C.; Ide, Satoshi; Ohta, Kazuaki; Shelly, David R.; Schwartz, Susan Y.; Rabbel, Wolfgang; Thorwart, Martin, and Kao, Honn. Deep low-frequency earthquakes in tremor localize to the plate interface in multiple subduction zones. *Geophysical Research Letters*, 36(19), 2009. ISSN 1944-8007. doi: 10.1029/2009GL040027. URL http://dx.doi.org/10.1029/2009GL040027. L19306. 34

Bru, G; Fernández-Merodo, JA; García-Davalillo, JC; Herrera, G, and Fernández, J. Site scale modeling of slow-moving landslides, a 3d viscoplastic finite element modeling approach. *Landslides*, 15(2):257–272, 2018. 88

Brückl, E.; Brunner, F. K.; Lang, E.; Mertl, S.; Müller, M., and Stary, U. The Gradenbach observatory—monitoring deep-seated gravitational slope deformation by geodetic, hydrological, and seismological methods. *Landslides*, 10(6):815–829, Dec 2013. ISSN 1612-5118. doi: 10.1007/s10346-013-0417-1. URL http://dx.doi.org/10.1007/s10346-013-0417-1. 13, 61

Brückl, Ewald. Large landslides with seismicity. *Rock Mechanics and Engineering Volume 4: Excavation, Support and Monitoring*, page 365, 2017. 31

Burtin, A; Bollinger, L; Cattin, R; Vergne, J, and Nábělek, J L. Spatiotemporal sequence of Himalayan debris flow from analysis of high-frequency seismic noise. *Journal of Geophysical Research*, 114:F04009, 2009. doi: 10.1029/2008JF001198. 19

Burtin, A.; Hovius, N.; McArdell, B. W.; Turowski, J. M., and Vergne, J. Seismic constraints on dynamic links between geomorphic processes and routing of sediment in a steep mountain catchment. *Earth Surface Dynamics*, 2(1):21–33, 2014. doi: 10.5194/esurf-2-21-2014. URL https://www.earth-surf-dynam.net/2/21/2014/. 16

Burtin, A.; Hovius, N., and Turowski, J. M. Seismic monitoring of torrential and fluvial processes. *Earth Surface Dynamics*, 4(2):285–307, 2016. doi: 10.5194/esurf-4-285-2016. URL https://www.earth-surf-dynam.net/4/285/2016/. 23, 28, 38

Burtin, Arnaud; Hovius, Niels; Milodowski, David T; Chen, Yue-Gau; Wu, Yih-Min; Lin, Ching-Weei; Chen, Hongey; Emberson, Robert, and Leu, Peih-Lin. Continuous catchment-scale monitoring of geomorphic processes with a 2-d seismological array. *Journal of Geophysical Research: Earth Surface*, 118(3):1956–1974, 2013. 16, 19

Cadman, John D. and Goodman, Richard E. Landslide noise. *Science*, 158(3805):1182–1184, 1967. ISSN 0036-8075. doi: 10.1126/science.158.3805.1182. URL http://science.sciencemag.org/content/158/3805/1182. 10

Caduff, Rafael; Schlunegger, Fritz; Kos, Andrew, and Wiesmann, Andreas. A review of terrestrial radar interferometry for measuring surface change in the geosciences. *Earth surface processes and landforms*, 40(2):208–228, 2015. 108

Caine, Nel. The rainfall intensity-duration control of shallow landslides and debris flows. *Geografiska annaler: series A, physical geography*, 62(1-2):23–27, 1980. 88

Caplan-Auerbach, J and Huggel, C. Precursory seismicity associated with frequent, large ice avalanches on Iliamna volcano, Alaska, USA. *Journal of Glaciology*, 53(180):128–140, 2007a. vii, 88

Caplan-Auerbach, Jacqueline and Huggel, Christian. Precursory seismicity associated with frequent, large ice avalanches on Iliamna volcano, Alaska, USA. *Journal of Glaciology*, 53 (180):128–140, 2007b. doi: 10.3189/172756507781833866. 61

Carrière, S. R.; Jongmans, D.; Chambon, G.; Bièvre, G.; Lanson, B.; Bertello, L.; Berti, M.; Jaboyedoff, M.; Malet, J.-P., and Chambers, J. E. Rheological properties of clayey soils originating from flow-like landslides. *Landslides*, Mar 2018. ISSN 1612-5118. doi: 10.1007/s10346-018-0972-6. URL `https://doi.org/10.1007/s10346-018-0972-6`. 60

Chen, Zuolin; Stewart, Robert; Bland, Henry, and Thurston, Jeff. Microseismic activity and location at Turtle Mountain, Alberta. volume 16, page 18. Consortium for Research in Elastic Wave Exploration Seismology, CREWES, University of Calgary, Canada, 2005. 13

Chouet, Bernard. Resonance of a fluid-driven crack: Radiation properties and implications for the source of long-period events and harmonic tremor. *Journal of Geophysical Research: Solid Earth*, 93(B5):4375–4400, 1988. ISSN 2156-2202. doi: 10.1029/JB093iB05p04375. URL `http://dx.doi.org/10.1029/JB093iB05p04375`. 19, 34

Chouet, Bernard A.; Page, Robert A.; Stephens, Christopher D.; Lahr, John C., and Power, John A. Precursory swarms of long-period events at redoubt volcano (1989—1990), alaska: Their origin and use as a forecasting tool. *Journal of Volcanology and Geothermal Research*, 62(1):95–135, 1994. ISSN 0377-0273. doi: http://dx.doi.org/10.1016/0377-0273(94)90030-2. URL `http://www.sciencedirect.com/science/article/pii/0377027394900302`. 1, 61

Colombero, C.; Comina, C.; Vinciguerra, S., and Benson, P. Microseismicity of an unstable rock mass: from field monitoring to laboratory testing. *Journal of Geophysical Research: Solid Earth*, 2018. ISSN 2169-9356. doi: 10.1002/2017JB014612. URL `http://dx.doi.org/10.1002/2017JB014612`. 2017JB014612. 14, 31, 34, 38, 88, 89

Corominas, Jordi; Moya, José; Ledesma, Alberto; Lloret, Antonio, and Gili, Josep A. Prediction of ground displacements and velocities from groundwater level changes at the vallcebre landslide (eastern pyrenees, spain). *Landslides*, 2(2):83–96, 2005. 88

Crosta, G B and Agliardi, F. Failure forecast for large rock slides by surface displacement measurements. *Canadian Geotechnical Journal*, 40(1):176–191, 2003. doi: 10.1139/t02-085. URL `https://doi.org/10.1139/t02-085`. 60

Cruden, D M and Varnes, D J. *Landslide Types and Processes*, volume 247. 1996. 23

Curilem, Gloria; Vergara, Jorge; Fuentealba, Gustavo; Acuña, Gonzalo, and Chacón, Max. Classification of seismic signals at Villarrica volcano (Chile) using neural networks and genetic algorithms. *Journal of volcanology and geothermal research*, 180(1):1–8, 2009. 25, 46, 48

Dammeier, F; Moore, J R; Haslinger, F, and Loew, S. Characterization of alpine rockslides using statistical analysis of seismic signals. *Journal of Geophysical Research*, 116:F04024, 2011. doi: 10.1029/2011JF002037. 27, 28

Dammeier, Franziska; Moore, Jeffrey R; Hammer, Conny; Haslinger, Florian, and Loew, Simon. Automatic detection of alpine rockslides in continuous seismic data using Hidden Markov Models. *Journal of Geophysical Research: Earth Surface*, 121(2):351–371, 2016. 1, 10, 22, 46

Deichmann, N.; Ansorge, J.; Scherbaum, F.; Aschwanden, A.; Bernard, F., and Gudmundsson, G. H. Evidence for deep icequakes in an alpine glacier. *Annals of Glaciology*, 31:85–90, 2000. doi: 10.3189/172756400781820462. 34

Deparis, J.; Jongmans, D.; Cotton, F.; Baillet, L.; Thouvenot, F., and Hantz, D. Analysis of rock-fall and rock-fall avalanche seismograms in the French Alps. *Bulletin of the Seismological Society of America*, 98(4):1781–1796, 2008. ISSN 0037-1106. doi: 10.1785/0120070082. URL `http://bssa.geoscienceworld.org/content/98/4/1781`. 10, 28

Derode, Benoit; Guglielmi, Yves; De Barros, Louis, and Cappa, Frédéric. Seismic responses to fluid pressure perturbations in a slipping fault. *Geophysical Research Letters*, 42(9):3197–3203, 2015. ISSN 1944-8007. doi: 10.1002/2015GL063671. URL `http://dx.doi.org/10.1002/2015GL063671`. 2015GL063671. 19

Dietze, M.; Mohadjer, S.; Turowski, J. M.; Ehlers, T. A., and Hovius, N. Seismic monitoring of small alpine rockfalls – validity, precision and limitations. *Earth Surface Dynamics*, 5(4):653–668, 2017a. doi: 10.5194/esurf-5-653-2017. URL `https://www.earth-surf-dynam.net/5/653/2017/`. 15

Dietze, M.; Turowski, J. M.; Cook, K. L., and Hovius, N. Spatiotemporal patterns, triggers and anatomies of seismically detected rockfalls. *Earth Surface Dynamics*, 5(4):757–779, 2017b. doi: 10.5194/esurf-5-757-2017. URL `https://www.earth-surf-dynam.net/5/757/2017/`. 15, 28, 43, 88

Dixon, N.; Hill, R., and Kavanagh, J. Acoustic emission monitoring of slope instability: development of an active waveguide system. *Proceedings of the Institution of Civil Engineers - Geotechnical Engineering*, 156(2):83–95, 2003. doi: 10.1680/geng.2003.156.2.83. URL `https://doi.org/10.1680/geng.2003.156.2.83`. 11, 20

Dixon, N.; Spriggs, M. P.; Smith, A.; Meldrum, P., and Haslam, E. Quantification of reactivated landslide behaviour using acoustic emission monitoring. *Landslides*, 12(3):549–560, Jun 2015. ISSN 1612-5118. doi: 10.1007/s10346-014-0491-z. 10, 21, 108

Dixon, N.; Smith, A.; Flint, J. A.; Khanna, R.; Clark, B., and Andjelkovic, M. An acoustic emission landslide early warning system for communities in low-income and middle-income countries. *Landslides*, Mar 2018. doi: 10.1007/s10346-018-0977-1. 10

Doi, I.; Matsuura, S.; Shibasaki, T., and Osawa, H. In *Seismic measurements in a mudstone landslide area*, 2015. 13

Ekström, Göran and Stark, Colin P. Simple scaling of catastrophic landslide dynamics. *Science*, 339(6126):1416–1419, 2013. ISSN 0036-8075. doi: 10.1126/science.1232887. URL `http://science.sciencemag.org/content/339/6126/1416`. 11

Ekström, Göran and Stark, Colin P. Simple scaling of catastrophic landslide dynamics. *Science*, 339:1416–1419, 2013. doi: 10.1126/science.1232887. 1, 10

Fäh, Donat and Koch, Karl. Discrimination between earthquakes and chemical explosions by multivariate statistical analysis: A case study for Switzerland. *Bulletin of the Seismological Society of America*, 92(5):1795–1805, 2002. doi: 10.1785/0120010166. URL `http://www.bssaonline.org/content/92/5/1795.abstract`. 25, 46

Farin, M; Mangeney, A, and Roche, O. Fundamental changes of granular flow dynamics, deposition and erosion processes at high slope angles: insights from laboratory experiments. *Journal of Geophysical Research*, 119, 2014. doi: 10.1002/2013JF002750. 26, 28, 113

Federico, A; Popescu, M; Elia, G; Fidelibus, C; Internò, G, and Murianni, A. Prediction of time to slope failure: a general framework. *Environmental Earth Sciences*, 66(1):245–256, 2012. 88

Fernández-Delgado, Manuel; Cernadas, Eva; Barro, Senén, and Amorim, Dinani. Do we need hundreds of classifiers to solve real world classification problems. *J. Mach. Learn. Res*, 15 (1):3133–3181, 2014. 53

Ferrari, Alessio; Ledesma, Alberto; Gonzalez, DA, and Corominas, Jordi. Effects of the foot evolution on the behaviour of slow-moving landslides. *Engineering geology*, 117(3-4):217–228, 2011. 88

Ferrazzini, Valerie; Aki, Keiiti, and Chouet, Bernard. Characteristics of seismic waves composing hawaiian volcanic tremor and gas-piston events observed by a near-source array. *Journal of Geophysical Research: Solid Earth*, 96(B4):6199–6209, 1991. 1

François, Bertrand; Tacher, Laurent; Bonnard, Ch; Laloui, Lyesse, and Triguero, Véronique. Numerical modelling of the hydrogeological and geomechanical behaviour of a large slope movement: the triesenberg landslide (liechtenstein). *Canadian Geotechnical Journal*, 44 (7):840–857, 2007. 88

Galgaro, A.; Tecca, P. R.; Genevois, R., and Deganutti, A. M. Acoustic module of the Acquabona (Italy) debris flow monitoring system. *Natural Hazards and Earth System Science*, 5(2):211–215, February 2005. URL `https://hal.archives-ouvertes.fr/hal-00299146`. 15

Gance, J; Malet, J-P; Supper, R; Sailhac, P; Ottowitz, D, and Jochum, B. Permanent electrical resistivity measurements for monitoring water circulation in clayey landslides. *Journal of Applied Geophysics*, 126:98–115, 2016. 2

Gance, Julien; Grandjean, Gilles; Samyn, Kévin, and Malet, Jean-Philippe. Quasi-Newton inversion of seismic first arrivals using source finite bandwidth assumption: Application to subsurface characterization of landslides. *Journal of Applied Geophysics*, 87:94–106, 2012. ISSN 0926-9851. doi: http://dx.doi.org/10.1016/j.jappgeo.2012.09.008. URL `http://www.sciencedirect.com/science/article/pii/S0926985112001735`. xxi, 61, 62, 63, 114

García, Alicia; Berrocoso, Manuel; Marrero, José M.; Fernández-Ros, Alberto; Prates, Gonçalo; De la Cruz-Reyna, Servando, and Ortiz, Ramón. Volcanic alert system (VAS) developed during the 2011–2014 El Hierro (Canary Islands) volcanic process. *Bulletin of Volcanology*, 76(6):825, May 2014. ISSN 1432-0819. doi: 10.1007/s00445-014-0825-7. URL `http://dx.doi.org/10.1007/s00445-014-0825-7`. 61

Gomberg, Joan; Bodin, Paul; Savage, William, and Jackson, Michael E. Landslide faults and tectonic faults, analogs?: The Slumgullion earthflow, Colorado. *Geology*, 23(1):41–44, 1995. doi: 10.1130/0091-7613(1995)023<0041:LFATFA>2.3.CO;2. URL `http://geology.gsapubs.org/content/23/1/41.abstract`. 2, 10, 11, 14, 46, 61, 89

Gomberg, Joan; Schulz, William; Bodin, Paul, and Kean, Jason. Seismic and geodetic signatures of fault slip at the Slumgullion landslide natural laboratory. *Journal of Geophysical Research: Solid Earth*, 116(B9), 2011. ISSN 2156-2202. doi: 10.1029/2011JB008304. URL `http://dx.doi.org/10.1029/2011JB008304`. B09404. xvii, xviii, 2, 14, 21, 31, 32, 33, 38, 41, 46, 88

Grandjean, Gilles; Pennetier, CÃ©line; Bitri, Adnan; Meric, Ombeline, and Malet, Jean-Philippe. Caractérisation de la structure interne et de l'état hydrique de glissements argilo-marneux par tomographie géophysique : l'exemple du glissement-coulée de Super-Sauze (Alpes du Sud, France). *Comptes Rendus Geoscience*, 338(9):587–595, 2006. ISSN 1631-0713. doi: http://dx.doi.org/10.1016/j.crte.2006.03.013. URL `http://www.sciencedirect.com/science/article/pii/S1631071306000745`. 63

Guzzetti, F; Peruccacci, S; Rossi, M, and Stark, C P. The rainfall-intensity duration control of shallow landslides and debris flows: an update. *Landslides*, 5:3–17, 2008. 88

Hammer, C.; Ohrnberger, M., and Fäh, D. Classifying seismic waveforms from scratch: a case study in the alpine environment. *Geophysical Journal International*, 192(1):425–439, 2013. doi: 10.1093/gji/ggs036. URL `http://gji.oxfordjournals.org/content/192/1/425.abstract`. 10, 25, 46

Hammer, Conny; Beyreuther, Moritz, and Ohrnberger, Matthias. A Seismic-Event Spotting System for Volcano Fast-Response Systems. *Bulletin of the Seismological Society of America*, 102(3):948–960, 2012. 25, 46, 48

Haque, Ubydul; Blum, Philipp; da Silva, Paula F.; Andersen, Peter; Pilz, Jürgen; Chalov, Sergey R.; Malet, Jean-Philippe; Auflič, Mateja Jemec; Andres, Norina; Poyiadji, Eleftheria; Lamas, Pedro C.; Zhang, Wenyi; Peshevski, Igor; Pétursson, Halldór G.; Kurt, Tayfun; Dobrev, Nikolai; García-Davalillo, Juan Carlos; Halkia, Matina; Ferri, Stefano; Gaprindashvili, George; Engström, Johanna, and Keellings, David. Fatal landslides in europe. *Landslides*, 13(6):1545–1554, Dec 2016. ISSN 1612-5118. doi: 10.1007/s10346-016-0689-3. URL `https://doi.org/10.1007/s10346-016-0689-3`. vii

Harba, Paulina and Pilecki, Zenon. Assessment of time–spatial changes of shear wave velocities of flysch formation prone to mass movements by seismic interferometry with the use of ambient noise. *Landslides*, 14(3):1225–1233, Jun 2017. doi: 10.1007/s10346-016-0779-2. 11

Harp, Edwin L.; Reid, Mark E.; Godt, Jonathan W.; DeGraff, Jerome V., and Gallegos, Alan J. Ferguson rock slide buries California State Highway near Yosemite National Park. *Land-*

slides, 5(3):331–337, Aug 2008. ISSN 1612-5118. doi: 10.1007/s10346-008-0120-9. URL https://doi.org/10.1007/s10346-008-0120-9. 13

Hartzell, Stephen; Leeds, Alena L., and Jibson, Randall W. Seismic response of soft deposits due to landslide: The mission peak, california, landslideseismic response of soft deposits due to landslide: The mission peak, california, landslide. *Bulletin of the Seismological Society of America*, 107(5):2008, 2017. doi: 10.1785/0120170033. URL +http://dx.doi.org/10.1785/0120170033. 14

Hawthorne, J.C. and Ampuero, J.-P. A phase coherence approach to identifying co-located earthquakes and tremor. *Geophysical Journal International*, 209(2):623–642, 2017. doi: 10.1093/gji/ggx012. URL +http://dx.doi.org/10.1093/gji/ggx012. 36

Helmstetter, A. and Janex, G. Ecoute sismique et acoustique du mouvement de terrain de Séchilienne (Massif de Belledonne). *Métrologie en Milieu Extrême, Collection EDYTEM*, 2017. 21

Helmstetter, A.; Ménard, G.; Hantz, D.; Lacroix, P.; Thouvenot, F., and Grasso, J.-R. Etude multidisciplinaire d'un effondrement dans la carrière de ciment de Saint-Martin-le-Vinoux. Journées Aléas Gravitaires, Strasbourg, France, 2011. xvii, 28, 29, 33, 35

Helmstetter, A.; Larose, E.; Baillet, L., and Mayoraz, R. Repeating quakes detected at Gugla rock-glacier and Alestch rockslide (Valais). 2017a. 23

Helmstetter, A.; Larose, E.; Baillet, L., and Mayoraz, R. Repeating quakes detected at Gugla rock-glacier and Alestch rockslide (Valais). Enviroseis, From process to signal - advancing environmental seismology, Ohlstadt, Germany, 2017b. 13

Helmstetter, Agnès and Garambois, Stéphane. Seismic monitoring of Séchilienne rockslide (French Alps): Analysis of seismic signals and their correlation with rainfalls. *Journal of Geophysical Research: Earth Surface*, 115(F3), 2010. ISSN 2156-2202. doi: 10.1029/2009JF001532. URL http://dx.doi.org/10.1029/2009JF001532. F03016. 11, 13, 21, 22, 25, 27, 31, 46, 47, 48, 61, 65, 76, 88, 89, 92, 107

Helmstetter, Agnès; Moreau, Luc; Nicolas, Barbara; Comon, Pierre, and Gay, Michel. Intermediate-depth icequakes and harmonic tremor in an Alpine glacier (Glacier d'Argentière, France): Evidence for hydraulic fracturing? *Journal of Geophysical Research: Earth Surface*, 120(3):402–416, 2015a. ISSN 2169-9011. doi: 10.1002/2014JF003289. URL http://dx.doi.org/10.1002/2014JF003289. 2014JF003289. 18, 23, 42

Helmstetter, Agnès; Nicolas, Barbara; Comon, Pierre, and Gay, Michel. Basal icequakes recorded beneath an Alpine glacier (Glacier d'Argentière, Mont Blanc, France): Evidence for stick-slip motion? *Journal of Geophysical Research: Earth Surface*, 120(3):379–401, 2015b. ISSN 2169-9011. doi: 10.1002/2014JF003288. URL http://dx.doi.org/10.1002/2014JF003288. 2014JF003288. 18, 19, 23, 34, 42

Hencher, S. R. Preferential flow paths through soil and rock and their association with landslides. *Hydrological Processes*, 24(12):1610–1630, 2010. ISSN 1099-1085. doi: 10.1002/hyp.7721. URL http://dx.doi.org/10.1002/hyp.7721. 19

Herring, T; King, R.W., and McClusky, S.C. Global kalman filter vlbi and gps analysis program (globk), version 5.0. *Internal Memorandum: Mass. Inst. of Technol., Cambridge, Mass*, 2003a. 91

Herring, T; King, R.W., and McClusky, S.C. Gamit, gps analysis at mit, release 10.3. *Internal Memorandum: Mass. Inst. of Technol., Cambridge, Mass*, 2003b. 91

Hibert, C; Mangeney, A; Grandjean, G, and Shapiro, N M. Slope instabilities in Dolomieu crater, Réunion Island: From seismic signals to rockfall characteristics. *Journal of Geophysical Research*, 116:F04032, 2011. doi: 10.1029/2011JF002038. 15, 19, 28

Hibert, C.; Mangeney, A.; Grandjean, G.; Baillard, C.; Rivet, D.; Shapiro, N. M.; Satriano, C.; Maggi, A.; Boissier, P.; Ferrazzini, V., and Crawford, W. Automated identification, location, and volume estimation of rockfalls at Piton de la Fournaise volcano. *Journal of Geophysical Research: Earth Surface*, 119(5):1082–1105, 2014. ISSN 2169-9011. doi: 10.1002/2013JF002970. URL `http://dx.doi.org/10.1002/2013JF002970`. 46, 48, 55, 65, 67, 76

Hibert, C.; Mangeney, A.; Grandjean, G.; Baillard, C.; Rivet, D.; Shapiro, N. M.; Satriano, C.; Maggi, A.; Boissier, P.; Ferrazzini, V., and Crawford, W. Automated identification, location, and volume estimation of rockfalls at Piton de la Fournaise volcano. *Journal of Geophysical Research: Earth Surface*, 119(5):1082–1105, 2014a. ISSN 2169-9011. doi: 10.1002/2013JF002970. URL `http://dx.doi.org/10.1002/2013JF002970`. 11, 15, 25, 27, 28

Hibert, C; Ekström, G, and Stark, C P. Dynamics of the Bingham Canyon Mine landslides from seismic signal analysis. *Geophysical Research Letters*, 41:4535–4541, 2014b. doi: 10.1002/2014GL060592. 1, 28

Hibert, C; Stark, C P, and Ekström, G. Seismology of the Oso-Steelhead landslide. *Nat. Hazards Earth Syst. Sci. Discuss.*, pages 7309–7327, 2014c. 1

Hibert, C.; Malet, J.-P.; Bourrier, F.; Provost, F.; Berger, F.; Bornemann, P.; Tardif, P., and Mermin, E. Single-block rockfall dynamics inferred from seismic signal analysis. *Earth Surface Dynamics*, 5(2):283–292, 2017a. doi: 10.5194/esurf-5-283-2017. URL `https://www.earth-surf-dynam.net/5/283/2017/`. xvii, 15, 23, 27, 28, 113

Hibert, Clement; Stumpf, André; Provost, Floriane, and Malet, Jean-Philippe. Automated classification of seismic sources in a large database: a comparison of random forests and deep neural networks. In *EGU General Assembly Conference Abstracts*, volume 19, page 4373, 2017. 45

Hibert, Clement; Mangeney, Anne; Grandjean, Gilles; Peltier, Aline; DiMuro, Andrea; Shapiro, Nikolai M.; Ferrazzini, Valerie; Boissier, Patrice; Durand, Virginie, and Kowalski, Philippe. Spatio-temporal evolution of rockfall activity from 2007 to 2011 at the piton de la fournaise volcano inferred from seismic data. *Journal of Volcanology and Geothermal Research*, 333-334:36 – 52, 2017b. ISSN 0377-0273. doi: https://doi.org/10.1016/j.jvolgeores.2017.01.007. URL `http://www.sciencedirect.com/science/article/pii/S0377027316303195`. 19, 28

Hibert, Clement; Provost, Floriane; Malet, Jean-Philippe; Maggi, Alessia; Stumpf, Andre, and Ferrazzini, Valerie. Automatic identification of rockfalls and volcano-tectonic earthquakes at the Piton de la Fournaise volcano using a Random Forest algorithm. *Journal of Volcanology and Geothermal Research*, 340:130 – 142, 2017c. ISSN 0377-0273. doi: https://doi.org/10.1016/j.jvolgeores.2017.04.015. URL `http://www.sciencedirect.com/science/article/pii/S0377027316303948`. 15, 22, 25, 58, 92, 112

Huang, Ching-Jer; Yin, Hsiao-Yuen; Chen, Chao-Yi; Yeh, Chih-Hui, and Wang, Chin-Lun. Ground vibrations produced by rock motions and debris flows. *Journal of Geophysical Research: Earth Surface*, 112(F2), 2007. ISSN 2156-2202. doi: 10.1029/2005JF000437. URL `http://dx.doi.org/10.1029/2005JF000437`. F02014. 16, 28

Hungr, Oldrich; Evans, S. G.; Bovis, M. J., and Hutchinson, J. N. A review of the classification of landslides of the flow type. *Environmental and Engineering Geoscience*, 7(3):221, 2001. doi: 10.2113/gseegeosci.7.3.221. URL `http://dx.doi.org/10.2113/gseegeosci.7.3.221`. 19

Hungr, Oldrich; Leroueil, Serge, and Picarelli, Luciano. The Varnes classification of landslide types, an update. *Landslides*, 11(2):167–194, Apr 2014. ISSN 1612-5118. doi: 10.1007/s10346-013-0436-y. URL `https://doi.org/10.1007/s10346-013-0436-y`. 9, 10, 18, 88

Hürlimann, M; Abancó, C; Moya, J, and Vilajosana, I. Results and experiences gathered at the rebaixader debris-flow monitoring site, central pyrenees, spain. *Landslides*, 11(6):939–953, 2014. xvii, 15, 28, 30

Hutchinson, J. Landslide risk—to know, to foresee, to prevent. *Geologica Tecnica & Ambientale*, 9:3–24, 2001. 88

Intrieri, E. and Gigli, G. Landslide forecasting and factors influencing predictability. *Natural Hazards and Earth System Sciences*, 16(12):2501–2510, 2016. doi: 10.5194/nhess-16-2501-2016. URL `https://www.nat-hazards-earth-syst-sci.net/16/2501/2016/`. 60

Itakura, Y; Fujii, N, and Sawada, T. Basic characteristics of ground vibration sensors for the detection of debris flow. *Physics and Chemistry of the Earth, Part B: Hydrology, Oceans and Atmosphere*, 25(9):717–720, 2000. 16

Iverson, R M. Regulation of landslide motion by dilatancy and pore pressure feedback. *Journal of Geophysical Research*, 110:F02015, 2005. doi: 10.1029/2004JF000268. 108

Iverson, Richard M. The physics of debris flows. *Reviews of Geophysics*, 358:245–296, 1997. 108

Jaboyedoff, Michel; Oppikofer, Thierry; Abellán, Antonio; Derron, Marc-Henri; Loye, Alex; Metzger, Richard, and Pedrazzini, Andrea. Use of lidar in landslide investigations: a review. *Natural Hazards*, 61(1):5–28, Mar 2012. ISSN 1573-0840. doi: 10.1007/s11069-010-9634-2. URL `https://doi.org/10.1007/s11069-010-9634-2`. 108

Jenatton, Liliane; Guiguet, Robert; Thouvenot, François, and Daix, Nicolas. The 16,000-event 2003-–2004 earthquake swarm in Ubaye (French Alps). *Journal of Geophysical Research: Solid Earth*, 112(B11), 2007. ISSN 2156-2202. doi: {10.1029/2006JB004878}. URL `http://dx.doi.org/10.1029/2006JB004878`. B11304. 47, 65

Joswig, M. Nanoseismic monitoring fills the gap between microseismic network and passive seismic. *First Break*, 26:117–124, 2008. 23

Kanamori, H; Given, J W, and Lay, T. Analysis of seismic body waves excited by the Mount St. Helens eruption of May 18, 1980. *Journal of Geophysical Research*, 89(B23):1856–1866, March 1984. 11

Kean, J. W.; Coe, J. A.; Coviello, V.; Smith, J. B.; McCoy, S. W., and Arattano, M. Estimating rates of debris flow entrainment from ground vibrations. *Geophysical Research Letters*, 42(15): 6365–6372. doi: 10.1002/2015GL064811. 16, 19

Keefer, D K. The importance of earthquake-induced landslides to long-term slope erosion and slope-failure hazards in seismically active regions. *Geomorphology*, 10:265–284, 1994. 88

Keefer, David K. Statistical analysis of an earthquake-induced landslide distribution—the 1989 loma prieta, california event. *Engineering geology*, 58(3-4):231–249, 2000. 88

Kilburn, Christopher RJ and Petley, David N. Forecasting giant, catastrophic slope collapse: lessons from vajont, northern italy. *Geomorphology*, 54(1-2):21–32, 2003. 88

Kishimura, K. and Izumi, K. Seismic signals induced by snow avalanche flow. *Natural Hazards*, 15(1):89–100, Jan 1997. ISSN 1573-0840. doi: 10.1023/A:1007934815584. URL `https://doi.org/10.1023/A:1007934815584`. 23

Kogelnig, Arnold; Hübl, Johannes; Suriñach, Emma; Vilajosana, Ignasi, and McArdell, Brian W. Infrasound produced by debris flow: propagation and frequency content evolution. *Natural hazards*, 70(3):1713–1733, 2014. 16, 21

Kumagai, Hiroyuki; Palacios, Pablo; Maeda, Takuto; Castillo, Diego Barba, and Nakano, Masaru. Seismic tracking of lahars using tremor signals. *Journal of Volcanology and Geothermal Research*, 183(1):112 – 121, 2009. ISSN 0377-0273. doi: https://doi.org/10.1016/j.jvolgeores.2009.03.010. 16

Laasri, El Hassan Ait; Akhouayri, Es-Saïd; Agliz, Dris; Zonta, Daniele, and Atmani, Abderrahman. A fuzzy expert system for automatic seismic signal classification. *Expert Systems with Applications*, 42(3):1013–1027, 2015. ISSN 0957-4174. doi: http://dx.doi.org/10.1016/j.eswa.2014.08.023. URL `http://www.sciencedirect.com/science/article/pii/S0957417414005053`. 46, 55

Lacroix, Pascal and Helmstetter, Agnes. Location of seismic signals associated with microearthquakes and rockfalls on the Séchilienne landslide, French Alps. *Bulletin of the Seismological Society of America*, 101(1):341–353, 2011. 11, 13, 23, 31, 61, 68, 70, 75, 76, 88, 92, 95

Lacroix, Pascal; Grasso, J-R; Roulle, J; Giraud, Grégory; Goetz, D; Morin, S, and Helmstetter, A. Monitoring of snow avalanches using a seismic array: Location, speed estimation, and relationships to meteorological variables. *Journal of Geophysical Research: Earth Surface*, 117(F1), 2012. 10

Langer, H.; Falsaperla, S.; Powell, T., and Thompson, G. Automatic classification and a-posteriori analysis of seismic event identification at Soufrière Hills volcano, Montserrat. *Journal of Volcanology and Geothermal Research*, 153(1-2):1–10, 2006. ISSN 0377-0273. doi: http://dx.doi.org/10.1016/j.jvolgeores.2005.08.012. URL `http://www.sciencedirect.com/science/article/pii/S0377027305003793`. 25, 46, 55

Larose, Eric. Environmental seismology: What can we learn from ambient noise? *The Journal of the Acoustical Society of America*, 141(5):3527–3527, 2017. doi: 10.1121/1.4987437. URL `https://doi.org/10.1121/1.4987437`. 14, 60

Larose, Eric; Carrière, Simon; Voisin, Christophe; Bottelin, Pierre; Baillet, Laurent; Guéguen, Philippe; Walter, Fabian; Jongmans, Denis; Guillier, Bertrand; Garambois, Stephane; Gimbert, Florent, and Massey, Chris. Environmental seismology: What can we learn on earth surface processes with ambient noise? *Journal of Applied Geophysics*, 116:62 – 74, 2015. ISSN 0926-9851. doi: https://doi.org/10.1016/j.jappgeo.2015.02.001. URL `http://www.sciencedirect.com/science/article/pii/S0926985115000403`. 14

Lavigne, F; Thouret, J-C; Voight, B; Young, K; LaHusen, R; Marso, J; Suwa, H; Sumaryono, A; Sayudi, DS, and Dejean, M. Instrumental lahar monitoring at merapi volcano, central java, indonesia. *Journal of Volcanology and Geothermal Research*, 100(1-4):457–478, 2000. 16

Lawrence, William ST. and Williams, Thomas R. Seismic signals associated with avalanches. *Journal of Glaciology*, 17(77):521–526, 1976. doi: 10.3189/S0022143000013782. 23

Le Roy, G.; Amitrano, D., and Helmstetter, A. Multidisciplinary study of rockfalls in Chartreuse massif. 2017. 14

Le Roy, G.; Helmstetter, A.; Amitrano, D.; Guyoton, F., and Roux-Mallouf, R. Le. Seismic characterization of rock falls from detachment to propagation. 2018. xvii, 14, 29

Lebourg, Thomas; Binet, Stéphane; Tric, Emmanuel; Jomard, Herve, and El Bedoui, S. Geophysical survey to estimate the 3d sliding surface and the 4d evolution of the water pressure on part of a deep seated landslide. *Terra Nova*, 17(5):399–406, 2005. 2

Lenti, Luca; Martino, Salvatore; Paciello, Antonella; Prestininzi, Alberto, and Rivellino, Stefano. *Seismometric Monitoring of Hypogeous Failures Due to Slope Deformations*, pages 309–315. Springer Berlin Heidelberg, Berlin, Heidelberg, 2013. ISBN 978-3-642-31445-2. doi: 10.1007/978-3-642-31445-2_40. URL `https://doi.org/10.1007/978-3-642-31445-2_40`. 13

Leprettre, Benoît. *Reconnaissance de signaux sismiques d'avalanches par fusion de données estimées dans les domaines temps, temps-fréquence et polarisation*. PhD thesis, Université Joseph Fourier (Grenoble), 1996. 10

Lévy, C; Baillet, L; Jongmans, D; Mourot, P, and Hantz, D. Dynamic response of the Chamousset rock column (Western Alps, France). *Journal of Geophysical Research*, 115:F04043, 2010. doi: 10.1029/2009JF001606. 14, 31, 88

Levy, Clara; Jongmans, Denis, and Baillet, Laurent. Analysis of seismic signals recorded on a prone-to-fall rock column (Vercors massif, French Alps). *Geophysical Journal International*, 186(1):296–310, 2011. ISSN 1365-246X. doi: 10.1111/j.1365-246X.2011.05046.x. URL `http://dx.doi.org/10.1111/j.1365-246X.2011.05046.x`. xvii, 29, 40, 61, 89

Levy, Clara; Mangeney, Anne; Bonilla, Fabian; Hibert, Clément; Calder, Eliza S., and Smith, Patrick J. Friction weakening in granular flows deduced from seismic records at the Soufrière Hills Volcano, Montserrat. *Journal of Geophysical Research: Solid Earth*, 120(11): 7536–7557, 2015. ISSN 2169-9356. doi: 10.1002/2015JB012151. URL `http://dx.doi.org/10.1002/2015JB012151`. 2015JB012151. 11, 15, 19, 27, 28, 65

Lindner, Gerald; Schraml, Klaus; Mansberger, Reinfried, and Hübl, Johannes. Uav monitoring and documentation of a large landslide. *Applied Geomatics*, 8(1):1–11, 2016. 3

Lipovsky, B. P. and Dunham, E. M. Tremor during ice-stream stick slip. *The Cryosphere*, 10(1): 385–399, 2016. doi: 10.5194/tc-10-385-2016. URL https://www.the-cryosphere.net/10/385/2016/. 18, 40

Lockner, DiA; Byerlee, JD; Kuksenko, V; Ponomarev, A, and Sidorin, A. Quasi-static fault growth and shear fracture energy in granite. *Nature*, 350(6313):39, 1991. 42

Lomax, Anthony; Michelini, Alberto, and Curtis, Andrew. *Earthquake Location, Direct, Global-Search Methods*, pages 1–33. Springer New York, 2009. ISBN 978-3-642-27737-5. doi: 10.1007/978-3-642-27737-5_150-2. URL http://dx.doi.org/10.1007/978-3-642-27737-5_150-2. 23

Lotti, A.; Saccorotti, G.; Fiaschi, A.; Matassoni, L.; Gigli, G.; Pazzi, V., and Casagli, N. Seismic Monitoring of a Rockslide: The Torgiovannetto Quarry (Central Apennines, Italy). In Lollino, Giorgio; Giordan, Daniele; Crosta, Giovanni B.; Corominas, Jordi; Azzam, Rafig; Wasowski, Janusz, and Sciarra, Nicola, editors, *Engineering Geology for Society and Territory - Volume 2*, pages 1537–1540, Cham, 2015. Springer International Publishing. ISBN 978-3-319-09057-3. 13

Lube, Gert; Cronin, Shane J.; Manville, Vernon; Procter, Jonathan N.; Cole, Susan E., and Freundt, Armin. Energy growth in laharic mass flows. *Geology*, 40(5):475, 2012. doi: 10.1130/G32818.1. 16

Maggi, Alessia; Ferrazzini, Valérie; Hibert, Clément; Beauducel, François; Boissier, Patrice, and Amemoutou, Amandine. Implementation of a multistation approach for automated event classification at Piton de la Fournaise volcano. *Seismological Research Letters*, 88 (3), May 2017. doi: 10.1785/0220160189. URL https://hal.archives-ouvertes.fr/hal-01481992. 25, 58, 112

Mainsant, G.; Jongmans, D.; Chambon, G.; Larose, E., and Baillet, L. Shear-wave velocity as an indicator for rheological changes in clay materials: Lessons from laboratory experiments. *Geophysical Research Letters*, 39(19), 2012b. ISSN 1944-8007. doi: 10.1029/2012GL053159. URL http://dx.doi.org/10.1029/2012GL053159. L19301. 2, 11, 60

Mainsant, Guenole; Larose, Eric; Brönnimann, Cornelia; Jongmans, Denis; Michoud, Clément, and Jaboyedoff, Michel. Ambient seismic noise monitoring of a clay landslide: Toward failure prediction. *Journal of Geophysical Research: Earth Surface*, 117(F1), 2012a. ISSN 2156-2202. doi: 10.1029/2011JF002159. URL http://dx.doi.org/10.1029/2011JF002159. F01030. 2, 11, 14, 60

Mainsant, Guénolé; Chambon, Guillaume; Jongmans, Denis; Larose, Eric, and Baillet, Laurent. Shear-wave-velocity drop prior to clayey mass movement in laboratory flume experiments. *Engineering Geology*, 192:26 – 32, 2015. ISSN 0013-7952. doi: https://doi.org/10.1016/j.enggeo.2015.03.019. URL http://www.sciencedirect.com/science/article/pii/S0013795215001076. 60

Malet, J.-P.; Laigle, D.; Remaître, A., and Maquaire, O. Triggering conditions and mobility of debris flows associated to complex earthflows. *Geomorphology*, 66(1–4):215–235, 2005. ISSN 0169-555X. doi: http://dx.doi.org/10.1016/j.geomorph.2004.09.014. URL http://www.sciencedirect.com/science/article/pii/S0169555X04002211. 2, 47, 62, 79, 89, 101

Malet, Jean-Philippe. *Flow-like landslides in the clay-shales of Southeast France. Morphology, behaviour and hydro-mechanical modelling*. Theses, Université Louis Pasteur - Strasbourg I, December 2003. URL `https://tel.archives-ouvertes.fr/tel-00010298`. 60, 62

Malet, Jean-Philippe; Ulrich, P.; Déprez, Aline; Masson, Frédéric; Lissak, C., and Maquaire, O. Continuous monitoring and near-real time processing of GPS observations for landslide analysis: a methodological framework. In In Margottini, C.; Canuti, P., and Sassa, K. (Eds), editors, *Proc.2nd World Landslide Forum*, volume 7 of *Landslide Science and Practice*, pages 201–209, Rome, Italy, October 2011. Springer. URL `https://hal.archives-ouvertes.fr/hal-01108736`. 91

Malet, Jean-Philippe; Ulrich, Patrice; Déprez, Aline; Masson, Frédéric; Lissak, Candide, and Maquaire, Olivier. Continuous monitoring and near-real time processing of gps observations for landslide analysis: a methodological framework. In *Landslide Science and Practice*, pages 201–209. Springer, 2013. 91

Manconi, Andrea and Coviello, Velio. Evaluation of the Raspberry Shakes seismometers to monitor rock fall activity in alpine environments. In *EGU General Assembly, Vienna, Austria*, 2018. 13

Marc, O.; Hovius, N.; Meunier, P.; Uchida, T., and Hayashi, S. Transient changes of landslide rates after earthquakes. *Geology*, 43(10):883, 2015. doi: 10.1130/G36961.1. URL `+http://dx.doi.org/10.1130/G36961.1`. 88

Marcial, Sergio; Melosantos, Arnaldo A; Hadley, Kevin C; LaHusen, Richard G, and Marso, Jeffrey N. Instrumental lahar monitoring at mount pinatubo. *Fire and mud: eruptions and lahars of Mount Pinatubo, Philippines, edited by: Newhall, CG and Punongbayan, RS, Washington Press, Seattle*, pages 1015–1022, 1996. 16

Massin, Frédérick; Ferrazzini, Valérie; Bachèlery, Patrick; Nercessian, Alexandre; Duputel, Zacharie, and Staudacher, Thomas. Structures and evolution of the plumbing system of Piton de la Fournaise volcano inferred from clustering of 2007 eruptive cycle seismicity. *Journal of Volcanology and Geothermal Research*, 202(1):96–106, 2011. 1

McCann, D.M. and Forster, A. Reconnaissance geophysical methods in landslide investigations. *Engineering Geology*, 29(1):59 – 78, 1990. ISSN 0013-7952. doi: https://doi.org/10.1016/0013-7952(90)90082-C. URL `http://www.sciencedirect.com/science/article/pii/001379529090082C`. 11

Meunier, Patrick; Hovius, Niels, and Haines, A John. Regional patterns of earthquake-triggered landslides and their relation to ground motion. *Geophysical Research Letters*, 34 (20), 2007. 88

Michlmayr, Gernot; Cohen, Denis, and Or, Dani. Sources and characteristics of acoustic emissions from mechanically stressed geologic granular media – a review. *Earth-Science Reviews*, 112(3):97 – 114, 2012. ISSN 0012-8252. doi: https://doi.org/10.1016/j.earscirev.2012.02.009. URL `http://www.sciencedirect.com/science/article/pii/S0012825212000293`. 10, 11, 20, 21

Michlmayr, Gernot; Chalari, Athena; Clarke, Andy, and Or, Dani. Fiber-optic high-resolution acoustic emission (ae) monitoring of slope failure. *Landslides*, 14(3):1139–1146, Jun 2017.

ISSN 1612-5118. doi: 10.1007/s10346-016-0776-5. URL https://doi.org/10.1007/s10346-016-0776-5. 11

Mikesell, T. D.; van Wijk, K.; Haney, M. M.; Bradford, J. H.; Marshall, H. P., and Harper, J. T. Monitoring glacier surface seismicity in time and space using rayleigh waves. *Journal of Geophysical Research: Earth Surface*, 117(F2), 2012. ISSN 2156-2202. doi: 10.1029/2011JF002259. URL http://dx.doi.org/10.1029/2011JF002259. F02020. 34

Navratil, Oldrich; Liébault, F; Bellot, H; Theule, J; Travaglini, E; Ravanat, X; Ousset, F; Laigle, D; Segel, V, and Fiquet, M. High-frequency monitoring of debris flows in the french alps. In *Proceedings of 12th interpraevent congress, Grenoble*, pages 281–291, 2012. 15

Neuberg, J; Luckett, R; Baptie, B, and Olsen, K. Models of tremor and low-frequency earthquake swarms on montserrat. *Journal of Volcanology and Geothermal Research*, 101(1):83 – 104, 2000. ISSN 0377-0273. doi: https://doi.org/10.1016/S0377-0273(00)00169-4. URL http://www.sciencedirect.com/science/article/pii/S0377027300001694. 61, 65

Norman, Emma C.; Rosser, Nick J.; Brain, Matthew J.; Petley, David N., and Lim, Michael. Coastal cliff-top ground motions as proxies for environmental processes. *Journal of Geophysical Research: Oceans*, 118(12):6807–6823, 2013. ISSN 2169-9291. doi: 10.1002/2013JC008963. URL http://dx.doi.org/10.1002/2013JC008963. 14

Occhiena, C.; Coviello, V.; Arattano, M.; Chiarle, M.; Morra di Cella, U.; Pirulli, M.; Pogliotti, P., and Scavia, C. Analysis of microseismic signals and temperature recordings for rock slope stability investigations in high mountain areas. *Natural Hazards and Earth System Sciences*, 12(7):2283–2298, 2012. doi: 10.5194/nhess-12-2283-2012. URL https://www.nat-hazards-earth-syst-sci.net/12/2283/2012/. 14

Okura, Yoichi; Kitahara, Hikaru; Ochiai, Hirotaka; Sammori, Toshiaki, and Kawanami, Akiko. Landslide fluidization process by flume experiments. *Engineering Geology*, 66(1):65 – 78, 2002. ISSN 0013-7952. doi: https://doi.org/10.1016/S0013-7952(02)00032-7. URL http://www.sciencedirect.com/science/article/pii/S0013795202000327. 117

Olivares, Lucio; Damiano, Emilia; Greco, Roberto; Zeni, Luigi; Picarelli, Luciano; Minardo, Aldo; Guida, Andrea, and Bernini, Romeo. An instrumented flume to investigate the mechanics of rainfall-induced landslides in unsaturated granular soils. *Geotechnical Testing Journal*, 32(2):108–118, 2009. 117

Palis, Edouard; Lebourg, Thomas; Tric, Emmanuel; Malet, Jean-Philippe, and Vidal, Maurin. Long-term monitoring of a large deep-seated landslide (La Clapiere, South-East French Alps): initial study. *Landslides*, 14(1):155–170, Feb 2017. ISSN 1612-5118. doi: 10.1007/s10346-016-0705-7. URL https://doi.org/10.1007/s10346-016-0705-7. 13

Paul Winberry, J.; Anandakrishnan, Sridhar; Wiens, Douglas A., and Alley, Richard B. Nucleation and seismic tremor associated with the glacial earthquakes of whillans ice stream, antarctica. *Geophysical Research Letters*, 40(2):312–315, 2013. ISSN 1944-8007. doi: 10.1002/grl.50130. URL http://dx.doi.org/10.1002/grl.50130. 40

Pérez-Guillén, C; Sovilla, B; Suriñach, E; Tapia, M, and Köhler, A. Deducing avalanche size and flow regimes from seismic measurements. *Cold Regions Science and Technology*, 121:25–41, 2016. 10

Petley, D. N. The evolution of slope failures: mechanisms of rupture propagation. *Natural Hazards and Earth System Sciences*, 4(1):147–152, 2004. doi: 10.5194/nhess-4-147-2004. URL `https://www.nat-hazards-earth-syst-sci.net/4/147/2004/`. 60, 88

Petley, David. Global patterns of loss of life from landslides. *Geology*, 40(10):927, 2012. doi: 10.1130/G33217.1. URL `+http://dx.doi.org/10.1130/G33217.1`. vii

Petley, David N.; Bulmer, Mark H., and Murphy, William. Patterns of movement in rotational and translational landslides. *Geology*, 30(8):719, 2002. doi: 10.1130/0091-7613(2002)030<0719:POMIRA>2.0.CO;2. URL `+http://dx.doi.org/10.1130/0091-7613(2002)030<0719:POMIRA>2.0.CO;2`. 88

Petley, David N.; Higuchi, Toru; Petley, Derek J.; Bulmer, Mark H., and Carey, Jonathan. Development of progressive landslide failure in cohesive materials. *Geology*, 33(3):201, 2005. doi: 10.1130/G21147.1. URL `+http://dx.doi.org/10.1130/G21147.1`. 60

Picarelli, Luciano; Urciuoli, Gianfranco, and Russo, Claudia. Effect of groundwater regime on the behaviour of clayey slopes. *Canadian Geotechnical Journal*, 41(3):467–484, 2004. 108

Pierson, Thomas C. Flow characteristics of large eruption-triggered debris flows at snow-clad volcanoes: constraints for debris-flow models. *Journal of Volcanology and Geothermal Research*, 66(1):283 – 294, 1995. ISSN 0377-0273. doi: https://doi.org/10.1016/0377-0273(94)00070-W. URL `http://www.sciencedirect.com/science/article/pii/037702739400070W`. Models of Magnetic Processes and Volcanic Eruptions. 28

Podolskiy, Evgeny A. and Walter, Fabian. Cryoseismology. *Reviews of Geophysics*, 54(4):708–758, 2016. ISSN 1944-9208. doi: 10.1002/2016RG000526. URL `http://dx.doi.org/10.1002/2016RG000526`. 2016RG000526. 1, 10, 18, 21

Podvin, Pascal and Lecomte, Isabelle. Finite difference computation of traveltimes in very contrasted velocity models: a massively parallel approach and its associated tools. *Geophysical Journal International*, 105(1):271–284, 1991. ISSN 1365-246X. doi: 10.1111/j.1365-246X.1991.tb03461.x. URL `http://dx.doi.org/10.1111/j.1365-246X.1991.tb03461.x`. 63

Poli, Piero. Creep and slip: Seismic precursors to the Nuugaatsiaq landslide (Greenland). *Geophysical Research Letters*, 44(17):8832–8836, 2017. ISSN 1944-8007. doi: 10.1002/2017GL075039. URL `http://dx.doi.org/10.1002/2017GL075039`. 2017GL075039. vii, 1, 11, 22, 42, 60, 61, 88

Pratt, Martin J.; Winberry, J. Paul; Wiens, Douglas A.; Anandakrishnan, Sridhar, and Alley, Richard B. Seismic and geodetic evidence for grounding-line control of Whillans Ice Stream stick-slip events. *Journal of Geophysical Research: Earth Surface*, 119(2):333–348, 2014. ISSN 2169-9011. doi: 10.1002/2013JF002842. URL `http://dx.doi.org/10.1002/2013JF002842`. 18

Provost, F.; Hibert, C., and Malet, J.-P. Automatic classification of endogenous landslide seismicity using the Random Forest supervised classifier. *Geophysical Research Letters*, 44(1):113–120, 2017. ISSN 1944-8007. doi: 10.1002/2016GL070709. URL `http://dx.doi.org/10.1002/2016GL070709`. 2016GL070709. xvii, 22, 25, 29, 33, 65, 66, 92

Provost, F; Malet, J P; Gance, J; Helmstetter, A, and Doubre, C. Automatic approach for increasing the location accuracy of slow-moving landslide endogenous seismicity: the apoloc method. *Geophysical Journal International*, page ggy330, 2018. doi: 10.1093/gji/ggy330. URL `http://dx.doi.org/10.1093/gji/ggy330`. 23, 61, 92, 95

Quang, Paul Bui; Gaillard, Pierre; Cano, Yoann, and Ulzibat, Munkhuu. Detection and classification of seismic events with progressive multi-channel correlation and hidden Markov models. *Computers & Geosciences*, 83:110–119, 2015. ISSN 0098-3004. doi: http://dx.doi.org/10.1016/j.cageo.2015.07.002. URL `http://www.sciencedirect.com/science/article/pii/S0098300415300108`. 46

RESIF/OMIV, . *RESIF - Réseau Sismologique et géodésique Français / OMIV- French Multidisciplinary Observatory of Versant Instabilities*, 2015. doi: http://dx.doi.org/10.15778/RESIF.MT. iii, xvii, 13, 22, 29, 33, 42, 43, 56, 65, 81

Richards, Kevin S. and Reddy, Krishna R. Critical appraisal of piping phenomena in earth dams. *Bulletin of Engineering Geology and the Environment*, 66(4):381–402, Nov 2007. ISSN 1435-9537. doi: 10.1007/s10064-007-0095-0. URL `https://doi.org/10.1007/s10064-007-0095-0`. 19

Röösli, Claudia; Helmstetter, Agnes; Walter, Fabian, and Kissling, Edi. Meltwater influences on deep stick-slip icequakes near the base of the Greenland Ice Sheet. *Journal of Geophysical Research: Earth Surface*, 121(2):223–240, 2016a. ISSN 2169-9011. doi: 10.1002/2015JF003601. URL `http://dx.doi.org/10.1002/2015JF003601`. 2015JF003601. 18

Roth, Michael; Dietrich, Michel; Blikra, Lars H., and Lecomte, Isabelle. *Seismic Monitoring of the Unstable Rock Slope Site at Aaknes, Norway*, pages 184–192. 2008. doi: 10.4133/1.2923645. URL `https://library.seg.org/doi/abs/10.4133/1.2923645`. 13

Rouse, C.; Styles, P., and Wilson, S.A. Microseismic emissions from flowslide-type movements in South Wales. *Engineering Geology*, 31(1):91–110, 1991. ISSN 0013-7952. doi: http://dx.doi.org/10.1016/0013-7952(91)90059-T. URL `http://www.sciencedirect.com/science/article/pii/001379529190059T`. 10, 61

Ruano, A.E.; Madureira, G.; Barros, O.; Khosravani, H.R.; Ruano, M.G., and Ferreira, P.M. Seismic detection using support vector machines. *Neurocomputing*, 135:273–283, 2014. ISSN 0925-2312. doi: http://dx.doi.org/10.1016/j.neucom.2013.12.020. URL `http://www.sciencedirect.com/science/article/pii/S0925231214000332`. 25, 46

Sabot, F.; Naaim, M.; Granada, F.; Suriñach, E.; Planet, P., and Furdada, G. Study of avalanche dynamics by seismic methods, image-processing techniques and numerical models. *Annals of Glaciology*, 26:319–323, 1998. doi: 10.3189/1998AoG26-1-319-323. 10, 23

Saito, M. Forecasting time of slope failure by tertiary creep. In *Proc. 7th Int. Conf on Soil Mechanics and Foundation Engineering, Mexico City*, volume 2, pages 677–683. Citeseer, 1969. 60, 88

Saito, Michitaka. Evidential study on forecasting occurrence of slope failure. *Trans. of the Dept. of Geomech.—Armenian Academy of Sciences, Yerevan, URSS*, 1979. 88

Schimmel, A. and Hübl, J. Automatic detection of debris flows and debris floods based on a combination of infrasound and seismic signals. *Landslides*, 13(5):1181–1196, Oct

2016. ISSN 1612-5118. doi: 10.1007/s10346-015-0640-z. URL https://doi.org/10.1007/s10346-015-0640-z. 16, 21

Schmutz, Myriam; GuÃ©rin, Roger; Andrieux, Pierre, and Maquaire, Olivier. Determination of the 3D structure of an earthflow by geophysical methods. *Journal of Applied Geophysics*, 68(4):500–507, 2009. ISSN 0926-9851. doi: http://dx.doi.org/10.1016/j.jappgeo.2008.12.004. URL http://www.sciencedirect.com/science/article/pii/S0926985109000020. 62

Schneider, D; Bartelt, P; Caplan-Auerbach, J; Christen, M; Huggel, C, and McArdell, B W. Insights into rock-ice avalanche dynamics by combined analysis of seismic recordings and a numerical avalanche model. *Journal of Geophysical Research*, 115:F04026, 2010. doi: 10.1029/2010JF001734. 19, 28

Scholz, Christopher H. Earthquakes and friction laws. *Nature*, 391(6662):37, 1998. 40

Schöpa, A.; Chao, W.-A.; Lipovsky, B.; Hovius, N.; White, R. S.; Green, R. G., and Turowski, J. M. Dynamics of the askja caldera july 2014 landslide, iceland, from seismic signal analysis: precursor, motion and aftermath. *Earth Surface Dynamics Discussions*, 2017:1–34, 2017. doi: 10.5194/esurf-2017-68. URL https://www.earth-surf-dynam-discuss.net/esurf-2017-68/. vii, 1, 11, 40, 42, 61, 88

Senfaute, G; Duperret, A, and Lawrence, J A. Micro-seismic precursory cracks prior to rock-fall on coastal chalk cliffs: a case study at Mesnil-Val, Normandie, NW France. *Natural Hazards and Earth System Sciences*, 9:1625–1641, 2009. 14, 42

Shelly, David R; Beroza, Gregory C; Ide, Satoshi, and Nakamula, Sho. Low-frequency earthquakes in shikoku, japan, and their relationship to episodic tremor and slip. *Nature*, 442 (7099):188, 2006. 34

Smith, A.; Dixon, N.; Meldrum, P.; Haslam, E., and Chambers, J. Acoustic emission monitoring of a soil slope: Comparisons with continuous deformation measurements. *Géotechnique Letters*, 4(4):255–261, 2014. doi: 10.1680/geolett.14.00053. 10, 108

Smith, A.; Dixon, N., and Fowmes, G. J. Early detection of first-time slope failures using acoustic emission measurements: large-scale physical modelling. *Géotechnique*, 67(2):138–152, 2017. doi: 10.1680/jgeot.15.P.200. 11, 20, 42, 108

Spillmann, Thomas; Maurer, Hansruedi; Green, Alan G.; Heincke, Björn; Willenberg, Heike, and Husen, Stephan. Microseismic investigation of an unstable mountain slope in the Swiss Alps. *Journal of Geophysical Research: Solid Earth*, 112(B7), 2007. ISSN 2156-2202. doi: 10.1029/2006JB004723. URL http://dx.doi.org/10.1029/2006JB004723. B07301. 11, 13, 21, 22, 23, 31, 46, 61, 70, 88

Stumpf, A.; Malet, J.-P.; Allemand, P., and Ulrich, P. Surface reconstruction and landslide displacement measurements with Pléiades satellite images. *ISPRS Journal of Photogrammetry and Remote Sensing*, 95:1–12, 2014. ISSN 0924-2716. doi: http://dx.doi.org/10.1016/j.isprsjprs.2014.05.008. URL http://www.sciencedirect.com/science/article/pii/S0924271614001269. 62, 76, 91

Stumpf, A.; Malet, J.-P.; Allemand, P.; Pierrot-Deseilligny, M., and Skupinski, G. Ground-based multi-view photogrammetry for the monitoring of landslide deformation and erosion.

Geomorphology, 231:130–145, 2015. ISSN 0169-555X. doi: http://dx.doi.org/10.1016/j.geomorph.2014.10.039. URL `http://www.sciencedirect.com/science/article/pii/S0169555X1400600X`. 62, 91

Stumpf, Andr' e and Kerle, Norman. Object-oriented mapping of landslides using Random Forests. *Remote Sensing of Environment*, 115(10):2564–2577, 2011. ISSN 0034-4257. doi: http://dx.doi.org/10.1016/j.rse.2011.05.013. URL `http://www.sciencedirect.com/science/article/pii/S0034425711001969`. 53, 62, 76

Stumpf, Andre; Malet, Jean-Philippe; Kerle, Norman; Niethammer, Uwe, and Rothmund, Sabrina. Image-based mapping of surface fissures for the investigation of landslide dynamics. *Geomorphology*, 186:12–27, 2013. ISSN 0169-555X. doi: http://dx.doi.org/10.1016/j.geomorph.2012.12.010. URL `http://www.sciencedirect.com/science/article/pii/S0169555X12005594`. xix, 18, 77, 78, 89, 101

Suriñach, E.; Furdada, G.; Sabot, F.; Biesca, B., and Vilaplana, J. M. On the characterization of seismic signals generated by snow avalanches for monitoring purposes. *Annals of Glaciology*, 32:268–274, 2001. doi: 10.3189/172756401781819634. 19, 23, 28

Suriñach, E; Vilajosana, I; Khazaradze, G; Biescas, B; Furdada, G, and Vilaplana, J M. Seismic detection and characterization of landslides and other mass movements. *Natural Hazards and Earth System Sciences*, 5:791–798, October 2005. doi: 10.5194/nhess-5-791-2005. URL `http://www.nat-hazards-earth-syst-sci.net/5/791/2005/nhess-5-791-2005.html`. 28

Surin, E; Sabot, F; Furdada, G; Vilaplana, JM, and others, . Study of seismic signals of artificially released snow avalanches for monitoring purposes. *Physics and Chemistry of the Earth, Part B: Hydrology, Oceans and Atmosphere*, 25(9):721–727, 2000. 10

Suwa, Hiroshi; Okano, Kazuyuki, and Kanno, Tadahiro. Behavior of debris flows monitored on test slopes of kamikamihorizawa creek, mount yakedake, japan. *International Journal of Erosion Control Engineering*, 2(2):33–45, 2009. 15

Taisne, B.; Brenguier, F.; Shapiro, N. M., and Ferrazzini, V. Imaging the dynamics of magma propagation using radiated seismic intensity. *Geophysical Research Letters*, 38(4), 2011. ISSN 1944-8007. doi: 10.1029/2010GL046068. URL `http://dx.doi.org/10.1029/2010GL046068`. L04304. 61, 67, 92

Tang, Chun'an; Li, Lianchong; Xu, Nuwen, and Ma, Ke. Microseismic monitoring and numerical simulation on the stability of high-steep rock slopes in hydropower engineering. *Journal of Rock Mechanics and Geotechnical Engineering*, 7(5):493 – 508, 2015. ISSN 1674-7755. doi: https://doi.org/10.1016/j.jrmge.2015.06.010. 11

Tarantola, Albert and Valette, Bernard. Generalized nonlinear inverse problems solved using the least squares criterion. *Reviews of Geophysics*, 20(2):219–232, 1982. ISSN 1944-9208. doi: 10.1029/RG020i002p00219. URL `http://dx.doi.org/10.1029/RG020i002p00219`. 68

Tary, Jean-Baptiste; Van der Baan, Mirko, and Eaton, David Wzfe. Interpretation of resonance frequencies recorded during hydraulic fracturing treatments. *Journal of Geophysical Research: Solid Earth*, 119(2):1295–1315, 2014a. ISSN 2169-9356. doi: 10.1002/2013JB010904. URL `http://dx.doi.org/10.1002/2013JB010904`. 19

Tary, Jean-Baptiste; Van der Baan, Mirko; Sutherland, Bruce, and Eaton, David W. Characteristics of fluid-induced resonances observed during microseismic monitoring. *Journal of Geophysical Research: Solid Earth*, 119(11):8207–8222, 2014b. ISSN 2169-9356. doi: 10.1002/2014JB011263. URL http://dx.doi.org/10.1002/2014JB011263. 19

Thomas, Amanda M.; Beroza, Gregory C., and Shelly, David R. Constraints on the source parameters of low-frequency earthquakes on the san andreas fault. *Geophysical Research Letters*, 43(4):1464–1471, 2016. ISSN 1944-8007. doi: 10.1002/2015GL067173. URL http://dx.doi.org/10.1002/2015GL067173. 2015GL067173. 34

Tonnellier, Alice; Helmstetter, Agnès; Malet, Jean-Philippe; Schmittbuhl, Jean; Corsini, Alessandro, and Joswig, Manfred. Seismic monitoring of soft-rock landslides: the Super-Sauze and Valoria case studies. *Geophysical Journal International*, 193(3):1515–1536, 2013. 2, 11, 13, 14, 21, 22, 31, 46, 47, 61, 62, 63, 65, 88, 89, 91, 95

Travelletti, J. and Malet, J.-P. Characterization of the 3D geometry of flow-like landslides: A methodology based on the integration of heterogeneous multi-source data. *Engineering Geology*, 128:30–48, 2012b. ISSN 0013-7952. doi: http://dx.doi.org/10.1016/j.enggeo.2011.05.003. URL http://www.sciencedirect.com/science/article/pii/S0013795211001165. 3, 62

Travelletti, Julien; Sailhac, Pascal; Malet, J-P; Grandjean, Gilles, and Ponton, J. Hydrological response of weathered clay-shale slopes: Water infiltration monitoring with time-lapse electrical resistivity tomography. *Hydrological Processes*, 26(14):2106–2119, 2012. 2

Uhlemann, Sebastian; Chambers, Jonathan; Wilkinson, Paul; Maurer, Hansruedi; Merritt, Andrew; Meldrum, Philip; Kuras, Oliver; Gunn, David; Smith, Alister, and Dijkstra, Tom. Four-dimensional imaging of moisture dynamics during landslide reactivation. *Journal of Geophysical Research: Earth Surface*, 122(1):398–418, 2017. 2

Van Asch, Th. W. J. Creep processes in landslides. *Earth Surface Processes and Landforms*, 9 (6):573–583, 1984. ISSN 1096-9837. doi: 10.1002/esp.3290090611. URL http://dx.doi.org/10.1002/esp.3290090611. 60

van Asch, Th.W.J.; Malet, J.-P., and van Beek, L.P.H. Influence of landslide geometry and kinematic deformation to describe the liquefaction of landslides: Some theoretical considerations. *Engineering Geology*, 88(1):59 – 69, 2006. ISSN 0013-7952. doi: https://doi.org/10.1016/j.enggeo.2006.08.002. URL http://www.sciencedirect.com/science/article/pii/S0013795206002407. 2, 60, 62, 89

Vázquez, R.; Suriñach, E.; Capra, L.; Arámbula-Mendoza, R., and Reyes-Dávila, G. Seismic characterisation of lahars at volcán de colima, mexico. *Bulletin of Volcanology*, 78(2):8, Feb 2016. ISSN 1432-0819. doi: 10.1007/s00445-016-1004-9. URL https://doi.org/10.1007/s00445-016-1004-9. 16, 19

Vilajosana, I; Suriñach, E; Abellán, A; Khazaradze, G; Garcia, D, and Llosa, J. Rockfall induced seismic signals: case study in Montserrat, Catalonia. *Natural Hazards and Earth System Sciences*, 8:805–812, 2008. doi: 10.5194/nhess-8-805-2008. URL http://www.nat-hazards-earth-syst-sci.net/8/805/2008/nhess-8-805-2008.html. 15, 65

Voisin, C.; Garambois, S.; Larose, E., and Massey, C. Seismic noise correlations and monitoring of the Utiku (New-Zealand) landslide. In *EGU General Assembly Conference Abstracts*, volume 15 of *EGU General Assembly Conference Abstracts*, pages EGU2013–5406, April 2013. 13

Von Rebeur-Paschwitz, Ernst. The earthquake of tokio, april 18, 1889. *Nature*, 40(1030):294, 1889. 1

Vouillamoz, N.; Rothmund, S., and Joswig, M. Characterizing the complexity of seismic signals at slow-moving clay-rich debris slides: The super-sauze (southeastern france) and pechgraben (upper austria) case studies. *Earth Surface Dynamics Discussions*, 2017:1–34, 2017. doi: 10.5194/esurf-2017-65. URL `https://www.earth-surf-dynam-discuss.net/esurf-2017-65/`. 13, 14, 31, 38, 65, 89

Walter, F.; Burtin, A.; McArdell, B. W.; Hovius, N.; Weder, B., and Turowski, J. M. Testing seismic amplitude source location for fast debris-flow detection at illgraben, switzerland. *Natural Hazards and Earth System Sciences*, 17(6):939–955, 2017a. doi: 10.5194/nhess-17-939-2017. URL `https://www.nat-hazards-earth-syst-sci.net/17/939/2017/`. 67

Walter, F.; Burtin, A.; McArdell, B. W.; Hovius, N.; Weder, B., and Turowski, J. M. Testing seismic amplitude source location for fast debris-flow detection at illgraben, switzerland. *Natural Hazards and Earth System Sciences*, 17(6):939–955, 2017b. doi: 10.5194/nhess-17-939-2017. URL `https://www.nat-hazards-earth-syst-sci.net/17/939/2017/`. 16, 21, 23, 28

Walter, Fabian; Dalban Canassy, Pierre; Husen, Stephan, and Clinton, John F. Deep icequakes: What happens at the base of Alpine glaciers? *Journal of Geophysical Research: Earth Surface*, 118(3):1720–1728, 2013a. ISSN 2169-9011. doi: 10.1002/jgrf.20124. URL `http://dx.doi.org/10.1002/jgrf.20124`. 18

Walter, M; Walser, M, and Joswig, M. Mapping rainfall-triggered slidequakes and seismic landslide-volume estimation at heumoes slopeall rights reserved. no part of this periodical may be reproduced or transmitted in any form or by any means, electronic or mechanical, including photocopying, recording, or any information storage and retrieval system, without permission in writing from the publisher. *Vadose Zone Journal*, 10(2):487–495, 2011. 2, 14, 89

Walter, M.; Arnhardt, C., and Joswig, M. Seismic monitoring of rockfalls, slide quakes, and fissure development at the Super-Sauze mudslide, French Alps. *Engineering Geology*, 128: 12–22, 2012a. ISSN 0013-7952. doi: http://dx.doi.org/10.1016/j.enggeo.2011.11.002. URL `http://www.sciencedirect.com/science/article/pii/S001379521100281X`. 2, 11, 13, 21, 47

Walter, M.; Arnhardt, C., and Joswig, M. Seismic monitoring of rockfalls, slide quakes, and fissure development at the Super-Sauze mudslide, French Alps. *Engineering Geology*, 128: 12–22, 2012b. ISSN 0013-7952. doi: http://dx.doi.org/10.1016/j.enggeo.2011.11.002. URL `http://www.sciencedirect.com/science/article/pii/S001379521100281X`. 61, 62, 65, 89

Walter, M.; Schwaderer, U., and Joswig, M. Seismic monitoring of precursory fracture signals from a destructive rockfall in the Vorarlberg Alps, Austria. *Natural Hazards and Earth System Sciences*, 12(11):3545–3555, 2012c. doi: 10.5194/nhess-12-3545-2012. URL `https://www.nat-hazards-earth-syst-sci.net/12/3545/2012/`. 88

Walter, Marco; Gomberg, Joan; Schulz, William; Bodin, Paul, and Joswig, Manfred. Slidequake generation versus viscous creep at softrock-landslides: Synopsis of three different scenarios at Slumgullion landslide, Heumoes slope, and Super-Sauze mudslide. *Journal of Environmental & Engineering Geophysics*, 18(4):269–280, 2013b. ISSN 1083-1363. doi: 10.2113/JEEG18.4.269. URL `http://jeeg.geoscienceworld.org/content/18/4/269`. 2, 11, 31, 46, 61, 65, 89

Wilkinson, PL; Anderson, MG, and Lloyd, DM. An integrated hydrological model for rain-induced landslide prediction. *Earth Surface Processes and Landforms*, 27(12):1285–1297, 2002. 88

Winberry, J. Paul; Anandakrishnan, Sridhar; Wiens, Douglas A.; Alley, Richard B., and Christianson, Knut. Dynamics of stick-slip motion, Whillans Ice Stream, Antarctica. *Earth and Planetary Science Letters*, 305(3):283 – 289, 2011. ISSN 0012-821X. doi: https://doi.org/10.1016/j.epsl.2011.02.052. URL `http://www.sciencedirect.com/science/article/pii/S0012821X11001312`. 18

Worni, Raphael; Huggel, Christian; Stoffel, M., and Pulgarín, B. Challenges of modeling current very large lahars at nevado del huila volcano, colombia. *Bulletin of Volcanology*, 74(2):309–324, Mar 2012. doi: 10.1007/s00445-011-0522-8. 16

Yamada, M; H, Kumagai; Y, Matsushi, and T, Matsuzawa. Dynamic landslide processes revealed by broadband seismic records. *Geophysical Research Letters*, 40:2998–3002, 2013. doi: 10.1002/grl.50437. 1

Yamada, Masumi; Mori, Jim, and Matsushi, Yuki. Possible stick-slip behavior before the Rausu landslide inferred from repeating seismic events. *Geophysical Research Letters*, 43(17):9038–9044, 2016. ISSN 1944-8007. doi: 10.1002/2016GL069288. URL `http://dx.doi.org/10.1002/2016GL069288`. 2016GL069288. 60, 61

Yamada, Masumi; Mangeney, Anne; Matsushi, Yuki, and Moretti, Laurent. Estimation of dynamic friction of the akatani landslide from seismic waveform inversion and numerical simulation. *Geophysical Journal International*, 206(3):1479–1486, 2016a. doi: 10.1093/gji/ggw216. URL `+http://dx.doi.org/10.1093/gji/ggw216`. vii, 1, 13, 22, 42

Yamada, Masumi; Mori, Jim, and Matsushi, Yuki. Possible stick-slip behavior before the Rausu landslide inferred from repeating seismic events. *Geophysical Research Letters*, 43(17):9038–9044, 2016b. ISSN 1944-8007. doi: 10.1002/2016GL069288. URL `http://dx.doi.org/10.1002/2016GL069288`. 2016GL069288. 11

Yin, HY; Huang, CJ; Chen, CY; Fang, YM; Lee, BJ, and Chou, TY. The present development of debris flow monitoring technology in taiwan—a case study presentation. In *5th International Conference on Debris-Flow Hazards Mitigation: Mechanics, Prediction and Assessment, edited by: Genevois, R., Hamilton, DL, and Prestininzi, A., Casa Editrice Universita La Sapienza, Roma*, pages 623–631, 2011. 16

Zigone, Dimitri; Voisin, Christophe; Larose, Eric; Renard, François, and Campillo, Michel. Slip acceleration generates seismic tremor like signals in friction experiments. *Geophysical Research Letters*, 38(1), 2011. ISSN 1944-8007. doi: 10.1029/2010GL045603. URL `http://dx.doi.org/10.1029/2010GL045603`. L01315. 18

Zimmer, Valerie L and Sitar, Nicholas. Detection and location of rock falls using seismic and infrasound sensors. *Engineering Geology*, 193:49–60, 2015. 15

Zobin, Vyacheslav M; Plascencia, Imelda; Reyes, Gabriel, and Navarro, Carlos. The characteristics of seismic signals produced by lahars and pyroclastic flows: Volcán de Colima, México. *Journal of Volcanology and Geothermal Research*, 179(1-2):157–167, 2009. 16

Résumé :

Ce projet de recherche vise à accroître les connaissances sur les mécanismes contrôlant la déformation des glissements de terrain argileux grâce à la combinaison de la surveillance sismique passive et de la surveillance géodésique. Des études récentes ont démontré que la surveillance sismique peut fournir des informations intéressantes sur la mécanique des glissements de terrain et, dans certains cas, fournir des précurseurs utiles pour la prévision des défaillances. L'installation récente de sismomètres sur les glissements de terrain a révélé une variété de signaux sismiques de magnitude (ML $<$ 1) soupçonnaient être générés par la déformation de la pente (chute, basculement, glissement, écoulement), Cette sismicité endogène doit être catégorisée. Une classification standard des sources sismiques endogènes est ainsi proposée; l'objectif de cette norme est de pouvoir comparer l'activité sismique de plusieurs glissements de terrain et d'identifier les mécanismes générant ces signaux sismiques ainsi que leur corrélation avec les forçages externes. Plusieurs propriétés de signal (durée, contenu spectral et forme de spectrogramme) sont prises en compte pour décrire les différentes classes de signaux et permettre une comparaison générique. Les observations montrent que des signaux similaires enregistrés sur différents sites présentent les mêmes propriétés et les sources sismiques possibles sont discutées compte tenu du type de déformation observé sur les pentes étudiées. Ces propriétés de signal sont utilisées comme caractéristiques pour classer les sources endogènes à l'aide d'algorithmes d'apprentissage automatique. En effet, la classification manuelle des enregistrements sismologiques longs prend du temps et peut être très subjective. Une méthode de classification automatique basée sur le calcul de 71 attributs sismiques et l'utilisation d'un classificateur supervisé est ainsi proposée. Aucun attribut n'a été sélectionné à priori afin de créer une méthode de classification générique multi-classes applicable à de nombreux contextes de glissements de terrain. La méthode peut être appliquée directement sur les résultats d'un détecteur simple. L'algorithme automatique récupère près de 90\% de sensibilité par rapport à un catalogue interprété manuellement considéré comme référence. Une nouvelle méthode (APOLoc) pour automatiser la localisation des sources sismiques est ensuite proposée. La localisation de la source est un problème difficile sur les glissements de terrain à cause des limitations imposées soit par la détection des erreurs sur l'arrivée des ondes sismiques, soit par l'utilisation de modèles de vitesse sismique inappropriés (ou trop simplistes). La méthode développée est itérative et utilise un modèle de vitesse précis à onde P (construit à partir de profils sismiques de réfraction) pour localiser les sources. Le prélèvement des ondes P est effectué initialement avec un algorithme basé sur Kurtosis et une première estimation de la localisation est calculée en analysant l'amplitude du signal; la sélection et la localisation sont ensuite améliorées de manière itérative jusqu'à ce que la corrélation des premières arrivées soit maximisée. Enfin, des catalogues avancés de sources sismiques sont construits pour des périodes d'observation à long terme et à court terme sur des glissements de terrain sélectionnés. Le nombre d'événements, leurs propriétés et leur emplacement sont corrélés au modèle de déformation de surface mesuré par les données radar GNSS et au sol et aux paramètres environnementaux tels que les précipitations, la fonte des neiges et les pressions interstitielles. Les taux d'activité sismique sont analysés et le régime de déformation de la pente est discuté. L'approche et les méthodes sont développées et testées sur les bases de données sismologiques et géodésiques acquises lors du glissement de Super-Sauze (Alpes du Sud-Est).

Mots-clés : Glissement de terrain, micro-sismicité/écoute sismique, tomographie sismique, machine learning, localisation de source.

Abstract :

This research project aims at increasing knowledge on the mechanisms controlling the deformation of clayey landslides through the combination of passive seismic and geodetic monitoring. Recent studies have demonstrated that seismic monitoring is able to give interesting information on landslide mechanics and in some case to provide precursory patterns useful for failure forecasting. The recent installation of seismometers on landslides revealed a variety of seismic signals of law magnitude (ML $<$ 1) suspected to be generated by slope deformation (falling, toppling, sliding, flowing), weathering of the slope material or fluid circulation. This endogenous seismicity needs to be categorized. We thus proposed a standard classification of the endogenous seismic sources; the objective of this standard is to be able to compare the seismic activity of several landslides and identify the mechanisms generating these seismic signals as well as their correlation with external forcing. Several signal properties (i.e. duration, spectral content and spectrogram shape) are taken into account to describe the different class of signals and allow generic comparison. We observe that similar signals recorded at different sites present the same properties and discussed the possible seismic sources considering the type of deformation observed on the studied slopes. These signal properties are used as features to classify the endogenous sources using machine learning algorithms. Indeed, manual classification of long seismological records is time-consuming and may be highly subjective. We proposed an automatic classification method based on the computation of 71 seismic attributes and the use of a supervised classifier. No attribute was selected a priori in order to create a generic multi-class classification method applicable to many landslide contexts. The method can be applied directly on the results of a simple detector. The automatic algorithm retrieves nearly 90\% of sensitivity in comparison to a manually interpreted catalogs considered as references. We then proposed a new method (APOLoc) for automatizing seismic source location. Source location is a difficult problem on landslides because of the limitations imposed either by picking errors on the seismic waves arrival and by the use of inappropriate (or too simplistic) seismic velocity models. We propose a methodology to take into account these two sources of error. The methodology is iterative and uses an accurate P-wave velocity model (constructed from refraction seismic profiles) to locate the sources. The picking of the P-wave arrivals is performed initially with a Kurtosis-based algorithm and a first estimate of the location is calculated by analyzing the amplitude of the signal; the picking and the location are then iteratively improved until the correlation of the first arrivals is maximized. Finally, advanced catalogs of seismic sources are constructed for both long-term and short-term observation periods at selected landslides. The number of events, their properties and their location are correlated to the surface deformation pattern measured by GNSS and ground-based radar data, and to environmental parameters such as rainfall, snowmelt and pore-water pressures. Seismic activity rates are analyzed, and the regime of slope deformation are discussed. The approach and the methods are developed and tested on the seismological and geodetic datasets acquired at the Super-Sauze landslide (Southeast French Alps).

Keywords : Landslide, landslide micro-seismicity, seismic tomography, machine learning, source location.